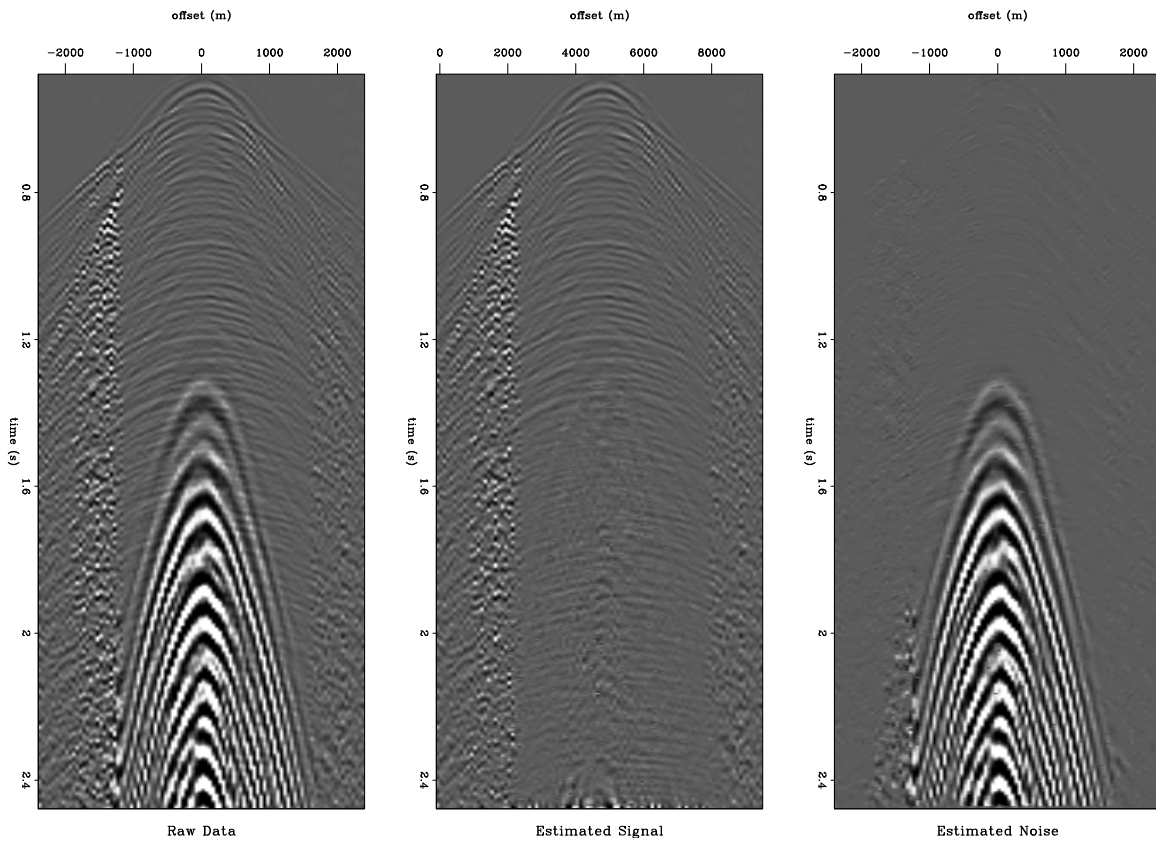


STANFORD EXPLORATION PROJECT

*Patricia Berge, James Berryman, Biondo Biondi, Brian Bonner, Morgan Brown,
Jon Claerbout, Robert Clapp, Sean Crawley, Sergey Fomel, Kurt Marfurt, Carmen Mora,
Marie Prucha, James Rickett, Paul Sava, Louis Vaillant, and Yi Zhao*

Report Number 102, October 1999



Copyright © 2001

by the Board of Trustees of the Leland Stanford Junior University

Stanford, California 94305

*Copying permitted for all internal purposes of the Sponsors of
Stanford Exploration Project*

Preface

The electronic version of this report¹ makes the included programs and applications available to the reader. The markings [ER], [CR], and [NR], are promises by the author about the reproducibility of each figure result.

Reproducibility is a way of organizing computational research, which allows both the author and the reader of a publication to verify the reported results at a later time. Reproducibility facilitates the transfer of knowledge within SEP and between SEP and its sponsors.

ER denotes Easily Reproducible and are the results of a processing described in the paper. The author claims that you can reproduce such a figure from the programs, parameters, and makefiles included in the electronic document. We assume you have a UNIX workstation with Fortran, Fortran90, C, X-Windows system and the software downloadable from our website (SEP makerules, SEPlib, and SEP latex package). Before the publication of the electronic document, someone other than the author tests the author's claim by destroying and rebuilding all ER figures. Some ER figures may not be reproducible by outsiders because they depend on data sets that are too large to distribute, or data that we do not have permission to redistribute.

CR denotes Conditional Reproducibility. The author certifies that the commands are in place to reproduce the figure if certain resources are available. SEP staff have only attempted to make sure that the makefile rules exist and the source codes referenced are provided. Some of the reason for the CR designation are: a proprietary data set, a parallel computer, a large amount of processing time (20 minutes or more), or commercial packages such as Matlab or Mathematica.

NR denotes Non-Reproducible. This class of figure is considered non-reproducible. SEP discourages authors from flagging their figures as NR except for artist drawings, scanings, etc.

Our testing is currently limited to IRIX 6.5 and LINUX 2.1, but the code should be portable to other architectures. Reader's suggestions are welcome. For more information on reproducing SEP's electronic documents, please visit

<<http://sepwww.stanford.edu/redoc/>>.

Jon Claerbout, Biondo Biondi, Robert Clapp, and Sergey Fomel

¹<http://sepwww.stanford.edu/private/docs/sep102>

SEP-102 — TABLE OF CONTENTS

Imaging

<i>Vaillant L. and Sava P.</i> , Common-azimuth migration of a North Sea dataset	1
<i>Biondi B.</i> , Offset plane waves vs. common-azimuth migration for sub-salt imaging	15
<i>Clapp R. G., Fomel S., and Prucha M.</i> , Iterative resolution estimation in Kirchhoff imaging	35
<i>Sava P.</i> , Enhancing common-image gathers with prestack Stolt residual migration	47
<i>Sava P.</i> , On Stolt common-azimuth residual migration	59
<i>Vaillant L. and Fomel S.</i> , On Stolt stretch time migration	65

Multidimensional filtering

<i>Crawley S.</i> , Interpolating missing data: convergence and accuracy, t and f	75
<i>Clapp R. G. and Brown M.</i> , Applying SEP's latest tricks to the multiple suppression problem	89
<i>Fomel S.</i> , Plane wave prediction in 3-D	99
<i>Brown M., Clapp R. G., and Marfurt K.</i> , Predictive signal/noise separation of ground-roll-contaminated data	109
<i>Rickett J.</i> , On non-stationary convolution and inverse convolution	125
<i>Prucha M.</i> , Revisiting the half-derivative filter	133

Reservoir characterization

<i>Berryman J. G., Berge P. A., and Bonner B. P.</i> , Estimating rock porosity and fluid saturation using only seismic velocities	139
<i>Mora C. and Biondi B.</i> , Seismic attribute sensitivity to velocity uncertainty	153
<i>Brown M. and Clapp R. G.</i> , Seismic pattern recognition via predictive signal/noise separation	175
<i>Berryman J. G.</i> , Origin of Gassmann's equations	185
<i>Berryman J. G.</i> , Seismic velocity decrement ratios for regions of partial melt near the core-mantle boundary	191

Hardware and Software

<i>Clapp R. G.</i> , Additions to SEPlib	199
<i>Clapp R. G., Brown M., Vaillant L., Mora C., Prucha M., and Zhao Y.</i> , SEP's data library .	217
<i>Biondi B., Clapp R. G., and Rickett J.</i> , Testing Linux multiprocessors for seismic imaging .	233
<i>Prucha M. L., Clapp R. G., Fomel S., Claerbout J., and Biondi B.</i> , Reproducible research - results from SEP-100	247
SEP article published or in press, 2000-01	253
SEP phone directory	255
Research personnel	257
SEP sponsors for 2000-01	261

Common-azimuth migration of a North Sea dataset

Louis Vaillant and Paul Sava¹

ABSTRACT

3-D prestack common-azimuth depth migration has a strong potential for imaging accurately complex media and handling multi-pathing. We apply the technique to North Sea real data for imaging a salt dome. The results obtained demonstrate the efficiency of the method in complex media. A detailed analysis of common-image gathers shows opportunities for improving the velocity model.

INTRODUCTION

Wave-equation migration techniques have benefited from a renewed interest now that some shortcomings of Kirchhoff migration have been highlighted (O'Brien and Etgen, 1998). Moreover, intensive computing resources now make 3-D prestack depth migration feasible with such techniques. Based on a recursive extrapolation of the recorded wavefield, wave-equation migration methods are potentially better able to handle multi-pathing problems induced by complex velocity structures. Thus, they offer an attractive alternative to Kirchhoff methods (Mosher et al., 1997; Biondi, 1997). Moreover, wave propagation is modeled out of the asymptotic approximation context.

Common-azimuth migration (Biondi and Palacharla, 1996) is a 3-D prestack depth migration technique based on the wave equation. It exploits the intrinsic narrow-azimuth nature of marine data to reduce its dimensionality and thus manages to cut the computational cost of 3-D imaging significantly. In this paper, we discuss the first application of this imaging technique to real data at SEP. For this purpose, Elf Aquitaine provided us with an interesting dataset recorded in the North Sea, which shows a salt dome and other 3-D structures. The complexity of the wave propagation in the medium, resulting from high velocity contrasts (lateral and longitudinal), yields multi-pathing and illumination problems, which makes this model both a serious challenge for imaging and an interesting test case for the common-azimuth migration.

DATA CHARACTERISTICS AND PROCESSING

Figure 1 shows a section of a velocity model created from our real dataset. It illustrates the most important interfaces and the lithology of the medium. This section has been used

¹email: louis@sep.stanford.edu, paul@sep.stanford.edu

to generate finite-difference synthetic data by Elf Aquitaine in cooperation with IFP² and has proved to be a test case for imaging below salt flanks (Prucha et al., 1998; Malcotti and Biondi, 1998). The geologic interpretation proposed by IFP comes from the analysis of the real dataset. This geologic model will be referred to regularly in this paper.

The recorded data covers an area of 13.5×4 km for a whole volume of seismic information as big as 45 gigabytes. The first step of our processing was to perform a gridding of the whole volume and then to apply a simple sequence $NMO/binning/NMO^{-1}$ for regularizing the data. As a first approach to the imaging problem, we stacked the data and migrated them using a 3-D zero-offset extended split-step algorithm (Stoffa et al., 1990). In order to get these preliminary results more quickly, we used this first migrated cube to extract a subset (Figure 1) from the whole data, which includes most target regions of interest, such as the top of salt and the salt flanks.

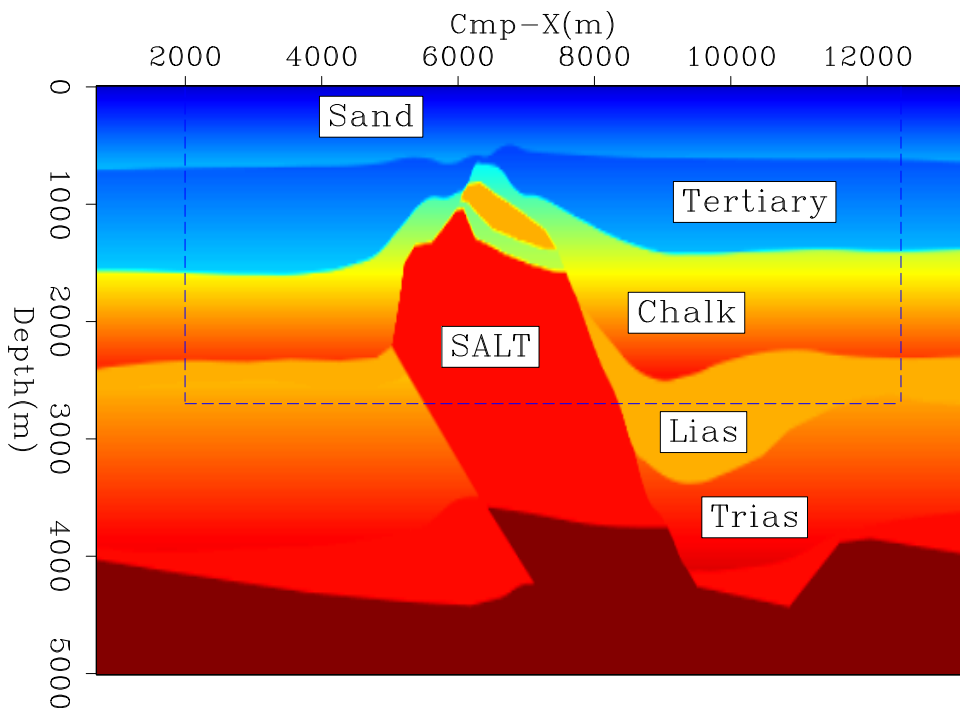


Figure 1: Synthetic velocity model elaborated from the North Sea data, with its lithology. The dashed box represents the subset migrated in this study. `louis1-L7d-vel-synth` [CR]

Because we wanted to examine how robust the method was with respect to lateral velocity variations, both in the cross-line and the in-line direction, we kept all the data along the Cmp-Y axis. By resampling the data in Cmp-X and in offset (Table 1) at the limit of aliasing, we reduced the cube dimension to less than 20 gigabytes, which is more reasonable costwise. From now on, “data” will always refer to this particular subset.

One could object that the most important imaging challenge for this particular model would be to focus the base of salt accurately, since it probably corresponds to the most com-

²Institut Français du Pétrole

plex propagation for the wavefield through the body itself. However, we chose not to image all the way down in this first test in order to limit the computational time. We also focused on improving the velocity model in the upper part. This choice helps us image deeper regions accurately, as we will see in the last sections of the paper.

	Cmp-X range	Cmp-X sampling	Cmp-Y range	Cmp-Y sampling	Offset range	Offset sampling
Raw data	0-13500 m	13.33 m	1600-5600 m	25.0 m	185-3570 m	25 m
Subset	2000-12500 m	20.0 m	1600-5600 m	25.0 m	200-3400 m	50 m

Table 1: Geometrical characteristics of the selected data

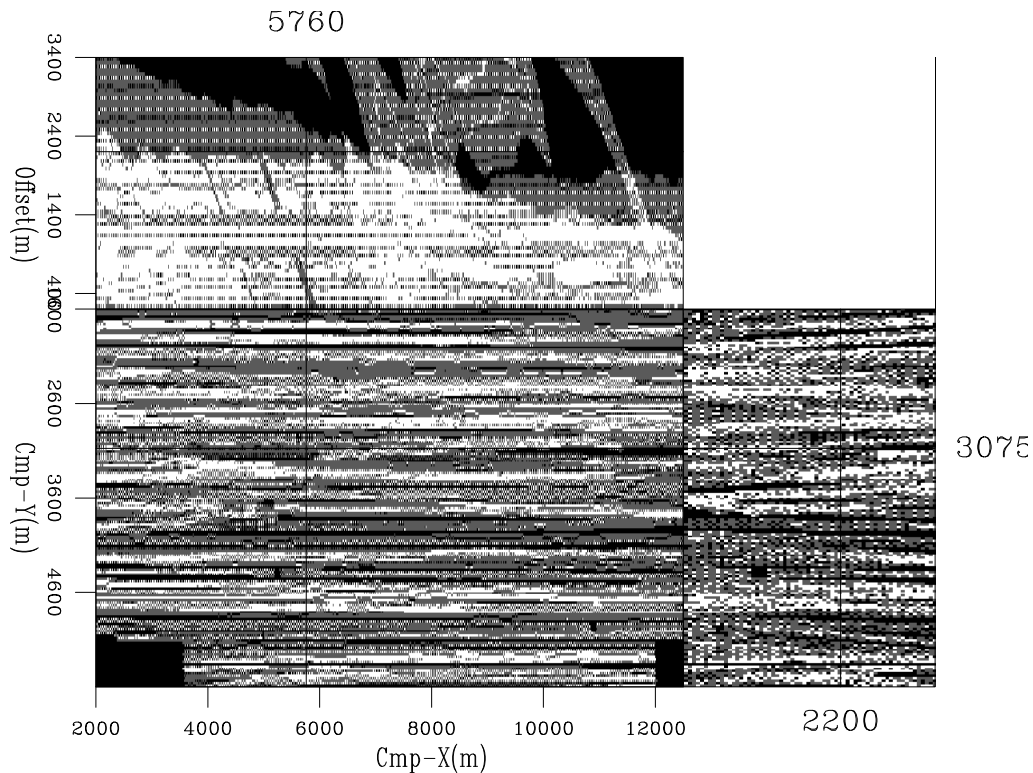


Figure 2: 3-D fold map of the data gridded with the parameters presented in Table 1. “Black” is zero-fold, and “white” corresponds to 8 traces per bin. `louis1-L7d-subset-fold` [CR]

After this gridding, the data shows an irregular repartition, especially on Cmp-X vs. offset planes (Figure 2). Apparently, several geophones in the middle of the streamers went down during the acquisition, which yields a very irregular fold for the binning and large areas with no offset information.

Azimuth moveout (Biondi et al., 1998) is the operator usually used for transforming the data to common-azimuth and putting them on a regular grid. We estimated that performing AMO on our data would need 7 days of computation, which is not negligible compared to

the cost of the migration itself (see paragraph below). Since the data were concentrated in a narrow azimuth band, we instead used a simple binning procedure, normalized by the fold. AMO will be used for a further comparison in the near future.

The common-azimuth data obtained by NMO/binning/NMO⁻¹ were migrated down to 2700m, with a depth spacing of 12.5m. We used 6 reference velocities for the extended split-step scheme that performs migration. With the dimensions indicated in Table 2, the 3-D prestack common azimuth migration ran in 26 days on 4 processors of our SGI Power Challenge (18 MIPS R8000 Processors, 2 Gbytes of memory). To put this in context, the zero-offset migration took about 12 hours on only 2 processors of the same machine.

	Number of samples					
	Cmp-X	Cmp-Y	Depth	Offset	Frequencies	Velocities
Subset	525	160	216	64	150	6

Table 2: Dimensions of the data and migration quantities

COMMON-AZIMUTH IMAGING RESULTS

Figure 3 shows a typical set of sections in the middle of the migrated cube. In the in-line section, the shallower part down to 1500m reveals high frequency details accurately imaged. The migration enhanced a graben structure, with normal faults and rocked blocks, around location Cmp-X=8000m, close to the top in the sand layer. The most energetic interfaces in the section, located approximately at depth 1500m, correspond to the limit tertiary/chalk in the geologic interpretation presented in Figure 1. The velocity model indicates a strong velocity contrast there, with more than 1000m/s difference between the two media.

The horizontal section at depth 900m highlights complex patterns inside the tertiary layer, imaged with a high resolution. Those can be interpreted as turbidite channels. The main direction of slumping is along the in-line, away from the salt dome. We can infer as a hypothesis that the upcoming salt may be the cause of the flow and of the resedimentation.

Both the depth section and the cross-line section show an oblique fault through the chalk layer just above the salt body. On one side of the fault inside the chalk appears a strong reflector, like a block of salt separated from the main body, or perhaps another lithologic feature. The bottom interface of the chalk layer with the Lias is imaged accurately.

The salt body in itself is well delimited on its right side. The top-left boundary is well focused after migration, though with a weaker amplitude. Although we can observe the sediments in the chalk bent upwards by the upcoming salt on the left-hand side, the boundary itself is not clearly recovered by the migration. We expect it to be almost vertical, with the beginning of the overhang below depth 2500m. In the cross-line direction, the top of salt reveals a complex shape, as seen in that section. The imaging there seems satisfactory, and the top of salt is quite continuous.

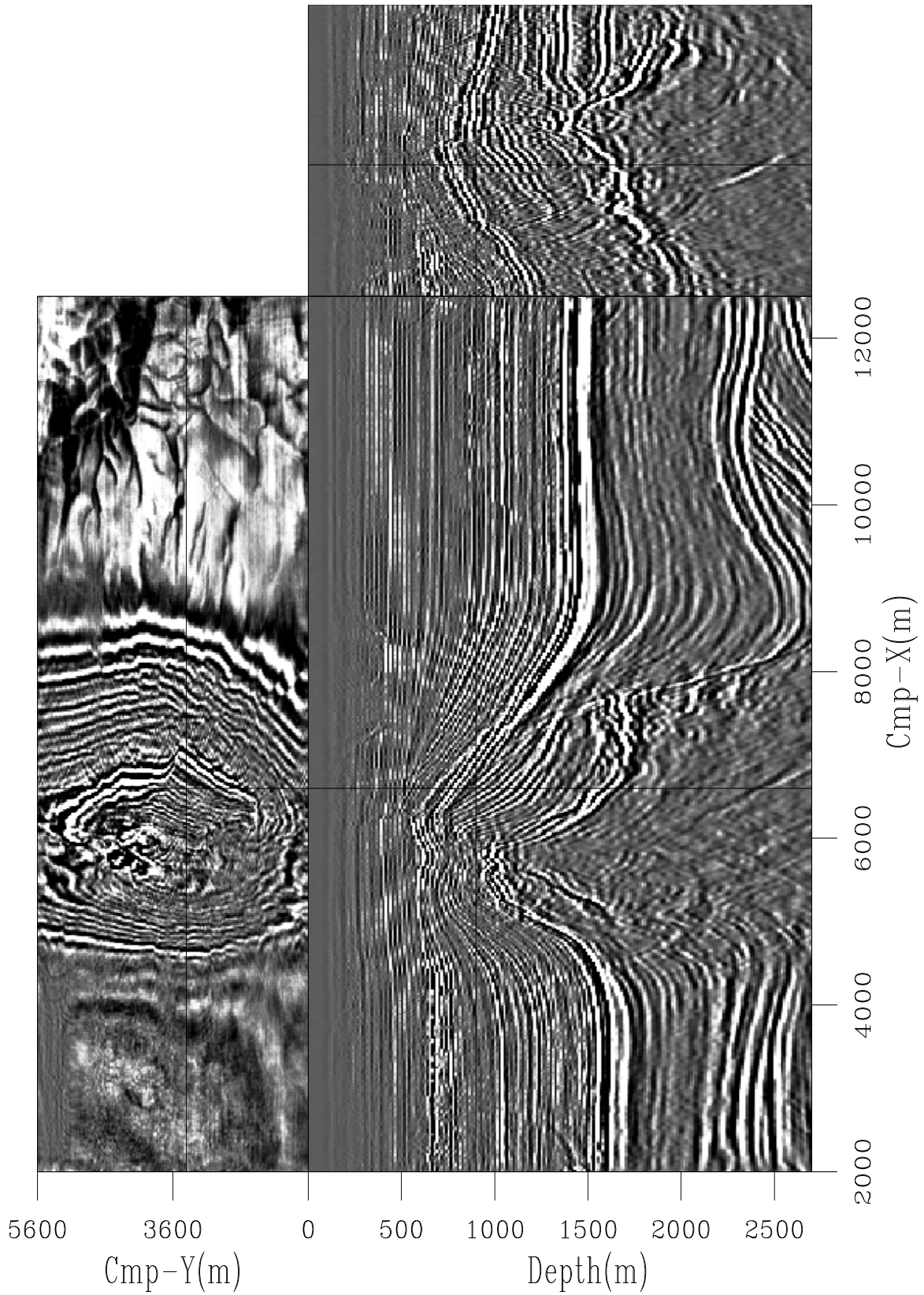


Figure 3: Sections of the migrated data at location: depth=900m, Cmp-X=6600m, Cmp-Y=3400m. `louis1-L7d-ComAz-mig-all` [CR]

Seismic imaging can be sketched as a two-step process: velocity estimation and migration. All modern migration algorithms require a simple and reliable way to extract prestack information for velocity estimation and updating. For this purpose, 3-D angle-domain common-image gathers can be easily computed in the wavenumber domain from the output of common-azimuth migration (Prucha et al., 1999; Sava, 1999). Those panels enhance valuable information for analysis when the velocity model is complex and induces multi-pathing.

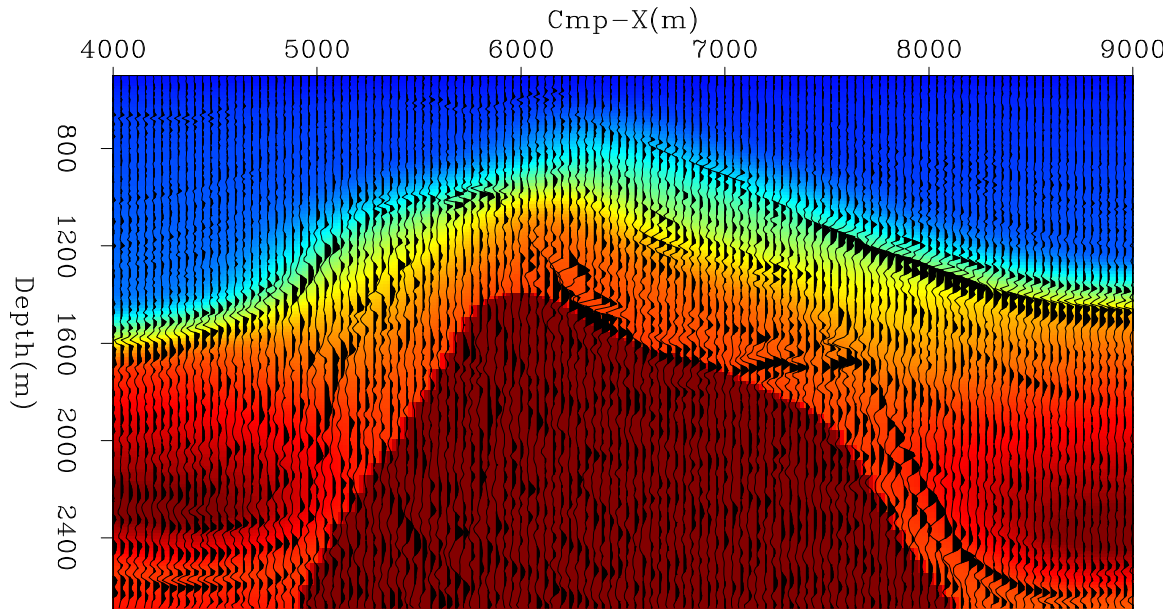


Figure 4: Close-up of the salt body. The near-angle migrated section has been superimposed on the velocity model. [louis1-L7d-ysect1-and-vel](#) [CR]

Figure 5 shows the same in-line section as before ($Cmp-Y=3400m$), with examples of the angle-domain common-image gathers that can be obtained from the migrated image. Unlike the image in figure 3, the section is not a stack over the angle axis but instead a near-angle image. Even if it increases the noise level, it also displays more events that are not stacked coherently because the velocity is not perfect. For the sake of clarity, we will next focus on this particular in-line section and will use it as a support for the analysis of our migration results.

In figure 5, panels (a) and (b) show that the reflectors corresponding to the interface Tertiary/salt are well aligned along the angle axis. Similarly, in panel (c), the complex interface chalk/Lias/Trias at the bottom-right of the section reveals flat gathers. The velocity at these interfaces is well determined. The top and the left-hand side of the salt body (panels (a) and (b)) are not perfectly flattened in the gathers. The inclusion labeled “I” above the salt that causes an energetic reflection yields a slightly high velocity anomaly since it is not accounted for in the velocity model (see figure 4).

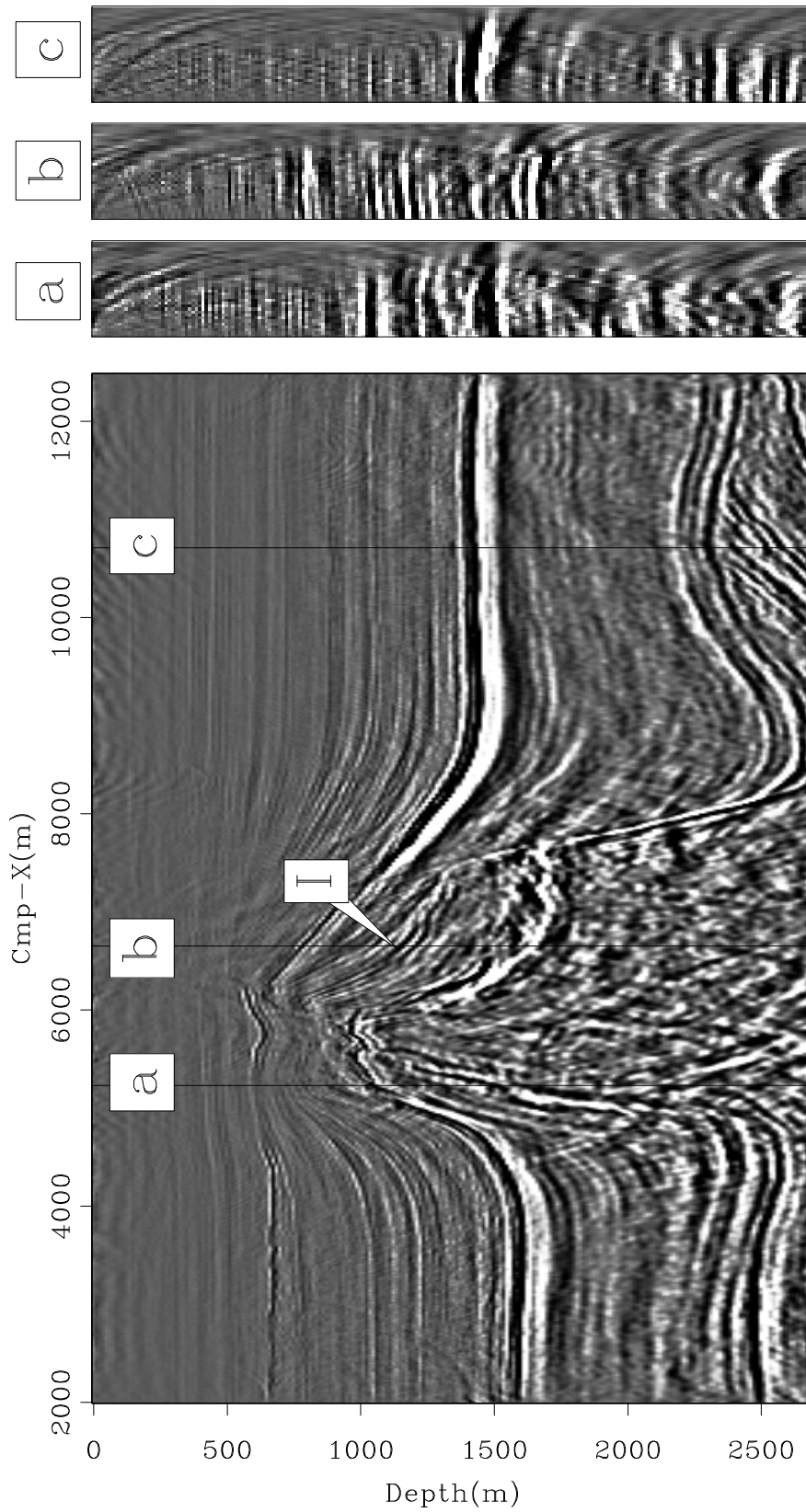


Figure 5: In-line near-angle section at location Cmp-Y=3400m and several angle-domain common-image gathers (a), (b) and (c) `louis1-L7d-ang-ysect1-set1` [CR]

DISCUSSION

The velocity model we used for the migration was obtained by reflection tomography using the S.M.A.R.T³ method (Jacobs et al., 1992; Ehinger and Lailly, 1995). We smoothed their result before running the common-azimuth migration. Our smoothing scheme preserved the exact shape of the salt body to avoid high velocity spreading into the surrounding model, which would degrade imaging.

Figure 6 shows common-image gathers along our main in-line section, illustrating details of the salt boundaries. When searching for these boundaries on the left-hand side, the event marked “R” seems relatively coherent compared to the ratio of noise that can be observed inside the salt. It may reasonably correspond to the salt flank we hope to image on the left-hand side. The event could as well be an internal multiple created by reflections on Tertiary/chalk or chalk/salt interfaces around event “I”. Additionally, Ogilvie and Purnell (1996) show how converted waves can also create spurious events sufficiently high in amplitude to confound interpretation.

If “R” is effectively the salt flank, its location after migration remains inaccurate, since we would expect it to be immediately against the reflectors bending upwards in the chalk. This event possibly comes from a wavefield seriously distorted while traveling through the salt body and recorded at large Cmp-X locations. In contrast, the salt boundary closer to the top is better migrated since the waves have not propagated through the dome and have instead been recorded at small Cmp-X locations. Panel (a) illustrates this hypothesis, showing flat gathers for the top of the salt edge and, below, reflectors bending upwards with angle around reflector “R”.

Furthermore, panels (b) and (c) intersect an area where the continuity of the salt top is broken. At this particular location, the zero-offset migration, being less sensitive to velocity variations, yields more continuous imaging (Figure 7). The common-image gathers show reflectors bending upwards, indicating a too low velocity. Similarly, on the right-hand side, the salt flank shows a too low velocity (panel (d)).

We can see from the analysis of common-image gathers that the velocity model obviously needs further improvements. Figure 4 shows the salt boundaries in the migrated section superimposed on the velocity model we used for imaging. Performing accurate imaging, especially deeper in the model, requires a more precise relocation of the major reflectors, such as the salt edges, with respect to the velocity model.

For this purpose, the information provided by the common-image gathers can be reinvested in a residual migration process to improve the focusing of the migrated sections. The next step, which is less straightforward, is to update the velocity model from the perturbation between the starting and the improved images (Biondi and Sava, 1999). This remains an open research subject.

Last, we compare the result of 3-D prestack common-azimuth migration with the 3-D

³Sequential Migration-Aided Reflection Tomography - KIM (Kinematic Inversion Methods), IFP consortium

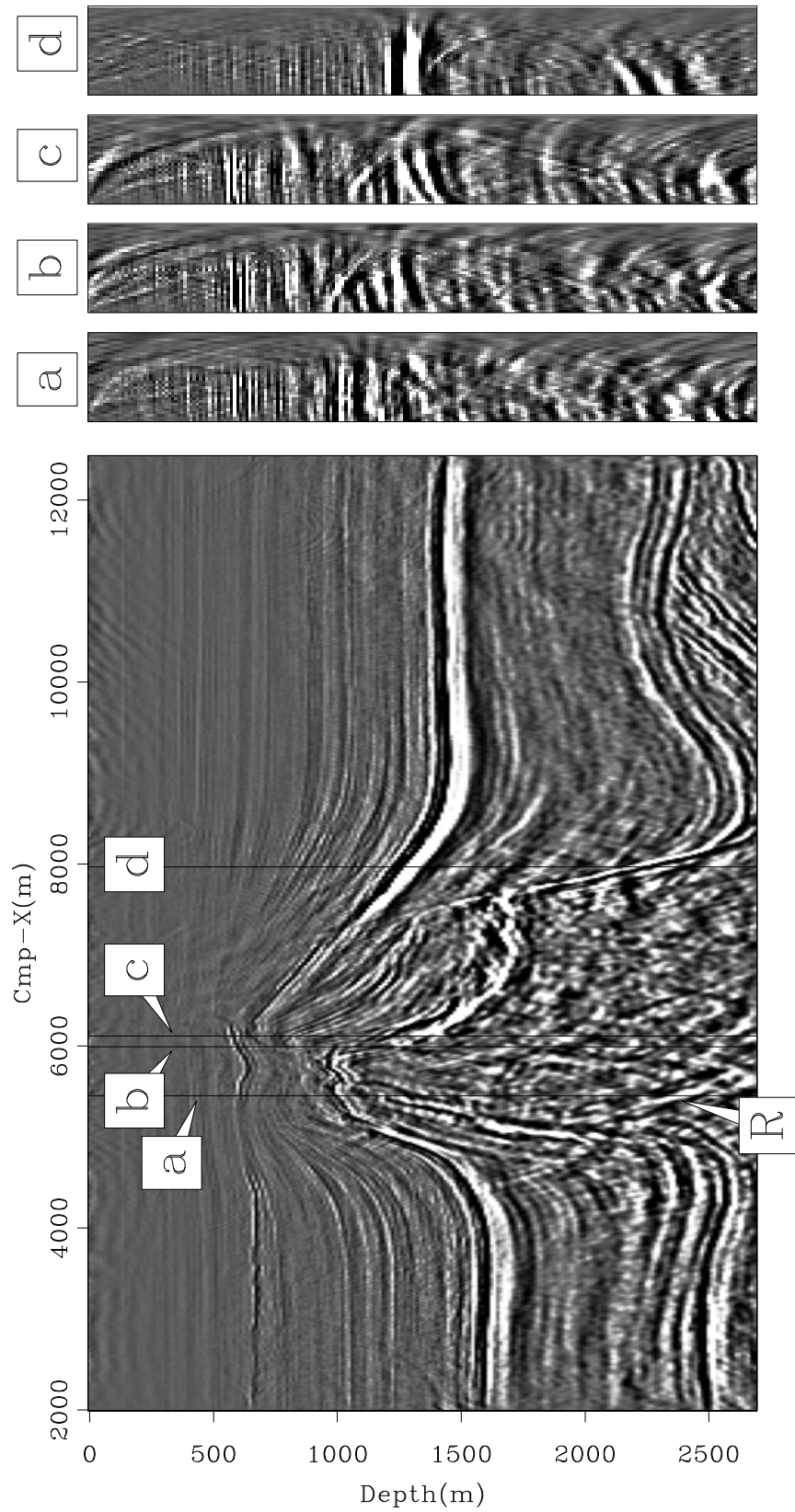


Figure 6: In-line near-angle section at location Cmp-Y=3400m with angle-domain common-image gathers [louis1-L7d-ang-ysect1-set2] [CR]

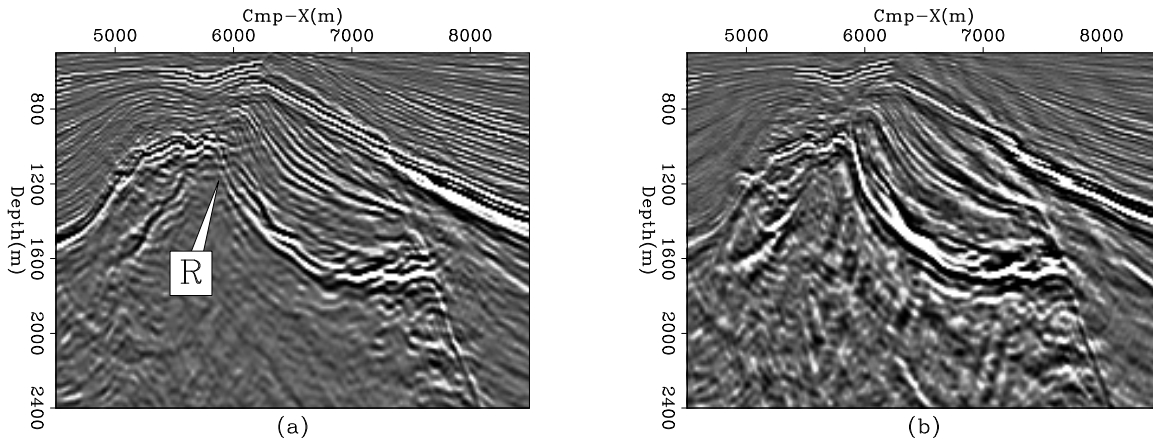


Figure 7: Close-up of the salt dome for the common-azimuth migrated image (a) and the section migrated with zero-offset extended split-step algorithm (b). “R” points out the reflector of interest. The clip percentile is the same on both images (96). `louis1-L7d-salt-ComAz-and-ZOmig` [CR]

prestack preserved-amplitude depth migration (PAPsDM) result, courtesy of the Ecole des Mines de Paris (Xu et al., 1999). Figure 8 shows both results, which are derived from the same velocity model. However, their implementation of the ray+Born formalism (Thierry et al., 1999a,b) for elaborating the PAPsDM algorithm yields an image in impedance perturbation rather than in reflectivity (as in the case of 3-D prestack common-azimuth migration). In order to make the migrated images more comparable, we differentiated their result along the depth axis. Although this conserves the shapes of the reflectors, the conversion to reflectivity implies (in theory) differencing perpendicularly to the reflectors, which is not straightforward.

Both sections (a) and (b) in figure 8 display many similarities. The sides of the salt body seem accurately imaged in both cases, especially on the left-hand side where the chalk layer bends upwards. However, common-azimuth migration produces a result significantly more accurate for the top of salt and for the complex lithologic interfaces in that area. Moreover, the reflector marked “S”, which may correspond to the salt boundary, is not visible in the PAPsDM image. The PAPsDM migrated section could probably be improved by using a larger offset range in the cross-line direction (700m here). Interestingly enough, handling multiple arrivals does not yield a significantly better image, since the result of 3-D PAPsDM with, respectively, first, strongest, and multiple arrival are similar at 97% (Gilles Lambaré, personal communication).

CONCLUSION

Real data offers an opportunity to test our imaging techniques further. Common-azimuth migration is an attractive method for seismic imaging in complex media and remains a subject for further research. Its computational cost, illustrated in this particular example, can make it an attractive alternative to widespread Kirchhoff methods. The imaging of the North Sea

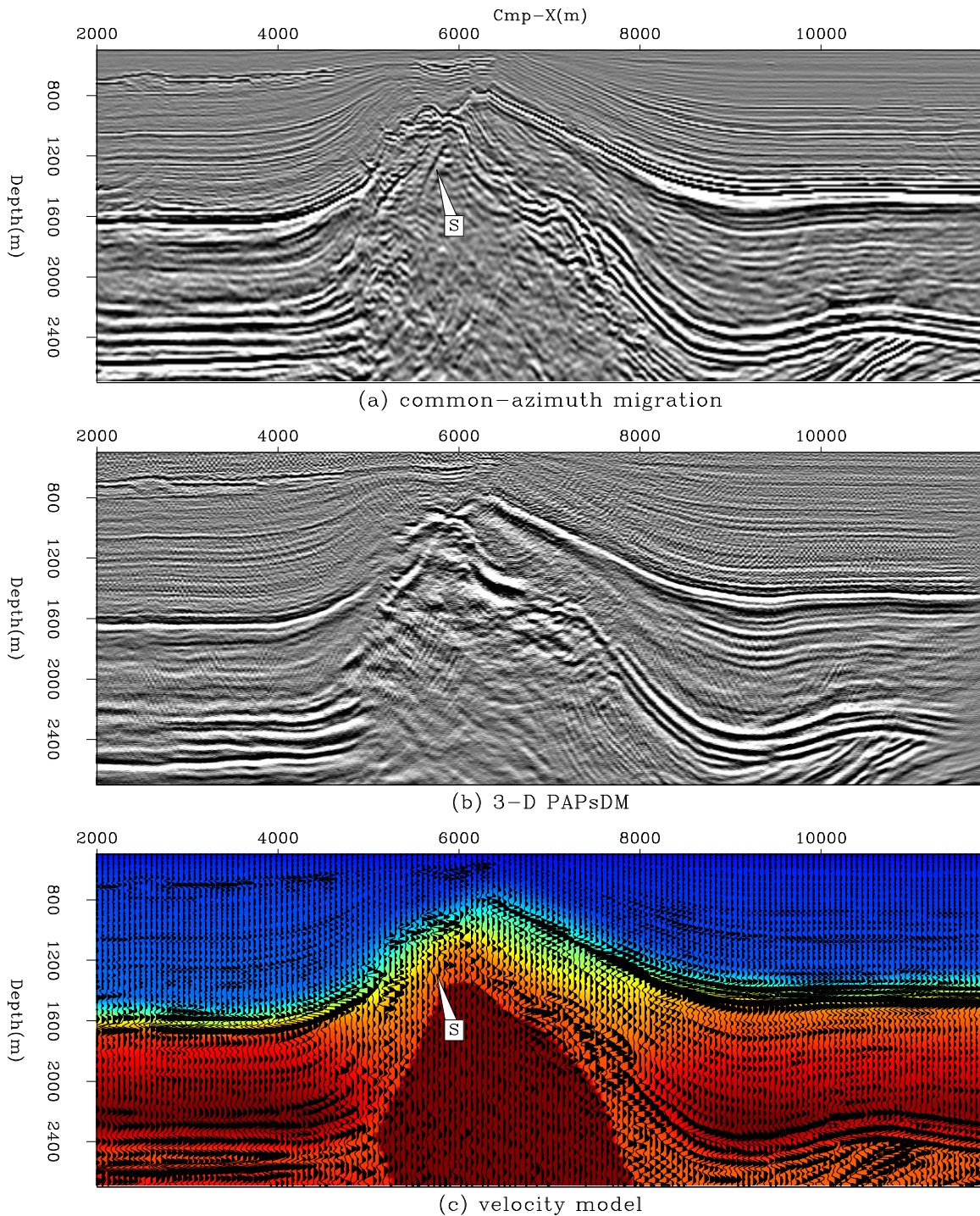


Figure 8: Comparison between the sections at Cmp-X=4100m migrated using 3-D prestack common-azimuth migration (a) and 3-D PAPS DM (b). The third section (c) shows the common-azimuth migrated image superimposed on the velocity model. The PAPS DM result is courtesy of the Ecole des Mines de Paris. [louis1-L7d-ComAz-vs-PAPS DM] [CR]

data reveals lithologic structures focused with high resolution. Angle-domain common-image gathers highlight imaging insufficiencies around the steepest parts of salt flanks. They also offer opportunities for residual migration and velocity estimation. An extended migration scheme, which incorporates a wider range of data in the cross-line direction to account for lateral velocity variations, is being examined (Vaillant and Biondi, 1999).

ACKNOWLEDGEMENTS

The authors would like to thank Elf Aquitaine for providing the data and the velocity model and the research group of the Ecole des Mines de Paris for sharing their results with us. Sincere thanks to Bob Clapp as well, who concurrently developed an upgraded version of SEPlib3D that can now handle huge 3-D datasets and made this study possible. We would like to acknowledge Biondo Biondi for his useful comments and stimulating discussions.

REFERENCES

- Biondi, B., and Palacharla, G., 1996, 3-D prestack migration of common-azimuth data: *Geophysics*, **61**, no. 6, 1822–1832.
- Biondi, B., and Sava, P., 1999, Wave-equation migration velocity analysis: *SEP-100*, 11–34.
- Biondi, B., Fomel, S., and Chemingui, N., 1998, Azimuth moveout for 3-D prestack imaging: *Geophysics*, **63**, no. 2, 574–588.
- Biondi, B., 1997, Azimuth moveout + common-azimuth migration: Cost-effective prestack depth imaging of marine data: 67th Annual Internat. Mtg., Soc. Expl. Geophys., Expanded Abstracts, 1375–1378.
- Ehinger, A., and Lailly, P., 1995, Velocity model determination by the SMART method, part 1: Theory: 65th Annual Internat. Mtg., Soc. Expl. Geophys., Expanded Abstracts, 739–742.
- Jacobs, J. A. C., Delprat-Jannaud, F., Ehinger, A., and Lailly, P., 1992, Sequential migration-aided reflection tomography: A tool for imaging complex structures: 62nd Annual Internat. Mtg., Soc. Expl. Geophys., Expanded Abstracts, 1054–1057.
- Malcotti, H., and Biondi, B., 1998, Accurate linear interpolation in the extended split-step migration: *SEP-97*, 61–72.
- Mosher, C. C., Foster, D. J., and Hassanzadeh, S., 1997, Common angle imaging with offset plane waves: 67th Annual Internat. Mtg., Soc. Expl. Geophys., Expanded Abstracts, 1379–1382.
- O'Brien, M. J., and Etgen, J. T., 1998, Wavefield imaging of complex structures with sparse point-receiver data: 68th Annual Internat. Mtg., Soc. Expl. Geophys., Expanded Abstracts, 1365–1368.

- Ogilvie, J. S., and Purnell, G. W., 1996, Effects of salt-related mode conversions on subsalt prospecting: *Geophysics*, **61**, no. 2, 331–348.
- Prucha, M. L., Clapp, R. G., and Biondi, B. L., 1998, Imaging under the edges of salt bodies: Analysis of an Elf North Sea dataset: *SEP-97*, 35–44.
- Prucha, M. L., Biondi, B. L., and Symes, W. W., 1999, Angle-domain common image gathers by wave-equation migration: *SEP-100*, 101–112.
- Sava, P., 1999, Enhancing common-image gathers with prestack Stolt residual migration: *SEP-102*, 47–60.
- Stoffa, P. L., Fokkema, J. T., de Luna Freire, R. M., and Kessinger, W. P., 1990, Split-step Fourier migration: *Geophysics*, **55**, no. 4, 410–421.
- Thierry, P., Lambaré, G., Podvin, P., and Noble, M., 1999a, 3-D preserved amplitude prestack depth migration on a workstation: *Geophysics*, **64**, no. 1, 222–229.
- Thierry, P., Operto, S., and Lambaré, G., 1999b, Fast 2-D ray+Born migration/inversion in complex media: *Geophysics*, **64**, no. 1, 162–181.
- Vaillant, L., and Biondi, B., 1999, Extending common-azimuth migration: *SEP-100*, 125–134.
- Xu, S., Thierry, P., and Lambaré, G., 1999, 3-D migration/inversion in complex media: 69th Annual Internat. Mtg., Soc. Expl. Geophys., Expanded Abstracts, to be presented.

Offset plane waves vs. common-azimuth migration for sub-salt imaging

*Biondo Biondi*¹

ABSTRACT

Offset plane wave migration and common-azimuth migration are among the most promising wave-equation migration methods for efficiently imaging 3-D marine data sets. Offset plane wave migration has some computational advantages over common-azimuth migration, but common-azimuth is more accurate. Sub-salt images produced by common-azimuth migration are better focused than the corresponding images produced by offset plane wave migration. These differences can be attributed to an approximation intrinsic to offset plane wave migration: the offset plane wave components are downward continued separately, instead of being allowed to mix as they should be in media with laterally varying velocity.

Offset plane wave migration also approximates the cross-line offset ray parameter of the plane-waves with zero. A theoretical analysis of the migration errors caused by this approximation is confirmed by the imaging results. The shallow reflectors dipping at 45 degrees with respect to the acquisition axes are poorly imaged by offset plane wave migration.

INTRODUCTION

In a previous report (Biondi, 1999a) I showed that common-azimuth prestack migration produces better sub-salt images than a single arrival Kirchhoff migration. In this report Vaillant and Sava (1999) show excellent preliminary results of common-azimuth migration of a salt body in the North Sea, and again favorable comparison with the results obtained using a most-energetic arrival Kirchhoff-like migration. The evidence is mounting that wave-equation migration, even when applied using approximate methods as common-azimuth, has the potential to produce better images than Kirchhoff methods when strong lateral velocity variations cause multi-pathing of the reflected energy. Full-volume imaging of deep targets when steep reflectors require huge migration aperture is another area of applications for efficient wave-equation migration methods that is gaining interest. In these cases the cost of Kirchhoff migration is large, and downward continuation methods become attractive from the computational point of view.

¹email: biondo@sep.stanford.edu

Offset plane wave migration (Ottolini and Claerbout, 1984; Mosher et al., 1997) is another approximate wave-equation method that has been recently applied to the migration of 3-D prestack marine data. Offset plane wave migration is related to common-azimuth migration, and has similar computational complexity. Therefore, a comparison between the two is of both practical and theoretical interest. Both methods have been applied to marine data transformed to common-azimuth data, and achieve computational efficiency by restricting the computational domain to a 4-D space from the 5-D space that is required by full downward continuation. Offset plane wave migration has the additional computational advantage that it can be performed as several independent migrations of 3-D cubes, while common-azimuth migration requires, at least in principle, to be performed on the whole 4-D data set simultaneously. This difference means that offset-plane wave migration requires less computations (about 10%) and has lower minimum-memory requirements to run efficiently. Though, for both methods the memory requirements are manageable on modern computers because the computational domain is further decomposed in temporal-frequency components. On the other hand, downward continuing the offset plane waves separately introduces errors when migration velocity has strong lateral variations, as in the case of sub-salt imaging. In this paper I show example of migration errors related to this approximation.

Another approximation introduced by offset plane wave migration is neglecting the cross-line component of the offset plane wave ray parameter vector and setting its value equal to zero. In this paper, I study the effects of this approximation with a theoretical analysis and with migration results. The approximation affects mostly the migration accuracy of reflections recorded at large offset from shallow reflectors with dips oriented at an angle with respect to the acquisition axes. The demonstration of this phenomenon is quite simple. It is based on the analytical proof that in constant velocity neglecting the cross-line component of the offset plane wave ray parameter vector is equivalent to reversing the correct order of two-pass migration. The correct order for two-pass prestack migration is: in-line prestack migration followed by cross-line zero-offset migration (Biondi, 1999b; Rosa et al., 1999). On the contrary, offset plane wave migration is equivalent to performing a cross-line zero offset migration followed by an in-line prestack migration.

The reversing of the correct order of two-pass migration produces the largest errors for shallow reflectors and large offsets. The errors become negligible for deep reflectors. Offset plane wave migration is thus a valuable tool for producing full-volume images of deep targets below relatively mild velocity functions, such as the imaging of salt flanks in deep waters. On the contrary, when shallow reflectors are important, or when strong lateral velocity variations are present, common-azimuth migration produces better images.

EFFICIENT WAVE-EQUATION MIGRATIONS OF COMMON-AZIMUTH DATA

The full downward continuation of 3-D prestack data can be expressed in the frequency-wavenumber domain by the following phase-shift operator

$$D_{z+\Delta z}(\omega, \mathbf{k}_m, \mathbf{k}_h) \approx D_z(\omega, \mathbf{k}_m, \mathbf{k}_h) e^{-ik_z \Delta z}, \quad (1)$$

where ω is the temporal frequency, \mathbf{k}_m is the midpoint-wavenumber vector, \mathbf{k}_h is the offset-wavenumber vector, and $v(\mathbf{s}, z)$ and $v(\mathbf{g}, z)$ are respectively the velocity at the source and receivers locations. The vertical wavenumber k_z is given by the Double Square Root (DSR),

$$k_z = \sqrt{\frac{\omega^2}{v^2(\mathbf{s}, z)} - \frac{1}{4} [(k_{x_m} - k_{x_h})^2 + (k_{y_m} - k_{y_h})^2]} + \sqrt{\frac{\omega^2}{v^2(\mathbf{g}, z)} - \frac{1}{4} [(k_{x_m} + k_{x_h})^2 + (k_{y_m} + k_{y_h})^2]}. \quad (2)$$

This operator is a function of the cross-line component of the offset wavenumber k_{y_h} , while common-azimuth data are independent of k_{y_h} because they are different from zero only at $y_h = 0$. Therefore, the exact full downward continuation is performed by applying a 5-D operator on a data set that is only 4-D. While accurate, this procedure is tremendously wasteful of computational efforts, because only a small subset of the 5-D wavefield contributes to the final image. The final image is formed by extracting the zero-offset cube from the downward-continued wavefield. This data extraction is equivalent to the summation of the wavefield along both offset-wavenumber axes. Most of the wavefield components destructively interfere in the imaging step. In fact, only a 4-D slice of the 5-D wavefield contributes to the image when no multipathing occurs, such as in constant velocity or in a vertically layered media. Even when multipathing occurs, most of the wavefield components destructively interfere in the imaging step.

It is therefore natural to limit the computational cost by reducing the dimensionality of the downward continuation operator from 5-D to 4-D. Both common-azimuth migration and offset plane wave migration achieve this goal, though in different ways.

Common-azimuth downward continuation

Common azimuth migration reduces the dimensionality of the continuation operator by restricting the wavefield to be common-azimuth at every depth level. It can be demonstrated that this approximation is exact in constant velocity (Biondi and Palacharla, 1996). This geometric condition is equivalent to selecting one particular value for the cross-line component of the offset wavenumber k_{y_h} as a function of the frequency ω , the other wavenumbers $(k_{x_m}, k_{y_m}, k_{x_h})$, and the propagation velocities $[v(\mathbf{g}, z), v(\mathbf{s}, z)]$. This value for k_{y_h} is then substituted into the expression for the full DSR of equation (2), to obtain the common-azimuth downward-continuation operator.

The analytical expression for k_{y_h} can be either obtained by geometric considerations or by a stationary-phase analysis, and is given as

$$\widehat{k}_{y_h} = k_{y_m} \frac{\sqrt{\frac{\omega^2}{v^2(\mathbf{g},z)} - \frac{1}{4}(k_{x_m} + k_{x_h})^2} - \sqrt{\frac{\omega^2}{v^2(\mathbf{s},z)} - \frac{1}{4}(k_{x_m} - k_{x_h})^2}}{\sqrt{\frac{\omega^2}{v^2(\mathbf{g},z)} - \frac{1}{4}(k_{x_m} + k_{x_h})^2} + \sqrt{\frac{\omega^2}{v^2(\mathbf{s},z)} - \frac{1}{4}(k_{x_m} - k_{x_h})^2}}. \quad (3)$$

The common-azimuth dispersion relation that is obtained by substituting equation (3) into equation (2) can be recast, after some algebraic manipulations, as a cascade of two dispersion relations. The first performs 2-D prestack downward-continuation along the in-line direction:

$$k_{z_x} = \sqrt{\frac{\omega^2}{v^2(\mathbf{s},z)} - \frac{1}{4}(k_{x_m} - k_{x_h})^2} + \sqrt{\frac{\omega^2}{v^2(\mathbf{g},z)} - \frac{1}{4}(k_{x_m} + k_{x_h})^2}, \quad (4)$$

and the second performs 2-D zero-offset downward continuation along the cross-line axis:

$$\widehat{k}_z = \sqrt{k_{z_x}^2 - k_{y_m}^2}. \quad (5)$$

This rewriting of the common-azimuth dispersion connects common-azimuth migration to the theory of two-pass migration. In the special case of constant velocity, this connection is easily established through Stolt migration formalism (Stolt, 1978). Stolt migration is performed by stretching the temporal frequency (or the vertical wavenumber axis) according to the dispersion relation used for downward continuation. The cascade of two Stolt migrations is equivalent to a single Stolt migration that uses the cascade of the two dispersion relations.

In particular, common-azimuth Stolt migration is equivalent to in-line prestack Stolt migration followed by Stolt cross-line zero-offset migration. In the next section, we will show that this two-pass migration is also kinematically equivalent to the exact full-prestack migration of common-azimuth data.

Offset plane-wave downward continuation

Offset plane wave migration reduces the computational complexity of downward continuation of common-azimuth data one step further than common-azimuth migration does. It approximates the application of the full 5-D operator expressed in equation (2) with the application of several 3-D downward continuation operators. These 3-D operators are applied to common-azimuth data after plane-wave decomposition along the offset axis. The first step of the method is thus the decomposition of the common-azimuth data into offset plane waves. Each plane wave is then independently downward continued. Full downward continuation of offset plane waves could be performed by applying following operator

$$D_{z+\Delta z}(\omega, \mathbf{k}_m, \mathbf{p}_h) \approx D_z(\omega, \mathbf{k}_m, \mathbf{p}_h) e^{-ik_z \Delta z}, \quad (6)$$

where the vertical wavenumber k_z is now function of the offset plane wave parameters $p_{x_h} = k_{x_h}/\omega$ and $p_{y_h} = k_{y_h}/\omega$; that is,

$$k_z = \sqrt{\frac{\omega^2}{v^2(\mathbf{s}, z)} - \frac{1}{4} \left[(k_{x_m} - \omega p_{x_h})^2 + (k_{y_m} - \omega p_{y_h})^2 \right]} + \sqrt{\frac{\omega^2}{v^2(\mathbf{g}, z)} - \frac{1}{4} \left[(k_{x_m} + \omega p_{x_h})^2 + (k_{y_m} + \omega p_{y_h})^2 \right]}. \quad (7)$$

Strictly speaking, only in vertically layered media can each plane wave be downward continued independently. The plane waves should be allowed to mix at each depth step when lateral velocity variations occur. Therefore, the computationally attractive feature of imaging each plane wave independently also causes limitations in accuracy. These limitations are difficult to study analytically, and thus in a following section I will analyze their effects by comparing migration results below a complex overburden (eg. a salt body).

In practice, because common-azimuth data has no cross-line offset axis, the plane wave decomposition is performed only as a function of the in-line offset ray parameter p_{x_h} , and the cross-line offset ray parameter p_{y_h} is assumed to be zero. This assumption introduces another approximation in the migration operator, that can be studied analytically.

When p_{y_h} is set to zero, equation (7) becomes:

$$\bar{k}_z = \sqrt{\frac{\omega^2}{v^2(\mathbf{s}, z)} - \frac{k_{y_m}^2}{4} - \frac{1}{4} (k_{x_m} - \omega p_{x_h})^2} + \sqrt{\frac{\omega^2}{v^2(\mathbf{g}, z)} - \frac{k_{y_m}^2}{4} - \frac{1}{4} (k_{x_m} + \omega p_{x_h})^2}. \quad (8)$$

This equation is equivalent to the offset plane wave equation presented by Mosher et al. (1997).²

It is easy to verify that if we assume $v(\mathbf{s}, z) \approx v(\mathbf{g}, z) = v(\mathbf{m}, z)$, the dispersion relation of equation (8) can be expressed as the cascade of a zero-offset downward continuation along the cross-line direction:

$$k_{z_y} = \sqrt{\frac{\omega^2}{v^2(\mathbf{m}, z)} - \frac{k_{y_m}^2}{4}}, \quad (9)$$

and prestack downward continuation along the in-line direction:

$$\bar{k}_z = \sqrt{k_{z_y}^2 - \frac{1}{4} (k_{x_m} - \omega p_{x_h})^2} + \sqrt{k_{z_y}^2 - \frac{1}{4} (k_{x_m} + \omega p_{x_h})^2}. \quad (10)$$

The interpretation of this decomposition is similar to the one discussed above for common-azimuth migration. A constant velocity offset plane wave migration that uses the dispersion relation of equation (8) is equivalent to a constant-velocity cross-line zero-offset migration, followed by a constant-velocity in-line prestack migration. The order between these migrations is thus reversed with respect to the correct order. We analyze the implications of this order reversal in the following section.

²Equation (8) is the same as equation (13) in their abstract.

COMPARING CONSTANT-VELOCITY MIGRATION OPERATORS

In constant velocity the summation surface of 3-D prestack migration is

$$t_D = \sqrt{\frac{z_\xi^2}{V^2} + \frac{(x_\xi - x_m + x_h)^2 + (y_\xi - y_m)^2}{V^2}} + \sqrt{\frac{z_\xi^2}{V^2} + \frac{(x_\xi - x_m - x_h)^2 + (y_\xi - y_m)^2}{V^2}}, \quad (11)$$

where (z_ξ, x_ξ, y_ξ) are the coordinates of the image point, (x_m, y_m) are the midpoint coordinates in data space, x_h is the in-line offset in data space, t_D is recording time in data space, and V is the medium velocity.

It is easy to verify that this summation surface is equivalent to the summation surface defined by the cascade of the two following expressions:

$$t_D = \sqrt{\frac{z_{\bar{x}}^2}{V^2} + \frac{(x_\xi - x_m + x_h)^2}{V^2}} + \sqrt{\frac{z_{\bar{x}}^2}{V^2} + \frac{(x_\xi - x_m - x_h)^2}{V^2}}, \quad (12)$$

$$z_{\bar{x}} = \sqrt{z_\xi^2 + (y_\xi - y_m)^2}. \quad (13)$$

Equation (12) defines the summation path for 2-D prestack migration and corresponds to the dispersion relation in equation (4). Equation (13) defines the summation path for 2-D zero-offset migration and corresponds to the dispersion relation in equation (5). The straightforward interpretation of this result is that two-pass migration, in the correct order, is equivalent to full prestack migration, when the velocity is constant.

The dispersion relations of offset plane wave migration [equation (9) and equation (10)] respectively correspond to the following summation paths

$$t_D = \sqrt{\frac{z_{\bar{y}}^2}{V^2} + \frac{4(y_\xi - y_m)^2}{V^2}}, \quad (14)$$

$$z_{\bar{y}} = \sqrt{z_\xi^2 + (x_\xi - x_m + x_h)^2} + \sqrt{z_\xi^2 + (x_\xi - x_m - x_h)^2}. \quad (15)$$

The summation surface of offset plane wave migration is thus equivalent the cascade of these two paths. As noted before, the order of the two migration is reversed with respect to the correct one, and thus errors are introduced in the migration operator.

Figure 1 provides an intuitive understanding of the approximations involved in reversing the order of the migrations. The grey surface shown in the left panel of Figure 1 is the summation surface that should be used to image a diffractor at 500 m depth from data at a constant offset of 4,000 m, and assuming a constant velocity of 2,500 m/s. Two sets of contour lines are superimposed onto the surface. The inner set of contour lines corresponds to the exact summation surface, while the outer one corresponds to the surface defined by cascading the paths defined in equation (14) and equation (15). The right panel of Figure 1 shows the

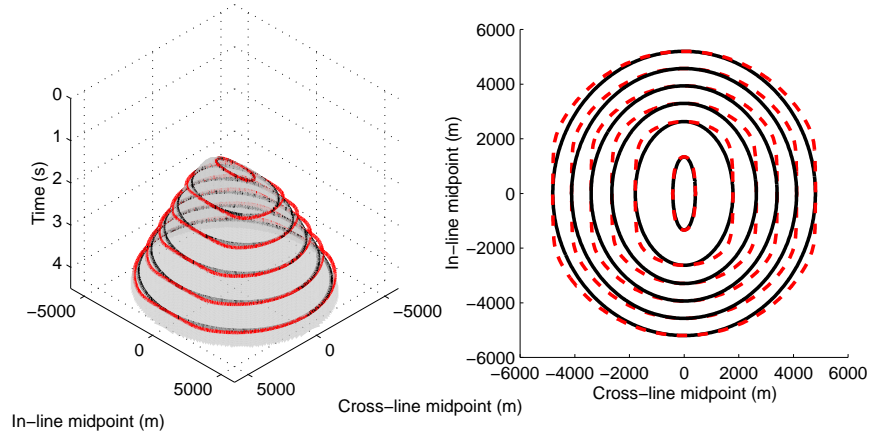


Figure 1: The grey surface shown in the left panel is the exact summation surface to image a diffractor at 500 m depth from data at a constant offset of 4,000 m, and assuming a constant velocity of 2,500 m/s. The solid contour lines correspond to the exact summation surface, while the dashed contour lines correspond to the approximate summation surface.

`biondo1-planecheops` [ER]

same contour lines in plane view. The solid lines correspond to the exact summation surface, while the dashed lines correspond to the approximate summation surface. Figure 1 graphically demonstrates that even in constant velocity, offset plane wave migration introduces an error for reflectors that are not exactly dipping in either the in-line direction or the cross-line direction.

The analysis of the offset plane wave migration impulse response, or spreading surface, provides an alternative perspective to the analysis of the migration errors. The spreading surface of full 3-D prestack migration is the ellipsoid:

$$\frac{4(x_{\xi} - x_m)^2}{t_D^2 V^2} + \frac{4(y_{\xi} - y_m)^2}{t_D^2 V^2 - 4h^2} + \frac{4z_{\xi}^2}{t_D^2 V^2 - 4h^2} = 1. \quad (16)$$

It can be split as the cascade of the in-line prestack migration ellipse:

$$\frac{4(x_{\xi} - x_m)^2}{t_D^2 V^2} + \frac{4z_{\bar{x}}^2}{t_D^2 V^2 - 4h^2} = 1, \quad (17)$$

and the cross-line zero-offset semicircle:

$$\frac{(y_{\xi} - y_m)^2}{z_{\bar{x}}^2} + \frac{z_{\xi}^2}{z_{\bar{x}}^2} = 1. \quad (18)$$

The impulse response of offset plane wave migration, as defined by the dispersion relation in equation (8), is defined by the cascade of the following two impulse responses

$$\frac{4(y_{\xi} - y_m)^2}{t_D^2 V^2} + \frac{z_{\bar{y}}^2}{t_D^2 V^2} = 1, \quad (19)$$

$$\frac{4(x_{\xi} - x_m)^2}{z_{\bar{y}}^2} + \frac{4z_{\xi}^2}{z_{\bar{y}}^2 - 4h^2} = 1. \quad (20)$$

Figure 2 compares the exact impulse response of 3-D prestack migration and the offset plane wave approximation. The grey surface shown in the left panel of Figure 2 is the exact spreading surface for an impulse recorded at 2.5 s, at an offset of 4,000 m, and assuming a constant velocity of 2,500 m/s. The inner set of contour lines corresponds to the exact summation surface, while the outer one corresponds to the surface defined by cascading the paths defined in equation (19) and equation (20). The right panel of Figure 2 shows the same contour lines in plane view. The solid lines correspond to the exact spreading surface, while the dashed lines correspond to the approximate spreading surface. It is apparent that the approximation is worse for shallow reflectors dipping at 45 degrees with respect to the acquisition axes. This qualitative analysis is confirmed by the numerical results shown in the next section.

At zero offset the order of the in-line and cross-line migrations is obviously irrelevant; it is intuitive that the errors introduced by reversing the correct migration order increases with offset. To analyze the errors as a function of offset, Figure 3 compares the exact impulse response of 3-D prestack migration and the offset plane wave approximation at an offset of 8,000 m, and assuming the same constant velocity as in Figure 2 (2,500 m/s). The left panel of Figure 3 shows the exact spreading surface for an impulse recorded at 3.73 s. To make Figure 3 directly comparable with Figure 2, the impulse time was chosen to locate the bottom of the ellipsoid at exactly the same depth as in Figure 2, and the contour lines were drawn at the same depths as in Figure 2. It is apparent that at constant reflector depth the errors increase as the offset increases.

MIGRATION RESULTS OF THE SEG-EAGE SALT DATA SET

In the previous two sections I have analyzed the theoretical differences between common-azimuth migration and offset plane wave migration. In this section, I compare the migration results.

The theoretical analysis identified two approximations that are made in offset plane wave migration: first, the setting of the cross-line offset ray parameter to zero, and second, downward continuing the offset plane waves separately, when in lateral varying media they should be allowed to mix. To enable the independent analysis of the effects of both approximations, I run three migration programs:

- (A) Common-azimuth migration
- (B) Hybrid offset plane wave migration (with plane-wave mixing)

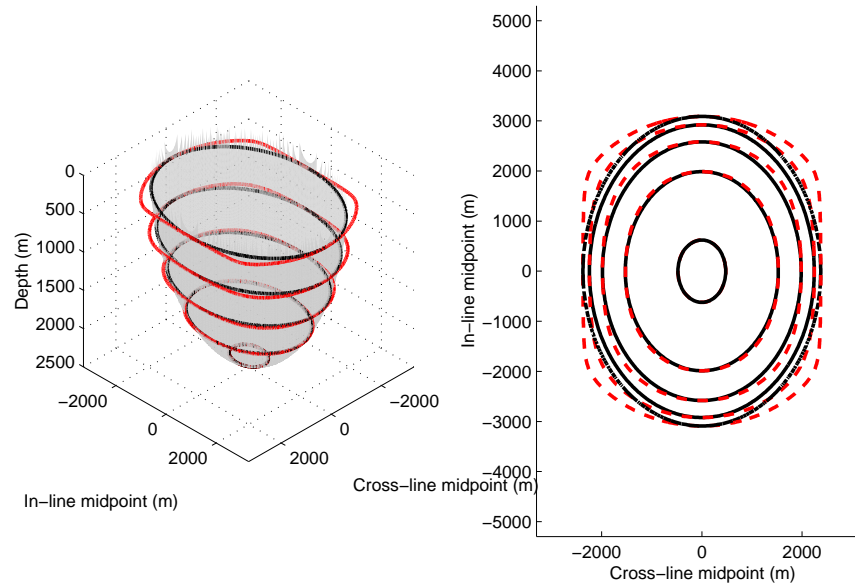


Figure 2: The grey surface shown in the left panel is the exact spreading surface for an impulse at at 2.5 s, an offset of 4,000 m, and assuming a constant velocity of 2,500 m/s. The solid contour lines correspond to the exact spreading surface, while the dashed contour lines correspond to the approximate spreading surface. `biondo1-planeellips` [ER]

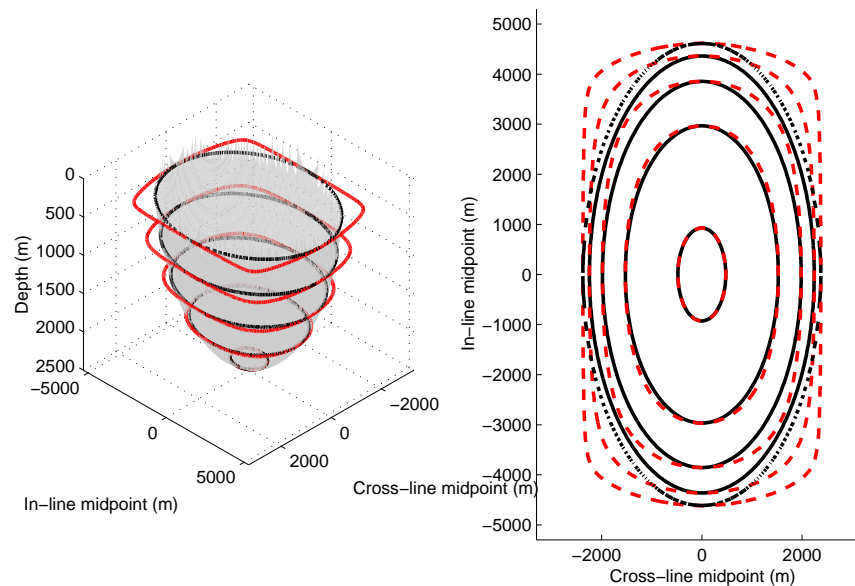


Figure 3: The grey surface shown in the left panel is the exact spreading surface for an impulse at at 3.73 s, an offset of 8,000 m, and assuming a constant velocity of 2,500 m/s. The solid contour lines correspond to the exact spreading surface, while the dashed contour lines correspond to the approximate spreading surface. `biondo1-planeellips8km` [ER]

(C) Offset plane wave migration (without plane-wave mixing).

All three programs implement the downward-continuation operators in the frequency-wavenumber domain and adapt to lateral velocity variations by an extended split-step method (Stoffa et al., 1990). When required, the offset-plane wave decomposition was performed inside the migration by Fourier transforms, relying on the well-known relations between ray parameters and wavenumbers ($p_{x_h} = k_{x_h}/\omega$ and $p_{y_h} = k_{y_h}/\omega$). Both the offset plane wave migration (C) and the hybrid offset plane wave migration (B) apply the dispersion relation in equation (8). The only difference between the two is that in (C) the offset-wavenumber axis is not transformed into the space domain when applying the split-step correction; that is, each offset-wavenumber (plane-wave) component is downward continued independently for all depths. On the other hand, the only difference between migration (A) and migration (B) is that in migration (B) the cross-line offset wavenumber was set to zero, while in migration (A) it was evaluated using equation (3).

The input data set was the same for all three programs, and the same as I used for my previous comparison of common-azimuth migration and Kirchhoff migration (Biondi, 1999a). The Salt Model C3-NA data set (SEG-EAGE, 1997; Clapp et al., 1999) was transformed to effective common-azimuth data by applying Azimuth Moveout (Biondi et al., 1998). The regularized common-azimuth data set was binned with a 20 meter CMP spacing in both the in-line and cross-line directions, and with 100 meter sampling along the in-line offset direction. The data were muted with a “deep” mute because the early arrivals are contaminated by all sorts of modeling noise. This mute affected the imaging of the shallow events. A more careful mute could accomplish both noise removal and shallow event preservation.

With respect to the previous tests, I increased the number of reference velocities from four to six. I wanted to verify the hypothesis that the poor imaging of a fault by common-azimuth migration was caused by having used too few reference velocities (Figure 5 in the previous report). Indeed, the fault is much better imaged when six reference velocities are used (Figure 10 in this report).

Comparison of common-azimuth migration with hybrid offset plane wave migration

The comparison of the constant-velocity migration operators presented in the previous sections indicates that the errors introduced by setting the cross-line offset ray parameter to zero are the largest for relatively shallow reflectors. Confirming the theoretical analysis, the differences between the images produced by common-azimuth migration (A) and the hybrid offset plane wave migration (B) are the largest in the shallow part of the image. Reflections from faults above the salt body and the salt flanks are affected when their dips are oriented at about 45 degrees with respect to the acquisition axes. In the sub-salt area there are no noticeable differences between the results produced by migrations (A) and (B). However, because this synthetic data set has a short maximum offset (2.4 km), these results are not necessarily indicative of migration performances for sub-salt imaging of real data sets, that are usually collected with much longer maximum offsets (4-6 km).

The next four figures compare the upper portion (down to a maximum depth of 1,500 m) of two in-line sections and two cross-line sections obtained by migrations (A) and (B). Figure 4 compares the in-line sections obtained by common-azimuth migration (A) and the hybrid offset plane wave migration (B). Migration (B) fails to image properly segments of the two large faults above the salt body. The image degradation is larger for the lower parts of the faults, contrary to the expectations induced by the theoretical analysis presented in the previous section. The relatively small degradation of the shallower parts of the faults can be explained by the muting applied to the early arrivals in the data. This muting reduced the effective maximum offset of the early reflections and thus decreased the errors introduced by offset plane wave migration. Further investigations of this aspect of the results are warranted.

Figure 5 compares the in-line sections obtained by common-azimuth migration (A) and the hybrid offset plane wave migration (B). The left flank of the salt body is better imaged by migration (A) than by migration (B). Migration (B) fails also to focus properly the ridge on the top of the salt visible in panel a) at in-line location of about 7,000 m.

Figure 6 compares the cross-line sections obtained by common-azimuth migration (A) and the hybrid offset plane wave migration (B). Both the right and left flank of the salt are better imaged by migration (A) than by migration (B). Migration (A) produces also a better image of the fault located at cross-line location of about 6,000 m

Figure 7 compares the cross-line sections obtained by common-azimuth migration (A) and the hybrid offset plane wave migration (B). Again, migration (B) fails to image the lower segment of the fault located at cross-line location of about 6,000 m, and the ridge on the top of the salt located at cross-line location of about 8,000 m. Notice that this is the same ridge visible in the in-line sections shown in Figure 5.

Comparison of common-azimuth migration with offset plane wave migration

The velocity above the salt body does not vary rapidly in the lateral directions. Therefore the images obtained by the hybrid offset plane wave migration (B) and the “real” offset plane wave migration (C) are very similar. On the contrary, below the salt body, the approximation introduced by downward-continuing the offset plane wave separately causes significant problems in the imaging of the sub-salt reflectors. The next four figures compare the deeper portion (starting from a minimum depth of 1,500 m) of two in-line sections and two cross-line sections obtained by migrations (A) and (C). The sub-salt images are considerably noisier than the above-salt images. To facilitate the analysis, I show also the corresponding sections of the velocity model.

Figure 8 compares the in-line sections obtained by common-azimuth migration (A) and the offset plane wave migration (C); Figure 9 shows the corresponding section of the velocity model. The bottom of the salt body, and in particular the dipping segment at the left edge of the salt, is better imaged by migration (A) than by migration (C). In the shadow of the salt body, the image of the basement is also more continuous in panel a) than in panel b).

Figure 10 compares the in-line sections obtained by common-azimuth migration (A) and

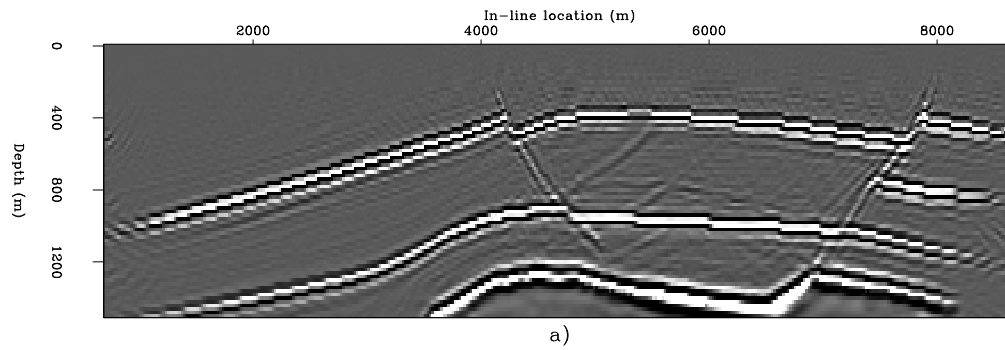


Figure 4: In-line sections (cross-line location 5,990 m) from the images obtained with a) common-azimuth migration (A), b) the hybrid offset plane wave migration (B). `biondo1-Both-salt-over-x5990` [CR]

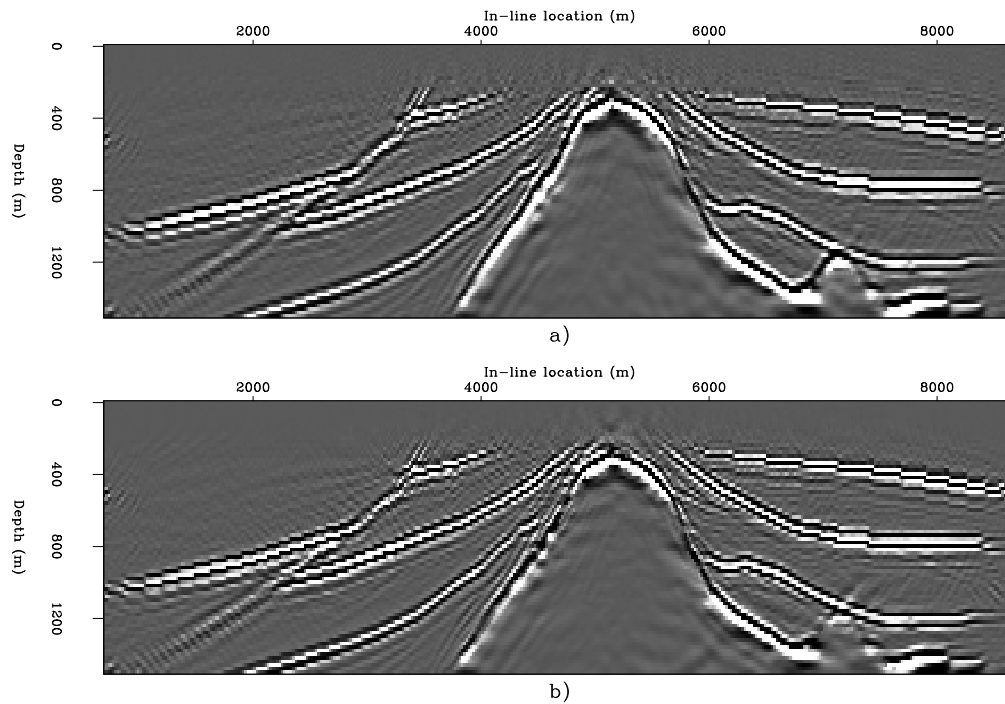


Figure 5: In-line sections (cross-line location 8,070 m) from the images obtained with a) common-azimuth migration (A), b) the hybrid offset plane wave migration (B). `biondo1-Both-salt-over-x8070` [CR]

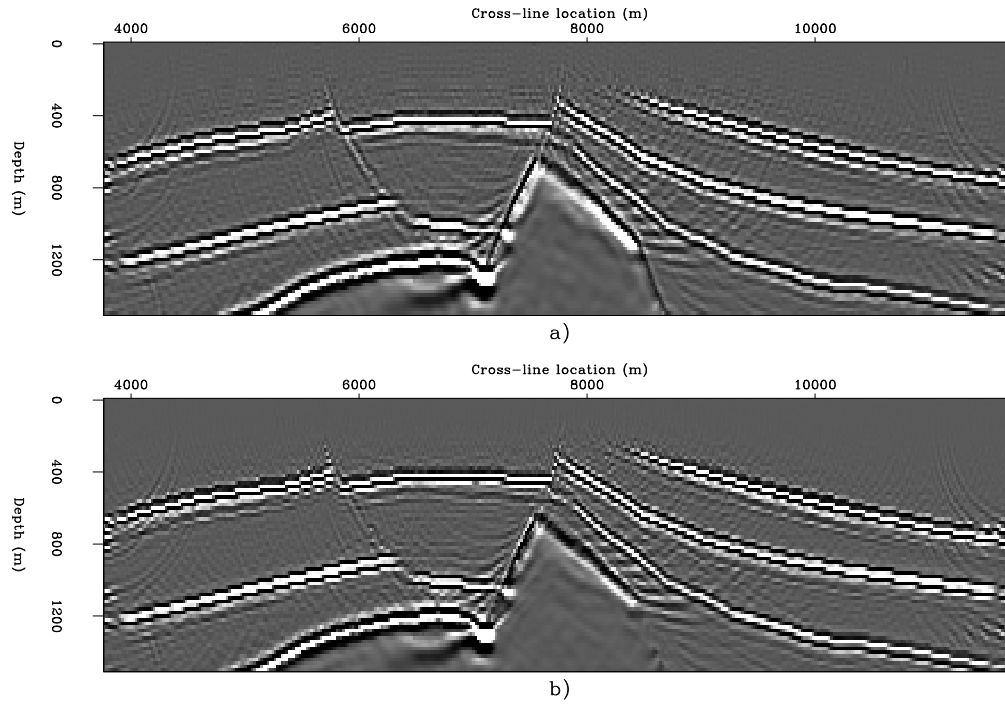


Figure 6: Cross-line sections (in-line location 4,420 m) from the images obtained with a) common-azimuth migration (A), b) the hybrid offset plane wave migration (B). `biondo1-Both-salt-over-y4420` [CR]

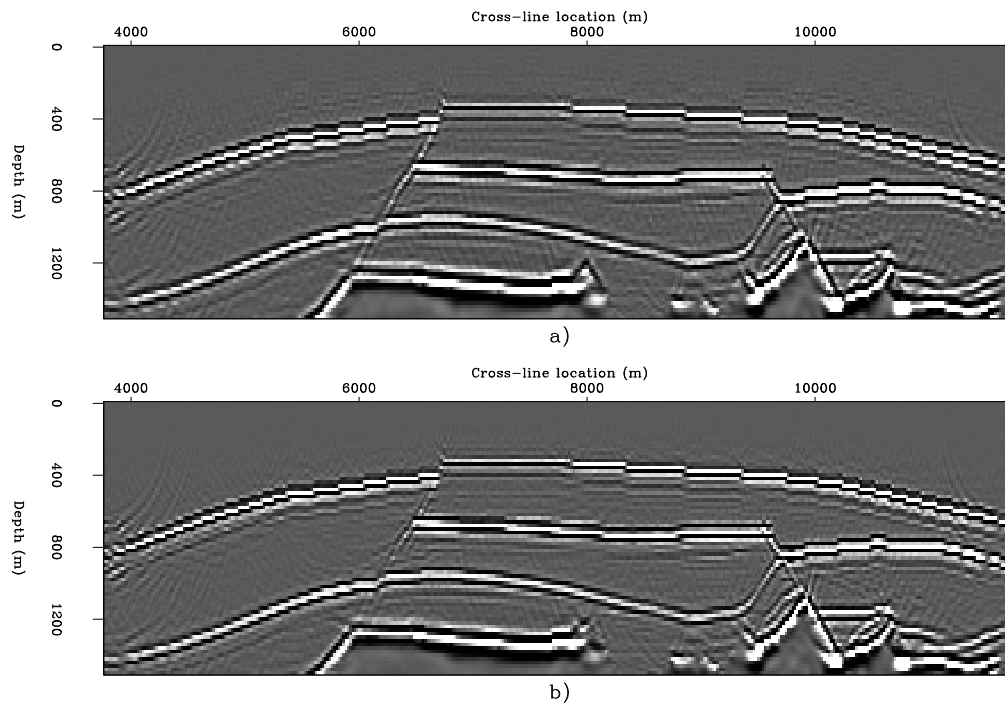


Figure 7: Cross-line sections (in-line location 6,960 m) from the images obtained with a) common-azimuth migration (A), b) the hybrid offset plane wave migration (B). `biondo1-Both-salt-over-y6960` [CR]

the offset plane wave migration (C); Figure 11 shows the corresponding section of the velocity model. Both sand lenses visible in the right part of the sections are better imaged by migration (A) than by migration (C); in particular, the deeper lens just above the basement reflector is more clearly defined in panel a) than in panel b). The image of the basement is also more continuous in panel a) than in panel b). Possibly the most interesting difference is in the imaging of the anticlinal structure broken by converging normal faults visible in between the two sand lenses. Migration (A) produces an image, though fairly faint, of this structure even in the shadow of the salt body. In contrast, the structure disappears from the image produced by migration (C) as soon as it gets in the shadow of the salt body.

Figure 12 compares the cross-line sections obtained by common-azimuth migration (A) and the offset plane wave migration (C); Figure 13 shows the corresponding section of the velocity model. The dipping segment of the bottom of the salt that belongs to the fault plane cutting through the salt body (cross-line location 8,000 m) is better imaged by migration (A) than by migration (C). The basement reflector is also more continuous in panel a) than in panel b).

Figure 14 compares the cross-line sections obtained by common-azimuth migration (A) and the offset plane wave migration (C); Figure 15 shows the corresponding section of the velocity model. As for the in-line sections shown in Figure 10, both sand lenses visible in the right part of the sections are better imaged by migration (A) than by migration (C). Though discontinuous in places, the basement reflector is also better imaged by migration (A) than by migration (C). The bottom of the salt reflector right below the deep canyons in the salt body (in-line location 8,000-9,200 m) is fairly coherent in panel a), while it is discontinuous in panel b).

CONCLUSIONS

Both offset plane wave migration and common-azimuth migration are computationally efficient wave-equation methods to image marine 3-D prestack data. Offset plane wave migration introduces approximations that are avoided by common azimuth migration. The theoretical analysis and the imaging comparison presented in this paper produce a convincing and consistent analysis of the migration errors caused by these approximations.

The approximation that is most detrimental to sub-salt imaging is caused by downward-continuing the offset plane waves separately. In lateral varying media, wave-propagation theory predicts that plane-wave components should mix at every depth step. It is difficult to study analytically the effects of this approximation. But the imaging results show a consistent deterioration of sub-salt image quality when plane-wave components were not allowed to mix during the downward-continuation process.

The effects of setting the cross-line offset ray parameter to zero can be studied analytically, at least under the simplifying assumption of constant migration velocity. The fundamental insight for the theoretical analysis is provided by the decomposition of the dispersion relations used for common-azimuth migration and offset plane wave migration in the cascades of two

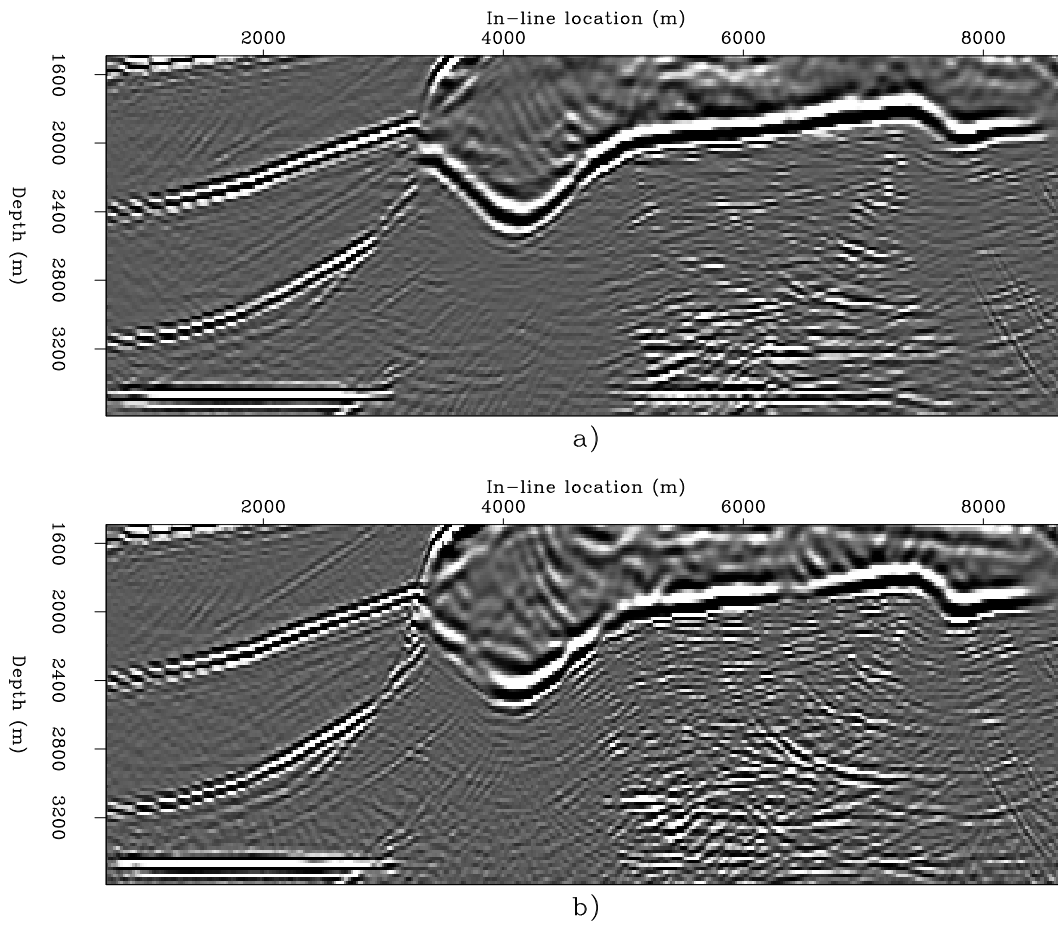


Figure 8: In-line sections (cross-line location 6,300 m) from the images obtained with a) common-azimuth migration (A), b) offset plane wave migration (C). `biondo1-Both-salt-under-x6300` [CR]

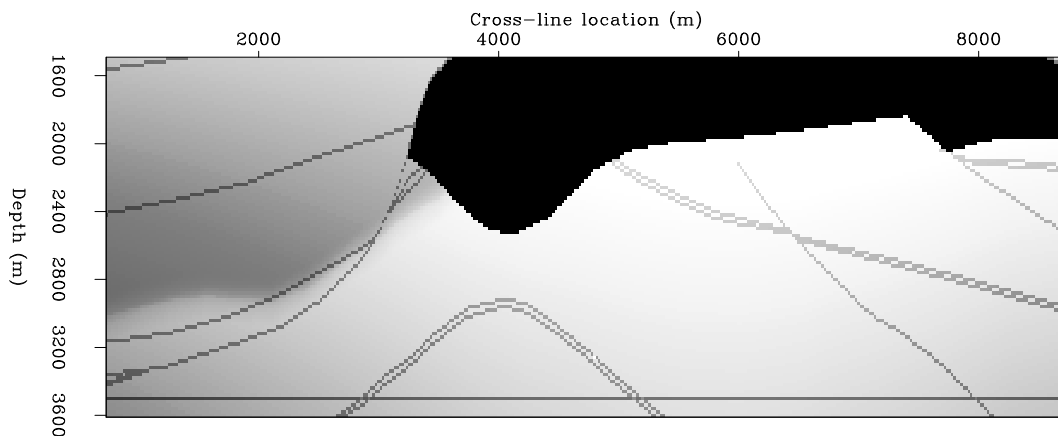


Figure 9: In-line section of the velocity model at cross-line location 6,300 m. `biondo1-Vel-salt-under-x6300` [CR]

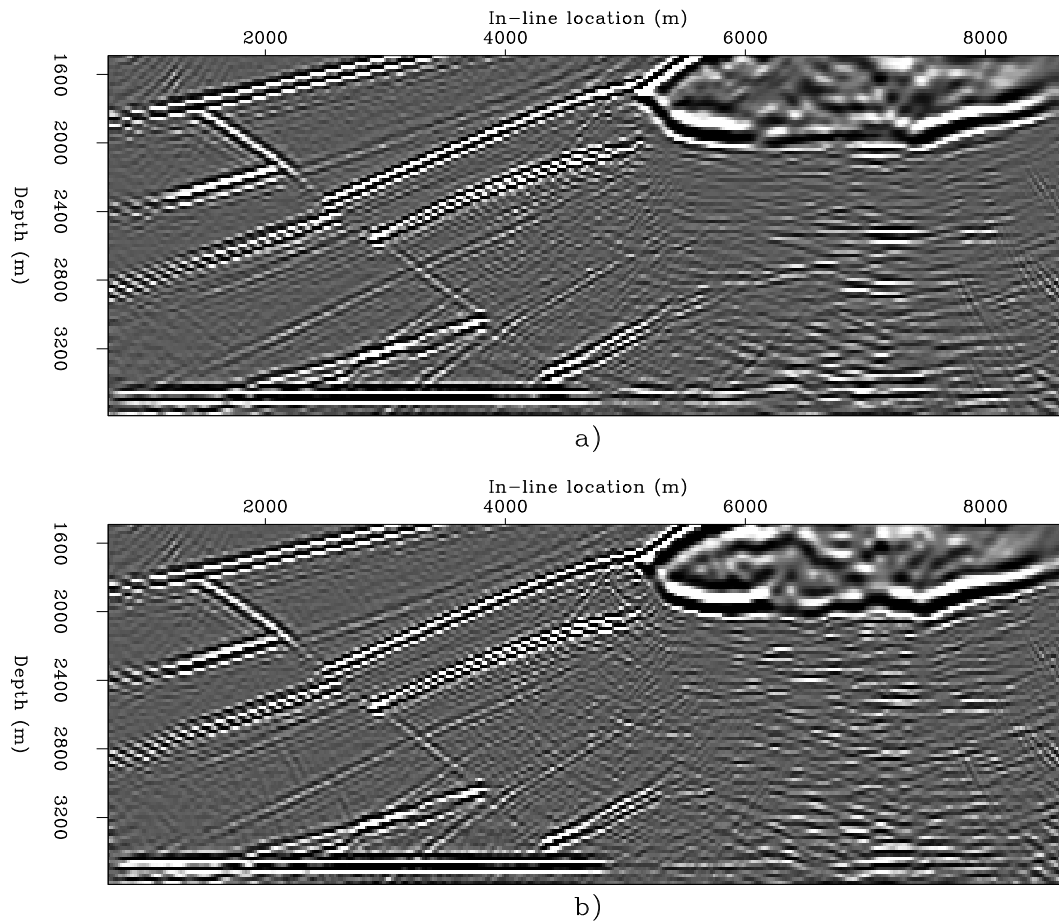


Figure 10: In-line sections (cross-line location 9,980 m) from the images obtained with a) common-azimuth migration (A), b) offset plane wave migration (C). `biondo1-Both-salt-under-x9980` [CR]

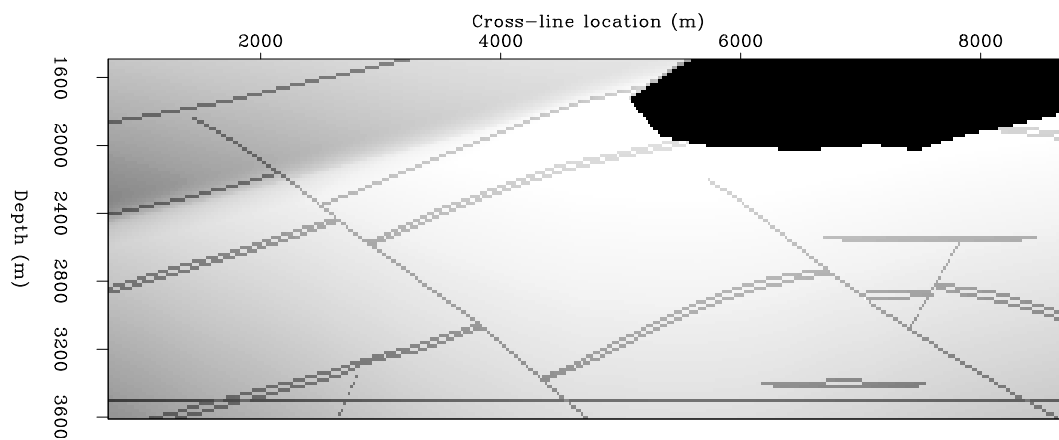


Figure 11: In-line section of the velocity model at cross-line location 9,980 m. `biondo1-Vel-salt-under-x9980` [CR]

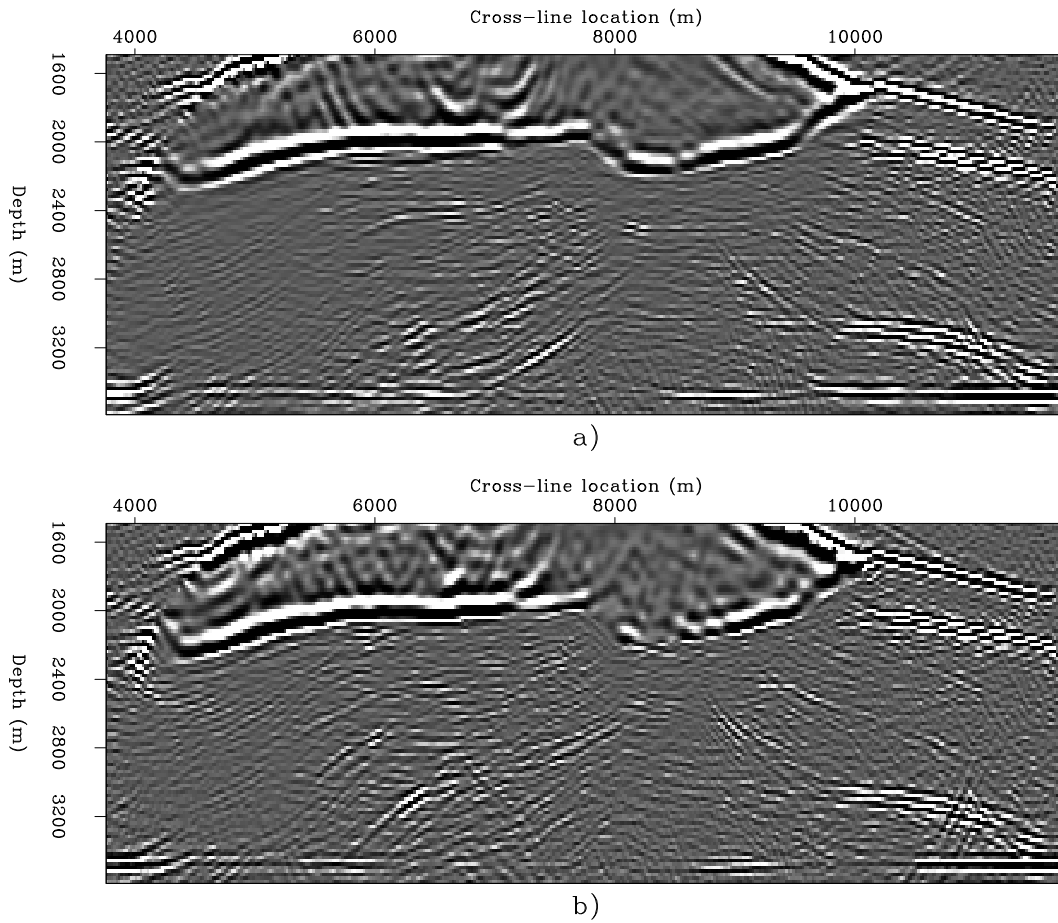


Figure 12: Cross-line sections (in-line location 5,180 m) from the images obtained with a) common-azimuth migration (A), b) offset plane wave migration (C). `biondo1-Both-salt-under-y5180` [CR]

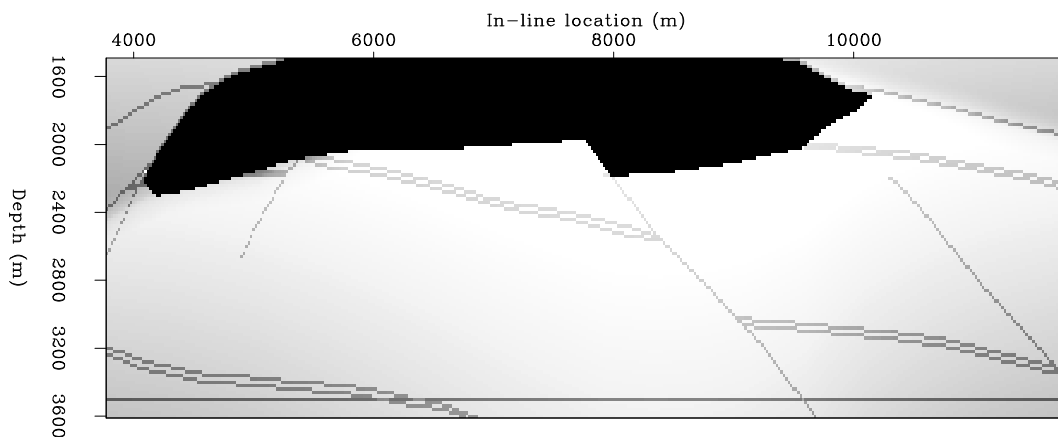


Figure 13: Cross-line section of the velocity model at in-line location 5,180 m. `biondo1-Vel-salt-under-y5180` [CR]

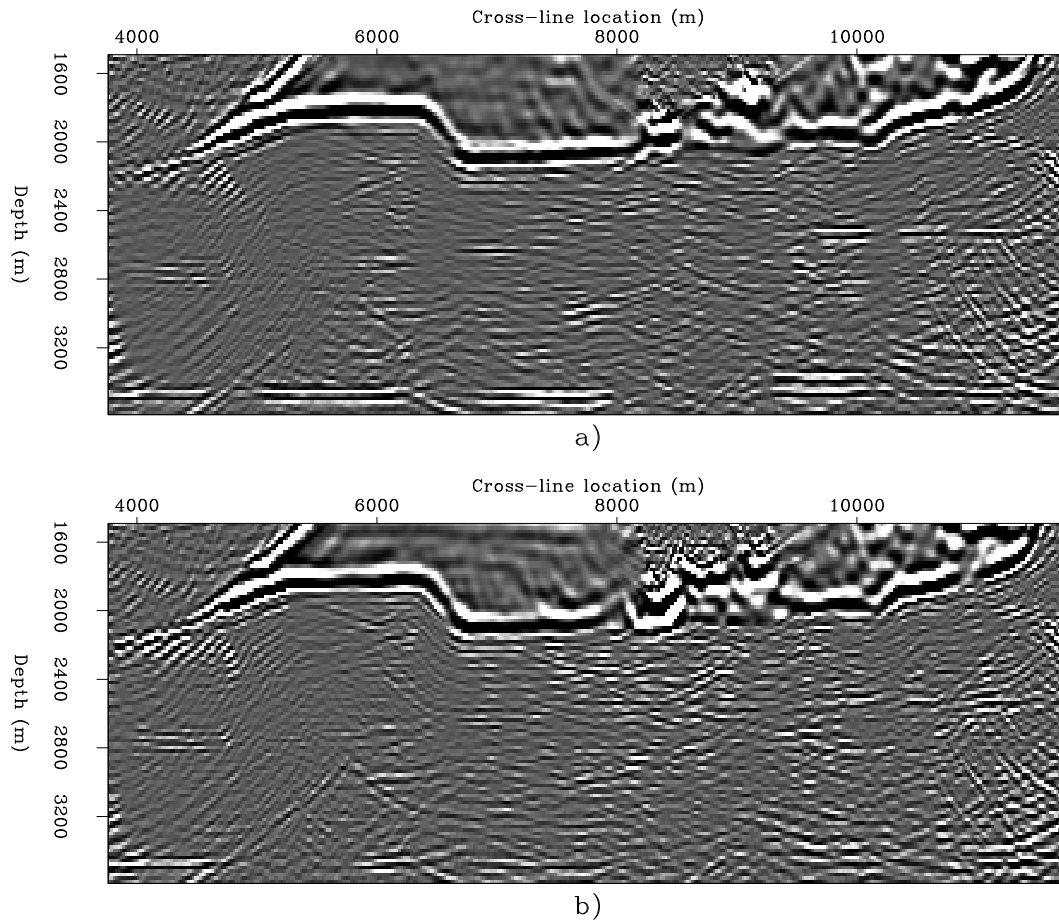


Figure 14: Cross-line sections (in-line location 7,300 m) from the images obtained with a) common-azimuth migration (A), b) offset plane wave migration (C). `biondo1-Both-salt-under-y7300` [CR]

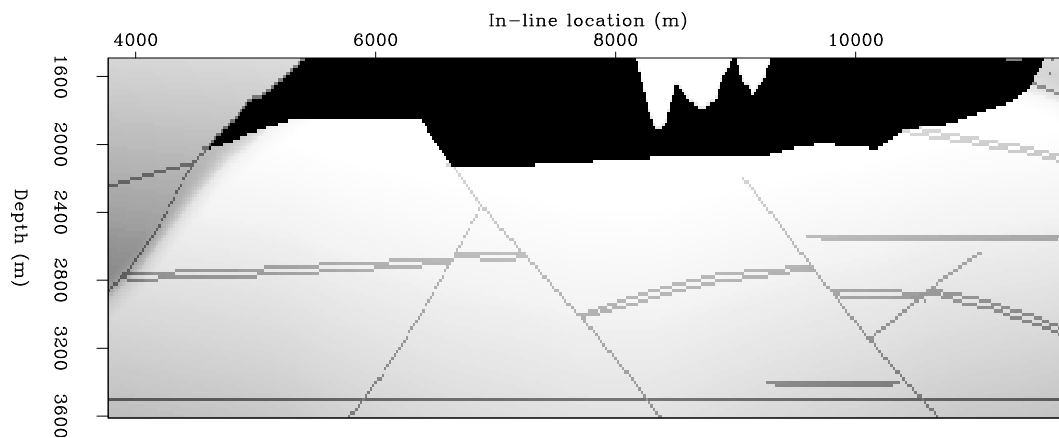


Figure 15: Cross-line section of the velocity model at in-line location 7,300 m. `biondo1-Vel-salt-under-y7300` [CR]

dispersion relations. This decomposition yields to a straightforward evaluation of the equivalent constant-velocity migration operators.

The imaging results confirm the predictions of the theoretical analysis that the shallow reflectors dipping at 45 degrees with respect to the acquisition axes are the most affected by this approximation. On the contrary, this approximation does not seem to have affected the imaging results of the deeper reflectors. However, my theoretical analysis predicts that the errors introduced by this approximation increase with offsets, and the synthetic data set used for this study has a shorter maximum offset (2.4 km) than data sets routinely recorded for sub-salt imaging (4-6 km). Therefore, the results presented in this paper are not conclusive to determine whether the imaging of deeper reflectors would be satisfactory with real data.

Offset plane-wave migration has some potential computational advantages with respect to common-azimuth migration. Therefore, the results presented in this paper indicate it could be a cost-effective migration method to produce full-volume images of deep targets below relatively mild velocity functions. Though more expensive, common-azimuth migration should produce better images below complex overburden (e.g. below salt bodies) and when shallow dipping reflectors are important to the overall interpretation.

ACKNOWLEDGEMENTS

This research was partially funded by the ACTI project # 4731U0015-3Q.

REFERENCES

- Biondi, B., and Palacharla, G., 1996, 3-D prestack migration of common-azimuth data: *Geophysics*, **61**, no. 6, 1822–1832.
- Biondi, B., Fomel, S., and Chemingui, N., 1998, Azimuth moveout for 3-D prestack imaging: *Geophysics*, **63**, no. 2, 574–588.
- Biondi, B., 1999a, Subsalt imaging by common-azimuth migration: *SEP-100*, 113–124.
- Biondi, B. L., 1999b, 3-D Seismic Imaging: <http://sepwww.stanford.edu/sep/biondo/Lectures/index.html>.
- Clapp, R. G., Brown, M., Vaillant, L., Mora, C., Prucha, M., and Zhao, Y., 1999, SEP Data Library: http://sepwww.stanford.edu/pub/docs/sepdata/lib/toc_html/.
- Mosher, C. C., Foster, D. J., and Hassanzadeh, S., 1997, Common angle imaging with offset plane waves: 67th Annual Internat. Mtg., Soc. Expl. Geophys., Expanded Abstracts, 1379–1382.
- Ottolini, R., and Claerbout, J. F., 1984, The migration of common-midpoint slant stacks: *Geophysics*, **49**, no. 3, 237–249.

Rosa, A., Cunha, C., Pedrosa, I., Panetta, J., Sinedino, S., and Braga, V., 1999, Two-pass 3-D prestack time migration: 6th Internat. Congr. Braz. Geophys. Soc., SBGf, RIO 99, CD-ROM.

SEG-EAGE, 1997, Salt Model Narrow-Azimuth Classic dataset (C3-NA): <http://archive.llnl.gov/SSD/classic/classicSalt.html#salt-c>.

Stoffa, P. L., Fokkema, J. T., de Luna Freire, R. M., and Kessinger, W. P., 1990, Split-step Fourier migration: *Geophysics*, **55**, no. 4, 410–421.

Stolt, R. H., 1978, Migration by Fourier transform: *Geophysics*, **43**, no. 1, 23–48.

Vaillant, L., and Sava, P., 1999, Common-azimuth migration of a North Sea dataset: SEP-**102**, 1–14.

Iterative resolution estimation in Kirchhoff imaging

Robert G. Clapp, Sergey Fomel, and Marie Prucha¹

ABSTRACT

We apply iterative resolution estimation to least-squares Kirchhoff migration. Resolution plots reveal low illumination areas on seismic images and provide information about image uncertainties.

INTRODUCTION

Kirchhoff prestack depth migration remains the most widely used method for seismic imaging in complex areas. The method is especially attractive for 3-D imaging because of its ability to handle naturally irregular acquisition geometries. The negative effect of irregular sampling on seismic images can be additionally balanced by applying the least-squares migration approach (Cole and Karrenbach, 1992), which has recently gained a lot of attention in the geophysical literature (Nemeth et al., 1999; Chavent and Plessix, 1999; Duquet and Marfurt, 1999).

According to the least-squares approach, the migration operator is constructed as a least-squares inverse of the forward Kirchhoff modeling (Tarantola, 1987). One can effectively approximate the inverse operator through an application of the conjugate-gradient technique. The conventional migration is then considered as the adjoint of the modeling operator, or, in other words, the first step of a conjugate-gradient iteration (Claerbout, 1992). A more accurate representation (i.e. additional conjugate-gradient steps) can compensate for irregularities and artifacts of irregular acquisition (Nemeth, 1996; Nemeth et al., 1999).

A blind least-squares approach cannot, however, compensate for lack of information in the input data. For example, if a particular area in the subsurface is not illuminated by reflection waves, a proper image of that area cannot be resolved by least-squares migration alone. In this case, part of the image will belong to the null space of the least-squares inverse problem. Spotting low-illumination areas is important both for making acquisition decisions and for evaluating the uncertainty of the existing images. Duquet et al. (1998) have proposed to use the inverse diagonal of the Hessian matrix as a measure of illumination in Kirchhoff imaging. Although this measure does provide useful information about the problem's well-posedness, a more rigorous approach to the solution uncertainty would be to estimate the corresponding model resolution operator (Jackson, 1972).

As shown by Berryman and Fomel (1996), the model resolution matrix can be estimated

¹email: bob@sep.stanford.edu,sergey@sep.stanford.edu,marie@sep.stanford.edu

in an iterative manner. The matrix approximation is constructed from the vectors, already appearing in the conjugate-gradient iteration. Therefore, it requires minimal additional computation with respect to an iterative least-squares inversion. The diagonal of the resolution matrix can serve as a rough direct estimate of the model uncertainty. A similar, although less efficient approach, was proposed by Minkoff (1996) and Yao *et al.* (1999), who applied it in conjunction with the LSQR method (Paige and Saunders, 1982).

In this paper, we apply the iterative technique of Berryman and Fomel (1996) for resolution estimation in Kirchhoff imaging. Synthetic and real data tests show that a resolution estimate can indeed provide valuable information about the uncertainty of Kirchhoff images and reveal image areas with illumination problems.

REVIEW OF RESOLUTION MATRICES

Model resolution operator \mathbf{R} defines the connection between the true model \mathbf{m} and the model estimate from least-squares inversion $\hat{\mathbf{m}}$, as follows:

$$\hat{\mathbf{m}} = \mathbf{R}\mathbf{m} . \quad (1)$$

In the case of least-squares Kirchhoff migration, \mathbf{m} corresponds to true reflectivity, $\hat{\mathbf{m}}$ is the output image, and the estimation process amounts to minimizing the least-square norm of the residual $\mathbf{r} = \mathbf{d} - \mathbf{L}\mathbf{m}$, where \mathbf{d} is the observed data, and \mathbf{L} is the Kirchhoff modeling operator. Recalling the well-known formula

$$\hat{\mathbf{m}} = (\mathbf{L}'\mathbf{L})^\dagger \mathbf{L}'\mathbf{d} , \quad (2)$$

where \mathbf{L}' stands for the adjoint operator (Kirchhoff migration), and the dagger symbol denotes the pseudo-inverse operator, we can deduce from formulas (3) and (2) that

$$\mathbf{R} = (\mathbf{L}'\mathbf{L})^\dagger (\mathbf{L}'\mathbf{L}) . \quad (3)$$

In the ideal case, when all model components are perfectly resolved, the model resolution matrix is equal to the identity. If the model is not perfectly constrained, the inverted $\mathbf{L}'\mathbf{L}$ matrix will be singular, and the model resolution will depart from being the identity. It means that the model contains some null-space components that are not constrained by the data. The diagonal elements of the resolution matrix will be less than one in the places of unresolved model components. Berryman and Fomel (1996) derive the following remarkably simple formula for the model resolution matrix:

$$\mathbf{R} = \sum_{i=1}^N \frac{\mathbf{g}_i \mathbf{g}_i'}{\mathbf{g}_i' \mathbf{g}_i} , \quad (4)$$

where N corresponds to the model size, and the \mathbf{g}_i 's are the model-space gradient vectors that appear in the conjugate-gradient process (Hestenes and Stiefel, 1952). In large-scale problems, such as a typical Kirchhoff migration, we cannot afford performing all N steps of

the conjugate-gradient process, required for the theoretical convergence of the model estimate to the one defined in formula (2). However, formula (4) is still valid in this case, if we replace number N with the actual number of steps. In this case, the matrix R corresponds to the actual resolution of our estimate. To reduce the computational effort, we can use formula (4) only with a few significant gradient vectors \mathbf{g}_i to obtain an effective approximation of the model resolution. The most significant \mathbf{g}_i 's will turn out to be those have large components in the direction of eigenvectors having large eigenvalues (or singular vectors have large singular values). The next section exemplifies this approach with synthetic and real data tests.

APPLICATION TO KIRCHHOFF IMAGING

Difficulties in Kirchhoff imaging

When attempting to image complex subsurfaces with Kirchhoff methods, many difficulties may arise. In particular, amplitude behavior of the imaged reflectors can be caused by totally different physical phenomenon. A reflector that appears to fade and disappear along some distance can have several causes, including a real change in reflectivity, an error in the velocity model, or an illumination problem. All of these provide valuable information, but it is important to know which one is causing the effect. By estimating the resolution of the data it is possible to identify areas of low illumination.

Resolution estimation algorithm

To test the resolution matrix estimation we inverted for a single output offset (225m) made from three data offsets (200, 225, and 250m). The Kirchhoff operator was a simple 2-D modeling operator and its adjoint using 2nd order, first-arrival eikonal traveltimes. For the synthetic case a smoothed version of the correct velocity model was used. The real data example uses a smoothed version of the SMART (Jacobs et al., 1992; Ehinger and Lailly, 1995) velocity model provided by Elf Aquitaine.

Results

We began our experiments on the synthetic Elf North Sea dataset. Figure 1 shows the result of conjugate gradient inversion. The deepest reflector seems to disappear as it passes under the edge of the salt body. This behavior is known to be caused by poor illumination (Prucha et al., 1998).

Figures 2 through 5 show the estimated resolution for the synthetic dataset, with increasing numbers of iteration. After only 5 iterations, there is high resolution along the major reflectors (black indicates high resolution, white indicates low resolution). Note that the area of poor illumination has low resolution. As the number of iterations increases, the areas between the reflectors become better resolved. This tells us that conjugate gradient algorithm is spending

most of its effort at low iterations resolving model components around the reflector. It moves onto the area between reflectors only at large iterations. This is not surprising behavior, since most of the energy in the model space is found around the reflectors so that is what will be minimized first.

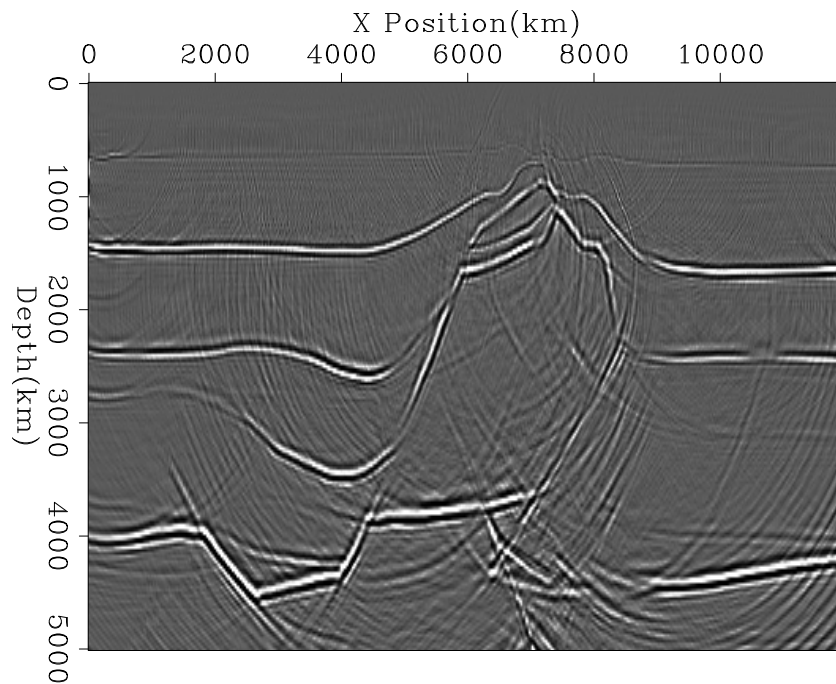


Figure 1: Inversion result on synthetic. `sergey1-synth-cg.5` [CR]

After experimenting with the synthetic dataset, we conducted the same trials on the real Elf North Sea dataset (Figure 6). Note that the x -axis in the real dataset is reversed from that in the synthetic so that the salt structure tilts to the left rather than the right. Figures 8 through 11 show the results of increasing the iterations for estimating the resolution. Once again, there are Kirchhoff-type artifacts in all of the figures. Note that we again see resolution energy beginning around the reflectors, spreading to areas between reflectors at higher iterations. We can see corresponding changes in our image. After 5 iterations the image shows strong energy along the primaries reflectors, but is generally low frequency, Figure 6. After 20 iterations we have an image with more noise, but also a significantly higher frequency image. The later iterations resolved smaller eigenvalues of the model, which corresponded to higher frequency, lower amplitude portions of the model space.

CONCLUSIONS

Iterative estimation of resolution supplies useful information when performing Kirchhoff imaging. Areas of low illumination are easily recognizable. In addition, the iterative nature of the algorithm provides useful information on what portion of the image is resolvable at each iteration.

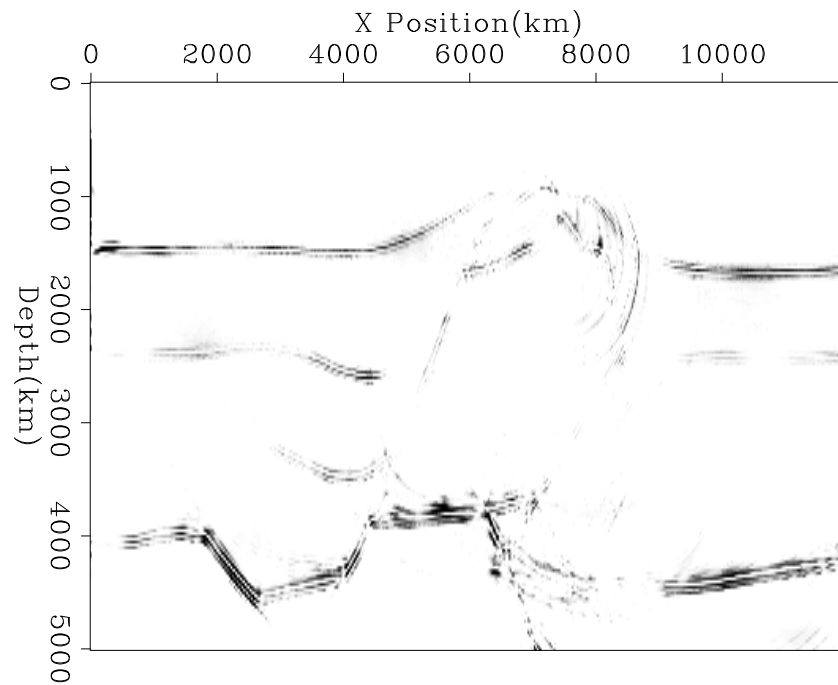


Figure 2: Resolution using conjugate gradient method after 5 iterations. Dark indicates higher resolution. `sergey1-mdiag-synth-cg.5` [CR]

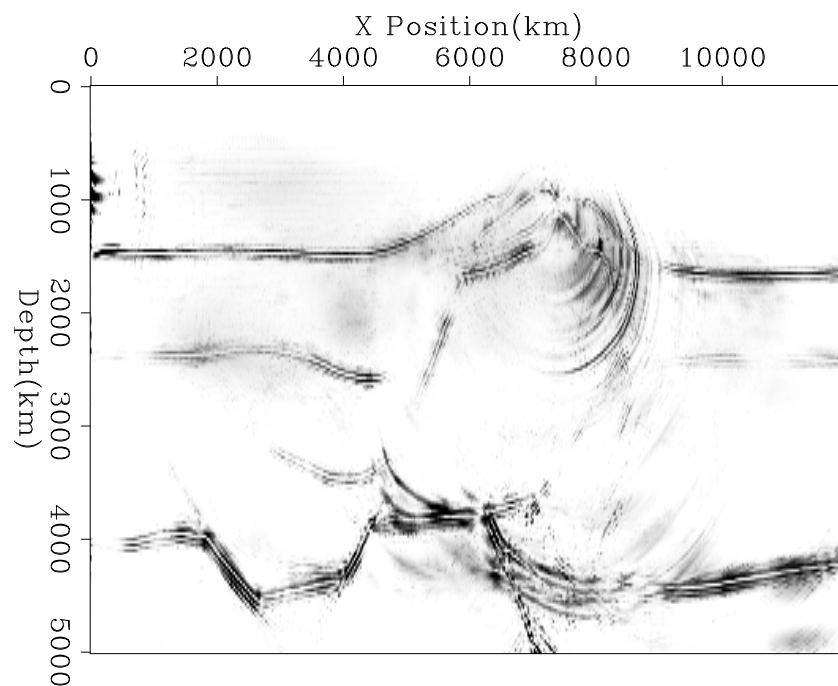


Figure 3: Resolution using conjugate gradient method after 10 iterations. Dark indicates higher resolution. `sergey1-mdiag-synth-cg.10` [CR]

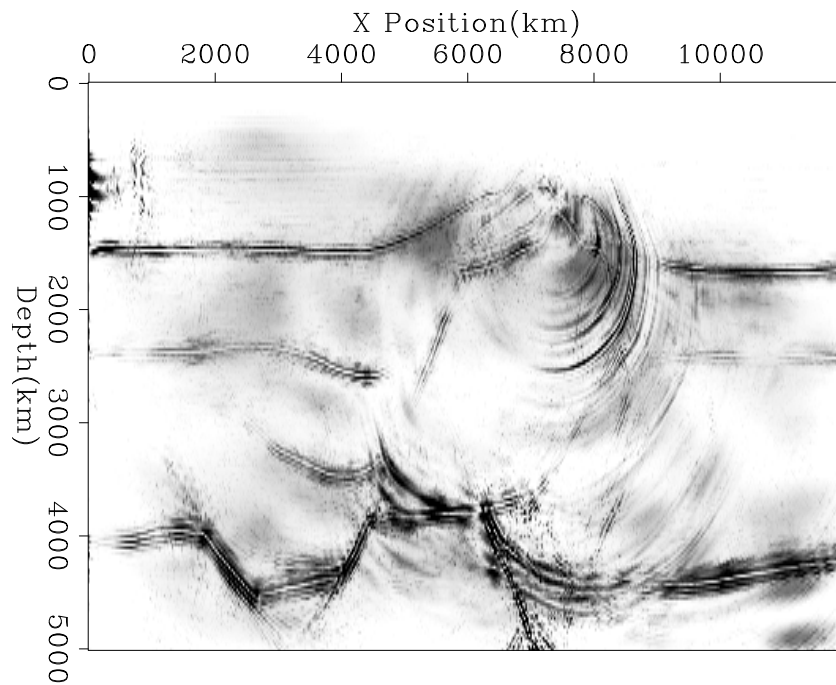


Figure 4: Resolution using conjugate gradient method after 15 iterations. Dark indicates higher resolution. `sergey1-mdiag-synth-cg.15` [CR]

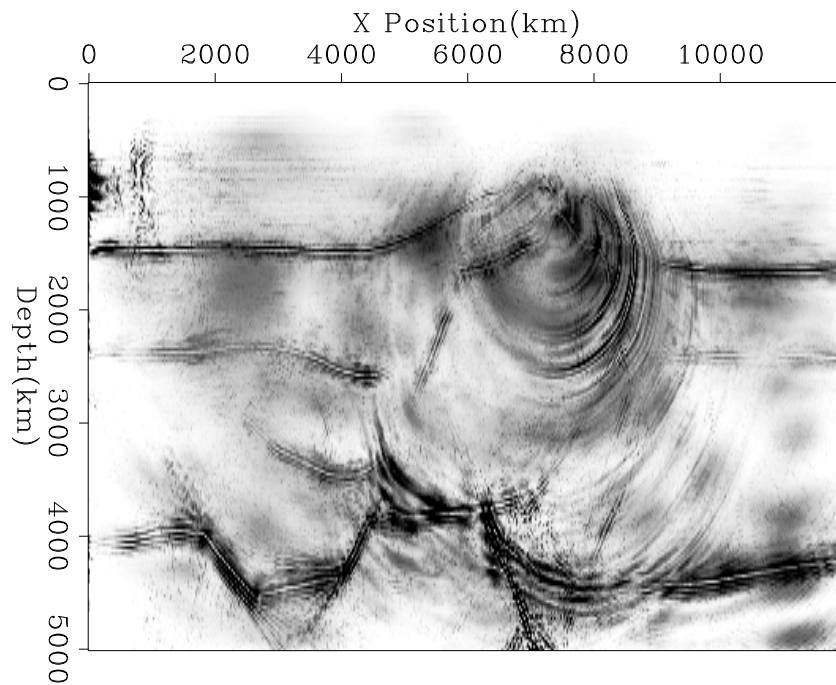


Figure 5: Resolution using conjugate gradient method after 20 iterations. Dark indicates higher resolution. `sergey1-mdiag-synth-cg.20` [CR]

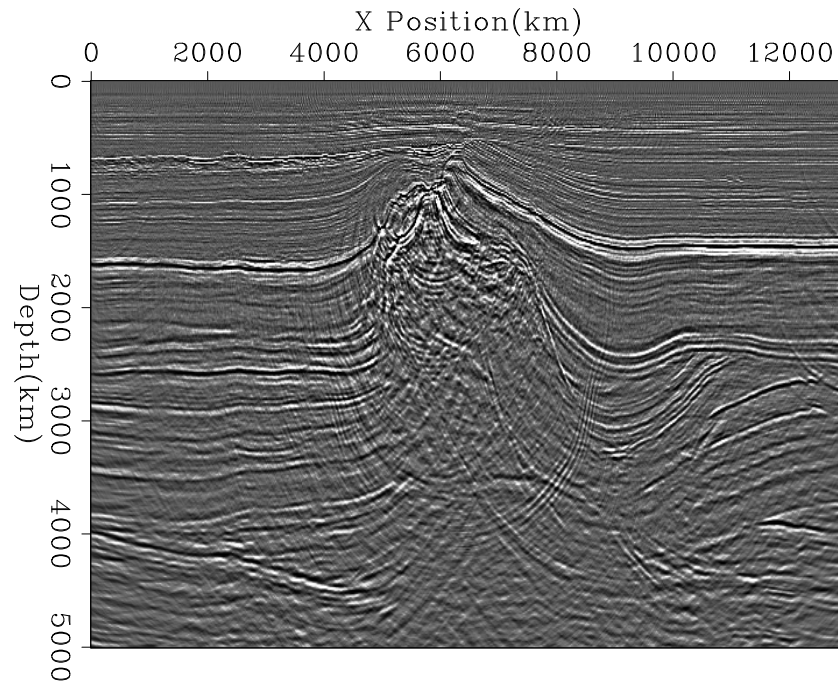


Figure 6: Inversion result on real data after 5 iterations. `sergey1-real-cg.5` [CR]

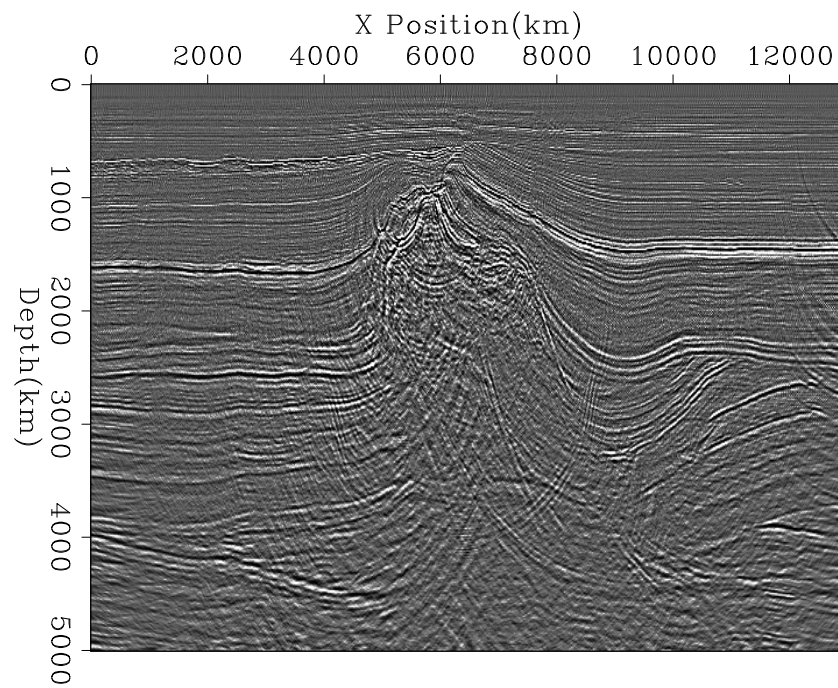


Figure 7: Inversion result on real data after 20 iterations. `sergey1-real-cg.20` [CR]

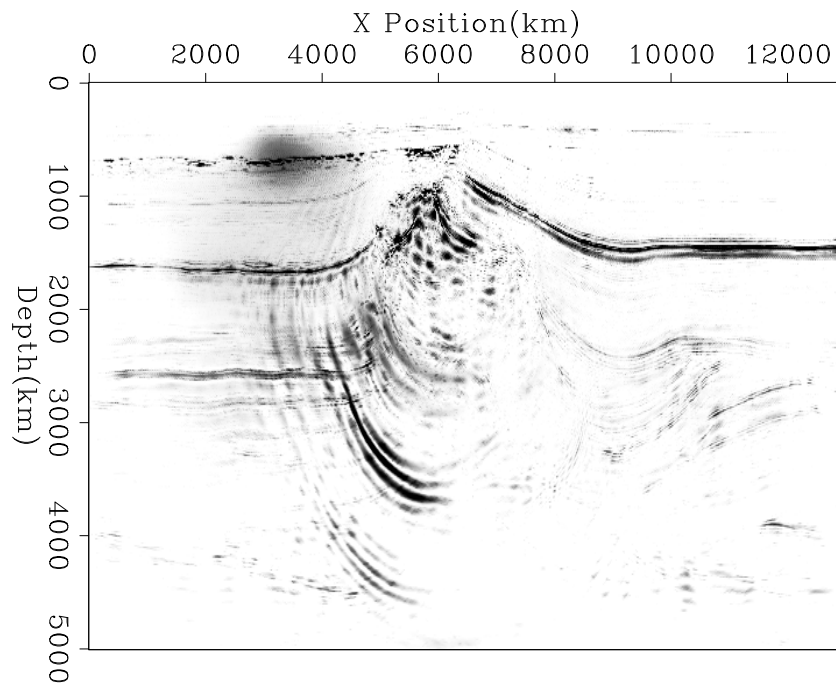


Figure 8: Resolution using conjugate gradient method after 5 iterations of the real data.
`sergey1-mdiag-real-cg.5` [CR]

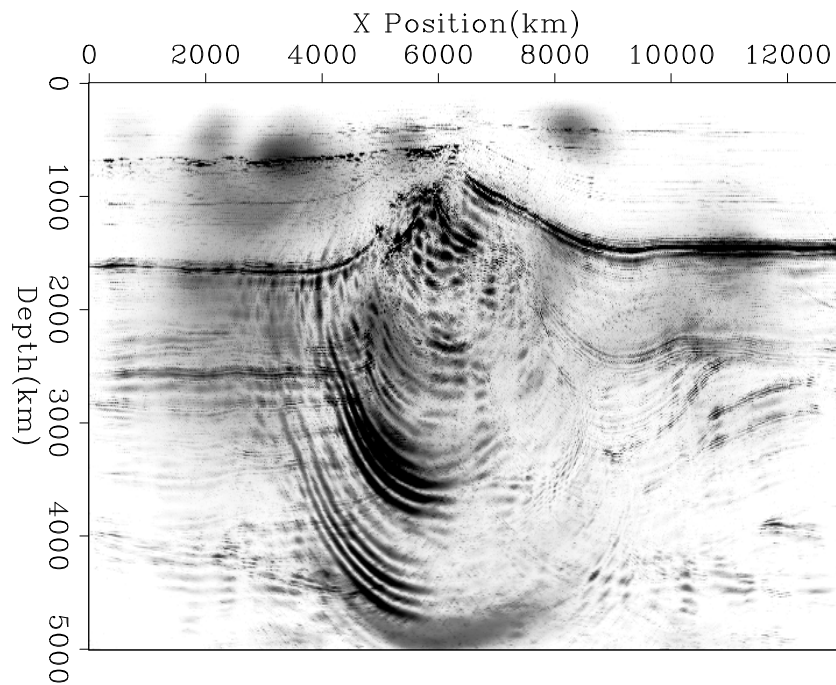


Figure 9: Resolution using conjugate gradient method after 10 iterations of the real data.
`sergey1-mdiag-real-cg.10` [CR]

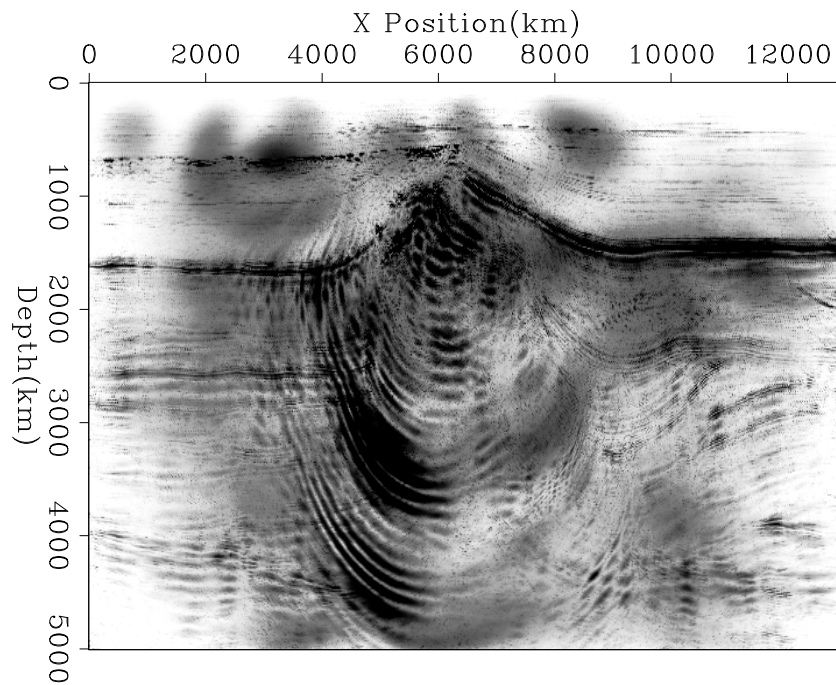


Figure 10: Resolution using conjugate gradient method after 15 iterations of the real data.
`sergey1-mdiag-real-cg.15` [CR]

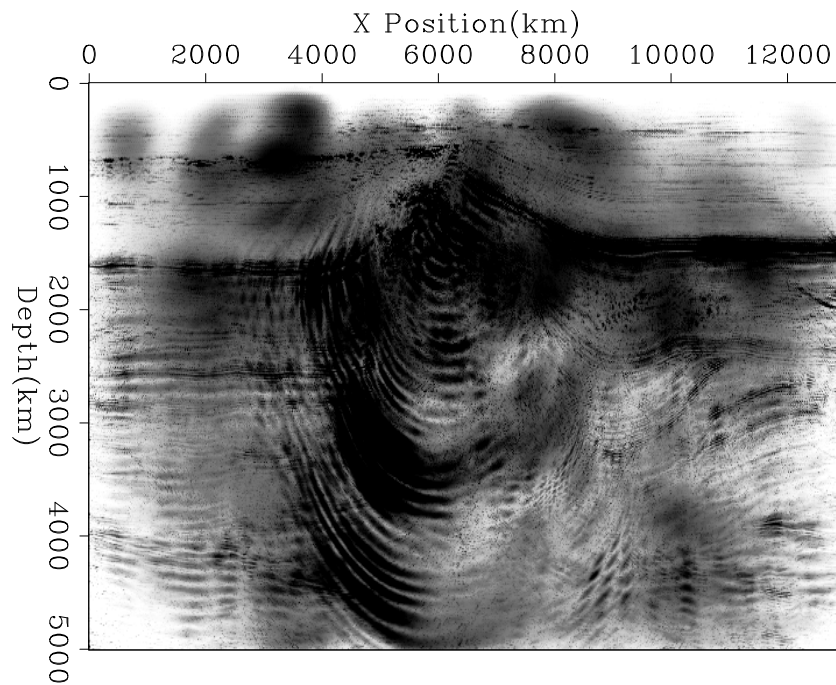


Figure 11: Resolution using conjugate gradient method after 20 iterations of the real data.
`sergey1-mdiag-real-cg.20` [CR]

ACKNOWLEDGMENTS

We would like to thank Jim Berryman who did the original work on the resolution matrix and provided insightful observation in the course of writing this paper.

REFERENCES

- Berryman, J. G., and Fomel, S., 1996, Iterative methods of optimization with application to crosswell tomography: *SEP-93*, 109–132.
- Chavent, G., and Plessix, R.-E., 1999, An optimal true-amplitude least-square prestack depth-migration operator: *Geophysics*, **64**, no. 2, 508–515.
- Claerbout, J. F., 1992, *Earth Soundings Analysis: Processing Versus Inversion*: Blackwell Scientific Publications.
- Cole, S., and Karrenbach, M., 1992, Least-squares Kirchhoff migration: *SEP-75*, 101–110.
- Duquet, B., and Marfurt, K. J., 1999, Filtering coherent noise during prestack depth migration: *Geophysics*, **64**, no. 4, 1054–1066.
- Duquet, B., Marfurt, K. J., and Dellinger, J. A., 1998, Efficient estimates of subsurface illumination for Kirchhoff prestack depth migration: 68th Annual Internat. Mtg., Soc. Expl. Geophys., Expanded Abstracts, 1116–1119.
- Ehinger, A., and Lailly, P., 1995, Velocity model determination by the smart method, part 1: Theory: 65th Annual Internat. Mtg., Soc. Expl. Geophys., Expanded Abstracts, 739–742.
- Hestenes, M. R., and Stiefel, E., 1952, Methods of conjugate gradients for solving linear systems: *J. Res. NBS*, **49**, 409–436.
- Jackson, D. D., 1972, Interpretation of inaccurate, insufficient, and inconsistent data: *Geophys. J. Roy. Astron. Soc.*, **28**, 97–109.
- Jacobs, J. A. C., Delprat-Jannaud, F., Ehinger, A., and Lailly, P., 1992, Sequential migration aided reflection tomography: A tool for imaging complex structures: 62nd Annual Internat. Mtg., Soc. Expl. Geophys., Expanded Abstracts, 1054–1057.
- Minkoff, S. E., 1996, A computationally feasible approximate resolution matrix for seismic inverse problems: *Geophys. J. Internat.*, **126**, 345–359.
- Nemeth, T., Wu, C., and Schuster, G. T., 1999, Least-squares migration of incomplete reflection data: *Geophysics*, **64**, no. 1, 208–221.
- Nemeth, T., 1996, *Imaging and filtering by least-squares migration*: Ph.D. thesis, The University of Utah.

- Paige, C. C., and Saunders, M. A., 1982, LSQR: An algorithm for sparse linear equations and sparse least squares: *ACM Trans. Math. Software*, **8**, 43–71.
- Prucha, M. L., Clapp, R. G., and Biondi, B. L., 1998, Imaging under the edges of salt bodies: Analysis of an Elf North Sea dataset: *SEP-97*, 35–44.
- Tarantola, A., 1987, *Inverse problem theory*: Elsevier.
- Yao, Z. S., Roberts, R. G., and Tryggvason, A., 1999, Calculating resolution and covariance matrices for seismic tomography with the LSQR method: *Geophys. J. Internat.*, **138**, 886–894.

Enhancing common-image gathers with prestack Stolt residual migration

Paul Sava¹

ABSTRACT

Wave-equation migration velocity analysis is a two-step process: first, we estimate the perturbation between a starting image and a better-focused image, and then invert for the perturbation in slowness that explains the perturbation in image obtained in the first step. The key to success is to obtain a sharp image, with flat common-image gathers at every location. In this paper, I show how prestack Stolt residual migration and common-image gathers come together, and lead to a successful image enhancement procedure with which we can transform a given image into a better-focused one.

INTRODUCTION

Wave-equation migration velocity analysis (Biondi and Sava, 1999) has recently emerged as a promising new technology with the potential to overcome the difficulties encountered in complex structures by travelttime-based velocity analysis methods.

Briefly, in wave-equation migration velocity analysis (WEMVA), we iteratively update the slowness model with perturbations in slowness (ΔS) obtained by inversion from perturbations in image (ΔR), which, by definition, is the difference between the current image and a better-focused image (Figure 1). The key ingredient of WEMVA is the better-focused image with which we compare the original image. Here, residual migration plays a very important role, because it has remarkable properties of image enhancement.

Several residual migration methods are capable of improving the migrated images. A good choice is Stolt prestack residual migration, which is not only fast and robust, but can also be formulated as a velocity-independent procedure (Sava, 1999).

Another important element of WEMVA is the ability to convert images to angle-domain common-image gathers (Prucha et al., 1999) to assess the quality of the velocity used in imaging. When the velocity is incorrect, different events in CIGs are not flat, but rather point up or down, and therefore are a very clear guide to where and how the velocity map needs improvement.

In this paper, I present an example of how residual migration can be used to improve the quality of images. I use a synthetic model with features relevant to real data in complex

¹email: paul@sep.stanford.edu

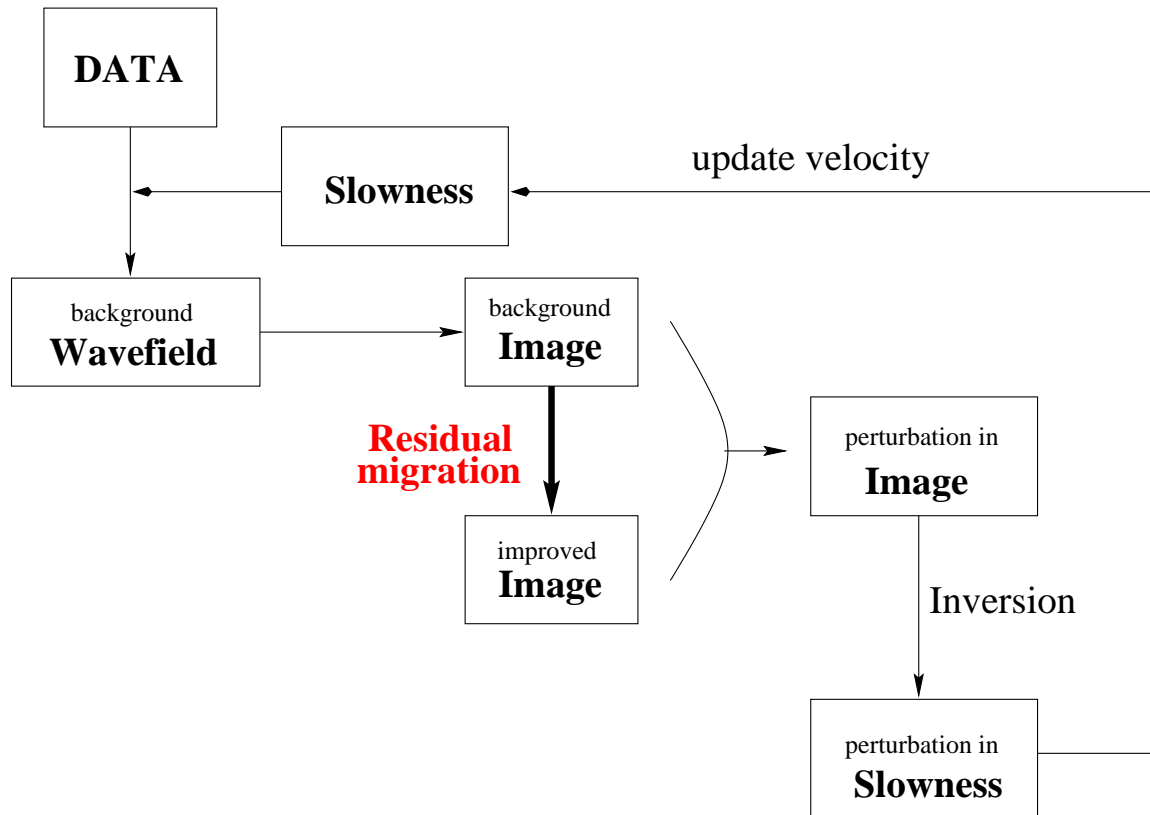


Figure 1: WEMVA flow chart. We start with the recorded data and an initial guess about the slowness model (background slowness). We compute the background wavefield by recursive downward continuation from the surface and image (background image). We then apply an image enhancement procedure (residual migration) to get a better-focused image. From the two images we compute the perturbation in image, which we can invert for the perturbation in slowness. Finally, we update the background slowness and repeat the loop until convergence is achieved. [paul1-flow](#) [NR]

structures: dipping beds, reverse faults, and zones of severe distortion. Throughout the project, I make extensive use of angle-domain CIGs.

IMAGE ENHANCEMENT THEORY

Residual migration has proved to be a useful tool in imaging and in velocity analysis. Recent publications show that Stolt residual migration can be applied in the prestack domain (Stolt, 1996), and, furthermore, that it can be posed as a velocity-independent process (Sava, 1999). Consequently, we can use Stolt residual migration in the prestack domain to obtain a better-focused image without making any assumption about the velocity. This is why Stolt residual migration in the prestack domain appears to be a good choice for image enhancement after wave-equation migration.

Strictly speaking, Stolt prestack residual migration is a constant velocity process. However, with this process we obtain images that correspond to velocities that have a given *ratio* to the original one. Therefore, if the original velocity is variable, the new velocities are also not constant, but only slightly faster or slower than the reference. The true relationship between the original and new velocities is still not fully understood, and remains a subject for future research.

One possible measure of the degree to which the prestack image is focused is the flatness of the angle-domain common-image gathers (CIG) (Biondi, 1999; Prucha et al., 1999). An accurate velocity model is a sufficient condition for the CIGs to be flat. Once the CIGs are flat, summation of the flat events along the aperture-angle axis yields high-energy stacks, while summation along the nonflat events yields lower energy stacks.

The angle-domain common-image gathers are representations of the depth images in a coordinate system defined by depth, midpoint, and aperture-angle. The aperture-angles can be computed in the wavenumber domain as a function of the offset and depth wavenumbers (k_h, k_z) as ²

$$a_h = \arctan\left(\frac{k_h}{k_z}\right). \quad (1)$$

There are two major reasons for the representation of the angle-domain CIGs with the aperture-angle as the “offset” axis:

- The representation in aperture-angle contains valuable information for velocity analysis through the strong moveout of the events migrated with incorrect velocity (Prucha et al., 1999), as shown in Figure 7. This property is also true when we represent the CIGs as a function of the offset ray-parameter (p_h).
- Angle-domain CIGs where the angle axis is described through the offset ray-parameter (p_h) require knowledge about the velocity field. This is fine if we compute the CIGs

²Computing the aperture-angle with the equation (1) assumes that the reflection happens in the inline direction and that there is no azimuthal component to it. This assumption is correct in the 2-D case I analyze in this paper, but it is still an open question when dealing with 3-D data.

after wave-equation depth migration. However, it is much more difficult to assess the correct velocity of the images that have been obtained by residual migration. It is, at least for this application, better to replace p_h with a_h , as defined in the preceding equation.

We can use the information contained in the CIGs to generate better focused images from a suite of images obtained through residual migration for different ratios between the original and modified velocities (Sava, 1999). Since the velocity model is not constant, different ratios will flatten the events more or less in different regions of the image. It follows that the energy of the stack will also vary with the ratio at every location in the image. Therefore, we can pick a map of ratios that represents the highest energy stack, and implicitly the flattest CIGs. At the same time, we can also extract the image that corresponds to the highest energy. In the rest of the paper, I call this image the best focused image.

The full image-enhancement procedure is outlined in the flow-chart shown in Figure 2.

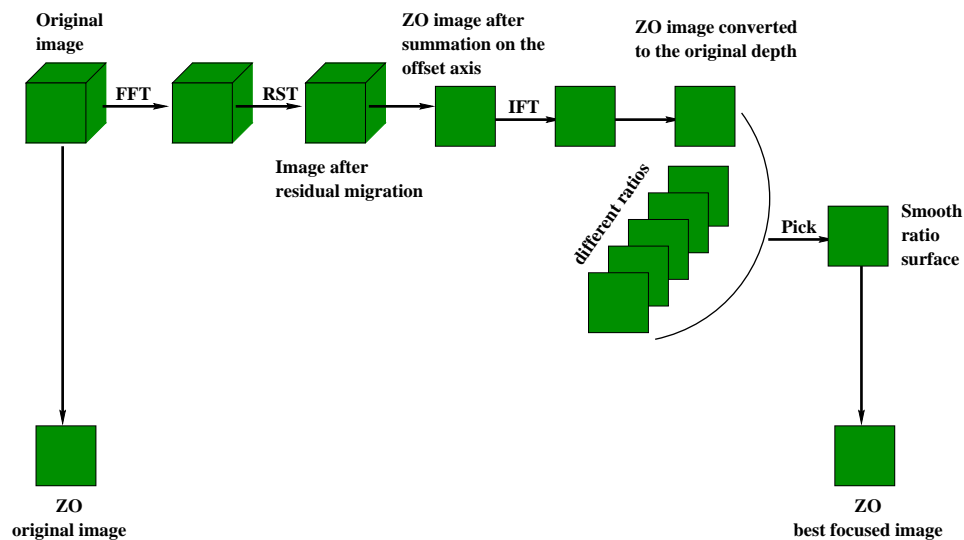


Figure 2: Image enhancement flowchart. We start with the prestack original image, Fourier transform it on all axes, apply residual migration with a given ratio, sum over the offset axis to obtain the zero-offset (ZO) image, and convert it to the original depth. We then repeat the same procedure to obtain ZO images for a suite of ratios and pick the maximum energy. Finally, we compare the ZO section before residual migration to the best focused ZO section after residual migration and optimal picking. `paul1-pick` [NR]

RESULTS

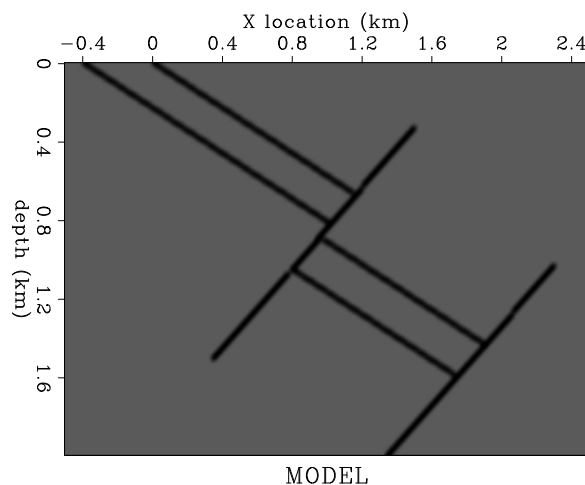
This section offers an example of image enhancement using prestack Stolt residual migration. Figures 3 and 4 show the reflectivity and the slowness model I consider in this example.

The model poses imaging difficulties because of the fast layer that is moved up along the reversed fault. Since the velocity in the layer is much faster than that of the surrounding material, the image under the upper section is expected to be heavily distorted when imaged with an approximate velocity. An easy way to highlight the distortion zone is through wavefront tracing (Sava and Fomel, 1997), which has been shown to approximate wave propagation very well, even in regions of high velocity contrast (Figure 5).

Such a model is especially relevant for regions with large velocity contrasts and steeply dipping boundaries, for example in the North Sea (Vaillant and Sava, 1999) or the Gulf of Mexico, around salt domes. Dipping events tend to move laterally at every offset when imaged with different velocities; therefore residual imaging processes that do not take into account this lateral movement, like residual move-out or warping (Rickett and Lumley, 1998), cannot fully correct the image, but can only increase the flatness of the CIGs. Although flat CIGs are a necessary condition for a correct image, they are not a sufficient one.

Figure 3: The reflectivity model.

`paul1-model` [ER]



First, I generate the data corresponding to an acquisition with a cable 3.2 km long (Figure 6). I then perform wave-equation modeling using an extended split-step algorithm (Stoffa et al., 1990; Biondi and Palacharla, 1996) to generate data, starting from the reflectivity map and the true slowness.

The next step is to create a starting image for the residual migration process by migrating the data with an approximate slowness model, obtained by removing the fast layers and smoothing the model laterally and vertically. The assumption I make is that even if we do not know much about the fast layer, we have a pretty good idea of the velocities on both sides of the fault.

Finally, in the residual migration step, I generate a suite of 41 images corresponding to velocity ratios (ρ) ranging from 0.9 to 1.1 (Figure 8). The values of ρ smaller than 1.0 correspond to new velocities that are higher than the original, while the values above 1.0 correspond to new velocities lower than the original (Sava, 1999).

By studying the different ρ images, we can identify two types of events:

- The first are the mildly dipping events, for example the layers, which do not show

Figure 4: The slowness maps. The upper panel is the true slowness used to generate the data (Figure 6). The lower panel is the smooth slowness I used to create the starting image (Figure 7). The smooth model is obtained by heavily smoothing the true slowness model, with the fast layer removed. `paul1-slow` [ER]

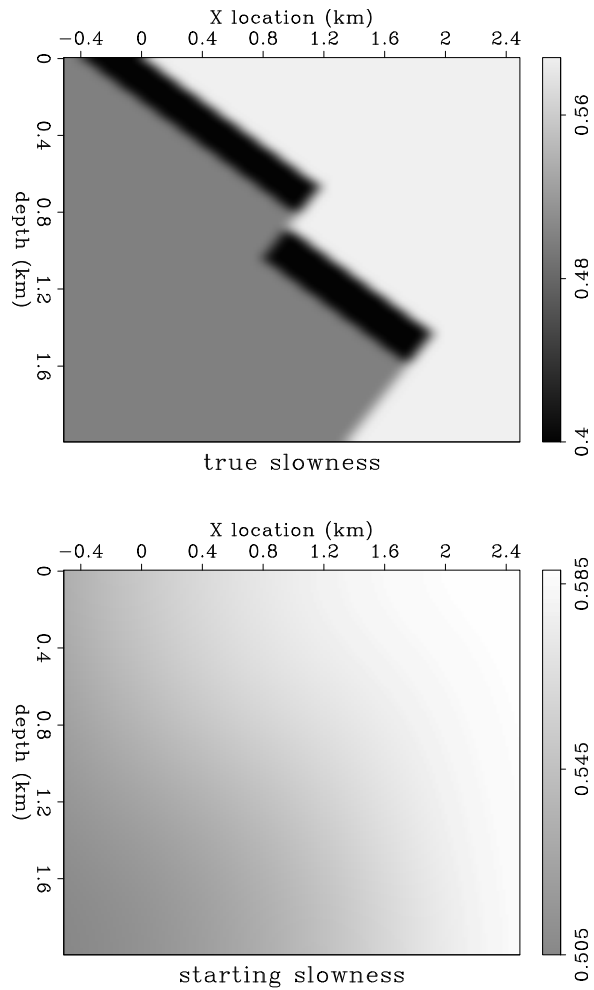
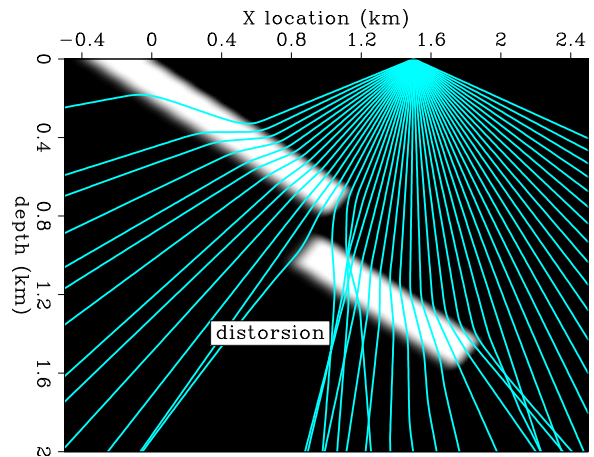


Figure 5: A zone of distortion is created by the fault and the upper segment of the fast layer. `paul1-rays` [ER]



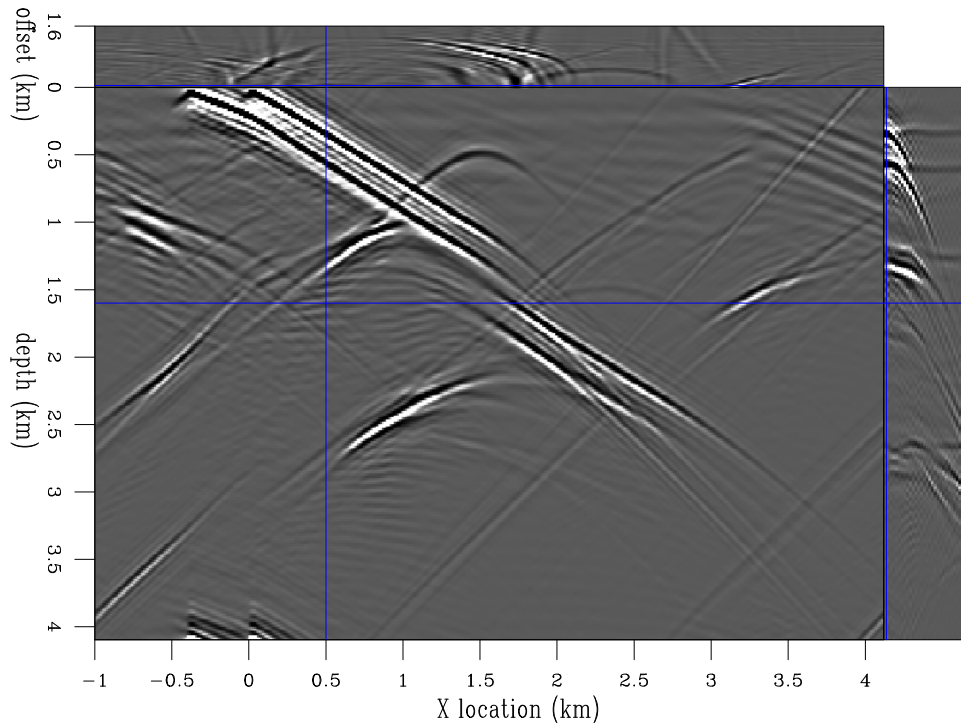


Figure 6: The data generated by wave-equation modeling from the reflectivity model (Figure 3) and the true slowness (upper panel in Figure 4). `paul1-data` [ER]

large lateral movement, but only changes in the moveout of the CIGs. We can obtain better images for these events simply by flattening the CIGs (residual moveout does a reasonably good job).

- Dipping events, such as the fault, which shows significant lateral movement (Figure 8), focus/defocus and present large moveouts in the CIGs. For these events, residual moveout is not appropriate, because it is not enough to flatten an event that is not in its right position. We need to use the more sophisticated procedure of residual migration.

Finally, I stack all these images along their aperture-angle axis, and pick the smooth surface that goes through the points of maximum energy (Figure 10). Once I obtain the surface, I can cut through the stacked slices (Figure 9) and extract the better-focused image (Figure 11).

A simple visual analysis of the images before and after residual migration reveals the areas of improvement. First, the segment of the fault below the fast layer (labeled A in Figure 11) moves toward its correct position to the right, and in better alignment with the segment above the fault. Also, we can clearly identify the better focusing of the reflectors situated in the shadow zone (labeled B and C in Figure 11). These two events are also more closely aligned with their ideal location (Figure 3).

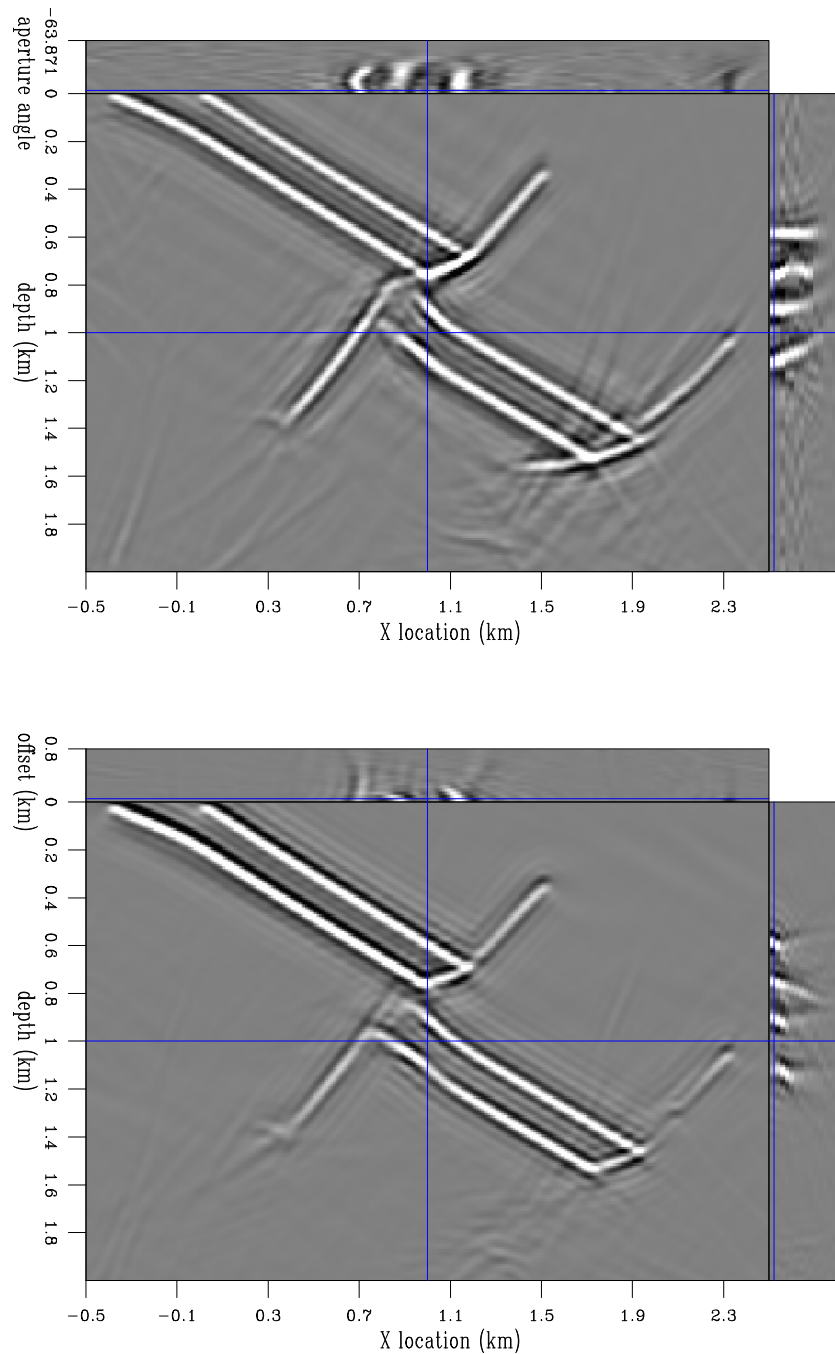


Figure 7: The image obtained by wave-equation migration with the wrong slowness model (Figure 4). The upper plot represents common-image gathers (where the third axis is the aperture-angle), while the bottom plot represents the same information as a function of offset. Properly migrated data should show flat events in the common-image gathers. Events pointing up are a sign of under-migration, while events pointing down are a sign of over-migration. The events with gathers pointing both up and down correspond to the situation when the near and far offsets are influenced by different types of perturbation in the velocity field. The images are not directly comparable, because in the CIG version more of the energy present at the near offsets is spread along the aperture-angle axis, and therefore some events become relatively stronger. `paul1-imageF` [ER]

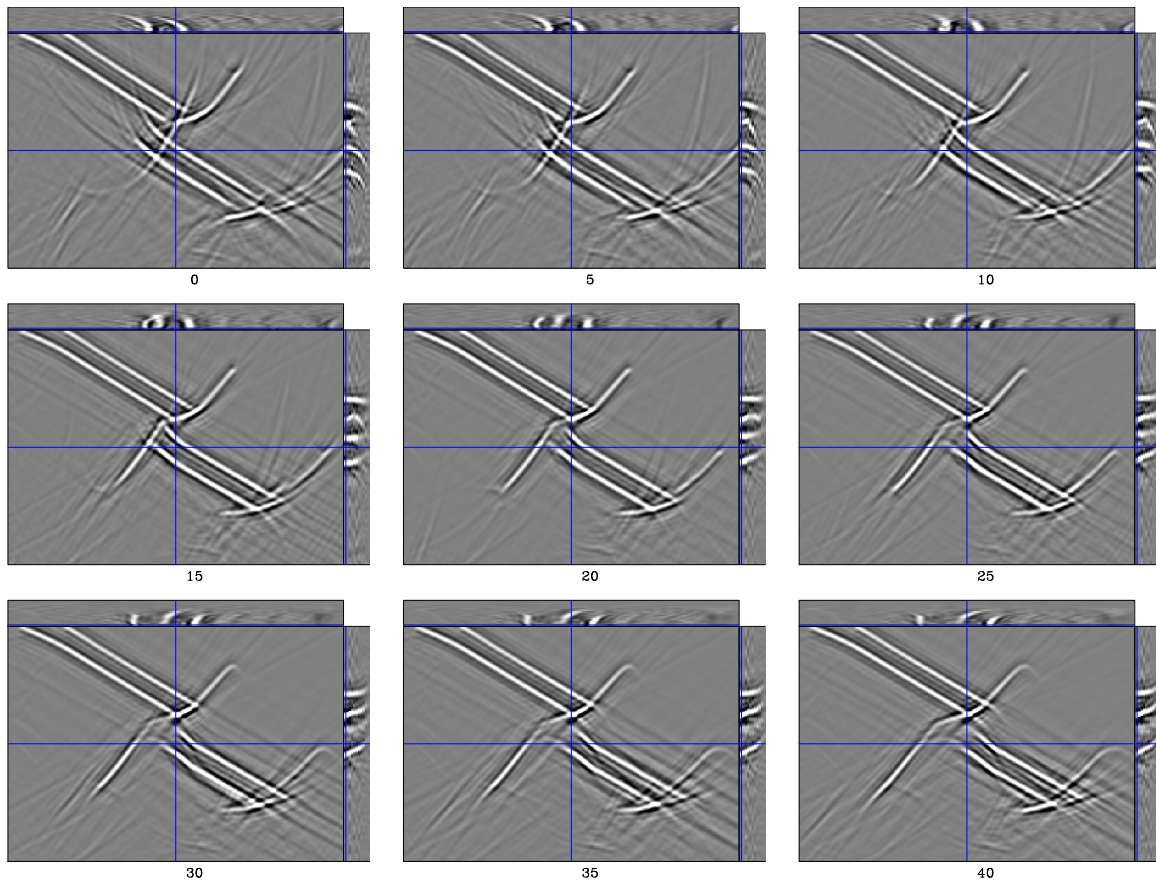


Figure 8: The images obtained after residual migration. Each panel corresponds to a different residual migration ratio (ρ), as follows: 0($\rho = 0.9$), 5($\rho = 0.925$), 10($\rho = 0.95$), 15($\rho = 0.975$), 20($\rho = 1.0$), 25($\rho = 1.025$), 30($\rho = 1.05$), 35($\rho = 1.075$), 40($\rho = 1.1$). The values of ρ smaller than 1.0 correspond to new velocities that are higher than the original, while the values above 1.0 correspond to new velocities lower than the original. The panel labeled 20 is the original image (Figure 7) with no residual migration ($\rho = 1.0$). `paul1-resmig` [ER,M]

Figure 9: The cube of stacked sections. Each plane represents an image at a given ratio. We can use this cube to extract both the surface of maximum energy, and the optimally focused image. Each stack has been converted to the original depth to reduce the vertical movement from one ratio to the other. `paul1-stack` [ER]

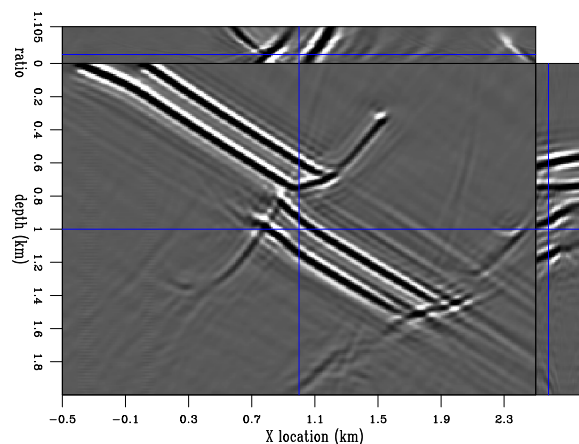


Figure 10: The surface of the picking ratio. This surface represents the values of the ratio (ρ) for which the events are flattest at every point in the common-image gathers. The flatness is measured by the energy of the stack along the angle of incidence axis – the flatter the event, the higher the energy. Dark colors represent values of ρ smaller than 1, while lighter colors represent values of ρ higher than 1. Contours are drawn at every 0.01 units on the ratio axis. `paul1-surface` [ER]

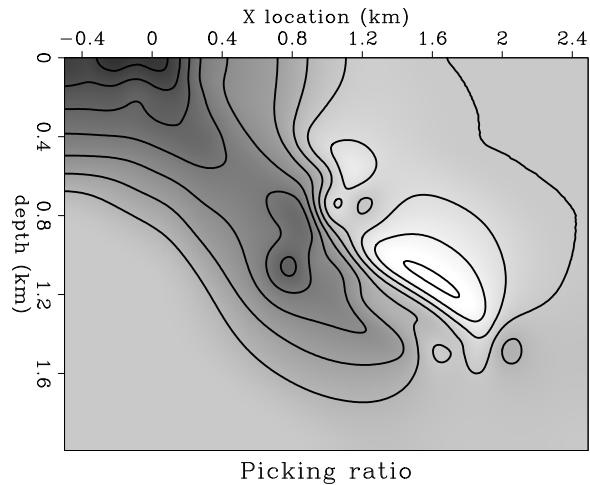
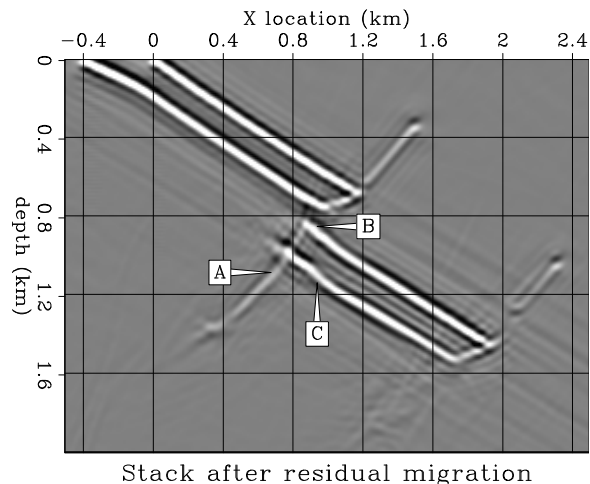
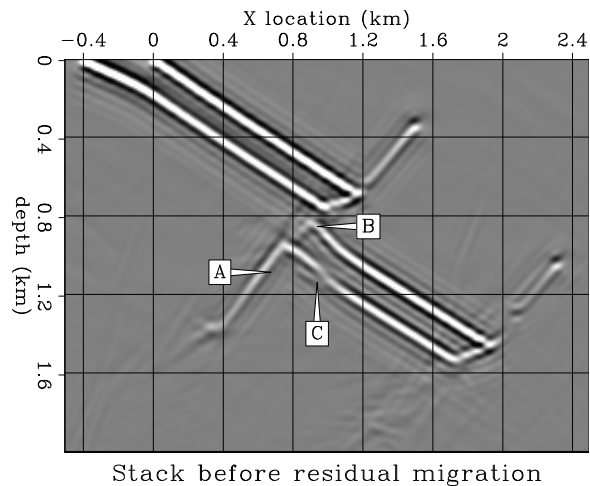


Figure 11: A comparison between the original image obtained through migration with the wrong velocity (Figure 7) and the improved image obtained after residual migration and picking using the best-focusing surface (Figure 10). The area of interest is located at the horizontal location 0.7 – 1.1 km and depth 0.8 – 1.0 km. The segment of the fault in the shadow of the fast layer is moved to the right toward its correct position (A). The top reflectors (B and C), also in the shadow of the fast layer, are moved almost to their correct position and are much more energetic in the best-focused image (below) than in the original image (above). `paul1-improved` [ER]



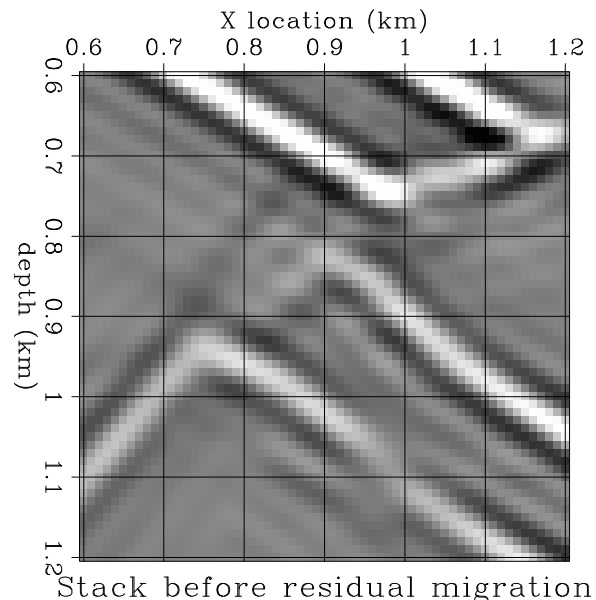
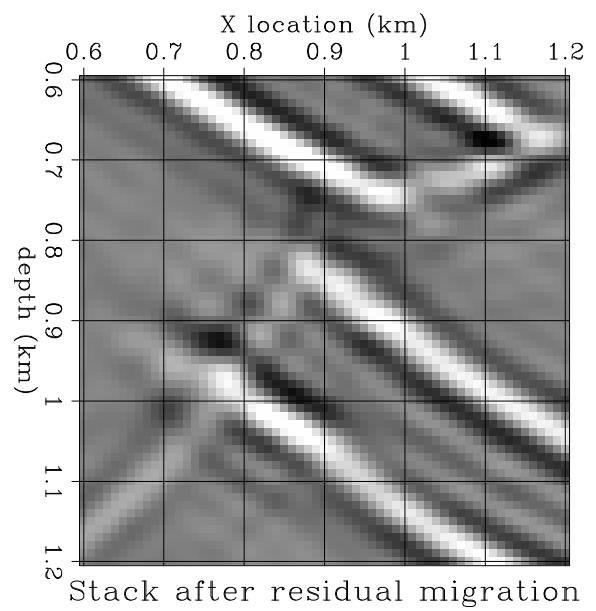


Figure 12: Same comparison as in Figure 11. Zoom over the zone of interest. `paul1-detail` [ER]



CONCLUSIONS

Velocity-independent Stolt residual migration improves the image focusing for a model with significance for seismic imaging problems in areas of large velocity contrast and limited illumination. In this study I have found that residual migration is applicable and can generate better-focused images. The entire process is cheap, with a cost comparable with that of a suite of Stolt migrations.

The potential pitfalls occur in the area of maximum energy picking. Complex situations, where different events cross along the ratio direction, pose a significant challenge for the automated picker. Better picking algorithms, or maybe interactive techniques, can resolve this problem. This is an area for future work, together with more experiments on both real and synthetic data.

Another direction for future work, with more relevance to velocity analysis, is the extension of the current method to prestack data and to 3-D common-azimuth data. Once we have obtained the picking surface, we can cut directly through the prestack images to get the one with the best focusing and the flattest CIGs.

ACKNOWLEDGMENTS

I would like to thank Biondo Biondi for numerous and stimulating discussions. I would also like to thank James Rickett for providing a most welcome challenge.

REFERENCES

- Biondi, B., and Palacharla, G., 1996, 3-D prestack migration of common-azimuth data: *Geophysics*, **61**, no. 6, 1822–1832.
- Biondi, B., and Sava, P., 1999, Wave-equation migration velocity analysis: *SEP-100*, 11–34.
- Biondi, B., 1999, Subsalt imaging by common-azimuth migration: *SEP-100*, 113–124.
- Prucha, M. L., Biondi, B. L., and Symes, W. W., 1999, Angle-domain common image gathers by wave-equation migration: *SEP-100*, 101–112.
- Rickett, J., and Lumley, D., 1998, A cross-equalization processing flow for off-the-shelf 4-D seismic data: *SEP-97*, 265–274.
- Sava, P., and Fomel, S., 1997, Huygens wavefront tracing: A robust alternative to conventional ray tracing: *SEP-95*, 101–113.
- Sava, P., 1999, Short note—on Stolt prestack residual migration: *SEP-100*, 151–158.
- Stoffa, P. L., Fokkema, J. T., de Luna Freire, R. M., and Kessinger, W. P., 1990, Split-step Fourier migration: *Geophysics*, **55**, no. 4, 410–421.

Stolt, R. H., 1996, Short note—a prestack residual time migration operator: *Geophysics*, **61**, no. 2, 605–607.

Vaillant, L., and Sava, P., 1999, Common-azimuth migration of a North Sea dataset: *SEP-102*, 1–14.

Short Note

On Stolt common-azimuth residual migration

Paul Sava¹

INTRODUCTION

This short note presents the extension of the velocity-independent Stolt residual migration introduced in a previous report (Sava, 1999) to common-azimuth (CA) data. The derivation is very similar to its 2-D equivalent and retains the important feature of being independent of any assumption about the velocity used to obtain the image being residually migrated.

Residual migration can be used for both image improvement and velocity analysis. As was previously shown (Biondi and Sava, 1999), we can use the differences between a given image and an improved version of it in wave-equation velocity analysis. Since full 3-D prestack velocity analysis using the wave equation is still not within reach owing to its huge computational cost, the common-azimuth approximation seems to be the proper technology usable for 3-D datasets. It is therefore necessary to devise the appropriate residual migration tools for common-azimuth data.

In the first part of this short note I present the derivation of the common-azimuth Stolt residual migration equations, followed in the second part by a simple synthetic example.

THEORY

Common-azimuth data represent subsets of 3-D datasets that have been recorded or transformed to zero cross-line offsets ($h_y = 0$). Stolt constant velocity migration for common-azimuth data involves the use of the following dispersion relation (Biondi and Palacharla, 1995):

$$k_{z_x} = \frac{1}{2} \sqrt{\left(\frac{\omega}{v}\right)^2 - (k_{m_x} - k_{h_x})^2} + \frac{1}{2} \sqrt{\left(\frac{\omega}{v}\right)^2 - (k_{m_x} + k_{h_x})^2}, \quad (1)$$

where the depth wavenumber of the common-azimuth dataset (k_z) is

$$k_z = \sqrt{k_{z_x}^2 - k_{m_y}^2}, \quad (2)$$

¹email: paul@sep.stanford.edu

and the midpoint and offset wavenumbers are defined as $\mathbf{k}_m = k_{m_x}\mathbf{x} + k_{m_y}\mathbf{y}$ and $\mathbf{k}_h = k_{h_x}\mathbf{x} + k_{h_y}\mathbf{y}$.

We can write equations (2) and (1) for a given reference velocity (v_0) as

$$k_{z_{x0}} = \frac{1}{2}\sqrt{\left(\frac{\omega}{v_0}\right)^2 - (k_{m_x} - k_{h_x})^2} + \frac{1}{2}\sqrt{\left(\frac{\omega}{v_0}\right)^2 - (k_{m_x} + k_{h_x})^2}, \quad (3)$$

and

$$k_{z0} = \sqrt{k_{z_{x0}}^2 - k_{m_y}^2}. \quad (4)$$

The goal of common-azimuth Stolt residual migrations is to obtain k_z (equations 2 and 1) from k_{z0} (equations 4 and 3).

If we express the frequency ω from equation (3) as

$$\omega^2 = v_0^2 \frac{[k_{z0}^2 + k_{m_y}^2 + k_{h_x}^2][k_{z0}^2 + k_{m_y}^2 + k_{m_x}^2]}{k_{z0}^2 + k_{m_y}^2}$$

and introduce it in equation (1), we obtain the common-azimuth residual migration equations

$$\left\{ \begin{array}{l} k_{z_x} = \frac{1}{2}\sqrt{\frac{v_0^2}{v^2} \frac{[k_{z0}^2 + k_{m_y}^2 + k_{h_x}^2][k_{z0}^2 + k_{m_y}^2 + k_{m_x}^2]}{k_{z0}^2 + k_{m_y}^2} - (k_{m_x} - k_{h_x})^2} \\ \quad + \frac{1}{2}\sqrt{\frac{v_0^2}{v^2} \frac{[k_{z0}^2 + k_{m_y}^2 + k_{h_x}^2][k_{z0}^2 + k_{m_y}^2 + k_{m_x}^2]}{k_{z0}^2 + k_{m_y}^2} - (k_{m_x} + k_{h_x})^2} \\ k_z = \sqrt{k_{z_x}^2 - k_{m_y}^2} \end{array} \right. \quad (5)$$

Note that for 2-D prestack data, ² equations (5) reduce to the 2-D prestack form (Sava, 1999):

$$k_z = \frac{1}{2}\sqrt{\frac{v_0^2}{v^2} \frac{[k_{z0}^2 + k_{h_x}^2][k_{z0}^2 + k_{m_x}^2]}{k_{z0}^2} - (k_{m_x} - k_{h_x})^2} + \frac{1}{2}\sqrt{\frac{v_0^2}{v^2} \frac{[k_{z0}^2 + k_{h_x}^2][k_{z0}^2 + k_{m_x}^2]}{k_{z0}^2} - (k_{m_x} + k_{h_x})^2},$$

which, furthermore, reduces to the well-known Stolt 2-D post-stack residual migration equa-

$$s_y = g_y \Leftrightarrow k_{m_y} = 0$$

$$k_z \equiv k_{z_x}$$

$$k_{z0} \equiv k_{z_{x0}}$$

tion (Stolt, 1996)³:

$$k_z = \sqrt{\frac{v_0^2}{v^2} [k_{z0}^2 + k_{m_x}^2]} - k_{m_x}.$$

As for the 2-D prestack data, the common-azimuth residual migration is velocity independent; that is, we need not make any assumption about the actual values of the velocities for the reference and improved migration, but only about their ratio. In this way, we can take an image and residually migrate it without knowing what velocity model has been used to image it in the first place.

EXAMPLE

In this section, I present a synthetic example of Stolt migration and residual migration for common-azimuth data. The model is represented by a set of four plane reflectors at different depths, with different lateral dimensions and varying reflectivity (Figure 1).

Figure 2 shows the result of Stolt modeling using the true velocity $v = 3.0$ km/s. Next, I apply Stolt migration with a velocity of $v_0 = 3.6$ km/s (Figure 3). Since the velocity is not the true one used to generate the data, the image is not focused correctly at the three original reflectors.

Finally, I use Stolt common-azimuth residual migration as described in the preceding section and with a velocity ratio $v_0/v = 1.2$ to get the image in Figure 4. Now the original reflectors are well-focused at their original locations.

CONCLUSIONS

In this short note, I have presented the extension of the velocity independent Stolt residual migration to common-azimuth data. Equations (5) can be used to obtain images corresponding to new velocities defined by a given ratio to the original velocity.

Such a residual migration method inherits the advantages and disadvantages of Stolt residual migration. Some of the most notable characteristics are:

- Speed: Because CA Stolt residual migration is essentially a Stolt migration, its cost is comparable to that of any Stolt migration.

3

$$vk_z = \sqrt{v_0^2 k_{z0}^2 + k_{m_x} (v_0^2 - v^2)}$$

$$\omega = \sqrt{\omega_0^2 + k_{m_x} (v_0^2 - v^2)}$$

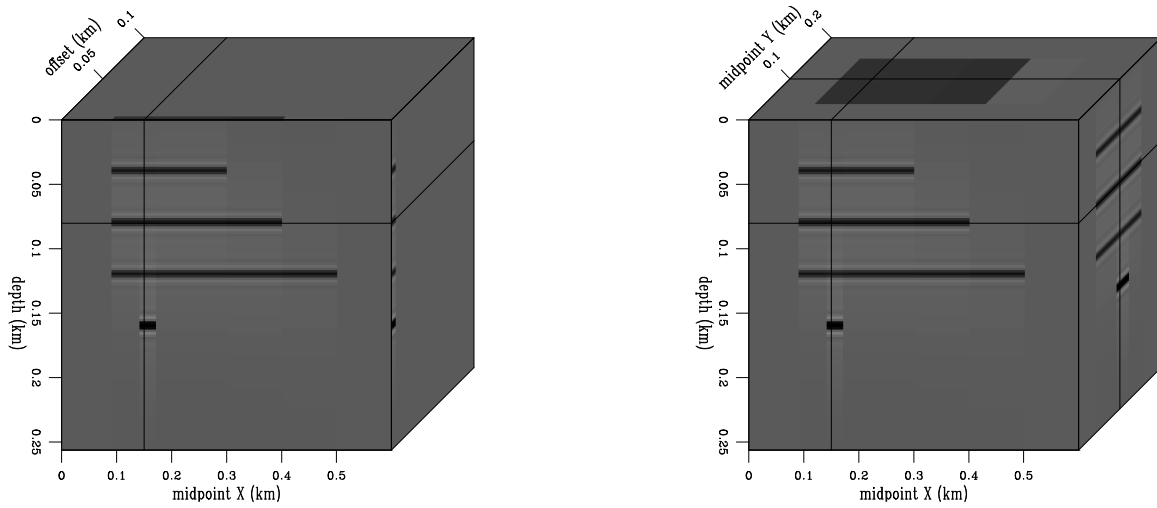


Figure 1: The reflectivity model. The right panel represents the zero-offset view in the common-azimuth space, while the left panel represents the prestack view for the inline selected on the right panel. `paul2-model` [ER]

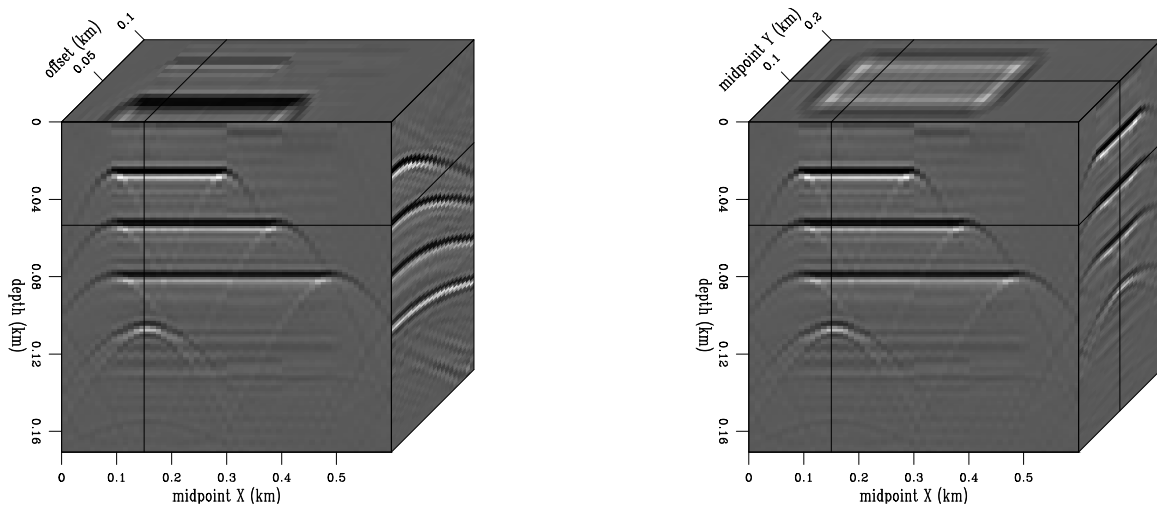


Figure 2: The data generated using Stolt common-azimuth modeling. The velocity used for modeling is $v = 3.0$ km/s. The right panel represents the zero-offset view in the common-azimuth space, while the left panel represents the prestack view for the inline selected on the right panel. `paul2-data` [ER]

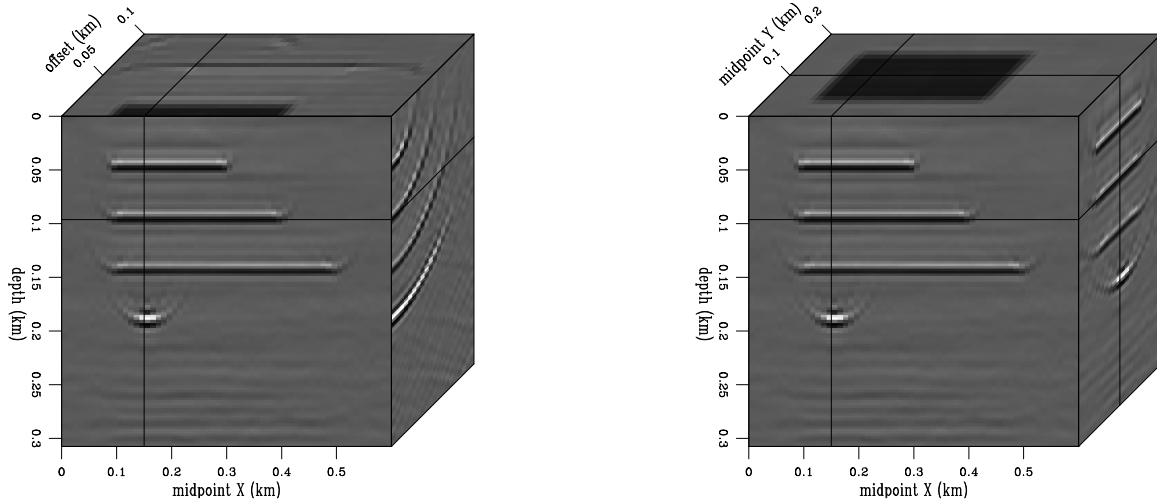


Figure 3: The image obtained using Stolt common-azimuth migration. The velocity used for migration is $v_0 = 3.6$ km/s. Since $v_0 > v$, the image is clearly over-migrated. The right panel represents the zero-offset view of the common-azimuth data, while the left panel represents the prestack view for the inline selected on the right panel. `paul2-mig` [ER]

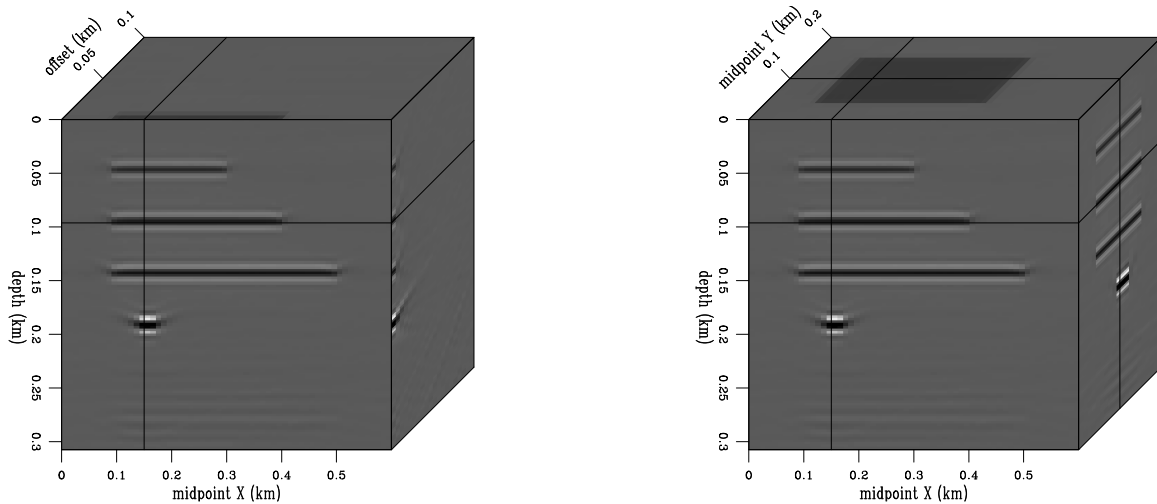


Figure 4: The image obtained using Stolt common-azimuth residual migration using velocity ratio $v_0/v = 1.2$. The image is nicely focused at zero-offset. The right panel represents the zero-offset view of the common-azimuth data, while the left panel represents the prestack view for the inline selected on the right panel. `paul2-rst` [ER]

- Constant velocity: Stolt migration assumes constant velocity. In theory, CA residual Stolt migration assumes constant velocity, too. In practice, however, if we residually migrate an image migrated with a variable velocity, we will obtain another image that has a corresponding variable velocity. In this case, however, the actual relationship between the velocities before and after residual migration is still not clarified and remains a subject for further research.
- Artifacts: Since Stolt CA residual migration is a frequency-domain method, it is susceptible to the same interpolation and wrap-around artifacts as the usual Stolt migration. Nevertheless, any technique used to reduce the Stolt artifacts (Levin, 1994; Fomel, 1998) can also be used for CA residual migration with the same efficiency.

REFERENCES

- Biondi, B., and Palacharla, G., 1995, 3-D prestack depth migration of common-azimuth data: SEP-84, 11–24.
- Biondi, B., and Sava, P., 1999, Wave-equation migration velocity analysis: SEP-100, 11–34.
- Fomel, S., 1998, Velocity continuation by spectral methods: SEP-97, 157–172.
- Levin, S. A., 1994, Stolt without artifacts? — dropping the Jacobian: SEP-80, 513–532.
- Sava, P., 1999, Short note—on Stolt prestack residual migration: SEP-100, 151–158.
- Stolt, R. H., 1996, Short note—a prestack residual time migration operator: Geophysics, 61, no. 2, 605–607.

On Stolt stretch time migration

Louis Vaillant and Sergey Fomel¹

ABSTRACT

We implement Stolt-stretch time migration with an analytical formulation for the optimal stretch parameter and show how it improves the quality of imaging. By a cascaded f - k migration approach with this algorithm, we manage to obtain time migration results on real data comparable to Gazdag's phase-shift method, with a high accuracy for steeply deeping events at a computational cost dramatically lowered.

INTRODUCTION

Time migration remains a very fast imaging process compared to prestack depth migration and therefore is still commonly used by seismic imaging contractors. Such an economical technique reveals itself useful as a first approach to a problem or for producing accurate images when the interval velocity varies only with depth. Among the many algorithms available for post-stack time migration, Stolt's is known as the fastest of all. It is derived from a wavefield downward-continuation in constant velocity. This constant velocity assumption yields the well-known shortcoming of Stolt's algorithm. In his classic paper, Stolt (1978) proposed as an approximation for $v(z)$ media a stretching of the time axis that is commonly called "Stolt-stretch" migration. In that context, the vertical heterogeneities of the velocity model are represented by a single nondimensional parameter W , substituted for a complicated function of several parameters. In the constant velocity case, W is equal to 1.0. In a medium where the velocity is increasing with depth, its value is constrained to lie between 0.0 and 1.0.

In practice, a frustrating drawback of the technique is that there was no constructive way to choose the parameter W . To overcome this heuristic guess, Fomel (1995) derived an explicit formulation for W based on Malovichko's formula for approximating traveltimes in vertically inhomogeneous media (Malovichko, 1978; Sword, 1987; Castle, 1988; de Bazelaire, 1988). In this paper, we implement Stolt-stretch time migration with this optimal choice for W and discuss its accuracy.

¹email: louis@sep.stanford.edu, sergey@sep.stanford.edu

STOLT STRETCH THEORY REVIEW

Stolt time migration can be summarized as the following sequence of transformations:

$$p_0(x, t_0) \rightarrow P_0(k_x, \omega_0) \rightarrow P(k_x, \omega) \rightarrow p(x, t), \quad (1)$$

where

$$P_0(k_x, \omega_0) = P(k_x, \omega(k_x, \omega_0)) \left| \frac{d\omega(k_x, \omega_0)}{d\omega_0} \right| \quad (2)$$

The function $\omega(k, \omega_0)$ is the dispersion relation and has the following expression in the constant velocity case:

$$\omega(k, \omega_0) = \text{sign}(\omega_0) \sqrt{\omega_0^2 - v^2 k_x^2} \quad (3)$$

The approximation suggested by Stolt (1978) for extending the method to $v(z)$ media involves a change of the time variable (Stolt-stretch):

$$s(t) = \sqrt{\frac{2}{v_0^2} \int_0^t \tau v_{rms}^2(\tau) d\tau}, \quad (4)$$

where $s(t)$ is the stretched time variable, v_0 is an arbitrarily chosen constant velocity, and $v_{rms}(t)$ is the root mean square velocity along the vertical ray, defined by

$$v_{rms}(t) = \frac{1}{t} \int_0^t v^2(\tau) d\tau. \quad (5)$$

This change of variable yields a transformed wave-equation for the wavefield extrapolation, in which Stolt replaces a slowly varying complicated function of several parameters (denoted by W) by its average value. Making this approximation yields a new dispersion relation in the transformed coordinate system:

$$\hat{\omega}(k_x, \hat{\omega}_0) = \left(1 - \frac{1}{W}\right) \hat{\omega}_0 + \frac{\text{sign}(\hat{\omega}_0)}{W} \sqrt{\hat{\omega}_0^2 - W v_0^2 k_x^2} \quad (6)$$

This factor W contains all the information about the heterogeneities of the medium. However, it has to be determined a priori, that is, before migration. This empirical choice for W was one of the drawbacks of the Stolt-stretch method. Fomel (1995) derived an analytical formulation of the Stolt-stretch parameter, based on Malovichko's formula for approximating traveltimes in vertically inhomogeneous media (Malovichko, 1978):

$$t_0 = \left(1 - \frac{1}{S(t)}\right) t + \frac{1}{S(t)} \sqrt{t^2 + S(t) \frac{(x - x_0)^2}{v_{rms}^2(t)}}, \quad (7)$$

where the function $S(t)$ defines the so-called parameter of heterogeneity:

$$S(t) = \frac{1}{v_{rms}^4 t} \int_0^t v^4(t) dt \quad (8)$$

Fomel proved that, for a given depth (or vertical traveltime), the optimal value of W is

$$W(t) = 1 - \frac{v_0^2 s^2(t)}{v_{rms}^2(t) t^2} \left(\frac{v^2(t)}{v_{rms}^2(t)} - S(t) \right), \quad (9)$$

where $v_{rms}(t)$ is the root mean square velocity along the vertical ray, and $t = \int_0^z \frac{dz}{v(z)}$ the vertical traveltime. The value of W used during Stolt migration is the average along the vertical profile of these $W(t)$. In the case of an homogeneous constant-velocity model, W is equal to 1.0, whereas it has to be less than 1.0 if the velocity increases monotonically with depth.

We can sum up the application of Stolt-stretch algorithm with the optimal parameter W by the following sequence of steps:

1. Stretch the time axis and determine the value of W along the vertical profile
2. Interpolate stretched time to a regular grid
3. 2-D FFT
4. Apply Stolt migration with the dispersion relation (6)
5. 2-D inverse FFT
6. Unstretch the time axis

APPLICATION

Following the study by Larner et al. (1989), we selected a dataset that includes steep dips in order to test the accuracy of our algorithms. The data is courtesy of Elf Aquitaine, was recorded in the North Sea, and shows a salt dome (Figure 3). Figure 1 shows (a) the data after NMO-stack and (b) after poststack Stolt migration, using a constant velocity of 2000 m/s. We notice that Stolt's method obviously yields undermigrated events on both sides of the salt body. Using a higher velocity to focus them better would have created overmigration artifacts at shallow reflectors. Stolt-stretch migrated section (c) using $W = 0.5$ should be compared with figure 2a.

Using the Stolt-stretch method with the optimal choice for W derived from equation (9) yields a better focusing of events at all depths (Figure 2a), compared to other values of W (Figures 1b and 1c, respectively for W equals 1.0 and 0.5). The $v(z)$ model used for migration is shown in Figure 4a and was obtained by averaging laterally the reference velocity model.

The reference method of migration for our study is the phase-shift approach proposed by Gazdag (1978). It is known to be perfectly accurate for all dips up to 90° in a $v(z)$ velocity field. A comparison between the phase-shift migration result (Figure 2b) and the section migrated with the Stolt-stretch approach shows almost no difference for flat events. However, a more detailed analysis reveals significant errors for steep events inside and around the salt body. The approximation made by stretching the time axis breaks for recovering steep events.

A way to overcome the difficulties encountered by Stolt's migration is to divide the whole process into a cascade, as suggested by Beasley et al. (1988). The theory of cascaded

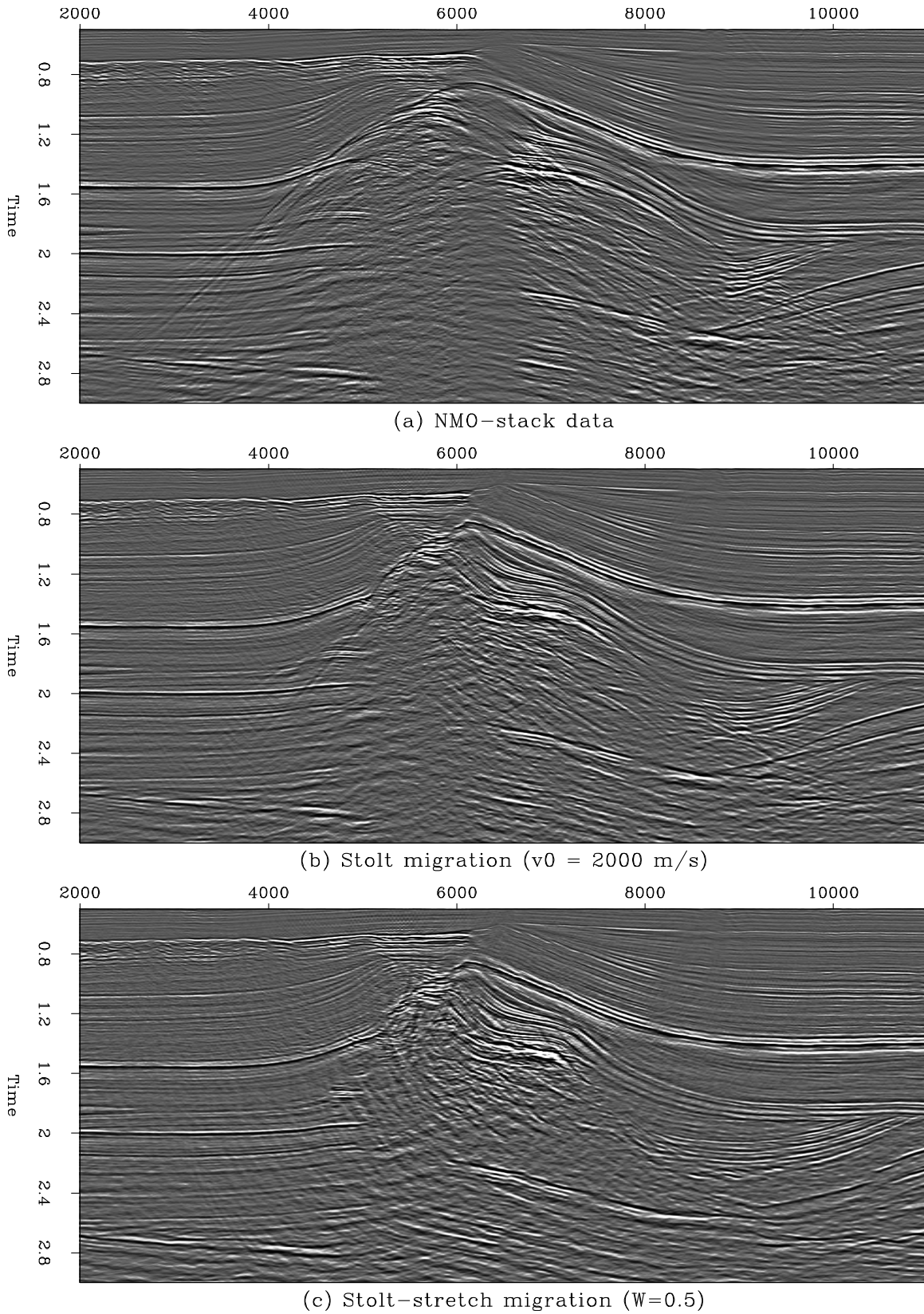


Figure 1: (a) Section of the North Sea data, after NMO-stack. (b) Section migrated using Stolt's method with $v_0=2000$ m/s. (c) Section migrated using Stolt-stretch with an arbitrary value $W = 0.5$ for the parameter of heterogeneity. [louis2-data-stolt-ststr](#) [ER]

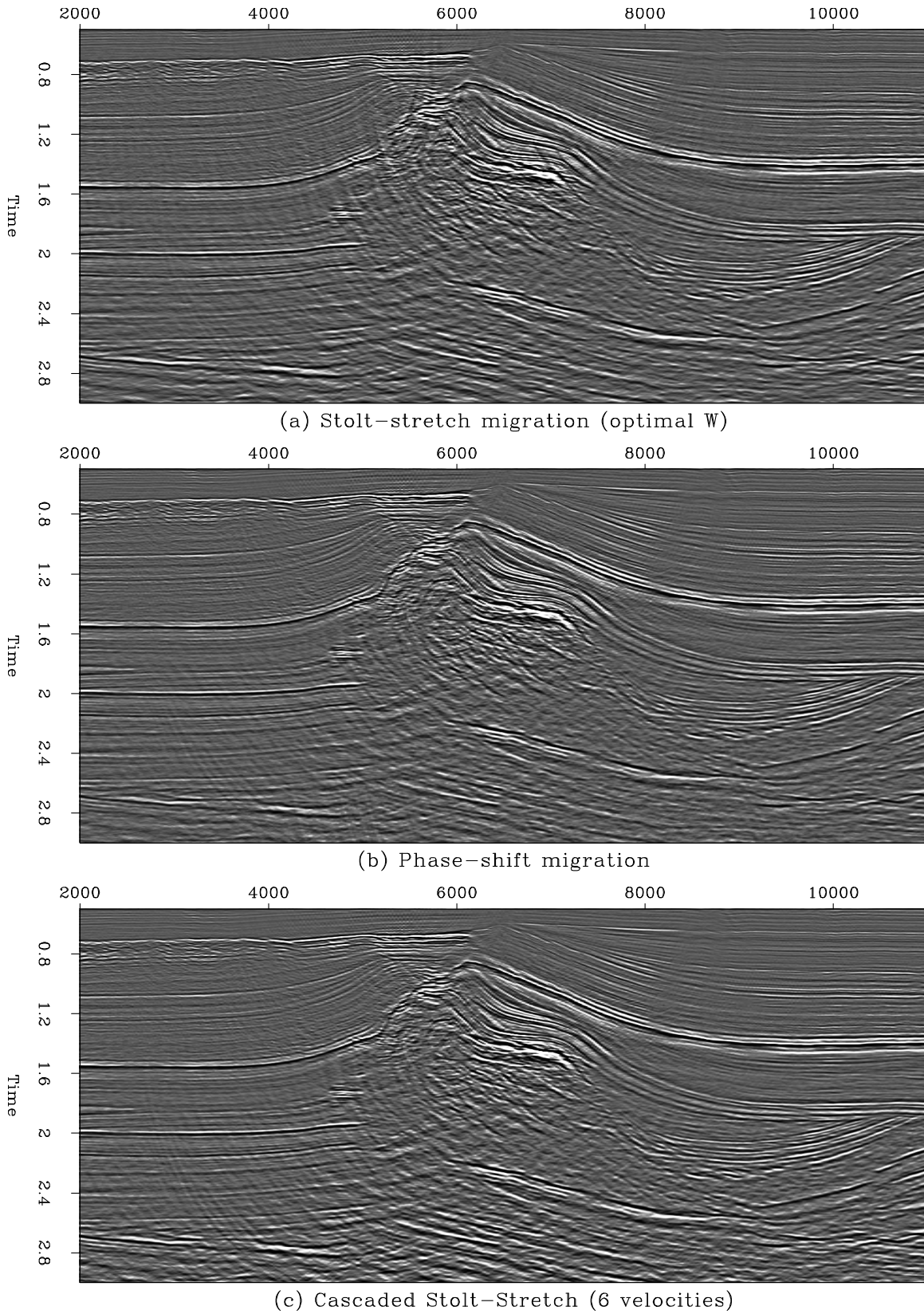


Figure 2: (a) Section migrated with the Stolt-stretch method using the optimal value (≈ 0.67) for the parameter W . (b) Section migrated with the phase-shift method. (c) Section migrated using the cascaded Stolt-stretch approach (6 velocities). `louis2-data-ststr-pshift-casc` [ER]

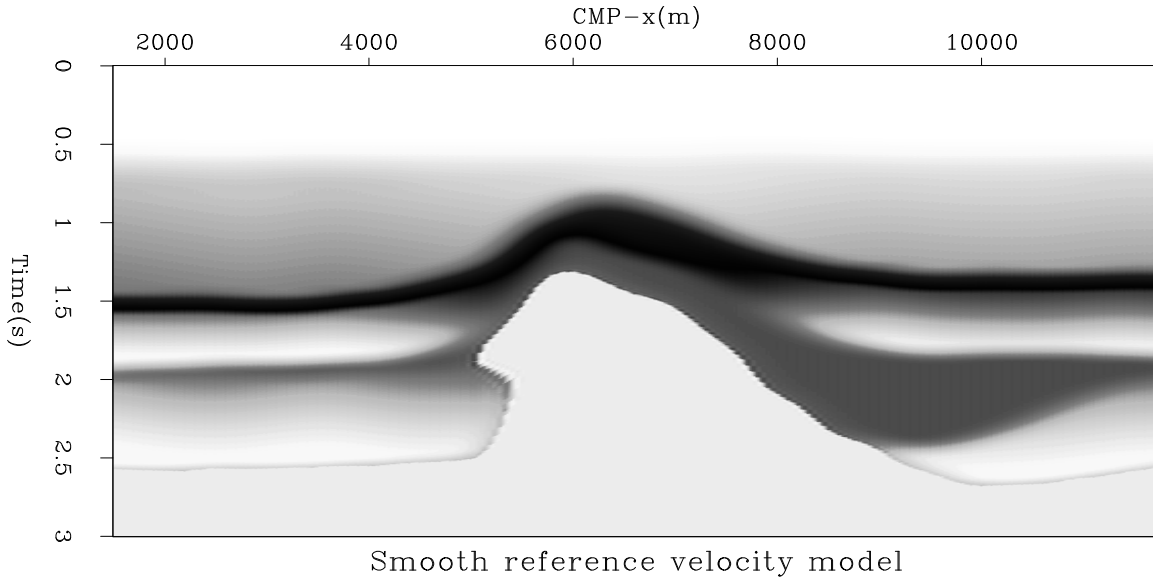


Figure 3: 2-D smooth reference velocity model `louis2-vel-model` [ER]

migration proves that f - k migration algorithms with a $v(t)$ velocity model like Stolt-stretch can be performed sequentially as a cascade of n migrations with smaller interval velocities $v_i(t)$, $i = 1, \dots, n$, such as $v^2(t) = \sum_{i=1,n} v_i^2(t)$. At a given vertical traveltime t , all the successive velocity models have to be constant, except the last one (Larner and Beasley, 1987). Typically, the first stage is done with a constant velocity model and can be computed using Stolt's algorithm, which is then accurate for all dips. Figure 4 illustrates such a cascade of velocity models in our particular case, with 3 and 6 stages.

As a consequence of this decomposition, each intermediate velocity model shows not only a smaller velocity but also less vertical heterogeneity. In other words, the Stolt-stretch parameter W estimated for each stage tends to be closer to 1.0, thus reducing the migration errors due to the approximation. Figure 2c shows the migration result using a 6-stage cascaded scheme. All the successive values of W were greater than 0.8. There are almost no differences with the phase-shift result (Figure 2b).

DISCUSSION

Even if the parameter W estimated from equation (9) is optimal in the sense that it minimizes migration errors for the Stolt-stretch method, no single choice of W yields acceptable results for all times and all dips (Beasley et al., 1988): some events are undermigrated, others overmigrated. Instead, the use of cascaded Stolt-stretch migration allows a reduction of the apparent dip perceived in each stage, since the migration velocity used is reduced to a fraction of the original model. A 20-stage cascade of migration with an algorithm accurate for dips up to 15° can yield accurate results for events dipping up to 65° (Larner and Beasley, 1987).

Figure 5 shows a close-up of the salt body region for all migration algorithms. The meth-

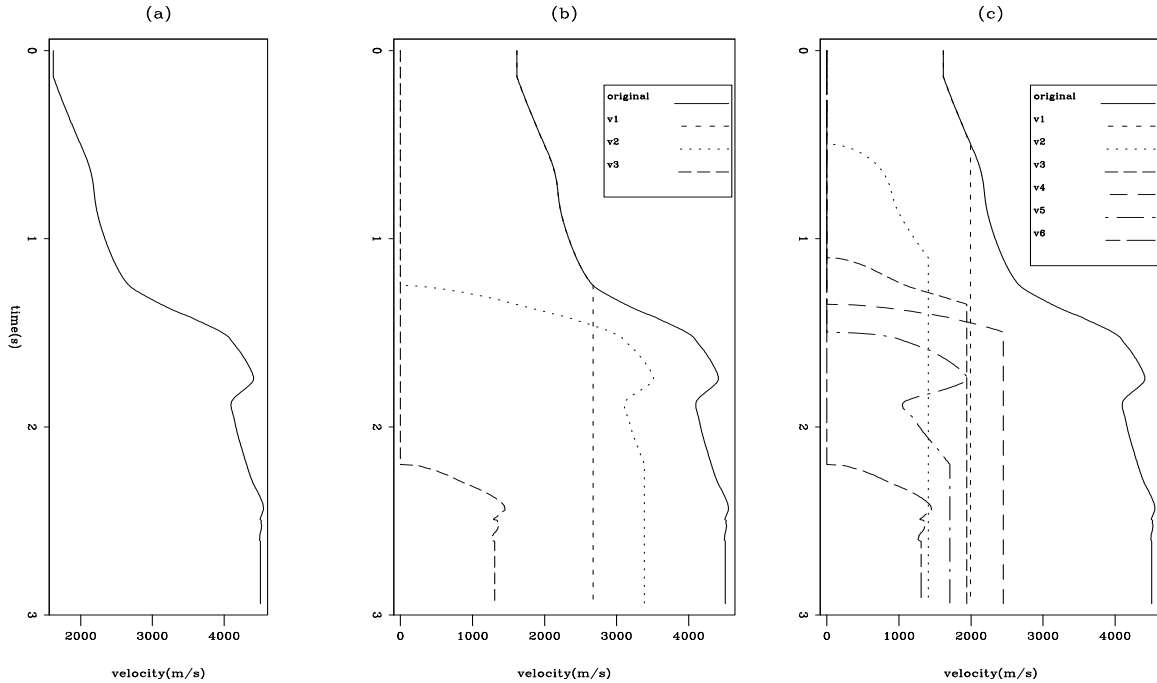


Figure 4: (a) Interval velocity model $v(t)$ estimated from the 2-D reference model. (b) Decomposition in a cascade of 3 models, such as $v^2 = v_1^2 + v_2^2 + v_3^2$. (c) Decomposition in a cascade of 6 models, such as $v^2 = v_1^2 + v_2^2 + v_3^2 + v_4^2 + v_5^2 + v_6^2$ [louis2-velocities] [ER]

ods have a different accuracy with respect to steep dips. We notice a gradual improvement of the result from Stolt-stretch to phase-shift as we increase the number of velocities in the cascaded Stolt-stretch scheme. In theory, the migration errors in the cascaded approach can be made as small as desired by increasing the number of stages. At the limit, it corresponds to the velocity continuation concept (Fomel, 1996).

In our case, six stages were enough to obtain a result comparable to phase-shift. In their comparative study on time migration algorithms, Lerner et al. (1989) have shown that four-stage cascaded $f-k$ migration is accurate for dips up to 85° , which is almost comparable to phase-shift, accurate for all dips. It is worth noting the computational cost difference between the two: on our example, phase-shift migration is about 80 times more expensive than Stolt-stretch!

Another way to look at the problem is to compare the impulse responses of the different algorithms (Figure 6), generated using the same velocity model as before (Figure 4a). There is a kinematic difference in the impulse response of Stolt-stretch compared to phase-shift. While Gazdag's phase-shift honors ray bending in any $v(z)$ model, Stolt-stretch is not that accurate. Both methods address non-hyperbolic moveout, but Stolt's stretching function is only designed to make the fitting curve look like an hyperbola close to the apex (Levin, 1983), and therefore induces residual migration errors. As seen in Figure 2a, Stolt-stretch result displays residual hyperbolic migration artifacts that are due to this fundamental kinematic difference. Cascading Stolt-stretch makes the impulse response of the migration converge towards the one of phase-

shift.

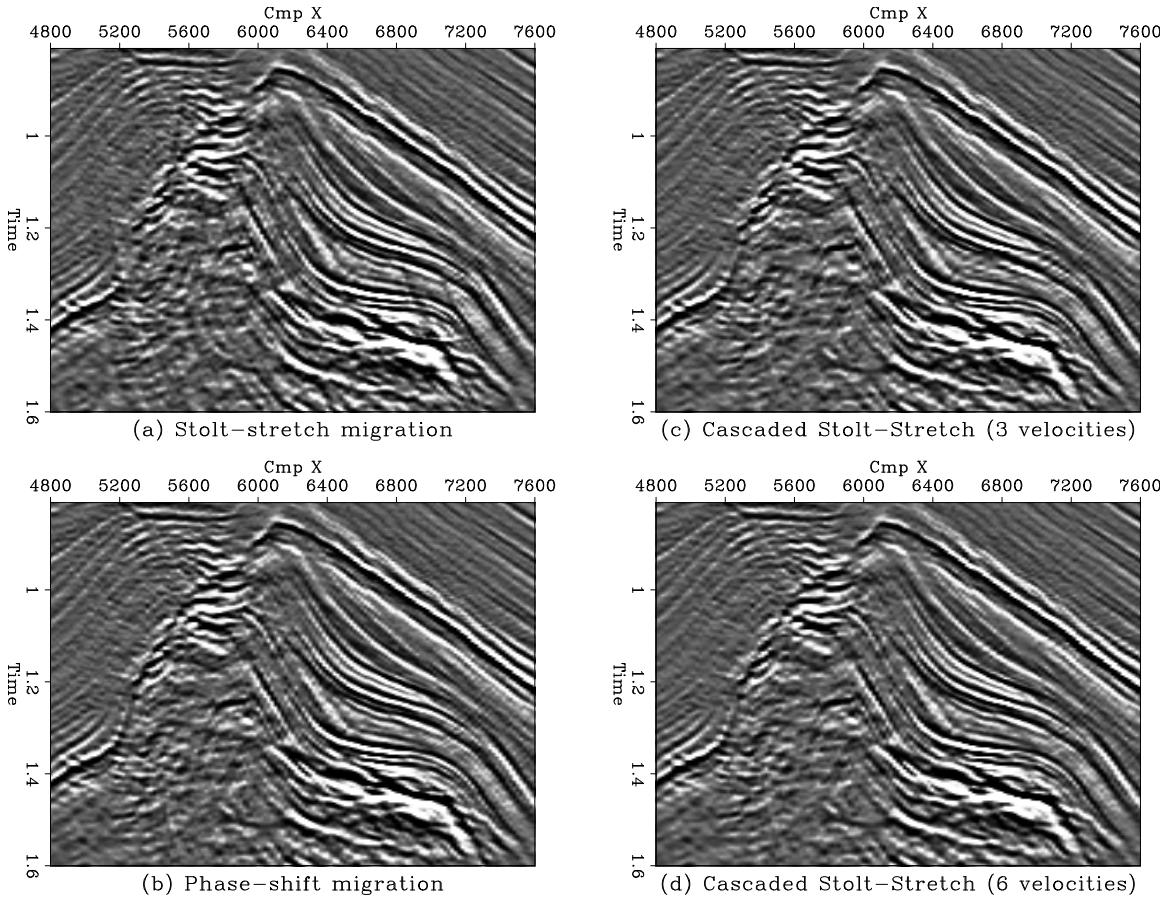


Figure 5: Zoom in the salt body area where steep dips are located. (a) Migration with the Stolt-stretch method. (b) Migration with the phase-shift method. (c) and (d) Migrations with the cascaded Stolt-stretch approach, using, respectively, 3 and 6 velocities. louis2-dip-zoom [ER]

Now that we are familiar with the role of W in the algorithm, a word should be said about v_0 , which is the second arbitrary parameter of the method. As introduced in equation (4), v_0 controls the length of the stretch. In theory, the migration result does not depend on the selected value, since the time stretch is undone after Stolt migration. However, in practice, high values of v_0 can yield an image with interpolation artifacts. In contrast, low values of v_0 yield a significantly stretched time axis, thus the inverse operation may lose information unless the data has been padded with enough zeroes. The cascaded scheme is particularly sensitive to such problems. As a tradeoff between values that are too high or too small, we used the mean of the velocity model extrema for v_0 .

Another technical aspect, the division by the Jacobian in equation (2), usually induces high amplitude artifacts for waves close to being evanescent, unless a threshold is introduced. Similarly, evanescent waves need to be scaled down to prevent migration artifacts. We used a simple linear weighting.

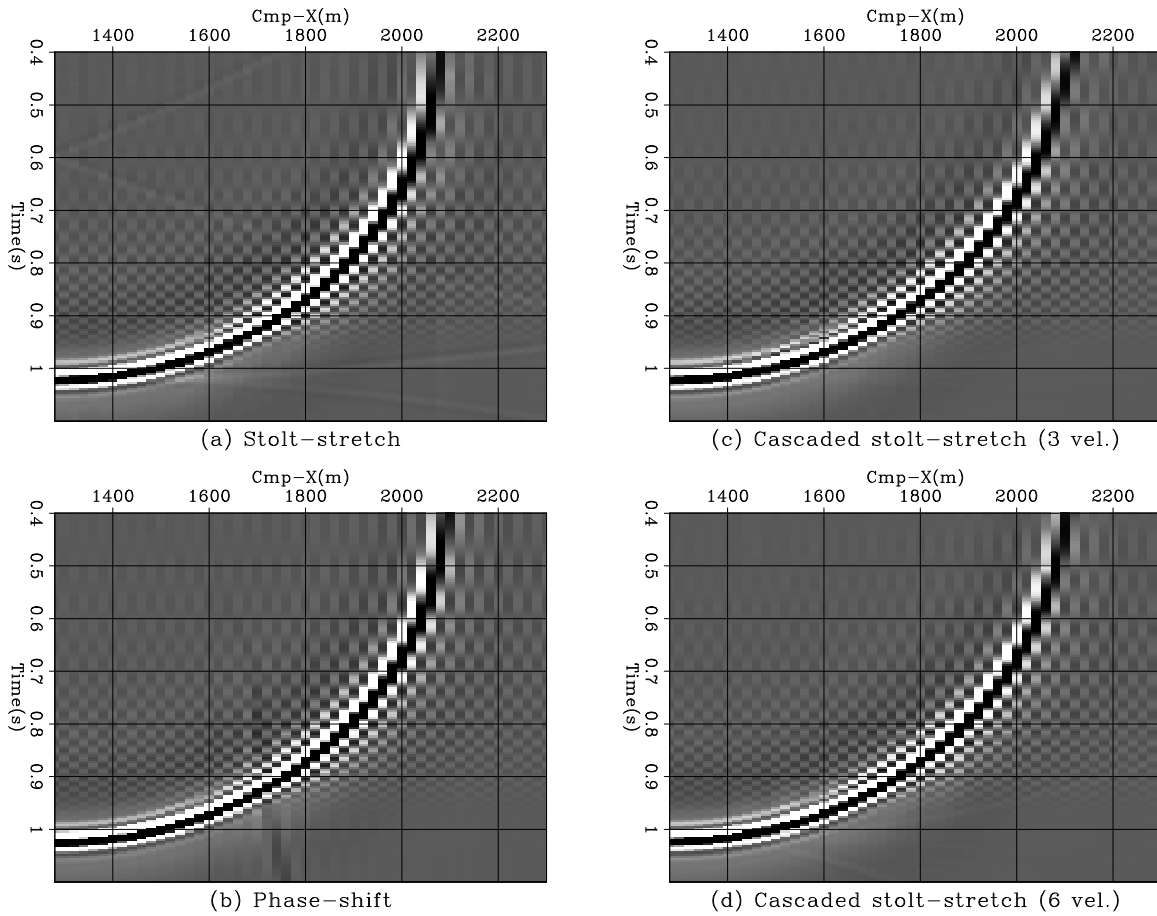


Figure 6: Impulses responses of the different operators. (a) Stolt-stretch. (b) Phase-shift. (c) and (d) Cascaded Stolt-stretch, with 3 and 6 velocities, respectively. louis2-imp-mig [ER]

CONCLUSION

We show that with an optimal choice for the Stolt-stretch parameter derived analytically and with a cascaded f - k migration approach, we manage to obtain time migration results comparable to Gazdag's phase-shift approach. Moreover, the method is considerably more computer-efficient and remains accurate for steeply deeping events.

ACKNOWLEDGEMENTS

The authors would like to thank Elf Aquitaine for providing the data used in this study.

REFERENCES

- Beasley, C., Lynn, W., Larner, K., and Nguyen, H., 1988, Cascaded frequency-wavenumber migration—Removing the restrictions on depth-varying velocity: *Geophysics*, **53**, no. 7, 881–893.
- Castle, R. J., 1988, Shifted hyperbolas and normal moveout: 58th Annual Internat. Mtg., Soc. Expl. Geophys., Expanded Abstracts, 894–896.
- de Bazelaire, E., 1988, Normal moveout revisited—Inhomogeneous media and curved interfaces: *Geophysics*, **53**, no. 2, 143–157.
- Fomel, S., 1995, Evaluating the Stolt stretch parameter: *SEP*–**84**, 61–74.
- Fomel, S., 1996, Migration and velocity analysis by velocity continuation: *SEP*–**92**, 159–188.
- Gazdag, J., 1978, Wave equation migration with the phase-shift method: *Geophysics*, **43**, no. 7, 1342–1351.
- Larner, K., and Beasley, C., 1987, Cascaded migrations—Improving the accuracy of finite-difference migration: *Geophysics*, **52**, no. 5, 618–643.
- Larner, K. L., Beasley, C. J., and Lynn, W. S., 1989, In quest of the flank: *Geophysics*, **54**, no. 6, 701–717.
- Levin, S., 1983, Remarks on two-pass 3-D migration error: *SEP*–**35**, 195–200.
- Malovichko, A. A., 1978, A new representation of the travelttime curve of reflected waves in horizontally layered media: *Applied Geophysics (in Russian)*, **91**, no. 1, 47–53.
- Stolt, R. H., 1978, Migration by Fourier transform: *Geophysics*, **43**, no. 1, 23–48.
- Sword, C. H., 1987, A Soviet look at datum shift: *SEP*–**51**, 313–316.

Short Note

Interpolating missing data: convergence and accuracy, t and f

Sean Crawley¹

INTRODUCTION

Prediction error filters (PEFs) can be used to interpolate seismic data, in the time domain (Claerbout, 1992) or in the frequency domain (Spitz, 1991). The theory for PEFs assumes stationarity, so typically the data are considered a little bit at a time in patches, and assumed to be locally stationary within a patch. An alternative is to use nonstationary filters, which effectively sets the patch size to one sample (or slightly larger). With small patches, filter calculation is an underdetermined problem, and some method for controlling the null space is required to get a good result. In this paper, I compare some different strategies for controlling the null space on a test data set. A more basic (and presumably prior) choice is which domain to do the interpolation in. Interpolation in (f, x) is well known. The frequency domain is fast, and both domains give good results on fairly noise-free data. Abma (1995) argues that (t, x) should resist noise better. Later in this paper, I test both domains with some sample noisy data, and my results confirm Abma's conclusions.

CONVERGENCE VERSUS ACCURACY

Estimating a bank of nonstationary prediction-error filters is likely to create an underdetermined problem, at least in those regions of the data (if any) where the filters are placed close together. The filter calculation then requires some damping equations or some method of controlling the null space in order to get satisfactory results. In 1D, Claerbout (1999) just preconditions the filter estimation with a smoother, and limits the number of iterations to control the null space. Clapp (1999) preconditions and also damps the preconditioned model variable. Shoepf and Margrave (1998) use an estimate of Q of the input trace to characterize the time-varying behavior of the input data. Brown (1999) regularizes the filters with a Laplacian. Filling in missing seismic traces with PEFs is actually a series of two linear optimizations. The second step, the missing data calculation, has its own set of null space issues, depending on the number of dips that are present in the data (Claerbout, 1992), which I do not go into

¹email: sean@sep.stanford.edu

here. The second step also depends, naturally, on a good result from the first step, the filter coefficient calculation. Adding the true data that we are trying to replace (which is unknown in principle but is known in test cases where we want to make difference plots and such) gives us three things to track as a function of iteration and algorithm: the residual of the PEF calculation problem, the residual of the missing data calculation problem, and the misfit between the interpolated data and the true data. Solving the two linear optimization steps by any of several methods will guarantee that the two residuals decrease and converge. No such guarantee exists for the difference between the interpolated and real data, and in fact running either of the two optimizations for too many iterations (where “too many” turns out to be far less than anything as intuitive as the number of model variables) increases that difference. Here I compare the behavior of those curves given different strategies for controlling the null space of the filter estimation step.

Formulations

A standard formulation for calculating PEFs from known data is to solve a linear least-squares problem like

$$\mathbf{0} \approx \mathbf{YCa} + \mathbf{r}_0, \quad (1)$$

where \mathbf{a} is a vector containing the PEF coefficients, \mathbf{C} is a filter coefficient selector matrix, and \mathbf{Y} denotes convolution with the input data. The coefficient selector \mathbf{C} is like an identity matrix, with a zero on the diagonal placed to prevent the fixed 1 in the zero lag of the PEF from changing. The \mathbf{r}_0 is a vector that holds the initial value of the residual, \mathbf{Ya}_0 . If the unknown filter coefficients are given initial values of zero, then \mathbf{r}_0 contains a copy of the input data. \mathbf{r}_0 makes up for the fact that the 1 in the zero lag of the filter is not included in the convolution (it is knocked out by \mathbf{C}). When there are many coefficients, it makes sense to add damping equations and/or to precondition the problem. Inserting the preconditioned variable \mathbf{Sp} (where \mathbf{S} is a somewhat arbitrary smoother) for \mathbf{a} and adding the also somewhat arbitrary roughener $\mathbf{R} = \mathbf{S}^{-1}$ to regularize the model, gives a formulation like

$$\mathbf{0} \approx \mathbf{YKSp} + \mathbf{r}_0 \quad (2)$$

$$\mathbf{0} \approx \epsilon \mathbf{Ip} \quad (3)$$

This is like the formulation used in Clapp (1999). Claerbout (1999) and Crawley (1999) set ϵ to zero and just limit the number of iterations. \mathbf{S} is a smoother, but if it is a helical smoother, it can still be quite small (2 or 3 points), so it does not add much to the cost of computation (Claerbout, 1998). In this case, the smoother works radially (Crawley et al., 1998).

Testing

A cube of seismic data with an interesting set of dips was used as a test case. Half the traces were replaced by zeroes and input to some different interpolation schemes based on the equations above. The important thing is the difference between the true data and the interpolated data we invent to take its place. Naturally, in a real problem the true data are unknown, but

it is interesting to see if we can infer anything useful about that difference from the residuals. Convergence of the filter estimation step for the different implementations is shown in Figure 1. The curve labels are:

- *Smoothed* means that the filters were calculated using the preconditioned optimization of equation (2), but that ϵ was zero, and so the damping (equation (3)) was effectively turned off.
- *Both* is similar but with $\epsilon \neq 0$.
- *Damped* used equations (1) and (3), except the damping equation really reads $\mathbf{0} \approx \mathbf{I}\mathbf{a}$, because there is no change of model variables. No preconditioning, but still damped with an identity. It seems sensible to replace this with a curve damped with a reasonable roughener, but that is just a slower way to get the results of the *Both* curve above.
- *Neither* was estimated using equation (1) alone, which is fine so long as the problem is overdetermined.

This test uses filters estimated in radial patches, with patch boundaries along various lines of constant radius or angle. The density of filters was chosen to give a good interpolation result, and to give patches that create an overdetermined problem at longer offsets and later times where the patches are largest, and an underdetermined problem where the patches are smaller. Not surprisingly, the residual of the filter estimation step goes down fastest when there is no restriction on the filters (the *Neither* curve). While a large filter estimation residual does imply something bad (that the filters do not make a good estimate of the data spectrum), a small filter estimation residual is not necessarily good. In this case, it just means the filters have too many degrees of freedom. The curves all start off about the same, with the two damped algorithms flattening out earlier and higher, because the damping simply prohibits them from putting enough energy in the filter coefficients to fit much of the data. The *Damped* curve looks bad, and continues to look bad in the later figures as well. Simply limiting the energy in the filter coefficients is not as sensible as limiting their roughness, which is what the damping effectively does for the curve labeled *Both*. In the *Both* curve, damping is applied to the preconditioned (roughened) variable \mathbf{p} , while in the *Damped* curve, the damping is on the actual filter coefficients \mathbf{a} . Changing the \mathbf{I} to a roughener just reprises the previous curve, but without the change of variables. The residual for the missing data calculation step is shown in Figure 2. A pleasing thing about all of these curves is that they converge after a handful of iterations. Figure 3 shows the real quantity of interest. Each curve is the norm of the difference between the interpolated data and the true data as a function of iteration in the second step of the interpolation. In every case (though just barely in a couple), the difference increases at later iterations. In principle the true data are unknown, so there is no reason for the difference not to increase. The PEFs are certain not to be perfect, and will eventually begin to add in some undesirable components. The misfit starts to go up after the residual from Figure 2 has bottomed out. Figure 4 shows the same curve, along with several others that all use the same algorithm (preconditioning, no damping), but different numbers of iterations, to calculate PEFs. With many iterations, the minimum value on a given curve increases. Too

Figure 1: Filter calculation residual as a function of iteration. Curves represent different filter calculation schemes. `sean1-curves.nrp` [CR]

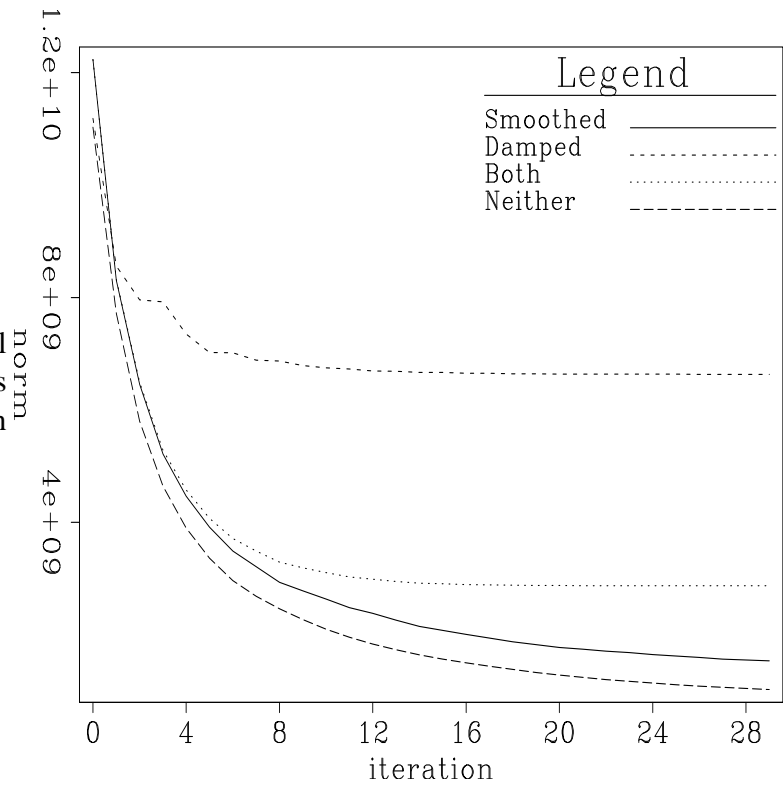
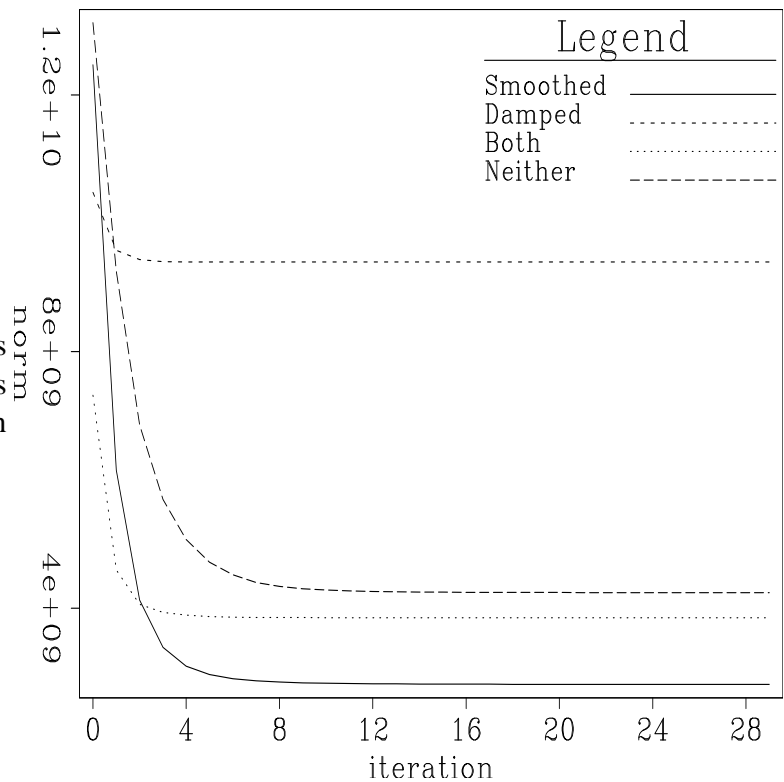
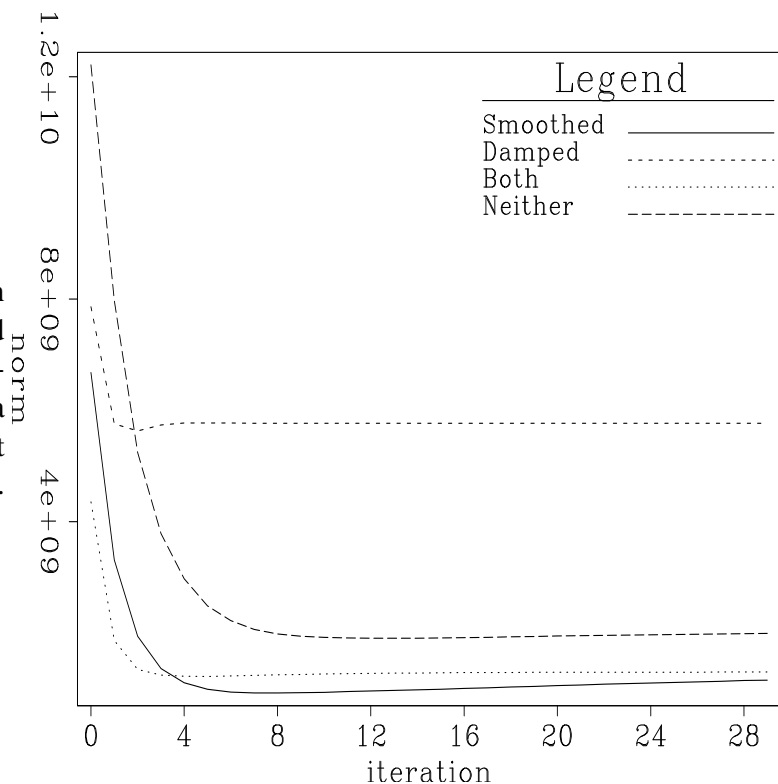


Figure 2: Missing data residual as a function of iteration. Curves represent different filter calculation schemes. `sean1-curves.nrd` [CR]



many iterations, either in calculating the filter coefficients or in calculating the missing data, degrades the result. In the case of the missing data iterations, the residual has bottomed out, as shown in Figure 5, which plots the data residual and norm of the misfit between interpolated and true data, as a function of iteration. In the case of the filter coefficient iterations, it is not obvious when to stop. Damping with the appropriate value of ϵ helps. Figure 6 shows the same sorts of curves as Figure 4, with a reasonable ϵ . Here the curves are fairly close together, so that running too many filter calculation iterations does not degrade the final result too much. The wrong value of ϵ causes the same problems as the wrong number of iterations without damping, however. Figure 7 shows the misfit between the true and interpolated data for different values of ϵ . With the damping, you need to find the correct value of ϵ , and without it, you need to find the correct number of iterations for calculating the PEF coefficients. Results tend to be somewhat less sensitive to ϵ , and choosing ϵ to make the two components of the filter calculation residual roughly balance is usually a safe choice (Lomask, 1998).

Figure 3: Norm of the misfit between the true data and the interpolated data. Horizontal axis displays number of iterations in the missing data calculation step. Curves represent different filter calculation schemes. `sean1-curves.nm` [CR]



Summary

What is the best thing to do? Preconditioning is cheap via the helix, and gives the best results, if you twiddle the parameters enough. Damping helps reduce the sensitivity to number of iterations, in favor of the somewhat less sensitive ϵ parameter. Generally I skip the damping, but that choice is somewhat data dependent.

Figure 4: Norm of the misfit between the true data and the interpolated data. Horizontal axis displays number of iterations in the missing data calculation step. Curves represent different numbers of iterations in the filter calculation step. `sean1-curves.nm.filtniter` [CR]

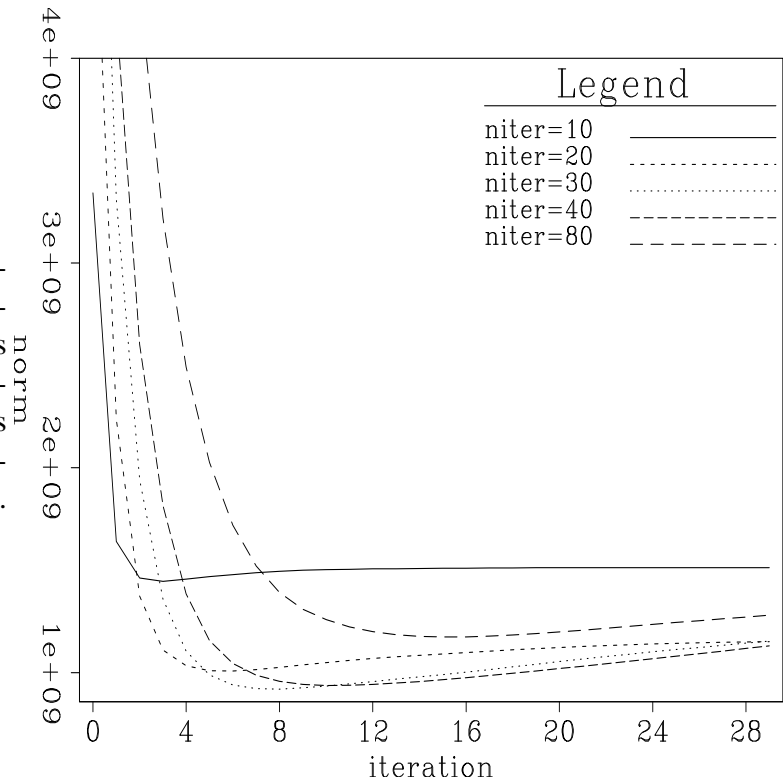


Figure 5: Norm of the missing data residual and the misfit between true and interpolated data. Misfit rises after the missing data residual flattens out. `sean1-curves.nrd.30` [CR]

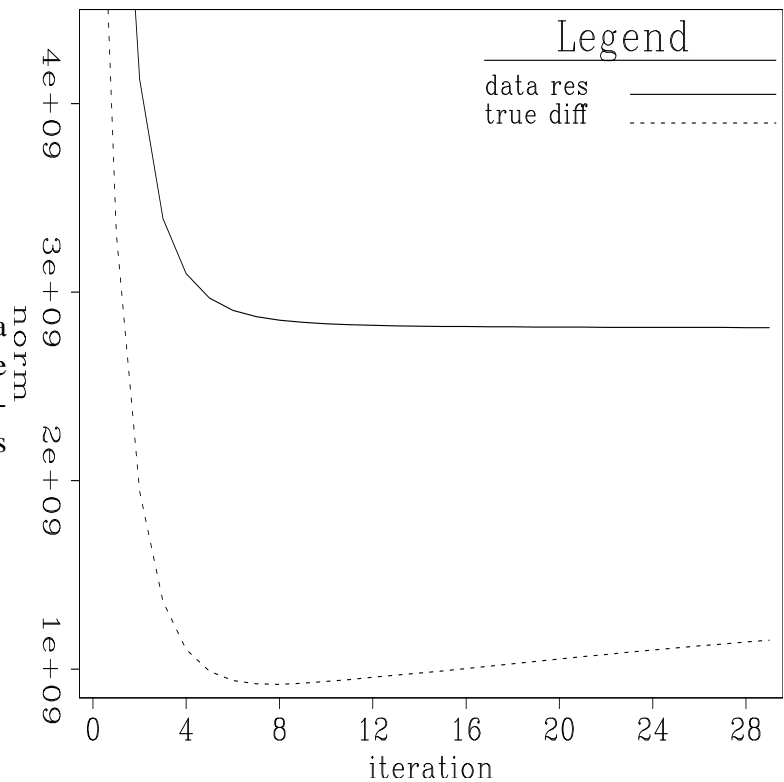


Figure 6: Norm of the misfit between true data and interpolated data. Curves represent different numbers of iterations in the filter calculation step.

sean1-curves.nm.slightdamp.fn
[CR]

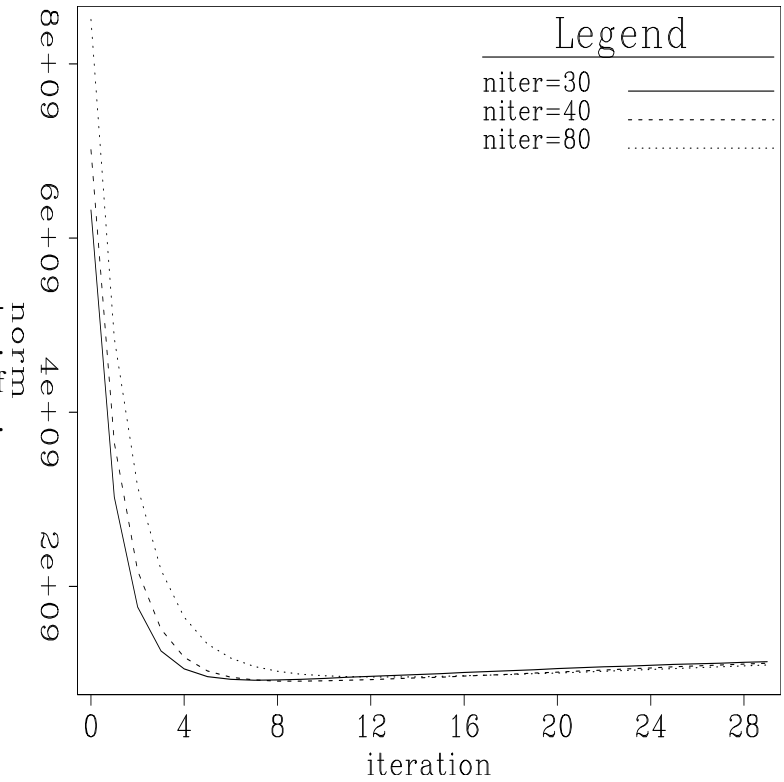
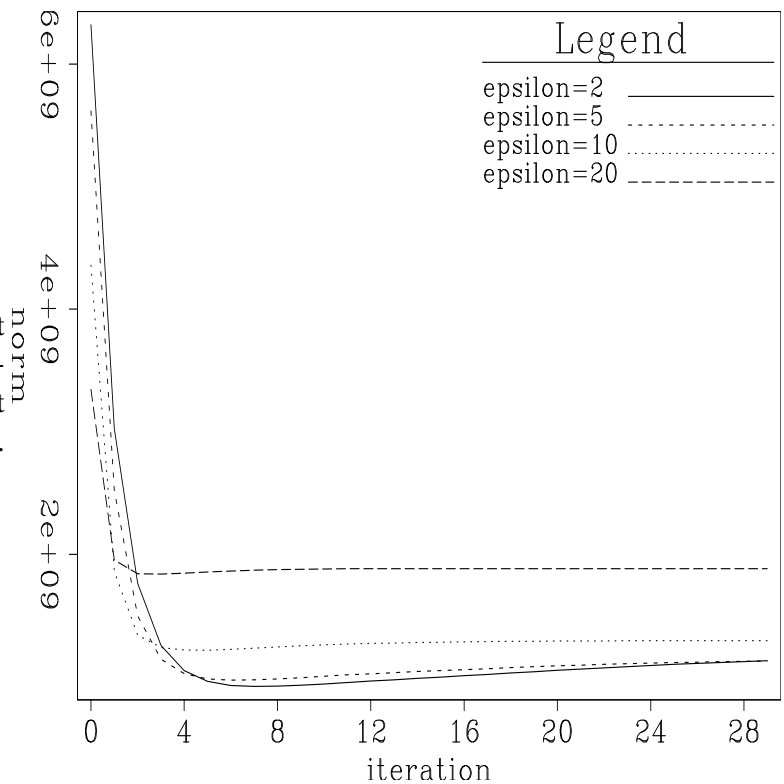


Figure 7: Norm of the misfit between true data and interpolated data. Curves represent different amounts of damping.

sean1-curves.nm.muchdamp [CR]



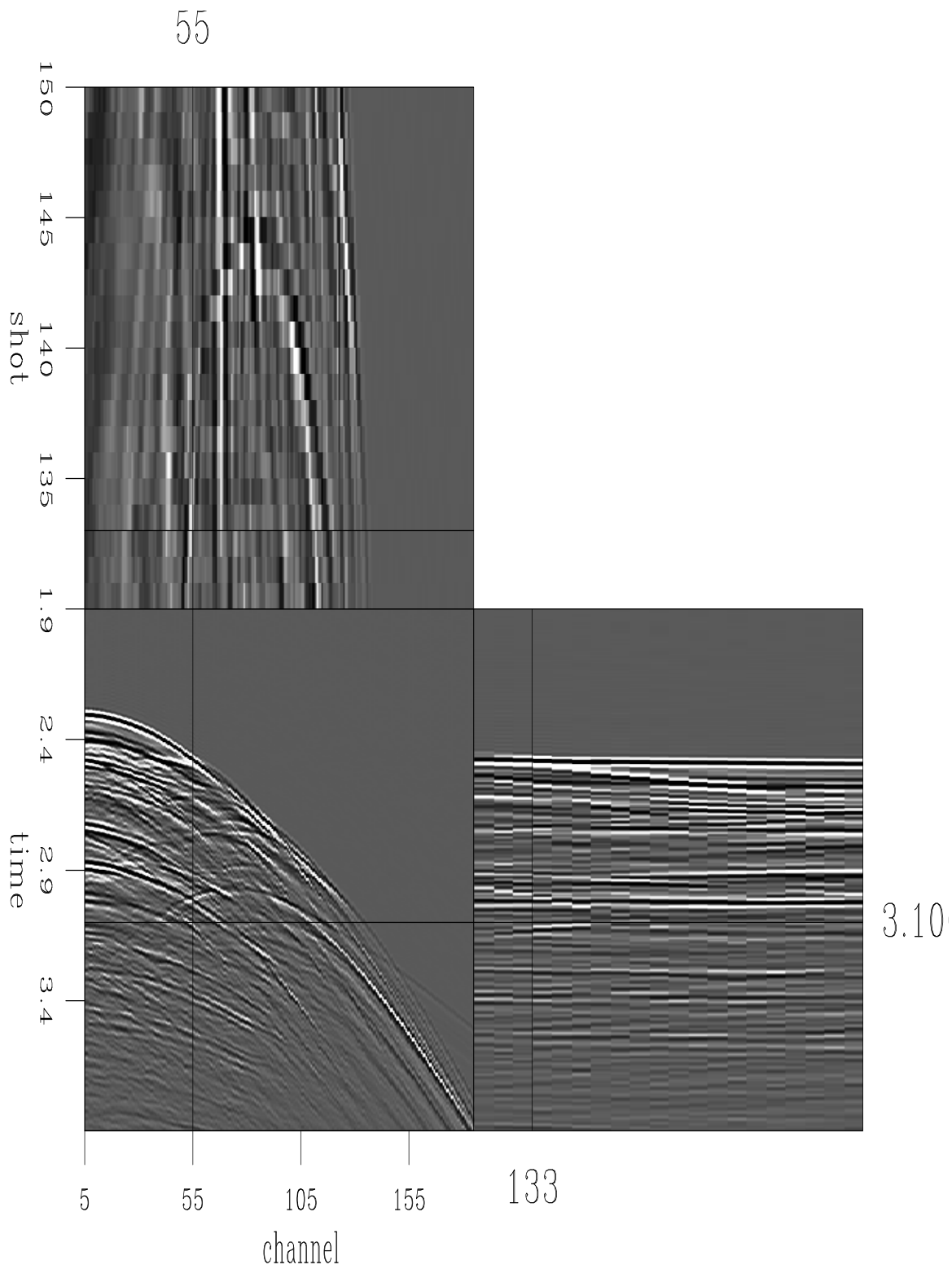


Figure 8: Sample interpolation output. This is one result using the test data from all the previous graphs. `sean1-102.smooth.out` [CR]

NOISE AND (F, X) INTERPOLATION

Interpolating in the frequency domain is generally faster than in the time domain, because convolution matrices turn diagonal and become multiplications. Normally, rather than bother with nonstationary convolution, the data are divided into patches and assumed to be locally stationary. As Margrave (1998) points out, Fourier transforms do not really imply stationarity, but nonstationary convolution in the time domain does not Fourier transform into a multiplication, but into a nonstationary combination, which is almost the same as a nonstationary convolution. It may turn out to be more or less expensive, depending on the number of nontrivial diagonals in the matrix, but it is not as quick as multiplication. With just enough effort to take out the obvious slack, I find that my own (t, x) interpolation takes several times longer than a canned commercial (f, x) interpolation (ProMAX), though that number varies significantly with parameterization, and might also vary a great deal with implementation. Unfortunately, I only had available an (f, x) version, and not (f, x, y) . To be fair, the time-domain figures in this section are calculated using just t and x . Interpolation in (t, x, y) produces nicer figures, and presumably so does (f, x, y) . So why bother with the time domain? One answer is noise. Abma (1995) shows that (t, x) PEFs are less likely to create spurious events in the presence of noise, because calculating a filter at each frequency is the time domain equivalent of calculating a filter that is long on the time axis. The effective time length of the filter tends to give it sufficient freedom that it can predict the ostensibly random noise. On relatively noise-free data (such as the data in Figure 8), time- and frequency-domain implementations both produce good results. Closeups of a (t, x) and (f, x) interpolation result are shown in Figures 9 and 10. There are some examples of events that are better interpolated in the time domain, such as the event dipping steeply to the right in the very middle of closeups. However, it may be that someone with more experience at tuning the (f, x) parameter knobs would make that difference disappear. At any rate, either result is fine. With increasing amounts of noise, the time domain interpolation produces better results. Interpolated noisy gathers are shown in Figures 11 and 12. Noisy close ups are shown in Figures 13 and 14. Coherent noise, like multiples, will look just like signal and be interpolated right along with it. In the case of multiples, this is exactly the point of the interpolation. Interpolating the multiples dealiases them and makes them easier to suppress.

Summary

Either domain works well on clean data. On uglier data, time domain interpolation seems to do better. Time domain filters are effectively shorter in time. Fewer degrees of freedom means they are less apt to predict noise.

REFERENCES

- Abma, R., 1995, Least-squares separation of signal and noise with multidimensional filters: Ph.D. thesis, Stanford University.

Figure 9: Closeup of time-domain interpolation result using noise-free input. `sean1-102.smooth.out.closeup` [CR]

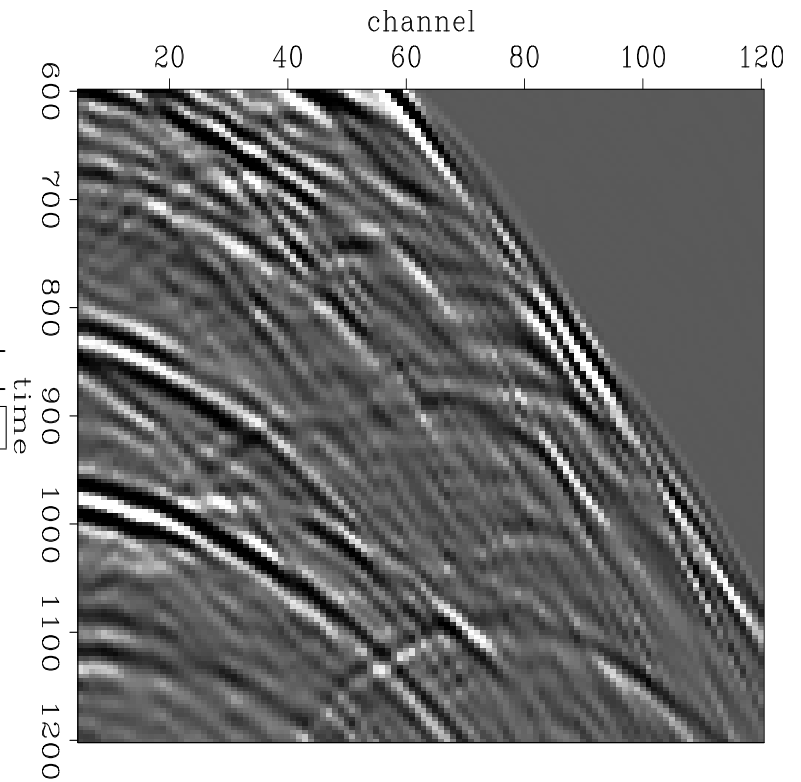
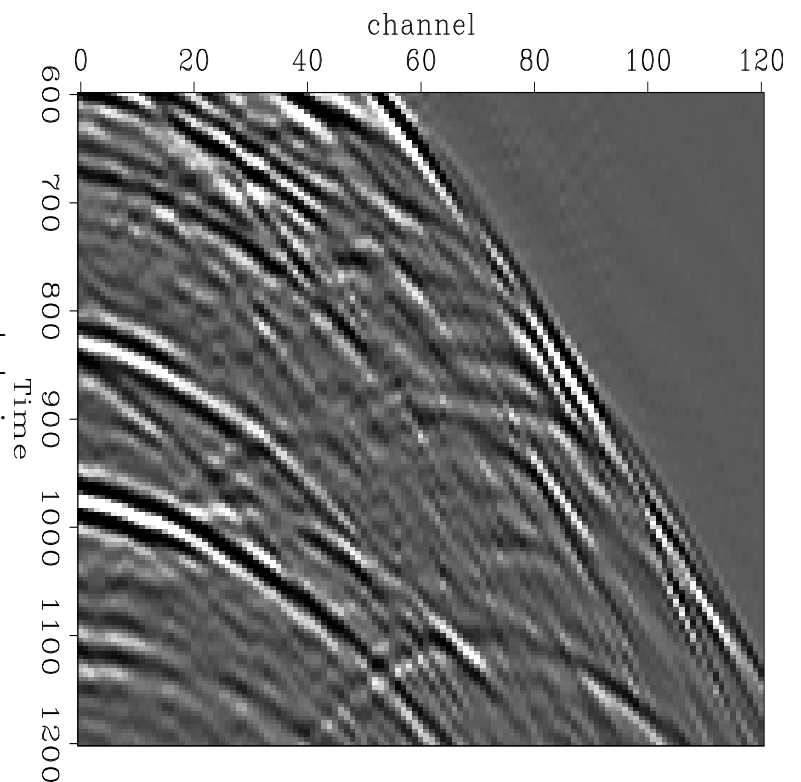


Figure 10: Closeup of frequency-domain interpolation result using noise-free input. `sean1-102.smooth.fx.out.closeup` [CR]



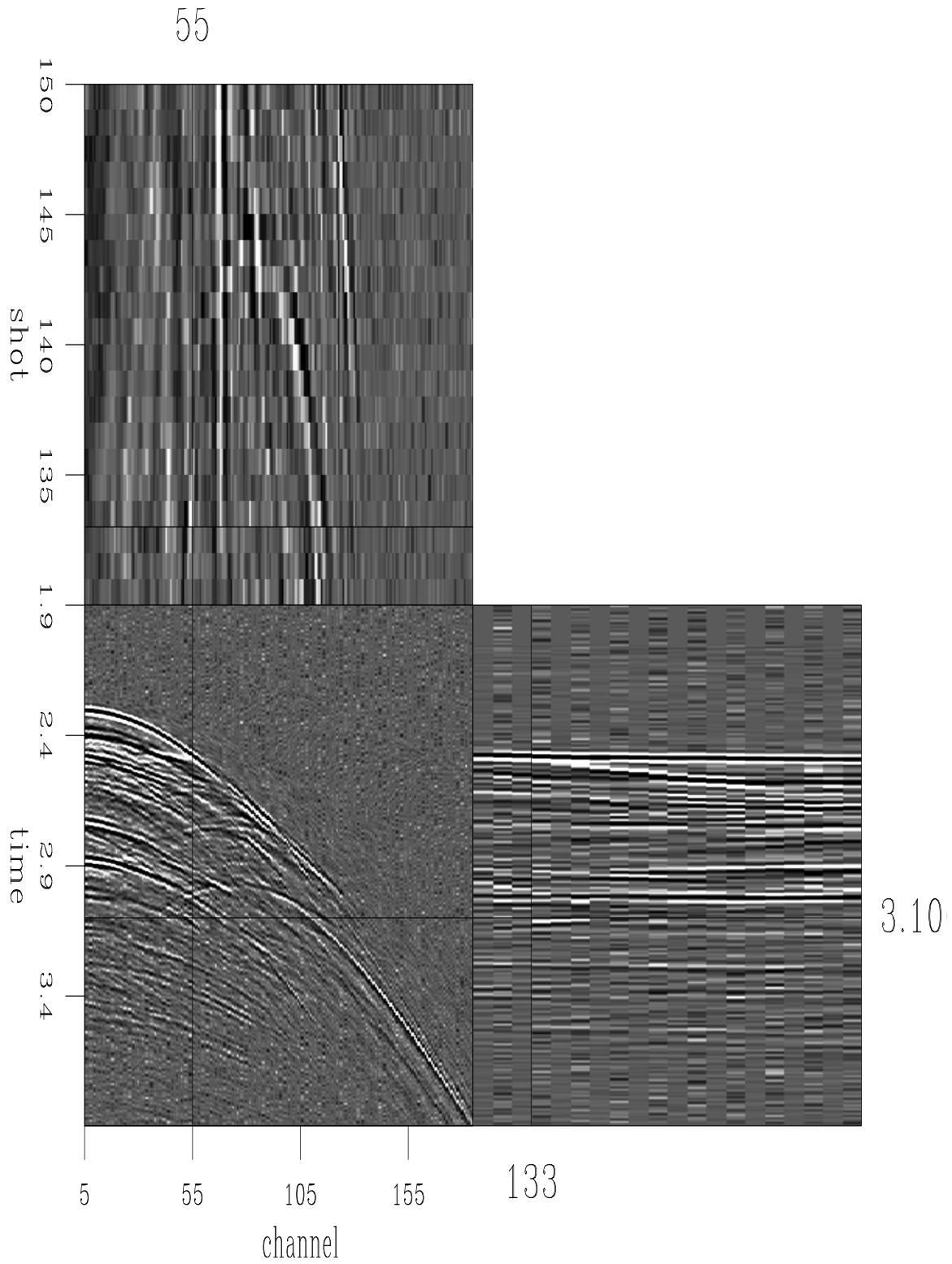


Figure 11: Time-domain interpolation result using noisy input. `sean1-102.smooth.noise.out`
[CR]

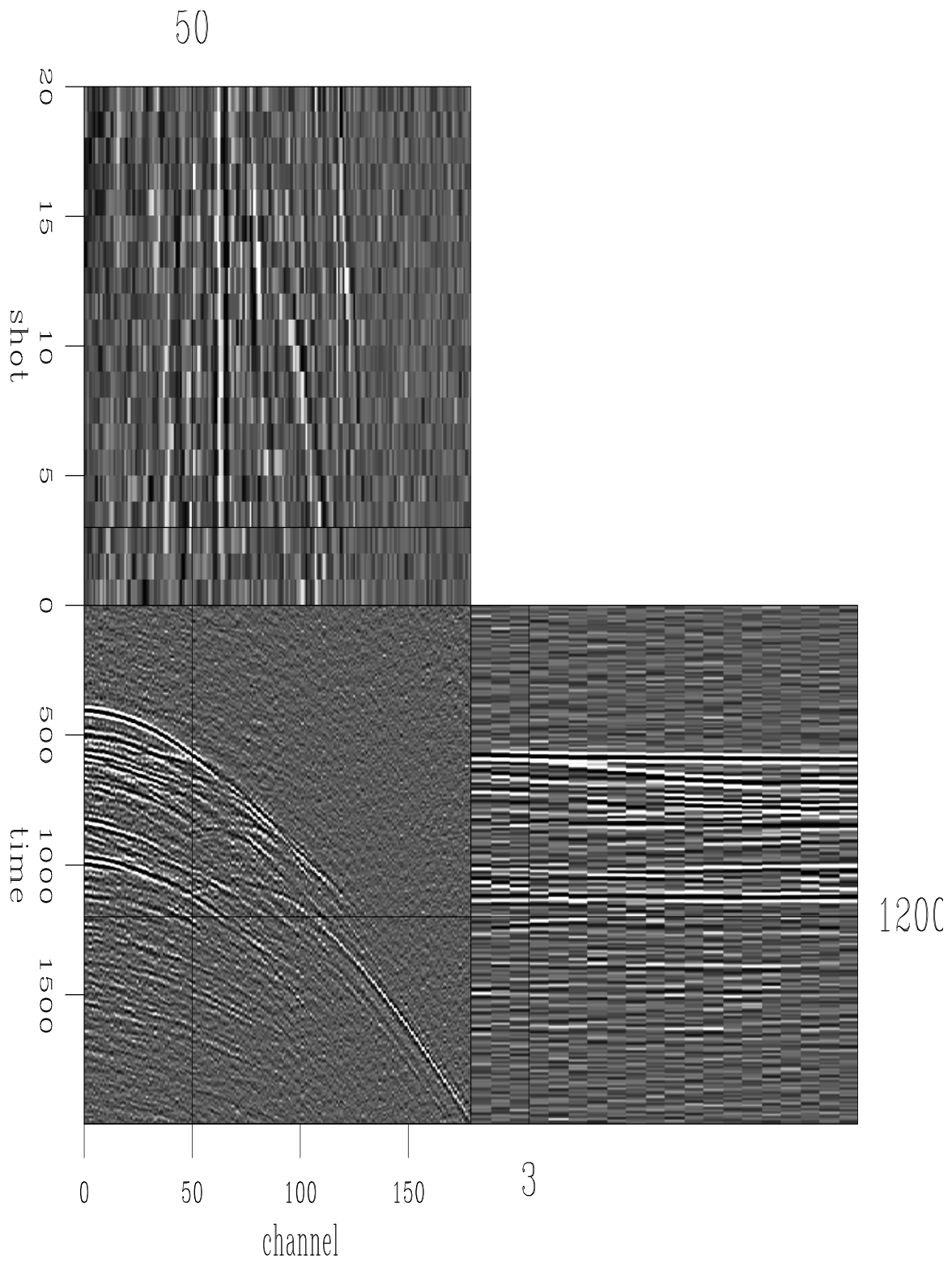


Figure 12: Frequency-domain interpolation result using noisy input. sean1-102.smooth.noise.fx.out [CR]

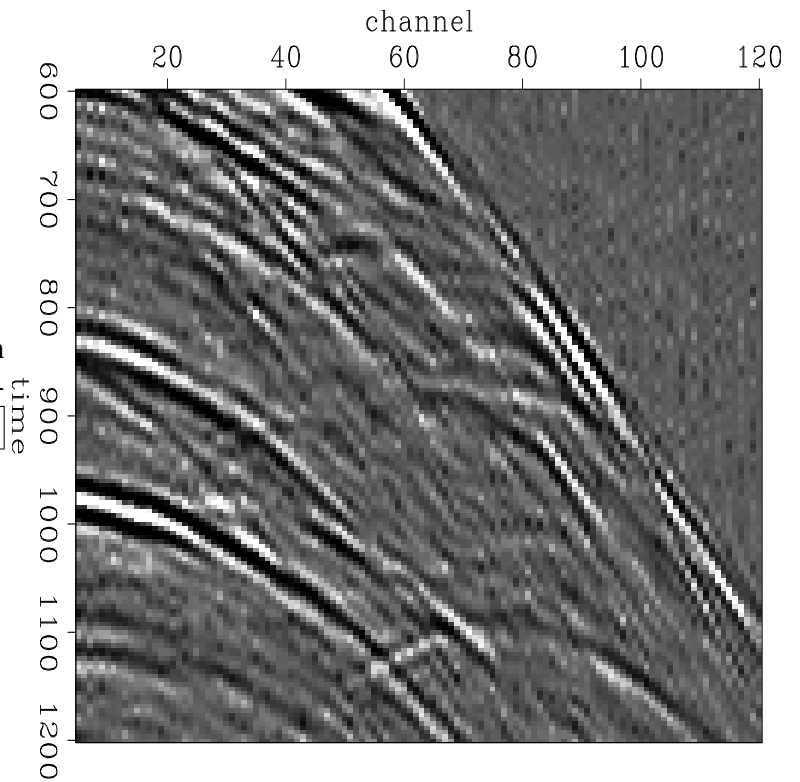


Figure 13: Closeup of time-domain interpolation result using noisy input. `sean1-102.smooth.noise.out.cp` [CR]

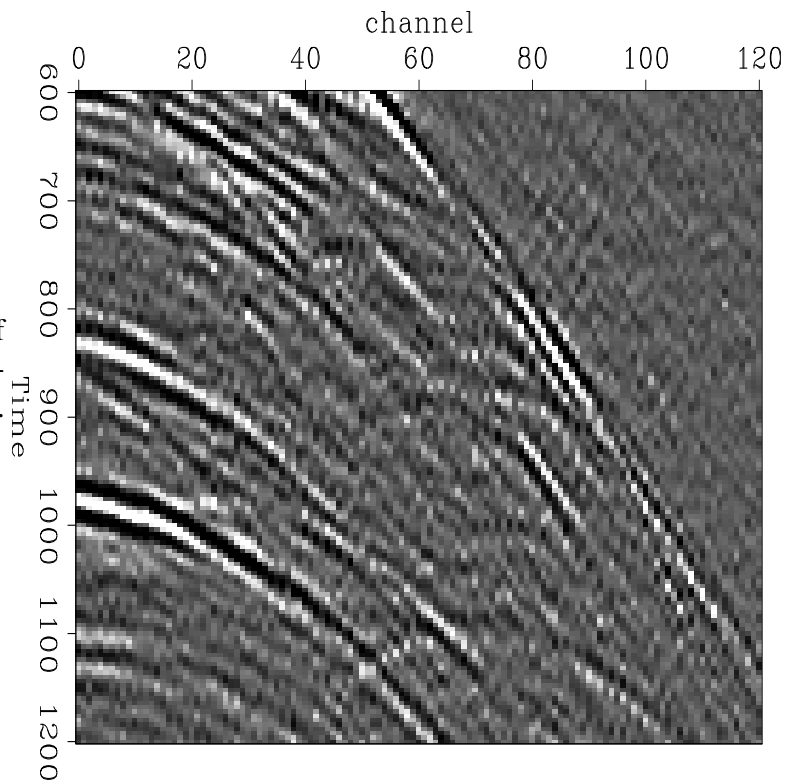


Figure 14: Closeup of frequency-domain interpolation result using noisy input. `sean1-102.smooth.noise.fx.out.cp` [CR]

- Brown, M., Clapp, R. G., and Marfurt, K., 1999, Predictive signal/noise separation of groundroll-contaminated data: SEP-102, 111–128.
- Claerbout, J. F., 1992, *Earth Soundings Analysis: Processing Versus Inversion*: Blackwell Scientific Publications.
- Claerbout, J. F., 1998, Multi-dimensional recursive filtering via the helix: *Geophysics*, **63**, no. 5, 1532–1541.
- Claerbout, J., 1999, *Geophysical estimation by example: Environmental soundings image enhancement: Stanford Exploration Project*, <http://sepwww.stanford.edu/sep/prof/>.
- Clapp, R. G., and Brown, M., 1999, Applying sep's latest tricks to the multiple suppression problem: SEP-102, 91–100.
- Crawley, S., Clapp, R., and Claerbout, J., 1998, Decon and interpolation with nonstationary filters: SEP-97, 183–192.
- Crawley, S., 1999, Interpolation with smoothly nonstationary prediction-error filters: SEP-100, 181–196.
- Lomask, J., 1998, Madagascar revisited: A missing data problem: SEP-97, 207–216.
- Margrave, G. F., 1998, Theory of nonstationary linear filtering in the fourier domain with application to time-variant filtering: *Geophysics*, **63**, no. 01, 244–259.
- Schoepp, A. R., and Margrave, G. F., 1998, Improving seismic resolution with nonstationary deconvolution: Improving seismic resolution with nonstationary deconvolution:, 68th Annual Internat. Mtg., Soc. Expl. Geophys., Expanded Abstracts, 1096–1099.
- Spitz, S., 1991, Seismic trace interpolation in the f-x domain: *Geophysics*, **56**, no. 06, 785–794.

Applying SEP's latest tricks to the multiple suppression problem

Robert G. Clapp and Morgan Brown¹

ABSTRACT

Two methods for suppressing multiples are proposed. In the first, multiple suppression is expressed as a signal to noise separation problem. The problem is solved in the time domain using space-varying Prediction Error Filters (PEFs). The second method shows how greater separation between primaries and multiples can be obtained by velocity space inversion using a Huber functional rather than the standard L_2 functional. Early results of both methods are encouraging.

INTRODUCTION

Multiple suppression is one of the biggest problems facing the seismic industry. Methods that have proven effective in 2-D are either cost-prohibitive or not easily extendible into 3-D (Berkhout and Verschuur, 1997; Verschuur and Berkhout, 1997; Sun, 1999). Spitz (1999) proposed forming the multiple suppression as a signal-to-noise separation in the frequency domain, but this method suffered from stability problems.

Until recently, an equivalent time domain method was not possible. Claerbout(1998) discovered that multi-dimensional time filters can be mapped into 1-D, therefore making it possible to do inverse filtering. Crawley et al. (1998) showed how non-stationary filters could more accurately predict seismic data. Fomel (1999) demonstrated how Spitz's method could be changed to work with time domain PEFs.

In the first section of the paper, we perform time domain multiple suppression by a two step method. We first estimate a space-varying PEF from data (a CMP gather) and a noise model (an estimate of the multiples obtain by downward continuing through the water column twice). We then separate out the signal (primaries) from the noise (multiples) by a simple inversion scheme.

In the second portion of the paper we present a better way to separate multiples in velocity space. Lumley et al. (1994) described a CMP gather as a sum of hyperbolic events. They then inverted this velocity-space transform into (τ, v) space, muted multiples, and transformed back into (t, h) space. Guitton and Symes (1999) showed that a Huber functional (Huber, 1973) produces a velocity scan where reflection energy is better behaved. We invert into (τ, v) using the Huber functional, rather than an L_2 functional. We show that the Huber method provides more

¹email: bob@sep.stanford.edu,morgan@sep.stanford.EDU

separation between primary and multiple trends, and therefore improved multiple suppression.

MULTIPLE SUPPRESSION USING SIGNAL-NOISE SEPARATION

Signal to noise separation has a long history at SEP (Harlan, 1986; Kostov, 1990; Claerbout, 1991). The method we use is similar to Abma's (1995) formation. Abma (1995) proposed solving the set of equations:

$$\begin{aligned} \mathbf{Nn} &\approx \mathbf{0} \\ \epsilon \mathbf{Ss} &\approx \mathbf{0} \\ \text{subject to } &\leftrightarrow \mathbf{d} = \mathbf{s} + \mathbf{n} \end{aligned} \quad (1)$$

where the operators \mathbf{N} and \mathbf{S} represent $t - x$ domain convolution with (PEF's) which decorrelate the unknown noise \mathbf{n} and signal \mathbf{s} , respectively, and the factor ϵ balances the energies of the residuals. For his problem he assumed that the noise was uncorrelated, therefore \mathbf{N} becomes the identity and \mathbf{S} is the PEF that best predicted the data in a given window [patching approach (Claerbout, 1992; Schwab and Claerbout, 1995)].

In the multiple problem the noise is not uncorrelated so we must find another way to find \mathbf{N} . Spitz (1999) proposed defining \mathbf{S} as $\mathbf{S} = \mathbf{DN}^{-1}$ where \mathbf{D} is a filter that characterizes the data rather than the signal. Using this new definition we get a new set of fitting goals:

$$\begin{aligned} \mathbf{Ns} &\approx \mathbf{Nd} \\ \epsilon \mathbf{DN}^{-1} &\approx \mathbf{0}. \end{aligned} \quad (2)$$

Following Fomel et al. (1997) we can set up the conversion by reformulating it as a preconditioned problem by a simple change of variables ($\mathbf{p} = \mathbf{DN}^{-1}$)

$$\begin{aligned} \mathbf{NND}^{-1}\mathbf{p} &\approx \mathbf{Nd} \\ \epsilon \mathbf{p} &\approx \mathbf{0}, \end{aligned} \quad (3)$$

where \mathbf{p} is just a dummy preconditioning variable.

Instead of using patching we followed the methodology of Crawley et al. (1998) and constructed and estimated a space varying filter.

$$\begin{aligned} \mathbf{0} &\approx \mathbf{DA}^{-1}\mathbf{p} \\ \mathbf{0} &\approx \mathbf{p} \end{aligned} \quad (4)$$

where \mathbf{A} is a radial smoother (Clapp et al., 1999). For \mathbf{N} we follow a similar procedure assuming an a priori model for the noise.

Synthetic example

At this early stage we decided to show how the method works on a simple synthetic. Figure 1 shows a sea floor with a series of water-bottom multiples. The amplitude of the reflector

increases as a function of angle, something that frequency methods have had difficult time handling. The multiple model was constructed by downward continuing (Bevc, 1995) the sea floor reflection, Figure 2. As a result the amplitude information is incorrect, but the kinematics is correct.

Figure 1: A simple CMP gather with multiples. `bob2-bee-cmp` [ER]

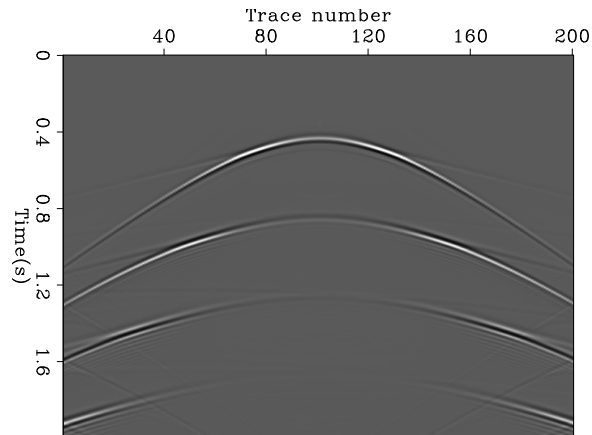
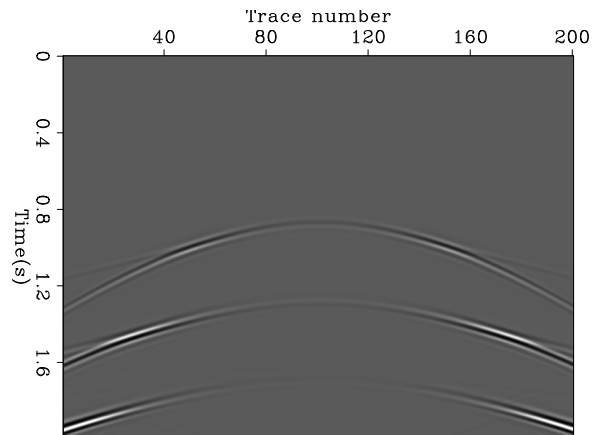


Figure 2: CMP gather in Figure 1 datumed to the surface and back to the seafloor. Note how the amplitude information is wrong but the general kinematics is correct. `bob2-bee-mult` [ER]



Once we have our data and noise model we estimated a space varying filter for each by applying fitting goal (4). To conserve memory we put a new filter every 15th point in time and third point in offset (Figure 4). These two filters were then used, and fitting goal (3) were applied. Figure 3 shows the result of the separation. We can see some residuals of the filter patches but generally we have done a good job in removing the multiple while preserving the signal.

Problems

At this preliminary stage there are still some problems to overcome. The separation technique is much more reliant on a stable filter than the interpolation (Crawley, 1999) or feature identification problem (Brown and Clapp, 1999). Some preliminary work on filter stability was done in (Sava and Fomel, 1999; Sava et al., 1998), but the problems associated with non-stationary

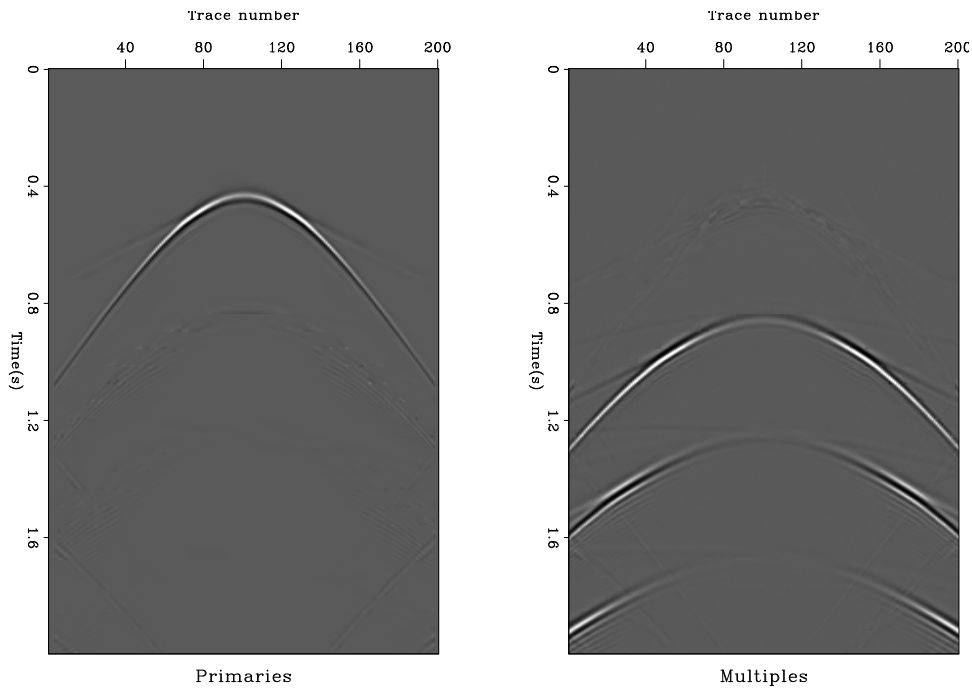


Figure 3: The estimated primaries and multiples from Figure 1. `bob2-signoi` [ER]

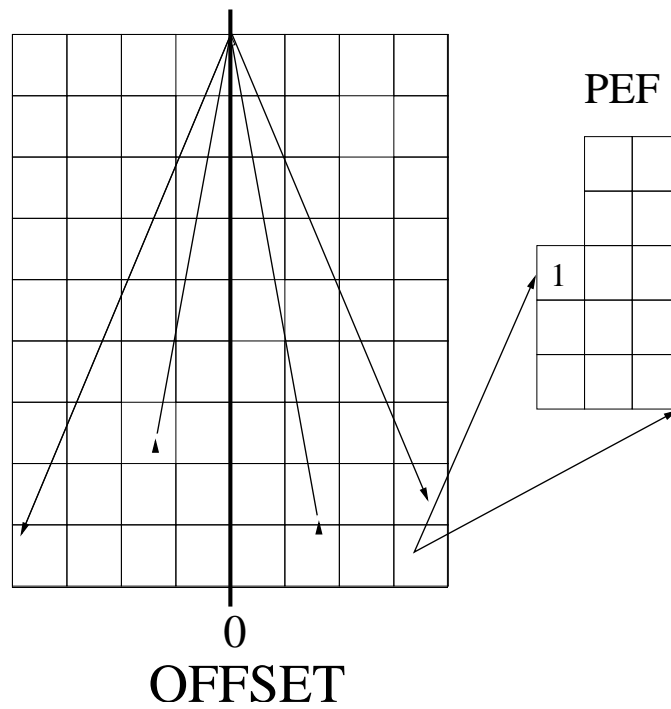


Figure 4: Space varying filter composition. A different filter is placed inside each patch. The filter estimation problem is done globally, with the filter coefficient smoothed in a radial direction. `bob2-pef` [NR]

filters are only beginning to be addressed (Rickett, 1999). To be effective in 3-D, the problem of spatial aliasing has to be dealt with.

HUBER VELOCITY SPACE MULTIPLE ELIMINATION

Transforming seismic data into another domain and then muting is a common multiple suppression technique. The common method is the parabolic radon transform (Foster and Mosher, 1992). This method has the advantage of having an analytic inverse (and is therefore faster), but involves approximating moveouts by parabolas. Lumley et al. (1994) used the more expensive hyperbolic transform and went a step further by forming it as an inversion problem,

$$\mathbf{d} \approx \mathbf{H}\mathbf{V}\mathbf{m}, \quad (5)$$

where:

\mathbf{d} is the CMP gather,

\mathbf{H} is a half derivative operator (Prucha, 1999),

\mathbf{V} is a velocity transform operator.

They then used an L_2 conjugate gradient algorithm to estimate a (τ, v) model and then muted out the multiples. Unfortunately both methods suffer from multiple and primary energy overlapping.

Huber separation

To get a better (τ, v) model we decided to replace the linear iterative solver used by Lumley et al. (1994) with the Fletcher-Reeves non-linear conjugate gradient conditions (Polak, 1997) and the Dennis-Schnabel line search method (Dennis and Schnabel, 1983). We replaced the L_2 function, with a Huber functional (Huber, 1973) that is less sensitive to large outliers. The Huber functional is L_2 until some cutoff value and then smoothly switches to L_1 (Figure 5). The idea is compromise between the convergence speed of L_2 and the less sensitive nature to outliers with the L_1 . Guitton and Symes(1999) showed that the Huber functional does a better job of localizing energy in (t, v) space. For multiples this mean that the primary and multiple trains are better separated.

To show the advantage of the Huber method over a straight L_2 we took a multiple contaminated CMP gather, Figure 6, and iterated on fitting goals (5). Figure 7 shows the envelope of the (τ, v) representation of both the Huber and L_2 approach. Note how the Huber result shows a more compact representation of the primary and multiple trains.

Figure 5: The L_2 , Huber, and L_1 functionals. `bob2-huber` [ER]

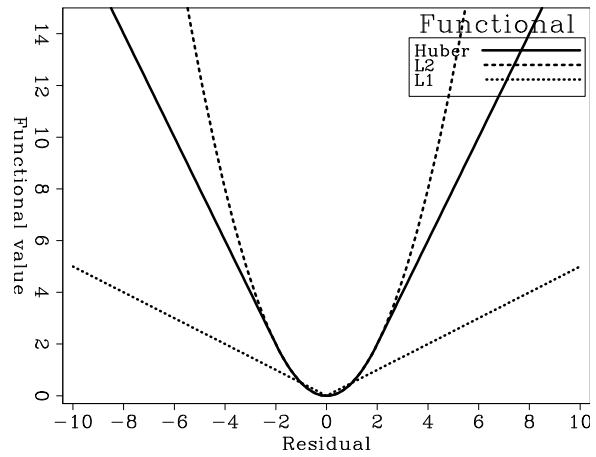
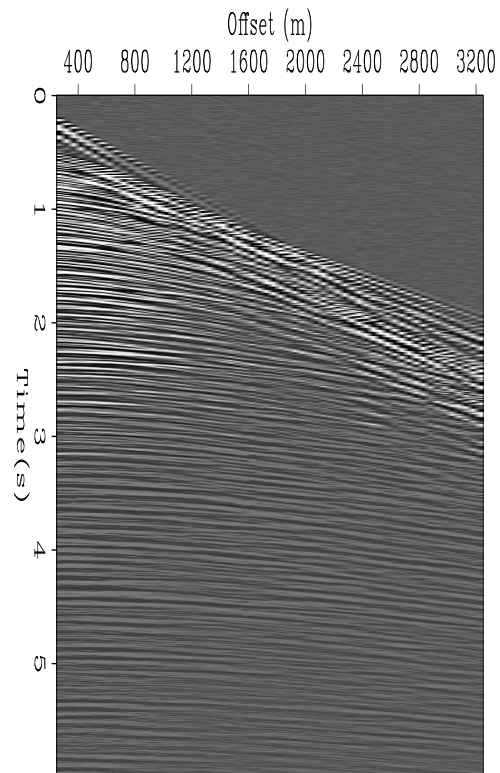


Figure 6: A multiple infested gather from the Mobil AVO dataset. `bob2-mobil` [ER]



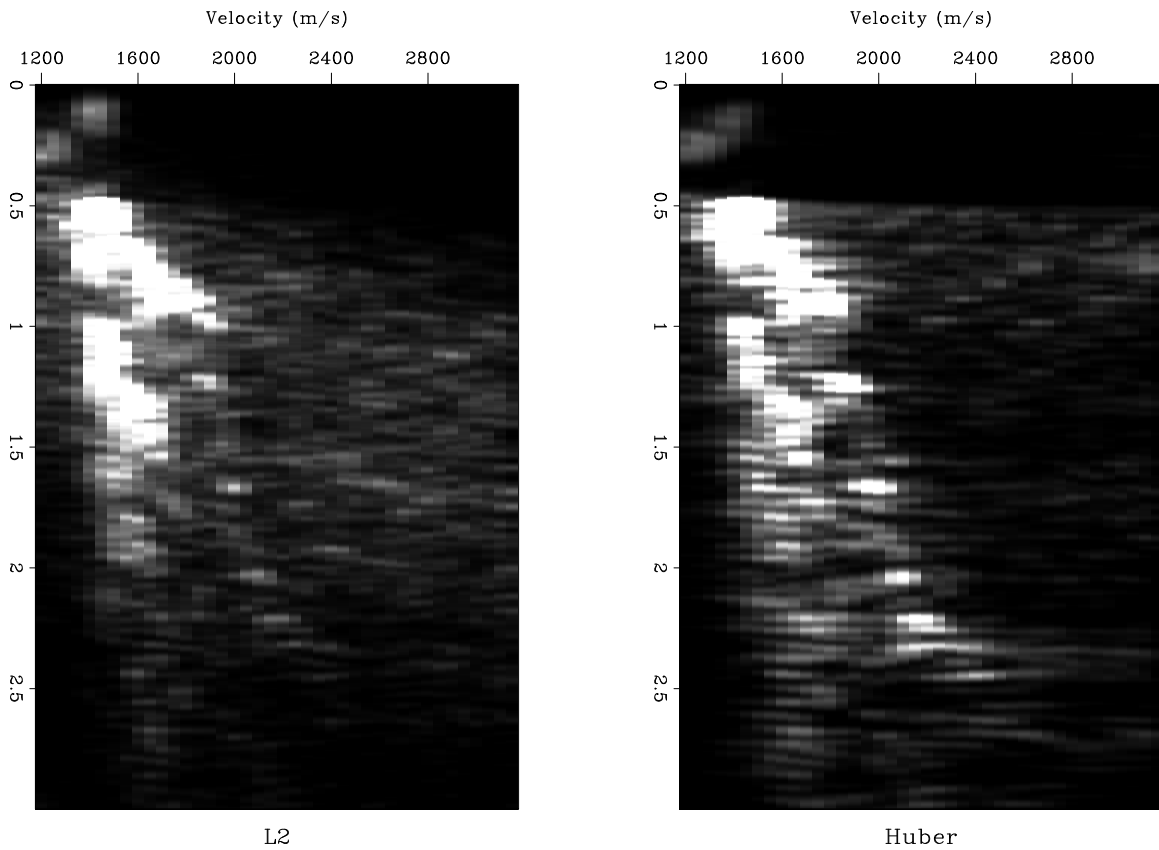


Figure 7: The envelope of the tau-velocity space representation of the Mobil AVO gather (Figure 6) using both an L_2 , left, and a Huber, right, functional. Note how the Huber gather shows more energy and better isolation of the primary train. Further, the L_2 approach show significantly more energy at high, unreasonable, velocities. `bob2-compare` [ER]

REFERENCES

- Abma, R., 1995, Least-squares separation of signal and noise with multidimensional filters: Ph.D. thesis, Stanford University.
- Berkhout, A. J., and Verschuur, D. J., 1997, Estimation of multiple scattering by iterative inversion, Part I: Theoretical considerations and examples: *Geophysics*, **62**, no. 5, 1586–1611.
- Bevc, D., 1995, Imaging under rugged topography and complex velocity structure: Ph.D. thesis, Stanford University.
- Brown, M., and Clapp, R. G., 1999, Seismic pattern recognition via predictive signal/noise separation: *SEP-102*, 177–186.
- Claerbout, J. F., 1991, Resolution and random signals-coherency central limit: *SEP-71*, 270–271.
- Claerbout, J. F., 1992, Nonstationarity and conjugacy: Utilities for data patch work: *SEP-73*, 391–400.
- Claerbout, J. F., 1998, Multi-dimensional recursive filtering via the helix: *Geophysics*, **63**, no. 5, 1532–1541.
- Clapp, R. G., Fomel, S., Crawley, S., and Claerbout, J. F., 1999, Directional smoothing of non-stationary filters: *SEP-100*, 197–209.
- Crawley, S., Clapp, R., and Claerbout, J., 1998, Decon and interpolation with nonstationary filters: *SEP-97*, 183–192.
- Crawley, S., 1999, Interpolating missing data: convergence and accuracy, t and f : *SEP-102*, 77–90.
- Dennis, and Schnabel, 1983, Numerical methods for unconstrained optimization and nonlinear equations: Prentice-Hall.
- Fomel, S., Clapp, R., and Claerbout, J., 1997, Missing data interpolation by recursive filter preconditioning: *SEP-95*, 15–25.
- Fomel, S., 1999, Personal communication:.
- Foster, D. J., and Mosher, C. C., 1992, Suppression of multiple reflections using the radon transform: *Geophysics*, **57**, no. 03, 386–395.
- Guitton, A., and Symes, W. W., 1999, Robust and stable velocity analysis using the Huber function: *SEP-100*, 293–314.
- Harlan, W. S., 1986, Signal-noise separation and seismic inversion: Ph.D. thesis, Stanford University.

- Huber, P. J., 1973, Robust regression: Asymptotics, conjectures, and Monte Carlo: *Ann. Statist.*, **1**, 799–821.
- Kostov, C., 1990, Seismic signals from a drillbit source: Ph.D. thesis, Stanford University.
- Lumley, D., Nichols, D., and Rekdal, T., 1994, Amplitude-preserved multiple suppression: SEP-**82**, 25–45.
- Polak, E., 1997, Optimization: Algorithms and consistent approximations: Springer-Verlag, New York.
- Prucha, M., 1999, Revisiting the half-derivative filter: SEP-**102**, 137–142.
- Rickett, J., 1999, On non-stationary convolution and inverse convolution: SEP-**102**, 129–136.
- Sava, P., and Fomel, S., 1999, Spectral factorization revisited: SEP-**100**, 227–234.
- Sava, P., Rickett, J., Fomel, S., and Claerbout, J., 1998, Wilson-Burg spectral factorization with application to helix filtering: SEP-**97**, 343–351.
- Schwab, M., and Claerbout, J., 1995, The interpolation of a 3 – D data set by a pair of 2 – D filters: SEP-**84**, 271–278.
- Spitz, S., 1999, Pattern recognition, spatial predictability, and subtraction of multiple events: *The Leading Edge*, **18**, no. 1, 55–58.
- Sun, Y., 1999, Anti-aliasing multiple prediction beyond two dimensions: SEP-**100**, 159–170.
- Vershuur, D. J., and Berkhout, A. J., 1997, Estimation of multiple scattering by iterative inversion, Part II: Practical aspects and examples: *Geophysics*, **62**, no. 5, 1596–1611.

Short Note

Plane wave prediction in 3-D

*Sergey Fomel*¹

INTRODUCTION

The theory of plane-wave prediction in three dimensions is described by Claerbout (1993, 1997). Predicting a local plane wave with T - X filters amounts to finding a pair of two-dimensional filters for two orthogonal planes in the 3-D space. Each of the filters predicts locally straight lines in the corresponding plane. The system of two 2-D filters is sufficient for predicting all but purely vertical plane waves, in which case a third 2-D filter for the remaining orthogonal plane is needed. Schwab (1998) discusses this approach in more detail.

Using two prediction filters implies dealing with two filtering output volumes for each input volume. In many applications, this situation leads to a lot of inconvenience. It happens, for example, when one uses the prediction output as a measure of coherency in the input volume (Claerbout, 1993; Schwab et al., 1996). Two outputs are obviously more difficult to interpret than one, and there is no natural way of combining them into one image. Another difficulty arises when plane-wave predictors are used for regularizing linear inverse problems (Clapp et al., 1997). In this case, we cannot apply an efficient recursive preconditioning (Claerbout, 1998a) unless the regularization operator is square, or, in other words, only one prediction filter is involved.

Helical filtering (Claerbout, 1998b) brings us new tools for addressing this problem. In this paper, I show how to combine orthogonal 2-D plane predictors into a single three-dimensional filter with similar spectral properties. The 3-D filter can then work for coherency measurements or for preconditioning 3-D inverse problems. The construction employs the Wilson-Burg method of spectral factorization, adapted for multidimensional filtering with the help of the helix transform (Sava et al., 1998).

I use simple synthetic examples to demonstrate the applicability of plane-wave prediction to 3-D problems.

¹email: sergey@sep.stanford.edu

FACTORIZING PLANE WAVES

Let us denote the coordinates of a three-dimensional space by t , x , and y . A theoretical plane wave is described by the equation

$$U(t, x, y) = f(t - p_x x - p_y y), \quad (1)$$

where f is an arbitrary function, and p_x and p_y are the plane slopes in the corresponding direction. It is easy to verify that a plane wave of the form (1) satisfies the following system of partial differential equations:

$$\begin{cases} \left(\frac{\partial}{\partial x} + p_x \frac{\partial}{\partial t} \right) U = 0 \\ \left(\frac{\partial}{\partial y} + p_y \frac{\partial}{\partial t} \right) U = 0 \end{cases} \quad (2)$$

The first equation in (2) describes plane waves on the $\{t, x\}$ slices. In the discrete form, it can be represented as a convolution with a two-dimensional finite-difference filter \mathbf{A}_x . Similarly, the second equation transforms into a convolution with filter \mathbf{A}_y , which acts on the $\{t, y\}$ slices. The discrete form of equations (2) involves a blocked convolution operator:

$$\begin{pmatrix} \mathbf{A}_x \\ \mathbf{A}_y \end{pmatrix} \mathbf{U} = \mathbf{0}. \quad (3)$$

In many applications, we are actually interested in the spectrum of the prediction filter, which approximates the inverse spectrum of the predicted data. In other words, we deal with the square operator

$$\begin{pmatrix} \mathbf{A}_x^T & \mathbf{A}_y^T \end{pmatrix} \begin{pmatrix} \mathbf{A}_x \\ \mathbf{A}_y \end{pmatrix} = \mathbf{A}_x^T \mathbf{A}_x + \mathbf{A}_y^T \mathbf{A}_y. \quad (4)$$

If we were able to transform this operator to the form $\mathbf{A}^T \mathbf{A}$, where \mathbf{A} is a three-dimensional minimum-phase convolution, we could use the three-dimensional filter \mathbf{A} in place of the inconvenient pair of \mathbf{A}_x and \mathbf{A}_y .

The problem of finding \mathbf{A} from its spectrum is known as spectral factorization. It is well understood for 1-D signals (Claerbout, 1976), but until recently it was an open problem in the multidimensional case. Helix transform maps multidimensional filters to 1-D by applying special boundary conditions and allows us to use the full arsenal of 1-D methods, including spectral factorization, on multidimensional problems (Claerbout, 1998b). A problem, analogous to (4), has already occurred in the factorization of the discrete two-dimensional Laplacian operator:

$$\Delta = \nabla^T \nabla = \begin{pmatrix} \mathbf{D}_x^T & \mathbf{D}_y^T \end{pmatrix} \begin{pmatrix} \mathbf{D}_x \\ \mathbf{D}_y \end{pmatrix} = \mathbf{H}^T \mathbf{H}, \quad (5)$$

where \mathbf{D}_x and \mathbf{D}_y represent the partial derivative operators along the x and y dimensions, respectively, and the two-dimensional filter \mathbf{H} has been named *helix derivative* (Claerbout, 1999; Zhao, 1999).

If we represent the filter \mathbf{A}_x with the help of a simple first-order upwind finite-difference scheme

$$\mathbf{U}_{x+1}^t - \mathbf{U}_x^t + p_x \left(\mathbf{U}_{x+1}^{t+1} - \mathbf{U}_{x+1}^t \right) = 0, \quad (6)$$

then, after the helical mapping to 1-D, it becomes a one-dimensional filter with the Z -transform

$$\mathbf{A}_x(Z) = 1 - p_x Z^{N_t+1} + (p_x - 1) Z^{N_t}, \quad (7)$$

where N_t is the number of samples on the t -axis. Similarly, the filter \mathbf{A}_y takes the form

$$\mathbf{A}_y(Z) = 1 - p_y Z^{N_t N_x+1} + (p_y - 1) Z^{N_t N_x}. \quad (8)$$

The problem is reduced to a 1-D spectrum factorization of

$$\begin{aligned} \mathbf{A}_x(1/Z)\mathbf{A}_x(Z) + \mathbf{A}_y(1/Z)\mathbf{A}_y(Z) = & -p_y \frac{1}{Z^{N_t N_x+1}} + (p_y - 1) \frac{1}{Z^{N_t N_x}} - \\ & p_x \frac{1}{Z^{N_t+1}} + (p_x - 1) \frac{1}{Z^{N_t-1}} + [p_x(1 - p_x) + p_y(1 - p_y)] \frac{1}{Z} + \\ & 2 + p_x(p_x - 1) + p_y(p_y - 1) + [p_x(1 - p_x) + p_y(1 - p_y)] Z + \\ & (p_x - 1) Z^{N_t-1} - p_x Z^{N_t+1} + (p_y - 1) Z^{N_t N_x} - p_y Z^{N_t N_x+1}. \end{aligned} \quad (9)$$

After a minimum-phase factor of (9) has been found, we can use it for 3-D forward and inverse convolution.

All examples in this paper actually use a slightly more sophisticated formula for 2-D plane-wave predictors:

$$\mathbf{A}_x(Z) = 1 + \frac{p_x}{2}(1 - p_x)Z^{N_t-1} + (p_x^2 - 1)Z^{N_t} - \frac{p_x}{2}(1 + p_x)Z^{N_t+1}. \quad (10)$$

Formula (10) corresponds to the Lax-Wendroff finite difference scheme (Clapp et al., 1997). It provides a valid approximation of the plane-wave differential equation for $-1 \leq p_x \leq 1$.

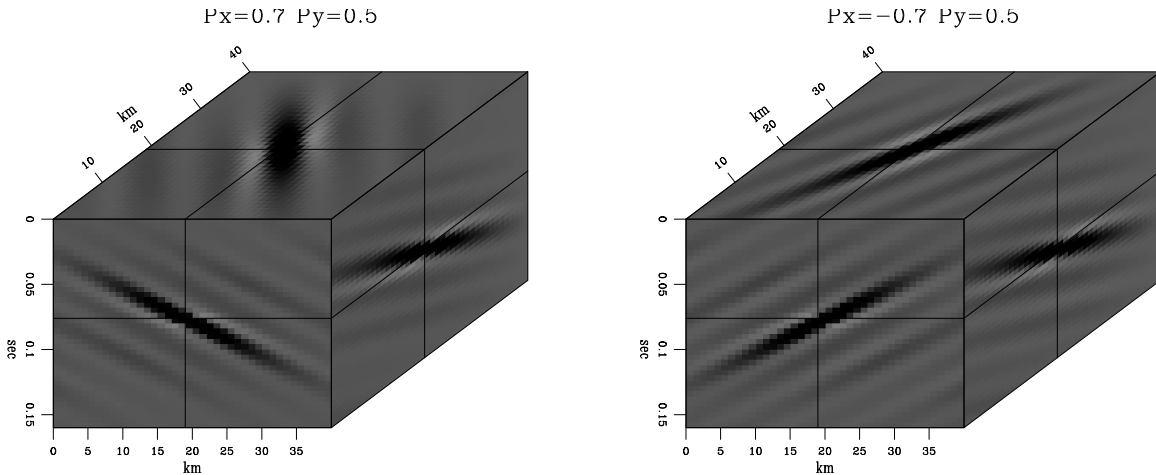


Figure 1: 3-D plane wave prediction with a 402-point filter. Left: $p_x = 0.7$, $p_y = 0.5$. Right: $p_x = -0.7$, $p_y = 0.5$. [sergey3-eplane](#) [ER]

Figure 2: Schematic filter shape for a 26-point 3-D plane prediction filter. The dark block represents the leading coefficient. There are 9 blocks in the first row and 17 blocks in the second row. `sergey3-shape` [NR]

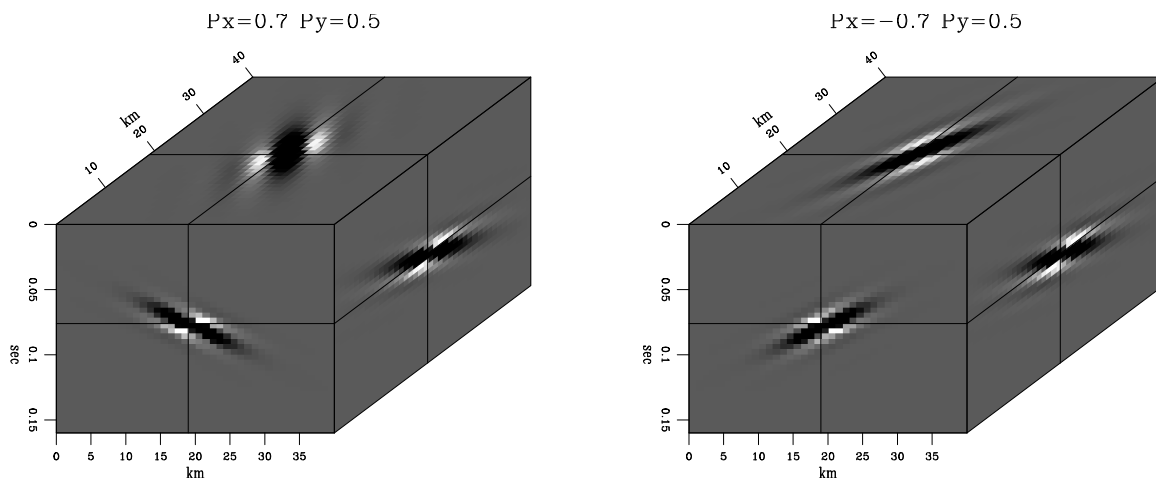
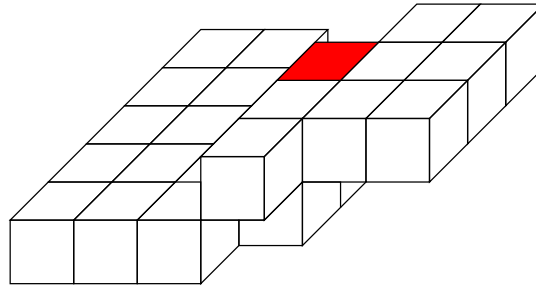


Figure 3: 3-D plane wave prediction with a 26-point filter. Left: $p_x = 0.7$, $p_y = 0.5$. Right: $p_x = -0.7$, $p_y = 0.5$. `sergey3-tplane` [ER]

Figure 1 shows examples of plane-wave construction. The two plots in the figure are outputs of a spike, divided recursively (on a helix) by $\mathbf{A}^T \mathbf{A}$, where \mathbf{A} is a 3-D minimum-phase filter, obtained by Wilson-Burg factorization. The factorization was carried out in the assumption of $N_t = 20$ and $N_x = 20$; therefore, the filter had $N_t N_x + 2 = 402$ coefficients. Using such a long filter may be too expensive for practical purposes. Fortunately, the Wilson-Burg method allows us to specify the filter length and shape beforehand. By experimenting with different filter shapes, I found that a reasonable accuracy can be achieved with a 26-point filter, depicted in Figure 2. Plane-wave construction for a shortened filter is shown in Figure 3. The predicted plane wave is shorter and looks more like a slanted disk. It is advantageous to deal with short plane waves if the filter is applied for local prediction of non-stationary signals.

In the next sections, I address the problem of estimating plane-wave slopes and show some examples of applying local plane-wave prediction in 3-D problems.

ESTIMATING PLANE WAVES

It may seem difficult to estimate the plane slope p_x for a Lax-Wendroff filter of the form (10) because p_x appears non-linearly in the filter coefficients. However, using the analytical form of the filter, we can easily linearize it with respect to the plane slope and set up a simple iterative scheme:

$$p_x^{(k+1)} = p_x^{(k)} + \Delta p_x^{(k)}, \quad (11)$$

where k stands for the iteration count, and $\Delta p_x^{(k)}$ is found from the linearized equation

$$(\mathbf{A}'_x \mathbf{U}) \Delta p_x = -\mathbf{A}_x \mathbf{U}, \quad (12)$$

where \mathbf{A}'_x is the derivative of \mathbf{A}_x with respect to p_x . To avoid unstable division by zero when solving equation (12) for Δp_x , Adding a regularization equation

$$\epsilon \nabla \Delta p_x \approx 0, \quad (13)$$

where ϵ is a small scalar regularization parameter, I solve system (12-13) in the least-square sense to obtain a smooth slope variation Δp_x at each iteration. In practice, iteration process (11) quickly converges to a stable estimate of p_x .

EXAMPLES

Two simple examples in this section demonstrate an application of 3-D local plane-wave prediction to the problems of discontinuity enhancement and missing data interpolation.

3-D discontinuity enhancement

Figure 4 shows a simple synthetic model of two plane waves, separated by a plane fault. The slope estimates for the two orthogonal directions are shown in Figure 5. We can see that the

Figure 4: A synthetic model, showing a fault between two plane waves of different slopes. `sergey3-cube` [ER]

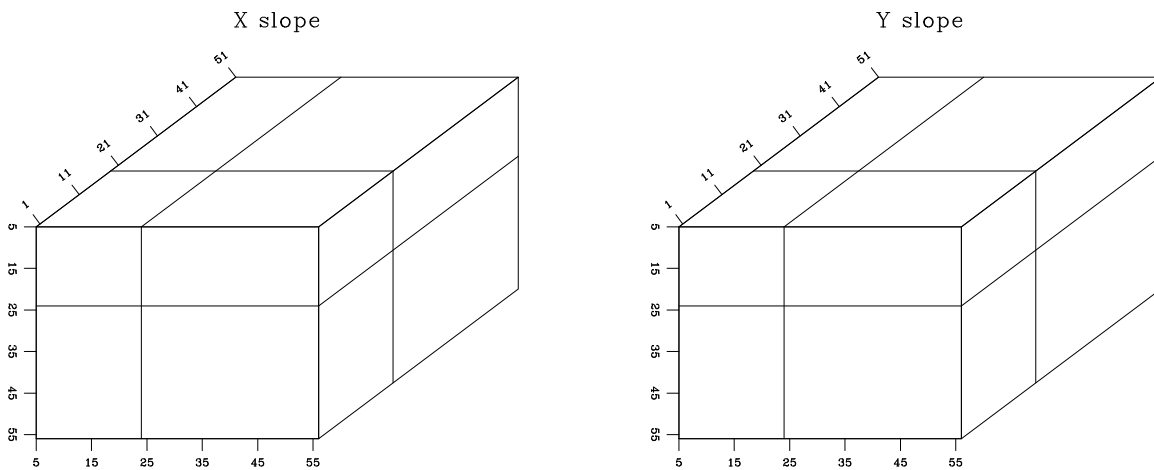
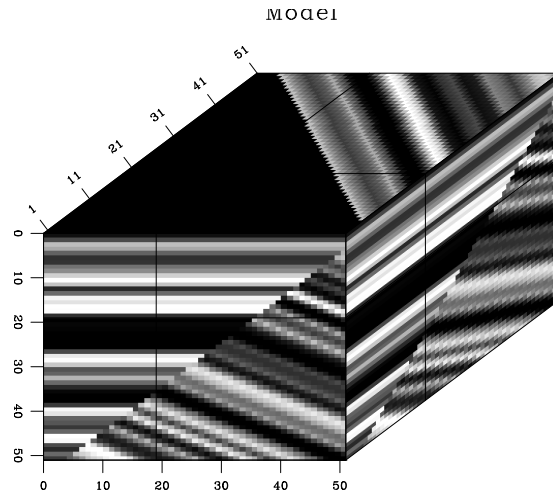
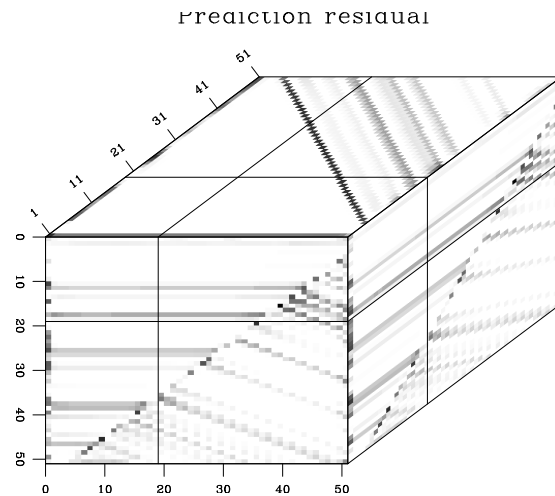


Figure 5: Plane wave slope estimates in the x and y directions (left and right plots, respectively) from the synthetic two-plane model. `sergey3-cslope` [ER]

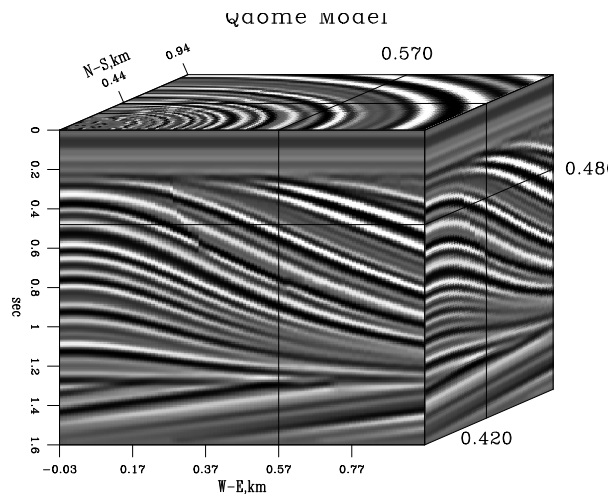
estimation procedure correctly identified the regions of constant slope. Finally, estimating a local 3-D plane-wave predictor by spectral factorization and convolving the resultant non-stationary filter with the input model, we obtain the prediction residual, shown in Figure 6. In the residual, both plane waves are effectively destroyed, and we observe a sharp image of the fault plane. This result compares favorably with results of alternative methods, collected by (Schwab, 1998).

Figure 6: Magnitude of the residual after convolving the synthetic two-plane model with a local 3-D plane wave filter. `sergey3-cmain` [ER]



3-D missing data interpolation

Figure 7: Claerbout's "qdome" synthetic model. `sergey3-qdome` [ER]



Figures 7 and 8 show Claerbout's "qdome" synthetic model (Claerbout, 1993, 1999) and its corresponding slope estimates. In a missing data interpolation experiment, I remove 75% of the traces in the original model, arriving at the missing data model, shown in the left plot of Figure 9. The missing data interpolation result is shown in the right plot of Figure 9. Most of the original signal, except for some high-curvature areas, has been restored. Local 3-D plane-wave predictors allow us to use the efficient interpolation technique of Fomel et al. (1997), based on recursive filter preconditioning.

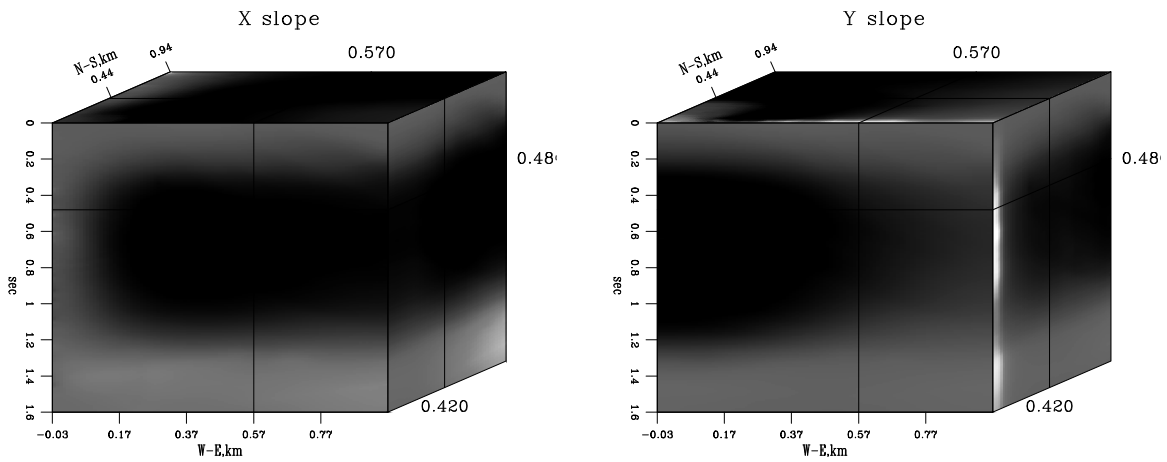


Figure 8: Plane wave slope estimates in the x and y directions (left and right plots, respectively) from the “qdome” model. `sergey3-qslope` [CR]

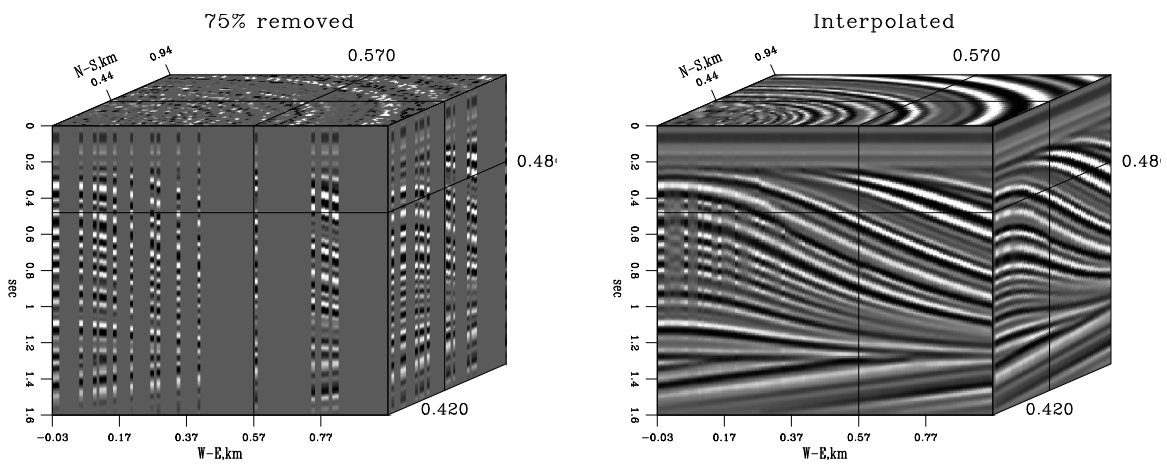


Figure 9: Left: “qdome” model with 75% of the randomly chosen traces removed. Right: result of missing data interpolation with a 3-D local plane-wave prediction filter. `sergey3-qmiss` [CR]

CONCLUSIONS

I have shown that a 3-D plane-wave prediction filter can be constructed from a pair of two-dimensional filters by using helix transform and a one-dimensional spectral factorization algorithm.

In all the examples, I used analytical finite-difference filters instead of more general prediction-error filters. A similar factorization idea could be applied to 3-D prediction-error filters. However, treating non-stationarity in this case is less straightforward and requires additional care (Crawley et al., 1998; Clapp et al., 1999).

3-D plane-wave prediction filters can find many interesting applications in data processing and inversion. An especially promising application is solution steering in tomography-type problems (Clapp et al., 1997; Clapp and Biondi, 1998).

ACKNOWLEDGMENTS

Jon Claerbout suggested the problem of 3-D plane wave prediction and the idea of its solution. Unfortunately, he is currently not able to share the authorship.

REFERENCES

- Claerbout, J. F., 1976, *Fundamentals of geophysical data processing*: Blackwell.
- Claerbout, J. F., 1993, 3-D local monoplane annihilator: *SEP-77*, 19–25.
- Claerbout, J. F., 1997, *Geophysical exploration mapping: Environmental soundings image enhancement*: Stanford Exploration Project.
- Claerbout, J., 1998a, Multidimensional recursive filters via a helix: *SEP-97*, 319–335.
- Claerbout, J., 1998b, Multidimensional recursive filters via a helix: *Geophysics*, **63**, no. 5, 1532–1541.
- Claerbout, J., 1999, *Geophysical estimation by example: Environmental soundings image enhancement*: Stanford Exploration Project, <http://sepwww.stanford.edu/sep/prof/>.
- Clapp, R. G., and Biondi, B. L., 1998, Regularizing time tomography with steering filters: *SEP-97*, 137–146.
- Clapp, R. G., Fomel, S., and Claerbout, J., 1997, Solution steering with space-variant filters: *SEP-95*, 27–42.
- Clapp, R. G., Fomel, S., Crawley, S., and Claerbout, J. F., 1999, Directional smoothing of non-stationary filters: *SEP-100*, 197–209.

- Crawley, S., Clapp, R., and Claerbout, J., 1998, Deconvolution and interpolation with nonstationary filters: *SEP-97*, 183–192.
- Fomel, S., Clapp, R., and Claerbout, J., 1997, Missing data interpolation by recursive filter preconditioning: *SEP-95*, 15–25.
- Sava, P., Rickett, J., Fomel, S., and Claerbout, J., 1998, Wilson-Burg spectral factorization with application to helix filtering: *SEP-97*, 343–351.
- Schwab, M., Holden, C., and Claerbout, J., 1996, Revealing geological discontinuities by local plane wave suppression: *SEP-92*, 29–47.
- Schwab, M., 1998, Enhancement of discontinuities in seismic 3-D images using a Java estimation library: Ph.D. thesis, Stanford University.
- Zhao, Y., 1999, Helix derivative and low-cut filters' spectral feature and application: *SEP-100*, 235–250.

Predictive signal/noise separation of ground-roll-contaminated data

Morgan Brown, Robert G. Clapp, and Kurt Marfurt¹

ABSTRACT

Coherent noise contamination is a first order problem plaguing the imaging of seismic data acquired in both land and marine environments. We present a new method for the predictive separation of coherent noise from prestack data which operates in the $t - x$ domain. We apply the new method to real 2-D receiver lines coming from a 3-D shot gather, and nondestructively separate hyperbolic ground roll from primary reflections. This method performs favorably compared to other common techniques, even with an imperfect model of the ground roll, a fact which makes the method attractive in cases where the noise is difficult or expensive to model explicitly.

INTRODUCTION

Historically, high acquisition costs and data with low signal-to-noise ratio have handicapped land-based seismic acquisition efforts. Chief among the causes of low S/N ratio is *ground roll*, which to first order consists of direct-arrival and scattered energy from the shot-generated Rayleigh (SV) wave. Larner et al. (1983) recognized that coherent noise often add constructively after conventional imaging steps, producing spurious signatures that obscure real primary reflections, or worse, may masquerade as primaries themselves. The authors argued convincingly that coherent noise events should be removed in the prestack domain; this argument is not disputed today.

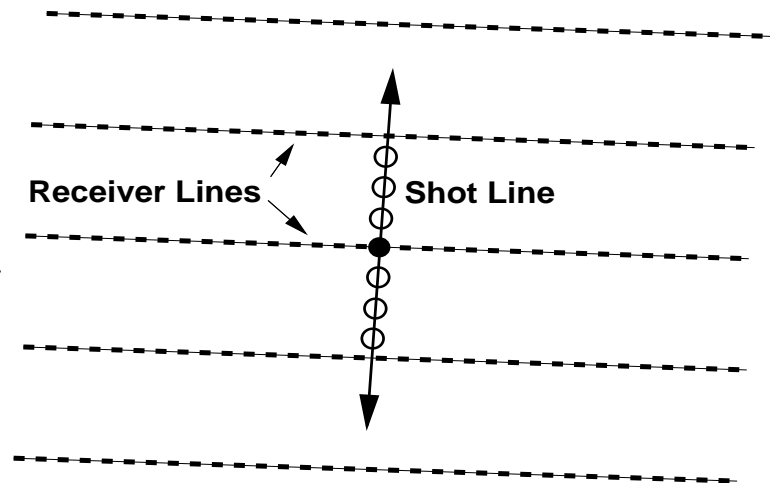
In (t, x, y) space, the ground roll falls nearly within a cone centered at the shot location. Traditional 2-D roll-along land surveys consist of a single receiver line with a shot in the center, such that the recorded ground roll lies at the apex of the cone and has nearly linear moveout. In 3-D surveys, the ground roll on a 2-D receiver line has hyperbolic moveout when there is crossline distance between the shot, as in the common “cross-spread” acquisition geometry, shown in Figure 1. A single 2-D receiver line from a 3-D shot gather from such a geometry is shown in Figure 2.

In many cases, regions containing ground roll are simply muted from the recorded data, since they are localized in $t - x$. Clearly, however, it is preferable to use both the near and far offsets, rather than trying to “outrun” the ground roll by recording at very far offsets. High acquisition cost or geological considerations may prevent the recording of far-offset reflec-

¹email: morgan@sep.stanford.edu, bob@sep.stanford.edu, kmarfurt@tank.agl.uh.edu

tions, especially for deep targets. Likewise, multicomponent seismic applications such as the determination of fracture orientation and shear wave extinction angles (Mueller, 1992; Li and Mueller, 1997), and also quantitative inversion techniques require both near and far offsets. Furthermore, as noted by Regone (1997), in regions of rugged topography, body waves sometimes convert into surface waves after scattering from near surface heterogeneities, creating a high velocity event that reaches into the far offsets. The need to adaptively identify and nondestructively filter ground roll is pressing, but the geographical variability of near surface geology gives ground roll wildly variable character, and prevents most current techniques of removal from achieving universal applicability.

Figure 1: So-called “cross-spread” 3-D land acquisition geometry. The spacing between the parallel receiver lines is much greater than the inline receiver spacing. morgan1-cross-spread [NR]



In spite of a long and successful tradition in ground roll suppression, field arrays often damage the recorded signal. Averaging operations imply an inherent loss of information, which in this case is the frequency content, and hence the resolving power, of the recorded signal. Incident primary reflections are never perfectly vertical, nor is the near surface perfectly laterally invariant, so a field array stack will always blur the wavelet. When the static shifts caused by near surface heterogeneities are strong, the blurring is significant. Often, as with Ocean Bottom Cable (OBC) or smaller-scale seismic applications, placement of arrays with adequate areal extent is impractical for logistical and/or economic reasons. Furthermore, traditional 2-D field arrays are ineffective in removing out-of-plane backscattered energy, so in many cases a 3-D array is required (Regone, 1997), adding considerably to the acquisition cost.

Often, as seen in Figure 2, ground roll occupies a much lower frequency band than the primary reflections, in which case the ground roll is easily removable by (ω, x) mute, at the expense of the low frequency component of the signal, which is crucial for acoustic impedance inversion (Sbar and Blankenship, 1998). $f - k$ (or “fan”) filtering (Treitel et al., 1967) is useful for removing linear events, but is sensitive to aliased data, and ground roll is almost always aliased at normal receiver spacing. The aliasing becomes even more pronounced in 3-D, since acquisition costs usually prevent adequate sample of the crossline.

Ground roll and primaries normally differ greatly in moveout, so in that sense, the Discrete Radon Transform (DRT) can remove the ground roll in 2-D or 3-D. However, Marfurt et al.

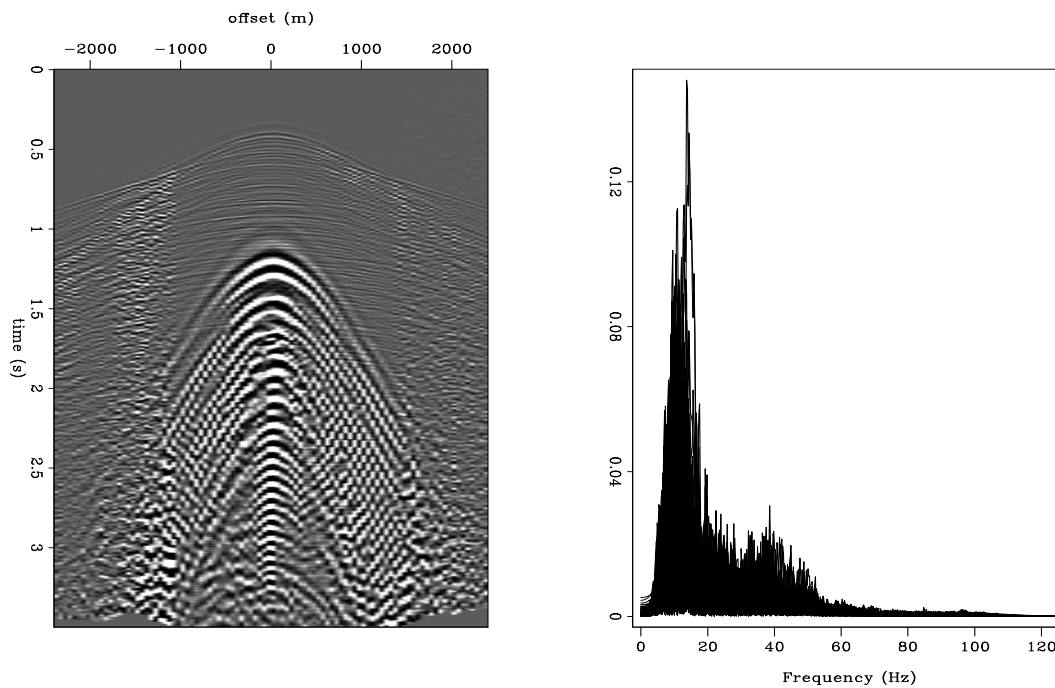


Figure 2: Left: Receiver line windowed from a 3-D shot gather of a Middle East cross-spread survey. Since the penetration depth of Rayleigh waves is a decreasing function of frequency, they are generally dispersive for $v(z)$ media. Strong, dispersive, aliased ground roll with hyperbolic moveout contaminates the lower portion of the section. The signal-to-noise ratio is quite low. Right: Data spectrum. Notice considerable separation of noise and signal spectra.

morgan1-dune-spectrum [ER]

(1996) point out the extreme sensitivity of the DRT mute process to aliasing, so an a priori moveout correction to the ground roll is required, which in turn may cause aliasing of the primaries themselves. Additionally, the DRT is unable to remove backscattered energy from the crossline direction. Still, when the ground roll in a single 2-D receiver line is almost perfectly hyperbolic, as it is for instances of very well-behaved near-surface geology, the DRT may adequately separate it from the signal (Wang, 1997).

Canales (1984) introduced a fundamentally new view of the signal/noise separation problem. Rather than viewing noise as something to be explicitly subtracted from data, he exploited the fact that seismic signal is usually predictable relative to random noise. When a prediction error filter (PEF) is estimated from a given dataset, Gaussian noise components of the data are in the nullspace of the estimation. It is a known (Claerbout, 1976) that the frequency response of a PEF approximates the inverse spectrum of the data from which the PEF was estimated. By computing a PEF ($f - x$ domain) from the noise-contaminated data, this approach obtains an “in situ” estimate of the signal power spectrum. Application of Wiener reconstruction (Castleman, 1996) then yields an optimal (least squares) estimate of the signal.

Coherent noise suppression is a more difficult matter, since it requires an indirect method of estimating the signal PEF, like that of Spitz (1999), who presented a predictive $f - x$ technique to suppress multiple reflections. We present a similar predictive signal/noise separation scheme in the $t - x$ domain which utilizes recent SEP advances in nonstationary filtering, and apply it to the removal of complicated ground roll in 2-D receiver lines which come from a 3-D land survey. This approach requires only a rough model of the ground roll, obviating the need for explicit modeling techniques, which are generally complicated and very costly. Clapp and Brown (1999) have applied the same methodology to suppress multiple reflections in prestack marine data.

METHODOLOGY

Canales’ (1984) implementation is in the $f - x$ domain, so he makes the implicit assumption that the data is time-stationary, i.e., that each trace is the convolution of a single time-invariant wavelet with the earth’s random reflectivity sequence. Computationally, this approach is very efficient. However, since ground roll is highly dispersive, and thus nonstationary, we instead choose a $t - x$ method utilizing nonstationary PEF’s (Claerbout, 1999; Crawley, 1999; Clapp et al., 1999).

Consider the recorded data to be the linear superposition of coherent signal plus coherent noise:

$$\mathbf{d} = \mathbf{s} + \mathbf{n}. \quad (1)$$

Also assume that both the signal and noise are predictable, i.e., made up of one or more local plane wave segments. The prediction error (residual) of the convolution of the signal and the noise with the corresponding nonstationary PEF’s \mathbf{S} and \mathbf{N} is then uncorrelated. Writing these ideas as convolutional “fitting goals”, we have

$$\mathbf{r}_n \equiv \mathbf{Nn} \approx 0$$

$$\mathbf{r}_s \equiv \epsilon \mathbf{S}\mathbf{s} \approx 0 \quad (2)$$

where \mathbf{S} and \mathbf{N} represent $t - x$ convolution with the nonstationary signal and noise PEF's, respectively, and the scaling factor ϵ balances the energies of the residuals. Equation (2) can be rewritten in an equivalent, but more familiar, notation as the minimization of a quadratic objective function:

$$Q(\mathbf{n}, \mathbf{s}) \equiv \|\mathbf{r}_n + \epsilon \mathbf{r}_s\|^2 = \|\mathbf{N}\mathbf{n} + \epsilon \mathbf{S}\mathbf{s}\|^2,$$

but we will hereafter use the notation of equation (2).

Rewriting the constraint equation (1), $\mathbf{n} = \mathbf{d} - \mathbf{s}$, allows us to eliminate \mathbf{n} from equation (2), and suggests a regularized least squares optimization problem for the unknown signal \mathbf{s}

$$\begin{aligned} \mathbf{N}\mathbf{s} &\approx \mathbf{N}\mathbf{d} \\ \epsilon \mathbf{S}\mathbf{s} &\approx 0, \end{aligned} \quad (3)$$

which is the approach used by Abma (1995). It can be easily shown (see Appendix A) that the predicted signal of equation (3) is the same as the optimal Wiener reconstruction (Castleman, 1996; Leon-Garcia, 1994) for the special case of uncorrelated signal and noise.

We now consider some issues involving the calculation of the nonstationary signal and noise PEF's, \mathbf{S} and \mathbf{N} .

- **Signal PEF**

Equation (3) treats the signal PEF \mathbf{S} as known, but this assumption appears circular since the unknown signal \mathbf{s} is itself required in order to estimate \mathbf{S} . Spitz (1999) proposes an estimate of the signal PEF in terms of a PEF, \mathbf{D} , estimated from the *data*, and a PEF, \mathbf{N} , estimated from a model of the noise.

$$\mathbf{S} = \mathbf{D}\mathbf{N}^{-1} \quad (4)$$

\mathbf{N}^{-1} is nonstationary *deconvolution*, now better-defined in more than one dimension since the advent of the helix transform (Claerbout, 1998). By conceptualizing equation (4) as a division of inverse spectra, Spitz' conjecture makes sense intuitively, that the unknown signal spectrum is the data spectrum scaled by the inverse of the noise spectrum. In the $t - x$ domain, we have seen heuristic proof of equation (4), and Sergey Fomel reports that a general proof is trivial in the $f - x$ domain.

- **Noise PEF**

The assumption that the noise PEF \mathbf{N} is known is also circular, since the noise is implicitly part of the unknown model. In many circumstances it is possible to explicitly model the noise well enough to estimate \mathbf{N} , like a convolutional model for multiples (i.e., the Delft SRME method of Verschuur et al. (1992)) Unfortunately, variation in near surface earth properties makes it nearly impossible to explicitly model ground roll to cover all observed cases from around the world, so it necessary to obtain the noise model directly from the data.

The noise model should be a first-order estimate of the noise - if it was perfect, the job would already be done. Ideally the noise model should contain the spatial correlation

of all noise events, which will realistically differ in amplitude from the actual noise by a small, arbitrary time- and space-variant scale factor. Of course, a small amount of signal will contaminate the noise model, but as the ground roll will have much higher amplitude than any embedded signal, we assume that the L_2 PEF estimation of \mathbf{N} will effectively ignore the embedded signal, though this is not always the case.

If the ground roll and signal are sufficiently well-separated in temporal frequency, application of a lowpass filter to the data may produce a satisfactory noise model. The degree to which the noise and signal are separated is dependent on many variables - geography, depth to target, geology, and source type, to name a few. Similarly, if a hyperbolic Radon transform focuses primaries well, then it may be possible to mute the primaries in $\tau - p$ space, then inverse transform to obtain a noise model. We have tested both approaches, and find that lowpass filtering is the most reliable, although this assertion is data-dependant. Clapp and Brown (1999) applied an L_1 iterative hyperbolic Radon transform to a multiple-infested 2-D seismic line, and found that the primaries were focused far better than for the usual L_2 least squares DRT.

Using Spitz' (1999) choice for the signal PEF, $\mathbf{S} = \mathbf{DN}^{-1}$, rewrite equation (3)

$$\begin{aligned} \mathbf{Ns} &\approx \mathbf{Nd} \\ \epsilon \mathbf{DN}^{-1}\mathbf{s} &\approx 0. \end{aligned} \quad (5)$$

Following Fomel et al. (1997), we precondition this iterative problem to improve performance. Make the change of variables

$$\mathbf{s} = (\mathbf{DN}^{-1})^{-1}\mathbf{p} = \mathbf{ND}^{-1}\mathbf{p}, \quad (6)$$

and rewrite equation (5):

$$\begin{aligned} \mathbf{NND}^{-1}\mathbf{p} &\approx \mathbf{Nd} \\ \epsilon \mathbf{p} &\approx 0. \end{aligned} \quad (7)$$

This unconstrained least squares optimization can be solved using any gradient-based iterative technique, as in Claerbout (1999).

RESULTS

We applied the technique to four 2-D receiver lines from a Middle East 3-D shot gather. One of these 2-D lines was shown earlier in Figure 2. The results are shown in Figures 3, 5, 6, and 7. Considering the low S/N, the extraction result is quite impressive. Many primary events which were hopelessly masked in the raw data become apparent after signal/noise separation. As proof of the power of this method of separation, compare Figure 3 to Figure 4, where the latter is simply the result of subtracting the noise model from the data, or equivalently, lowcut filtering. The lowcut filter very effectively suppresses the ground roll, but severely damages the low frequency portion of the signal. The difference between the two results reinforces the

fact that the predictive method can and will succeed with an imperfect noise model. Although the predictive method places some signal energy in the noise panel, the character of the signal seems preserved for the most part. Likely, any degradation of the signal within the noise cone is embedded signal which was *not* ignored in the estimation of \mathbf{N} .

DISCUSSION/CONCLUSIONS

Extension to 3-D

On our 4-processor SGI Origin 200, one normal-sized 2-D receiver line requires between 1 to 2 minutes of processing time, not including human interaction. For a full 3-D prestack survey, such performance is not damning, but some optimization is still desirable.

Since the spatial correlation of the events in a 3-D dataset are truly three dimensional, the best approach is to use three dimensional PEF's. Schwab (1998) notes that true 3-D PEF's more effectively whiten actual 3-D data than do ensembles of rotated 2-D filters. Events which appear incoherent in a 2-D slice may actually have hidden coherence in 3-D.

In 3-D, the way in which the data is sorted becomes an important issue. Among many different ways of sorting, two simple 3-D gathers for the cross-spread geometry (Figure 1) are common shot gathers (CSG) and common receiver-line gathers (CRLG). Define a CSG as the collection of records from all receiver lines in the survey for one shot, and similarly, a CRLG as the collection of records from one receiver line for all shots. Normally the shot spacing is far less than the receiver line spacing, so CRLG's are better sampled crossline than CSG's. This fact allows the use of fairly compact 3-D filters to predict the data in a CRLG, since the time delay between events is not large in the shot line direction. Still, the details involved in the choice of gather are strongly data-dependent, so these assertions are not exhaustive.

3-D prestack seismic data is five-dimensional, and redundant over one or more of these, depending on the survey design. A tantalizing possibility is to exploit this redundancy by reusing PEF's and predicted signal panels from nearby gathers as starting guesses.

Pros

- The predictive signal/noise separation method operates successfully, even when the noise is severely spatially aliased. The data need not be sampled finely in space to remove ground roll, a fact which is profound, considering the high cost of land-based seismic acquisition. Crawley (1998) shows another example of the feasibility of using PEF's to estimate aliased, coherent seismic signals.
- Ground roll comes in many different flavors. A method which exploits the particular moveout patterns of one observed case of ground roll is sure to fail on others. The predictive method is blind to this; assuming a first order separation gives a viable noise model, the specific moveout patterns of signal and noise are irrelevant.

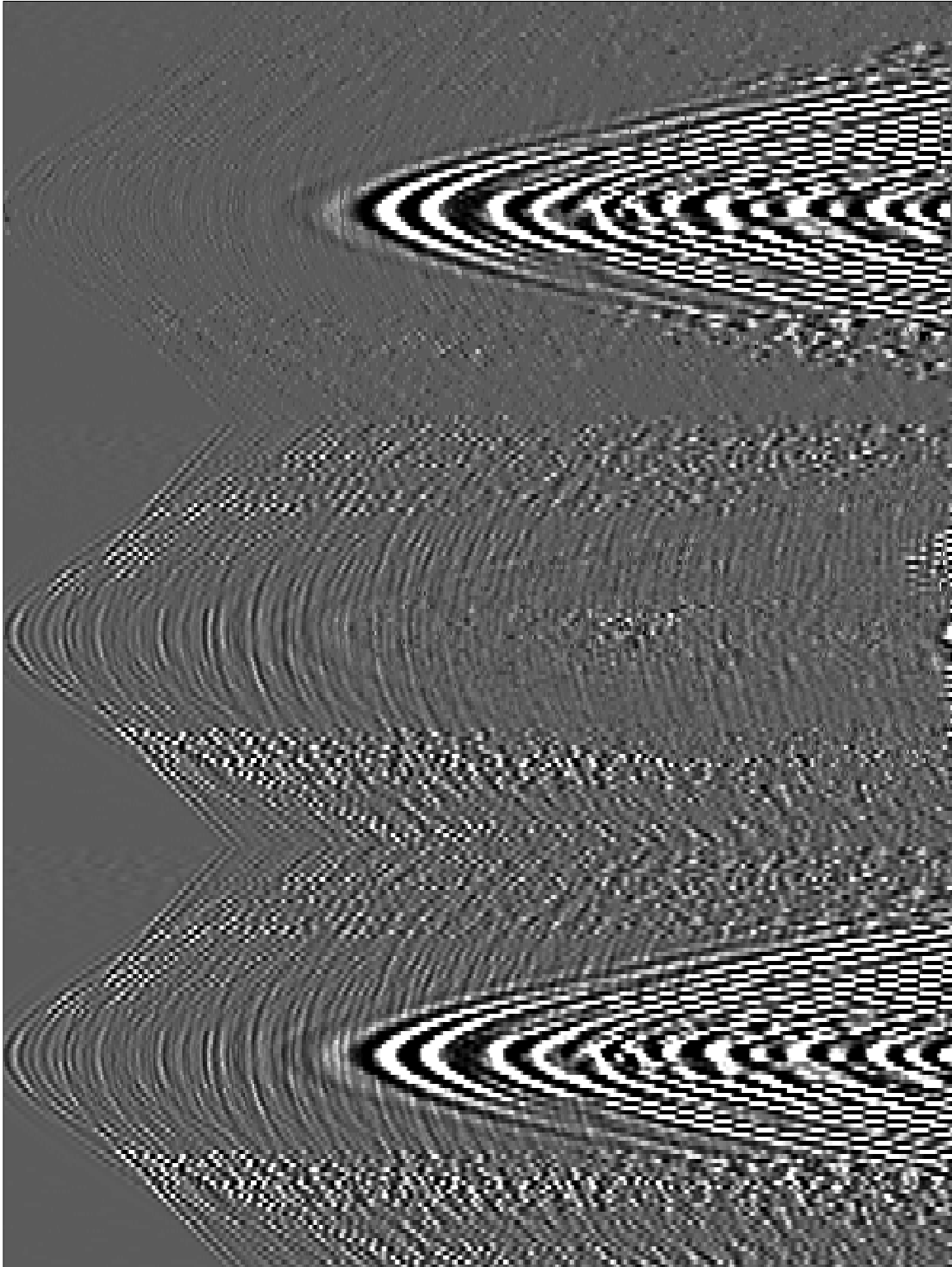


Figure 3: Receiver line #1 - predictive method results. From left to right: 1) Input data. 2) Predicted signal. 3) Difference, i.e., predicted noise. `morgan1-dune-pred-daterr` [ER]

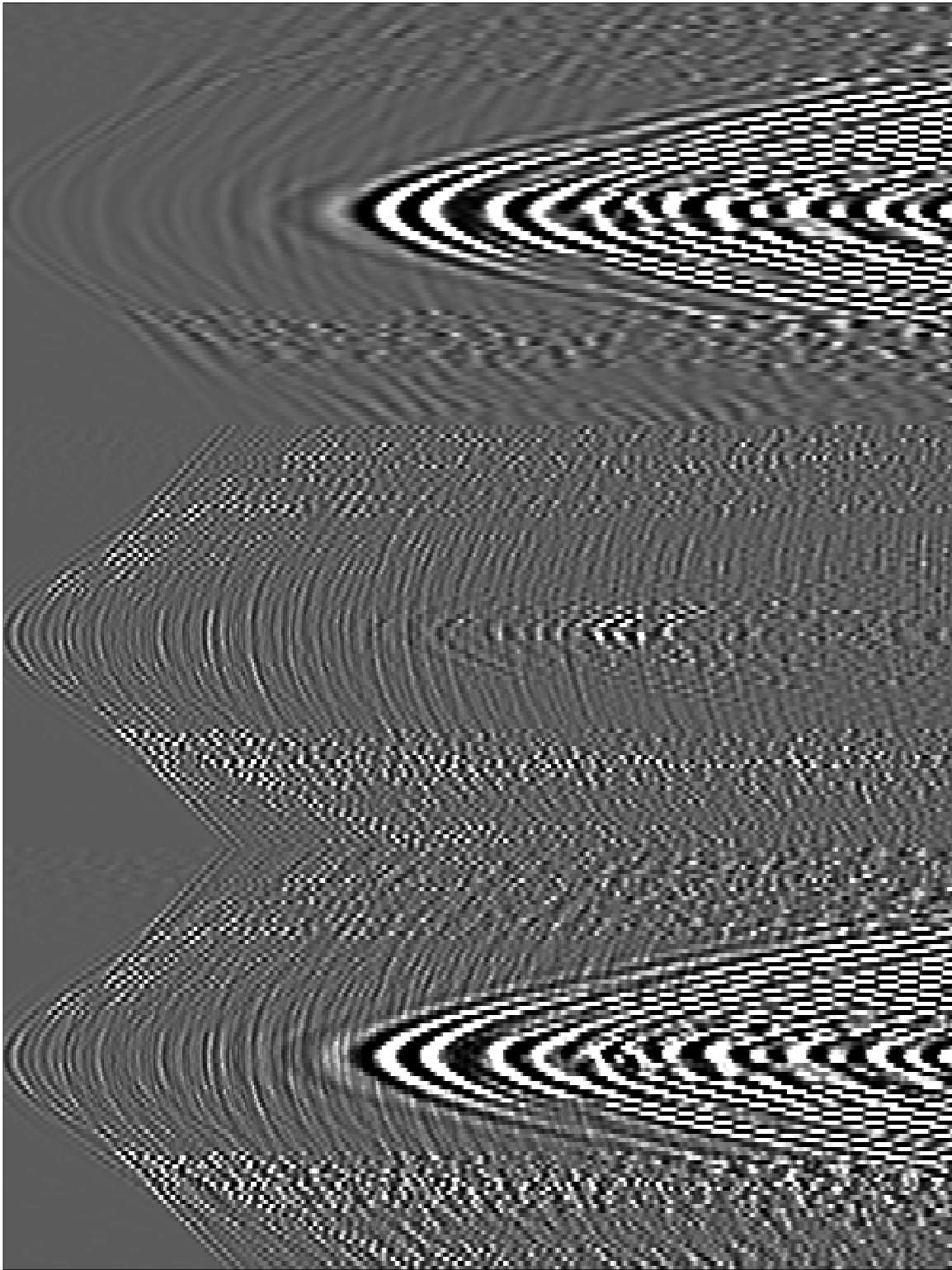


Figure 4: Receiver line #1 - highpass filter results. From left to right: 1) Input data. 2) Highpass (20 Hz cutoff) filter applied to data 3) Difference, i.e., noise model.
`morgan1-dune-locut-daterr` [ER]

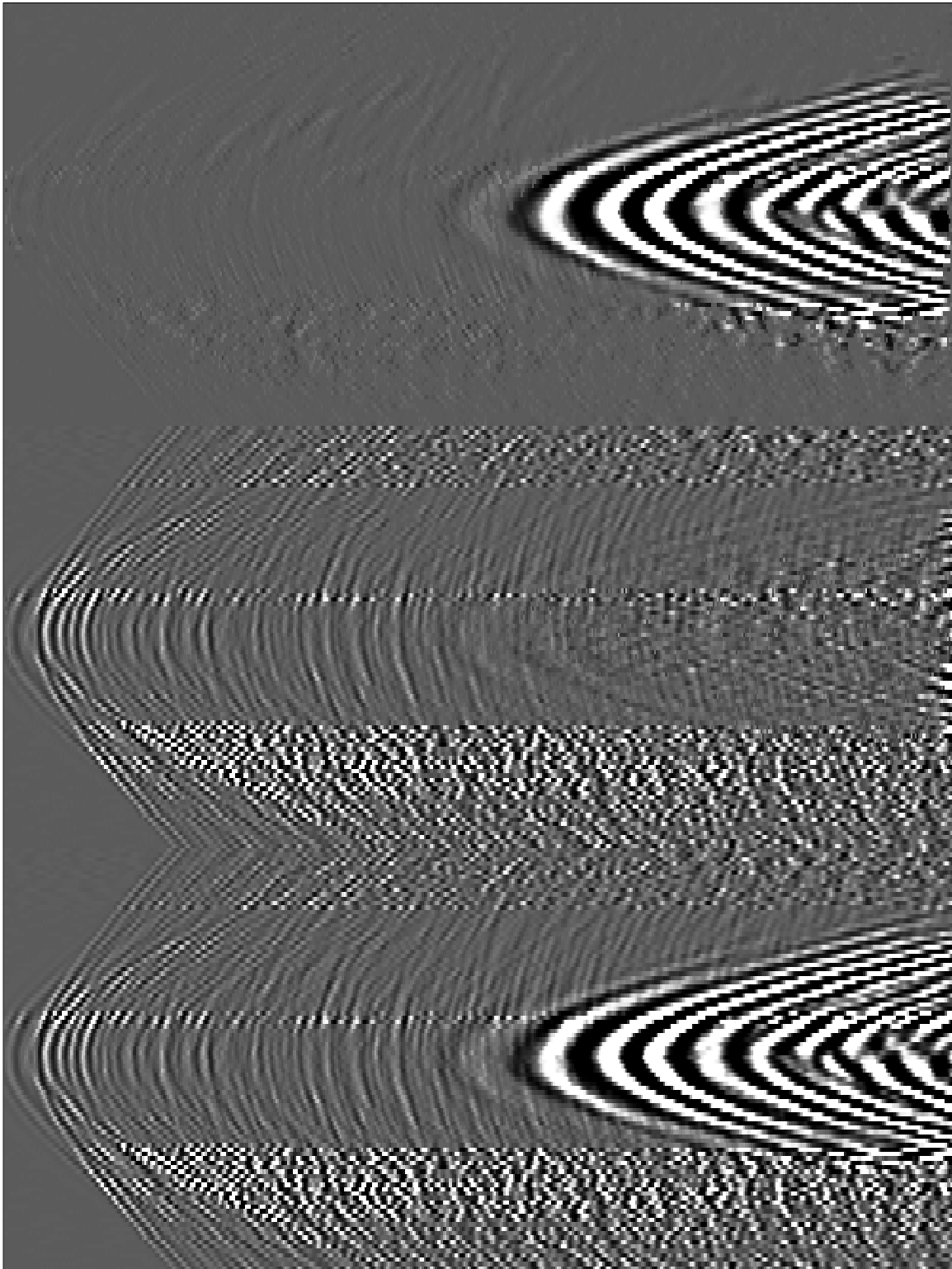


Figure 5: Receiver line #2 - predictive method results. From left to right: 1) Input data. 2) Predicted signal. 3) Difference, i.e., predicted noise. `morgan1-dune1-pred-daterr` [ER]

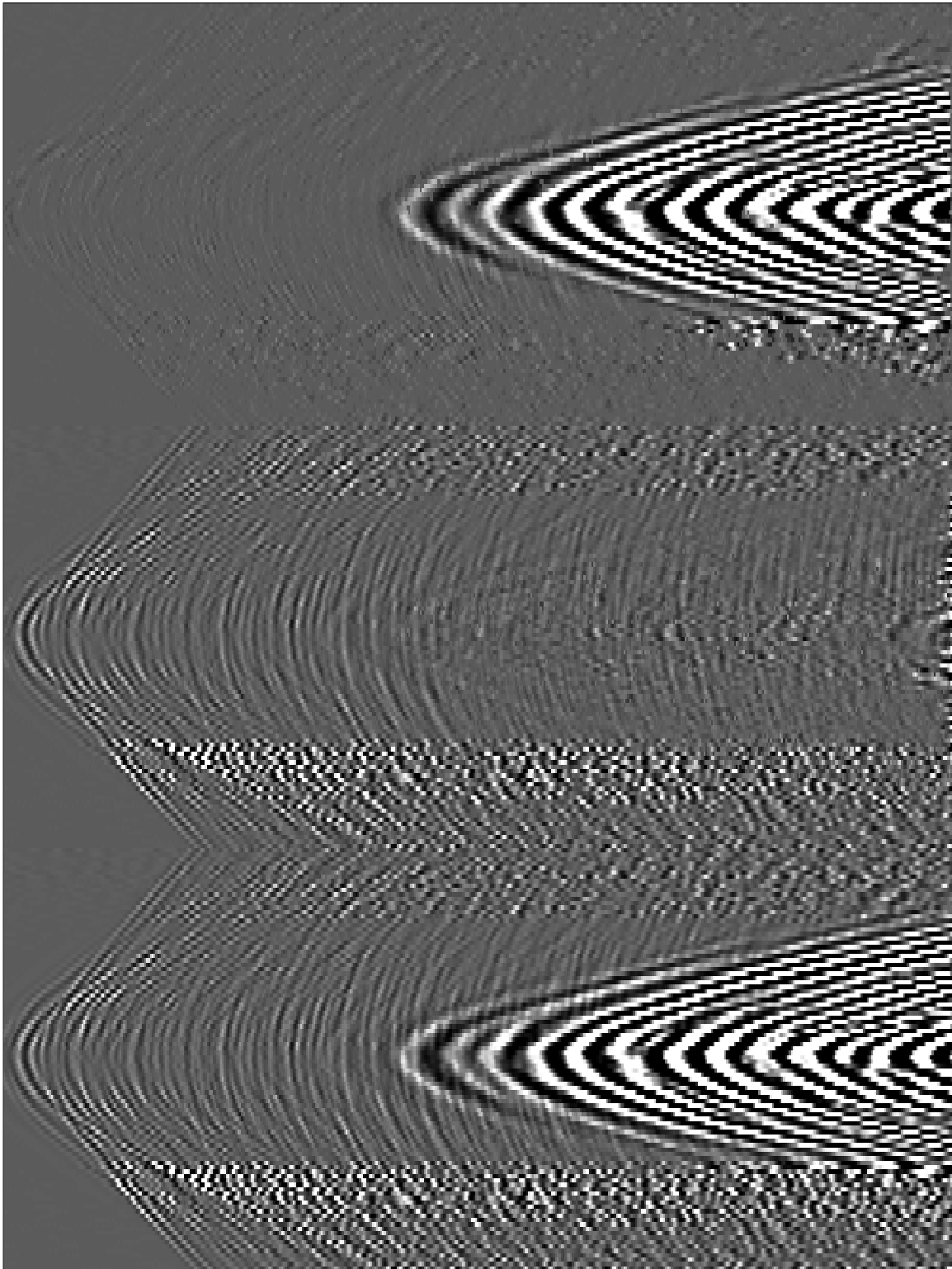


Figure 6: Receiver line #3 - predictive method results. From left to right: 1) Input data. 2) Predicted signal. 3) Difference, i.e., predicted noise. `morgan1-dune2-pred-daterr` [ER]

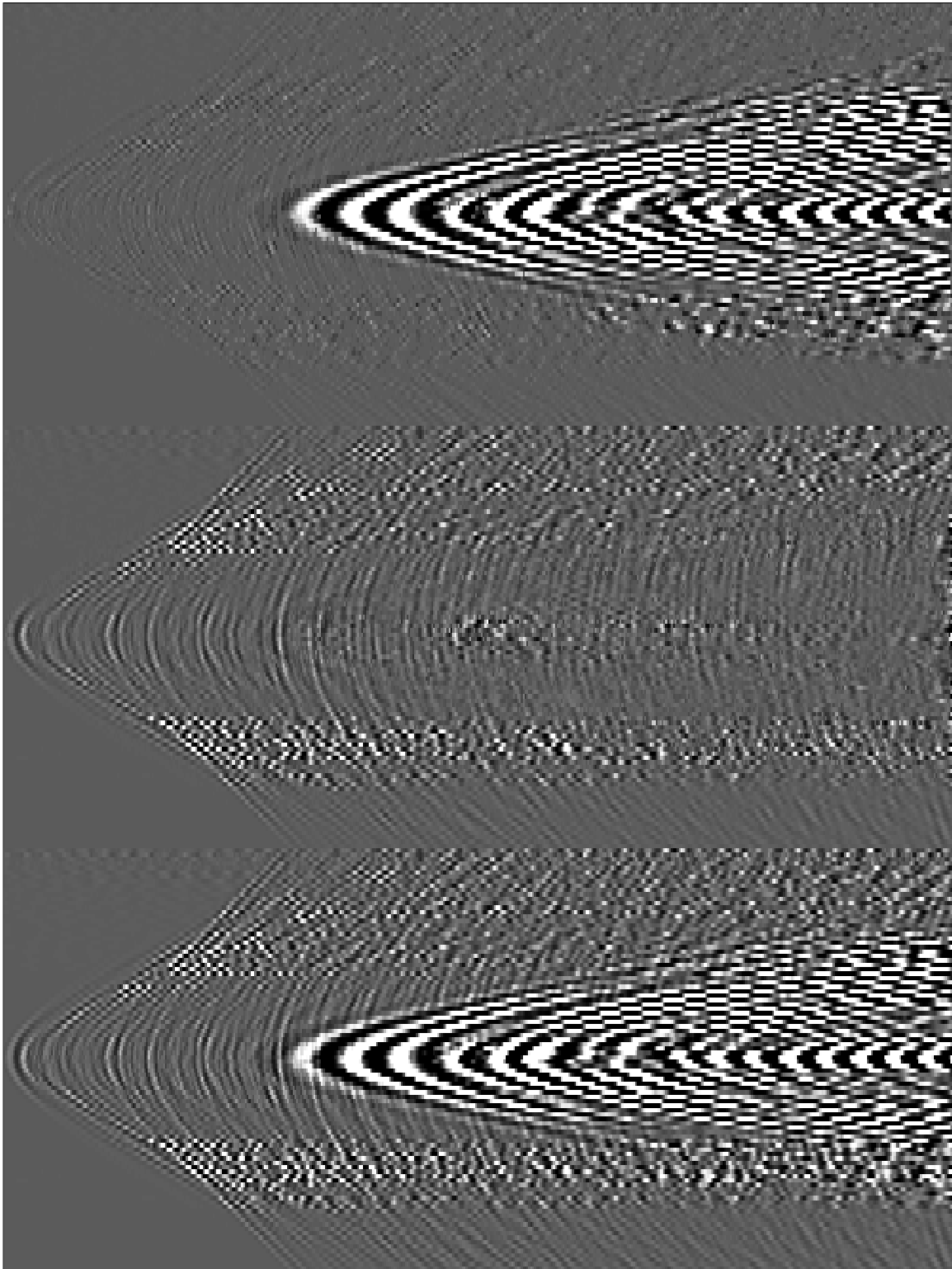


Figure 7: Receiver line #4 - predictive method results. From left to right: 1) Input data. 2) Predicted signal. 3) Difference, i.e., predicted noise. `morgan1-dune3-pred-daterr` [ER]

- Ground roll is almost always dispersive. The $f - x$ -based algorithm of Spitz (1999) is computationally more efficient than our $t - x$ domain algorithm, but it requires a time-invariant seismic wavelet. Ground roll is usually a potpourri of different wave trains, all with different dispersion rates, strongly violating this temporal stationarity assumption. The nonstationary $t - x$ domain technique has no such limitation. Nonstationary filtering *is* possible in the frequency domain, but the distinct computational advantage over time domain methods is lost.
- An effective, general method for ground removal in 3-D may have profound effects on the future of seismic acquisition. If severe ground roll necessitates the recording of extremely long offsets or the use of large receiver arrays, the ability to remove the ground roll robustly from single-sensor data will cut acquisition costs considerably. Such a ground roll removal technique could greatly assist smaller-scale survey efforts (environmental or university research) which do not boast the same resources as a large, multinational oil company.
- Parenthetically, it should be emphasized that we have presented a method to do signal/noise *separation*, not simply noise removal. The output estimated noise may contain useful information, such as shear wave velocities. Multicomponent seismology is a promising specialty which would certainly benefit from any additional constraints provided by a robust “noise” extraction.
- Considerable effort is currently expended in pursuit of the perfect noise model, particularly in multiple suppression. However the results presented here show that predictive signal/noise separation produces good results with an imperfect noise model. An open question remains: might more primitive methods of obtaining a multiple model suffice if passed to a predictive signal/noise separation algorithm?

Cons:

- As discussed in Appendix A, we are concerned that the current approach may not fully account for correlation between signal and noise.
- While the nonstationary $t - x$ PEF estimation is more robust than stationary $f - x$ methods in terms of accurately predicting all the coherent events, the cost is considerably higher. As mentioned above, the method must be optimized before it becomes an industry standard.
- Our approach is parameter-intensive. Fortunately, in practical cases, the parameter choices are similar for most data gathers in the same survey.

ACKNOWLEDGEMENTS

Thanks to Sergey Fomel for writing much of the core nonstationary PEF code used for this algorithm, and also for insightful discussions.

REFERENCES

- Abma, R., 1995, Least-squares separation of signal and noise with multidimensional filters: Ph.D. thesis, Stanford University.
- Canales, L. L., 1984, Random noise reduction: 54th Annual Internat. Mtg., Soc. Expl. Geophys., Expanded Abstracts, Session:S10.1.
- Castleman, K. R., 1996, Digital image processing: Prentice-Hall.
- Claerbout, J. F., 1976, Fundamentals of Geophysical Data Processing: Blackwell.
- Claerbout, J., 1998, Multidimensional recursive filters via a helix: *Geophysics*, **63**, no. 5, 1532–1541.
- Claerbout, J., 1999, Geophysical estimation by example: Environmental soundings image enhancement: Stanford Exploration Project, <http://sepwww.stanford.edu/sep/prof/>.
- Clapp, R. G., and Brown, M., 1999, Applying sep's latest tricks to the multiple suppression problem: *SEP-102*, 91–100.
- Clapp, R. G., Fomel, S., Crawley, S., and Claerbout, J. F., 1999, Directional smoothing of non-stationary filters: *SEP-100*, 197–209.
- Crawley, S., 1998, Shot interpolation for radon multiple suppression: *SEP-97*, 173–182.
- Crawley, S., 1999, Interpolation with smoothly nonstationary prediction-error filters: *SEP-100*, 181–196.
- Fomel, S., Clapp, R., and Claerbout, J., 1997, Missing data interpolation by recursive filter preconditioning: *SEP-95*, 15–25.
- Larner, K., Chambers, R., Yang, M., Lynn, W., and Wai, W., 1983, Coherent noise in marine seismic data: *Geophysics*, **48**, no. 7, 854–886.
- Leon-Garcia, A., 1994, Probability and random processes for electrical engineering: Addison-Wesley.
- Li, X.-Y., and Mueller, M. C., 1997, Case studies of multicomponent seismic data for fracture characterization: Austin chalk examples, *in* Marfurt, K. J., Ed., Carbonate seismology: Soc. Expl. Geophys., 337–372.
- Marfurt, K. J., Schneider, R. V., and Mueller, M. C., 1996, Pitfalls of using conventional and discrete Radon transforms on poorly sample data: *Geophysics*, **61**, no. 5, 1467–1482.
- Mueller, M. C., 1992, Using shear waves to predict lateral variability in vertical fracture intensity: *The Leading Edge*, **11**, no. 2, 29–35.
- Nemeth, T., 1996, Imaging and Filtering by Least Squares Migration: Ph.D. Thesis, University of Utah.

- Regone, C. J., 1997, Measurement and identification of 3-d coherent noise generated from irregular surface carbonates, *in* Marfurt, K. J., Ed., Carbonate seismology: Soc. Expl. Geophys., 281–305.
- Sbar, M. L., and Blankenship, C., 1998, Recoverable volume prediction from absolute acoustic impedance with errors: An example from the Nirvana, MC162 no. 3 well, Gulf of Mexico: Recoverable volume prediction from absolute acoustic impedance with errors: An example from the Nirvana, MC162 no. 3 well, Gulf of Mexico:, 68th Annual Internat. Mtg., Soc. Expl. Geophys., Expanded Abstracts, 910–913.
- Schwab, M., 1998, Enhancement of discontinuities in seismic 3-D images using a Java estimation library: Ph.D. thesis, Stanford University.
- Spitz, S., 1999, Pattern recognition, spatial predictability, and subtraction of multiple events: *The Leading Edge*, **18**, no. 1, 55–58.
- Treitel, S., Shanks, J. L., and Frasier, C. W., 1967, Some aspects of fan filtering: *Geophysics*, **32**, no. 5, 789–800.
- Verschuur, D. J., Berkhout, A. J., and Wapenaar, C. P. A., 1992, Adaptive surface-related multiple elimination: *Geophysics*, **57**, no. 9, 1166–1177.
- Wang, C.-S., 1997, 3-D ground roll suppression: 3-D ground roll suppression:, 67th Annual Internat. Mtg., Soc. Expl. Geophys., Expanded Abstracts, 1043–1046.

APPENDIX A

OPTIMAL SIGNAL EXTRACTION

The frequency domain representation of the Wiener optimal reconstruction filter for uncorrelated signal and noise is (Castleman, 1996; Leon-Garcia, 1994)

$$\mathbf{H} = \frac{\mathbf{P}_s}{\mathbf{P}_s + \mathbf{P}_n}, \quad (\text{A-1})$$

where \mathbf{P}_s and \mathbf{P}_n are the power spectra of the unknown signal and noise, respectively. Multiplication of \mathbf{H} with the data spectrum extracts the signal spectrum which is optimal in the least squares sense. Abma (1995) solved a constrained least squares problem to separate signal from spatially uncorrelated noise.

$$\begin{aligned} \mathbf{Nn} &\approx 0 \\ \epsilon \mathbf{Ss} &\approx 0 \end{aligned} \quad (\text{A-2})$$

subject to $\leftrightarrow \mathbf{d} = \mathbf{s} + \mathbf{n}$

which reduces to equation (2). Explicitly minimizing the quadratic objective function suggested by equations (A-2) or (2) leads to the following expression for the predicted signal:

$$\mathbf{s} = \left[\frac{\mathbf{N}'\mathbf{N}}{\mathbf{N}'\mathbf{N} + \epsilon^2\mathbf{S}'\mathbf{S}} \right] \mathbf{d} \quad (\text{A-3})$$

Recalling that the frequency response of the PEF is a smoothed approximation to the inverse spectrum of the data from which it was estimated

$$\begin{aligned} \mathbf{P}_s &\approx \mathcal{F} \left\{ \frac{\mathbf{1}}{\mathbf{S}'\mathbf{S}} \right\} \\ \mathbf{P}_n &\approx \mathcal{F} \left\{ \frac{\mathbf{1}}{\mathbf{N}'\mathbf{N}} \right\} \end{aligned} \quad (\text{A-4})$$

it is easy to show that the Wiener reconstruction result is equivalent to Abma's. Claerbout (1999) uses this approach, and we extended a variation of it to obtain the results obtained in this paper. When spatially coherent events cross, as they do with ground roll and primaries, they are not uncorrelated. We believe that in order to maintain a high degree of rigor in our future formulation of this problem, the correlation between signal and noise should be accounted for. A more general form of the Wiener optimal reconstructor (Castleman, 1996; Leon-Garcia, 1994) is

$$\mathbf{H} = \frac{\mathbf{P}_{ds}}{\mathbf{P}_d}, \quad (\text{A-5})$$

where \mathbf{P}_{ds} is the Fourier transform of the cross-correlation of the data and the unknown signal. Such a formulation is considerably less intuitive than equation (A-1), and we currently have no concrete ideas as to a starting point. Nemeth (1996) presents a more rigorous formulation for the separation of coherent noise and signal. As it is collected, the data is composed of overlapping signal and noise events, so the goal is to map the data to a domain where the signal and noise are uncorrelated, and thus separable without crosstalk. Nemeth's model is a composite vector, $[\mathbf{m}_s \ \mathbf{m}_n]^T$, consisting of the independent signal and noise model in the transformed (migrated) domain. His composite modeling operator, $[\mathbf{L}_s \ \mathbf{L}_n]$, is adjoint to migration, so his method accounts for the arbitrary moveout of real data - not the idealized hyperbolic moveout assumed for Radon-family transforms. The least squares inverse for Nemeth's model is

$$\begin{bmatrix} \mathbf{m}_s \\ \mathbf{m}_n \end{bmatrix} = \begin{bmatrix} \mathbf{L}_s^T \mathbf{L}_s & \mathbf{L}_s^T \mathbf{L}_n \\ \mathbf{L}_n^T \mathbf{L}_s & \mathbf{L}_n^T \mathbf{L}_n \end{bmatrix}^{-1} \begin{bmatrix} \mathbf{L}_s^T \\ \mathbf{L}_n^T \end{bmatrix} \mathbf{d} \quad (\text{A-6})$$

In the context of prediction-error filtering, the "model" would be the residual of some PEF convolved with the data, such that the signal and noise are separated in the model space. The cross terms in Nemeth's "inverse model covariance matrix," $\mathbf{L}^T \mathbf{L}^{-1}$, account for correlation between signal and noise. In practice, Nemeth's method is weakened by the need for an explicit ground roll model. However, if Nemeth's migration operators are cleverly replaced with prediction error filters, a similarly powerful formulation could probably be derived, one which is free from the need to model ground roll explicitly. In any case, Spitz' (1999) choice of signal predictor, $\mathbf{S} = \mathbf{D}\mathbf{N}^{-1}$ gives good results, and probably handles the correlation between signal and noise correctly. Though we don't show the result in this paper, we have found that when the *actual* noise model is used (synthetic data), the estimated signal is nearly perfect.

On non-stationary convolution and inverse convolution

*James Rickett*¹

ABSTRACT

Recursive inverse filtering with non-stationary filters is becoming a useful tool in a range of applications, from multi-dimensional inverse problems to wave extrapolation. I formulate causal non-stationary convolution and combination and their adjoints in such a way that it is apparent that the corresponding non-stationary recursive filters are true inverse processes. Stationary recursive inverse-filtering is stable if, and only if, the filter is minimum-phase. I show that recursive inverse-filtering with a filter-bank consisting of minimum-phase two-point filters is also unconditionally stable. However, I demonstrate that, for a more general set of minimum-phase filters, stability of non-stationary recursive inverse-filtering is not guaranteed.

INTRODUCTION

In the past, applications of non-stationary inverse filtering by recursion have been limited to problems in 1-D, such as time-varying deconvolution (Claerbout, 1998a). Theory presented no way of extending polynomial division to higher dimensions.

With the development of the helical coordinate system (Claerbout, 1998b), recursive inverse filtering is now practical in multi-dimensional space. Non-stationary, or adaptive (Widrow and Stearns, 1985), recursive filtering is now becoming an important tool for preconditioning a range of geophysical estimation (inversion) problems (Fomel et al., 1997; Clapp et al., 1997; Crawley, 1999), and enabling 3-D depth migration with a new breed of wavefield extrapolation algorithms (Fomel and Claerbout, 1997; Rickett et al., 1998; Rickett and Claerbout, 1998).

With these applications in mind, it is important to understand fully the properties of non-stationary filtering and inverse-filtering. Of particular concern is the stability of the non-stationary operators.

¹email: james@sep.stanford.edu

THEORY

Stationary convolution and inverse convolution

The convolution of a vector, $\mathbf{x} = (x_0 \ x_1 \ x_2 \ \dots \ x_{N-1})^T$, with a causal filter, $\mathbf{a} = (a_0 \ a_1 \ a_2 \ \dots \ a_{N_a-1})^T$, whose first element, $a_0 = 1$, and whose length, $N_a < N$, onto an output vector, $\mathbf{y} = (y_0 \ y_1 \ y_2 \ \dots \ y_{N-1})^T$, can be defined by the set of equations:

$$y_k = x_k + \sum_{i=1}^{\min(N_a-1, k-1)} a_i x_{k-i}. \quad (1)$$

This can be rewritten in linear operator notation, as $\mathbf{y} = \mathbf{A}\mathbf{x}$, where \mathbf{A} is a lower-triangular Toeplitz matrix representing convolution with the filter, \mathbf{a} .

The adjoint operator, \mathbf{A}' , which describes time-reversed filtering with filter \mathbf{a} , can similarly be expressed by considering the rows of the matrix-vector equation, $\mathbf{x} = \mathbf{A}'\mathbf{y}$, as follows,

$$x_k = y_k + \sum_{i=1}^{\min(N_a-1, N-1-k)} a'_i y_{k+i}. \quad (2)$$

The `helicon` Fortran90 module (Claerbout, 1998a) exactly implements the linear operator (and adjoint) pair described by equations (1) and (2).

Equation (1) explicitly prescribes internal boundary conditions near $k = 0$; however, since \mathbf{a} is causal, no particular care is needed near $k = N - 1$. On the other hand, equation (2) explicitly imposes internal boundary conditions near $k = N - 1$, and no care is needed near $k = 0$. It is possible to rewrite equations (1) and (2) in a more symmetric form; however, as written, the equations lead naturally to recursive inverses for operators, \mathbf{A} and \mathbf{A}' .

Rearranging equation (1), we obtain

$$x_k = y_k - \sum_{i=1}^{\min(N_a-1, k-1)} a_i x_{k-i}. \quad (3)$$

This provides a recursive algorithm, starting from $x_0 = y_0$ for solving the system of equations, $\mathbf{y} = \mathbf{A}\mathbf{x}$. Equation (3) describes the exact, analytic inverse of causal filtering with equation (1). In principle, given a filter, \mathbf{a} , and a filtered trace, \mathbf{y} , the above equation can recover the unfiltered trace, \mathbf{x} exactly; although in practice, with numerical errors, the division may become unstable if \mathbf{a} is not minimum phase. Similarly, if we inverse filter a trace with equation (3), we can recover the original by causal filtering with equation (1) subject to the stability of the inverse filtering process.

Equation (3) appears very similar to polynomial division. However, the output of polynomial division is an infinite series, while equation (3) is defined only in the range, $0 \leq k \leq N - 1$. As such, equation (3) describes polynomial division followed by truncation.

Equation (2) can also be rewritten as

$$y_k = x_k - \sum_{i=1}^{\min(N_a-1, N-1-k)} a'_i y_{k+i}, \quad (4)$$

which provides an exact recursive inverse to adjoint operator, \mathbf{A}' , that can be computed starting from $y_{N-1} = x_{N-1}$, and decrementing k .

Non-stationary convolution and combination

There are several possible approaches to generalizing convolution described by equation (1) to deal with non-stationarity. The simplest approach (Yilmaz, 1987) is to apply multiple stationary filters and interpolate the results. This approach, however, gives incorrect spectral response in the interpolated areas (Pann and Shin, 1976).

Following Claerbout (1998a) and Margrave (1998), I extend the concept of a filter to that of a filter-bank, which is a set of N filters: one filter for every point in the input/output space. I identify \mathbf{a}_j with the filter corresponding to the j^{th} location in the input/output vector, and the coefficient, $a_{i,j}$, with the i^{th} coefficient of the filter, \mathbf{a}_j .

Margrave (1998) describes two closely related alternatives which both reduce to normal convolution in the limit of stationarity. The first approach is to place the filters in the columns of the matrix, \mathbf{A} . This associates a single filter with a single point in the output space, and defines *non-stationary convolution*:

$$y_k = x_k + \sum_{i=1}^{\min(N_a-1, k-1)} a_{i, (k-i)} x_{k-i}. \quad (5)$$

In contrast, the second approach is to place individual filters in the rows of the matrix, \mathbf{A} , associating a single filter with a single point in the input space. This defines what Margrave (1998) refers to as *non-stationary combination*:

$$y_k = x_k + \sum_{i=1}^{\min(N_a-1, k-1)} a_{i, k} x_{k-i}. \quad (6)$$

The advantage of non-stationary convolution over non-stationary combination is that the response of equation (5) to an impulse at the j^{th} element of \mathbf{x} , is \mathbf{a}_j . A more general output is then a scaled superposition of filter-bank filters, which fits with Green's function theory for linear, constant coefficient, partial differential equations. Again, in contrast, the response of equation (6) to an impulse at the j^{th} element of \mathbf{x} , is the j^{th} column of non-stationary combination matrix, which bears no direct relationship to the filter, \mathbf{a}_j , or any other individual filter for that matter.

As an illustration, consider the differences between matrices, \mathbf{F}_{conv} and \mathbf{F}_{comb} below, which represent, respectively, non-stationary convolution and combination with a causal three-point

($N_f = 3$) filter-bank, \mathbf{f} , to vectors of length, $N = 5$. The two are equivalent in the stationary limit; however, while the columns of \mathbf{F}_{conv} contain filters, \mathbf{f}_j , the columns of \mathbf{F}_{comb} do not.

$$\mathbf{F}_{\text{conv}} = \begin{bmatrix} 1 & 0 & 0 & 0 & 0 & 0 \\ f_{10} & 1 & 0 & 0 & 0 & 0 \\ f_{20} & f_{11} & 1 & 0 & 0 & 0 \\ 0 & f_{21} & f_{12} & 1 & 0 & 0 \\ 0 & 0 & f_{22} & f_{13} & 1 & 0 \\ 0 & 0 & 0 & f_{23} & f_{14} & 1 \end{bmatrix}, \quad \mathbf{F}_{\text{comb}} = \begin{bmatrix} 1 & 0 & 0 & 0 & 0 & 0 \\ f_{11} & 1 & 0 & 0 & 0 & 0 \\ f_{22} & f_{12} & 1 & 0 & 0 & 0 \\ 0 & f_{23} & f_{13} & 1 & 0 & 0 \\ 0 & 0 & f_{24} & f_{14} & 1 & 0 \\ 0 & 0 & 0 & f_{25} & f_{15} & 1 \end{bmatrix}$$

It is also clear that while \mathbf{F}_{conv} and \mathbf{F}_{comb} are related, they are not simply adjoint to each other.

Adjoint non-stationary convolution and combination

The adjoint of non-stationary convolution can be written as

$$x_k = y_k + \sum_{i=1}^{\min(N_a-1, N-k-1)} a'_{i,k} y_{k+i}, \quad (7)$$

and the adjoint of non-stationary combination can be written as

$$x_k = y_k + \sum_{i=1}^{\min(N_a-1, N-k-1)} a'_{i,(k+i)} y_{k+i}. \quad (8)$$

For many applications, the adjoint of a linear operator is the same operator applied in a (conjugate) time-reversed sense. For example, causal and anti-causal filtering, integration, differentiation, upward and downward continuation, finite-difference modeling and reverse-time migration etc.

For non-stationary filtering, it is important to realize this is *not* the case: the adjoint of non-stationary convolution is time-reversed non-stationary combination, and vice-versa. Therefore, the output of adjoint combination is a superposition of scaled time-reversed filters, \mathbf{a}'_j . So for anti-causal non-stationary filtering, it may be advantageous to apply adjoint combination, as opposed to adjoint filtering.

Inverse non-stationary convolution and combination

As with the stationary convolution described above, formulae for non-stationary recursive inverse convolution and combination follow simply by rearranging the equations in (5) and (6). Similarly, their adjoints can be obtained by rearranging the equations in (7) and (8). The recursive formulae describing these inverse processes are given in Table 1.

Inverse NS convolution:	$x_k = y_k - \sum_{i=1}^{\min(N_a-1, k-1)} a_{i, (k-i)} x_{k-i}$	(9)
Inverse NS combination:	$x_k = y_k - \sum_{i=1}^{\min(N_a-1, k-1)} a_{i, k} x_{k-i}$	(10)
Adjoint inverse NS convolution:	$y_k = x_k - \sum_{i=1}^{\min(N_a-1, N-1-k)} a'_{i, k} y_{k+i}$	(11)
Adjoint inverse NS combination:	$y_k = x_k - \sum_{i=1}^{\min(N_a-1, N-1-k)} a'_{i, (k+i)} y_{k+i}$	(12)

Table 1: Recursive formulae for non-stationary (NS) inverse operators.

As with the stationary inverse convolution described above, it is apparent that subject to numerical errors, non-stationary inverse filtering with these equations in Table 1 is the exact, analytic inverse of non-stationary filtering with the corresponding forward operator described in equations (5) through (8): they are true inverse processes. If operator \mathbf{A} represents filtering with a non-stationary causal-filter, and \mathbf{B} represents recursive inverse filtering with the same filter then

$$\mathbf{AB} = \mathbf{BA} = \mathbf{I} \quad \text{and} \quad \mathbf{A}'\mathbf{B}' = \mathbf{B}'\mathbf{A}' = \mathbf{I}.$$

The `nhelicon` module (Claerbout, 1998a) implements the non-stationary combination operator/adjoint pair, described by equations (6) and (8), while `npolydiv` implements the corresponding inverse operators, described by equations (10) and (12).

The stability of non-stationary inverse filtering

A filter is stable if any bounded input produces a bounded output (Robinson and Treitel, 1980). Therefore, to prove that inverse filtering with a class of filters is stable, we have to demonstrate that all possible members of the class have bounded outputs for all bounded inputs. On the other hand to show that a class of filters is not stable, we just need to find a single example where a bounded input produces an unbounded output.

The stability of stationary recursive inverse filtering depends on the phase of the causal filter: if (and only if) the filter is minimum phase, then its inverse filter is stable. This raises the question: is non-stationary inverse filtering stable if all filters contained in the filter-bank are minimum-phase?

For the case of inverse filtering with a two-point filter ($N_a = 2$), equation (9) reduces to $x_0 = y_0$, and the following formula for $k > 0$:

$$x_k = y_k - a_{1, (k-1)} x_{k-1}. \quad (13)$$

Recursive substitution then produces an explicit formula for elements of \mathbf{x} in terms of elements of \mathbf{y} :

$$x_N = y_N - a_{1, (N-1)} y_{N-1} + a_{1, (N-1)} a_{1, (N-2)} y_{N-2} \dots + (-1)^N \left(\prod_{i=0}^{N-1} a_{1, i} \right) y_0. \quad (14)$$

For stability analysis, we need to understand how the above series behaves as $N \rightarrow \infty$. If the filters, \mathbf{a}_i , are all minimum phase, and there exists a real number, κ , such that $|a_{1,i}| \leq \kappa < 1$ for all i , then

$$\prod_{i=0}^{N-1} a_{1,i} \leq \kappa^N. \quad (15)$$

The above series will therefore converge, and stability is guaranteed. Furthermore, this proof can easily be extended to gapped two-point minimum-phase non-stationary filters, which correspond to matrices with ones on the main diagonal, and variable coefficients whose magnitude is less than one on a secondary diagonal.

There is a larger class ($N_a \geq 3$) of stable non-stationary recursive filters that can be obtained by repeatedly multiplying stable bidiagonal matrices. However, given a general non-stationary filter matrix, there is no straightforward way to determine whether it is a member of this stable class. In fact, it is relatively easy to find an example filter-bank consisting of minimum-phase individual filters whose recursive output is unbounded for finite input. Consider the filter-bank, \mathbf{f} , consisting of minimum-phase filters,

$$\begin{aligned} \mathbf{f}_{0,2,4\dots} &= (1 \ -0.9 \ 0), \text{ and} \\ \mathbf{f}_{1,3,5\dots} &= (1 \ 0.8) * (1 \ 0.8) = (1 \ 1.6 \ 0.64). \end{aligned} \quad (16)$$

Figure 1 shows the impulse response of non-stationary inverse filtering with this filter: clearly an unstable process.

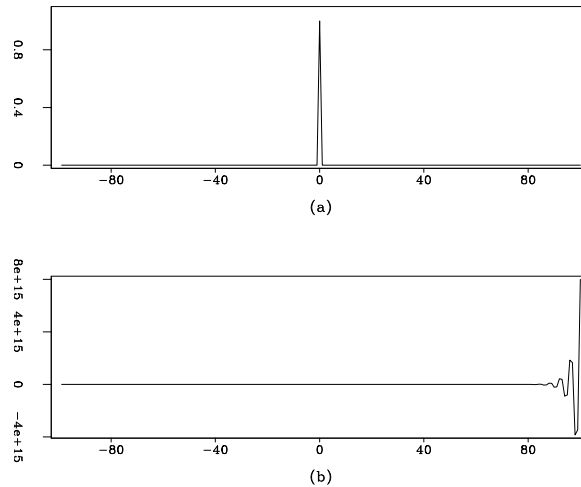


Figure 1: Impulsive input (a) and response (b) to non-stationary filtering with filter-bank defined in equation (16). james1-one [ER]

The instability stems from the fact that as N increases, so does the number of boundaries between different filters. Such rapid non-stationary filter variations, as in the example above, are pathological in the context of seismic applications, where filters are typically quasi-stationary. For these applications instability is rarely observed; however, we must be aware that we are not dealing with an unconditionally stable operator, and instability may rear its ugly head from time-to-time.

CONCLUSIONS

There are three important points to draw from this paper. Firstly, I have formulated causal non-stationary convolution and combination and their adjoints in such a way that it is apparent that the corresponding non-stationary recursive filters are true inverse processes. If you think of causal non-stationary filtering as a lower triangular matrix, then recursive inverse filtering applies the inverse matrix.

The second important point is that recursive inverse-filtering with a filter-bank consisting of minimum-phase two-point filters is *unconditionally stable*, and as such it is totally safe to apply in any circumstance.

However, the final point is that for a more general set of minimum-phase filters, stability of non-stationary recursive inverse-filtering is *not* guaranteed: use with care.

REFERENCES

- Claerbout, J. F., 1998a, Geophysical estimation by example: available on the World-Wide-Web at <http://sepwww.stanford.edu/prof/gee/>.
- Claerbout, J. F., 1998b, Multidimensional recursive filters via a helix: *Geophysics*, **63**, 1532–1541.
- Clapp, R. G., Fomel, S., and Claerbout, J., 1997, Solution steering with space-variant filters: *SEP-95*, 27–42.
- Crawley, S., 1999, Interpolation with smoothly nonstationary prediction-error filters: *SEP-100*, 181–196.
- Fomel, S., and Claerbout, J. F., 1997, Exploring three-dimensional implicit wavefield extrapolation with the helix transform: *SEP-95*, 43–60.
- Fomel, S., Clapp, R., and Claerbout, J., 1997, Missing data interpolation by recursive filter preconditioning: *SEP-95*, 15–25.
- Margrave, G. F., 1998, Theory of nonstationary linear filtering in the Fourier domain with application to time-variant filtering: *Geophysics*, **63**, no. 1, 244–259.
- Pann, K., and Shin, Y., 1976, A class of convolutional time-varying filters: *Geophysics*, **41**, no. 1, 28–43.
- Rickett, J., and Claerbout, J., 1998, Helical factorization of the Helmholtz equation: *SEP-97*, 353–362.
- Rickett, J., Claerbout, J., and Fomel, S., 1998, Implicit 3-D depth migration by wavefield extrapolation with helical boundary conditions: *SEP-97*, 1–12.
- Robinson, E. A., and Treitel, S., 1980, *Geophysical signal analysis*: Prentice-Hall.

Widrow, B., and Stearns, S. D., 1985, Adaptive signal processing: Prentice Hall.

Yilmaz, O., 1987, Seismic data processing: Soc. Expl. Geophys.

Short Note

Revisiting the half-derivative filter

Marie Prucha¹

INTRODUCTION

A primary goal in designing an iterative optimization method for inversion is to minimize the number of iterations necessary for convergence. Often, we tackle this by applying an appropriate filter.

When conjugate gradient (CG) methods are applied to a problem like velocity transform in 2-D, the principal artifact faced is the half-integration waveform (Claerbout, 1993, 1995). Logically, the best filter to suppress a half-integration waveform is the half-derivative filter. In practice, filters like the half-derivative filter have been reported as causing CG residuals to diverge (Lumley, 1994). However, when recently revisiting this approach, I encountered no similar obstacle to convergence.

For this work, I applied the half-derivative filter to a CG inversion used for velocity transformations for both a synthetic and a real case. I experimented with the order of the weighting functions in an attempt to improve the rate of convergence. The results in all of the cases showed that the half-derivative filter did not cause divergence in any of the cases and improved the convergence rate beyond that of CG inversion without the half-derivative filter.

THEORY

The origin of the half-derivative filter lies in the simple operation of causal integration (Claerbout, 1993). With each pass of causal integration, we are actually convolving the signal in the time domain with a scaled ramp function which is equivalent to multiplication in the frequency domain with the inverse of frequency. This can be expressed as:

$$t^{n-1} \text{step}(t) = FT \left(\frac{1}{(-i\omega)^n} \right) \quad (1)$$

¹email: marie @ sep.Stanford.edu

In two dimensions, the principal artifact that will affect our velocity transform occurs at $n = \frac{1}{2}$ (Claerbout, 1995). This leads to

$$\frac{1}{\sqrt{t}} \text{step}(t) = FT \left(\frac{1}{\sqrt{-i\omega}} \right) . \quad (2)$$

To compensate, we need to apply $FT(\sqrt{-i\omega})$, which, recalling that:

$$\frac{d}{dt} = FT(-i\omega) , \quad (3)$$

we can obtain by the formula

$$\frac{d}{dt} \frac{1}{\sqrt{t}} \text{step}(t) = FT(\sqrt{-i\omega}) . \quad (4)$$

So, to repair the principal artifact of 2-D hyperbola summation, we need to apply this filter – the half-derivative filter.

PRACTICE

The half-derivative filter belongs to a family of filters known as rho filters. Past attempts (Lumley, 1994) to apply these filters to a CG inversion have exhibited divergence after the first few iterations, despite the fact that CG iteration should never diverge when the operator is linear and the gradient is non-zero. Nevertheless, I attempted CG inversion of the system:

$$d = \mathbf{H} \mathbf{V} m , \quad (5)$$

where d = data, H = half-derivative filter, V = velocity transform operator, and m = model. This was applied to the CMP gathers seen in Figures 2 (synthetic) and 1 (real). These two figures also both show the residuals converging, the velocity scans resulting from the CG iterations, and the forward-modeled data. In an attempt to improve the rate of convergence, I re-ordered the equation as:

$$d = \mathbf{V} \mathbf{H} m \quad (6)$$

This also allowed convergence. Figures 3 and 4 show the convergence rate of the second system (6) to be better than that of the first system (5) and both of these are superior to the convergence speed for the trial with no half-derivative filter. It is interesting to note that the residuals decrease more and the half-derivative filter has a greater effect for the real CMP gather than for the synthetic CMP gather. This is most likely a result of dispersion from the finite-difference method used to create the synthetic data.

CONSIDERATION OF PAST EXPERIMENTS

Lumley (1994) observed that rho filters caused divergence during CG iteration. Although he did not use the actual half-derivative filter, his results indicated that the half-derivative filter

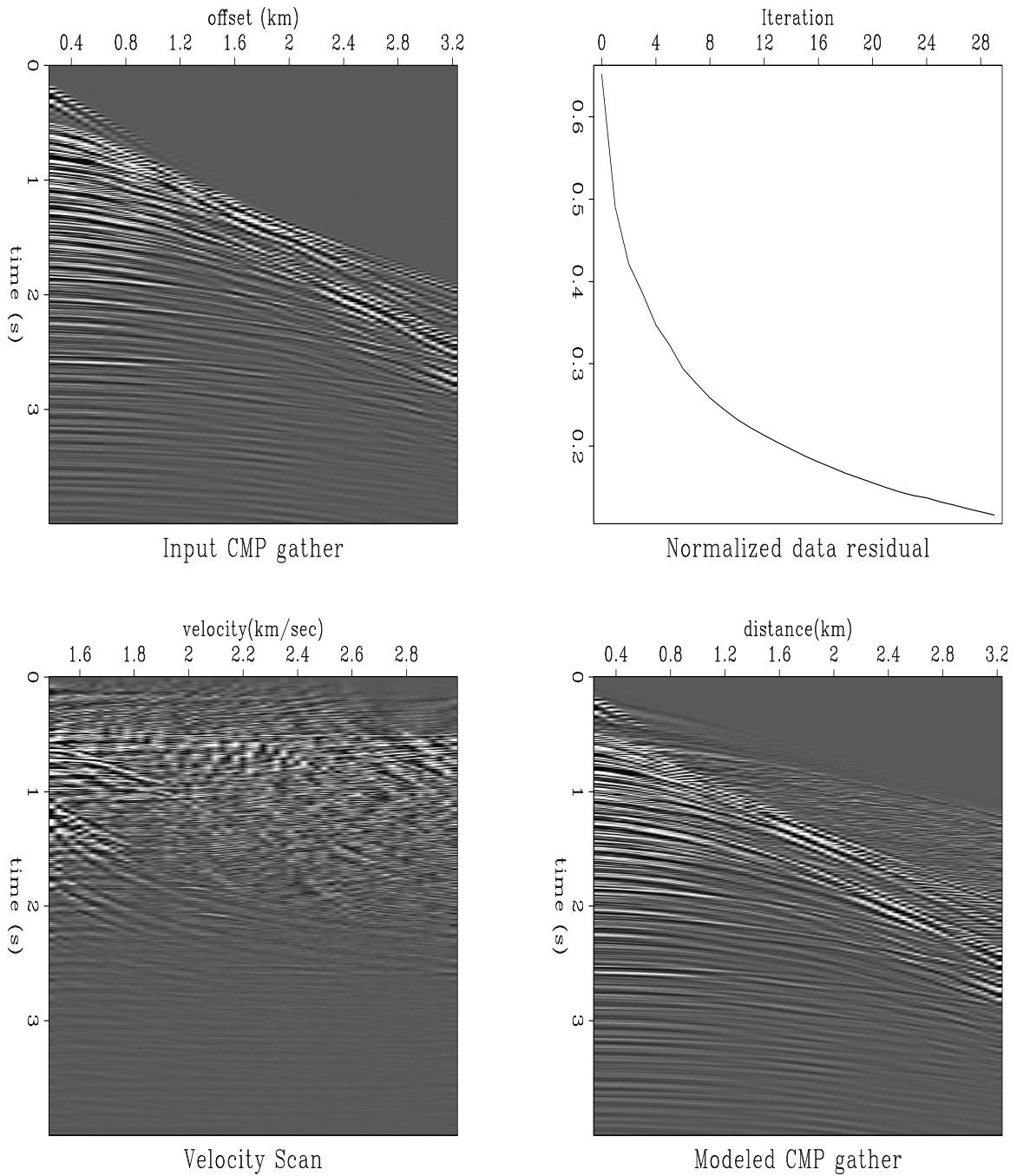


Figure 1: Top left: Real CMP gather. Top right: Residual power versus iteration. Bottom left: Representation of CMP gather in velocity space. Bottom right: Inversion of bottom left.

marie1-real.vel [ER]

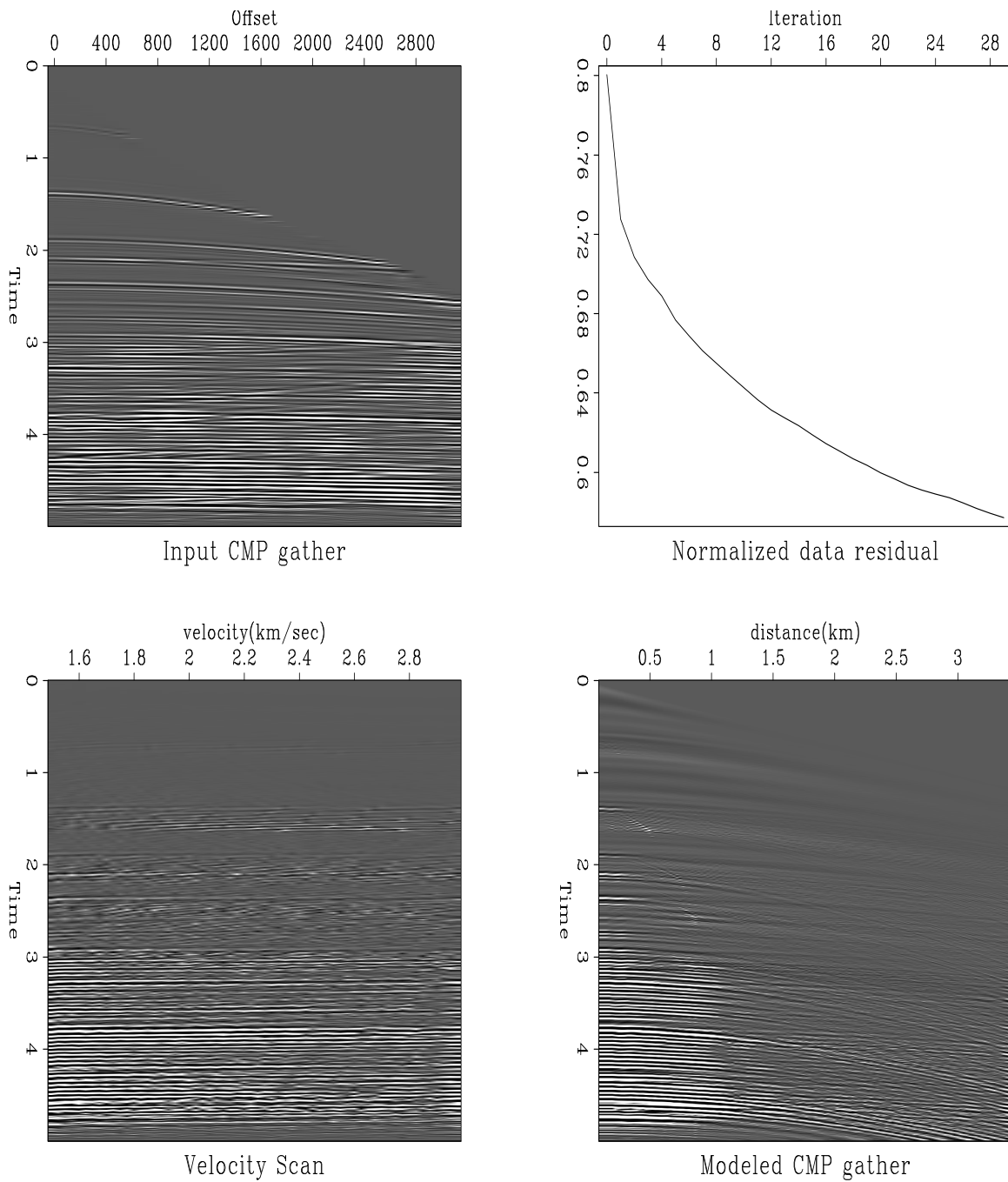


Figure 2: Top left: Synthetic CMP gather. Top Right: Residual power versus iteration. Bottom left: Representation of CMP gather in velocity space. Bottom right: Inversion of bottom left.

marie1-elf.vel [ER]

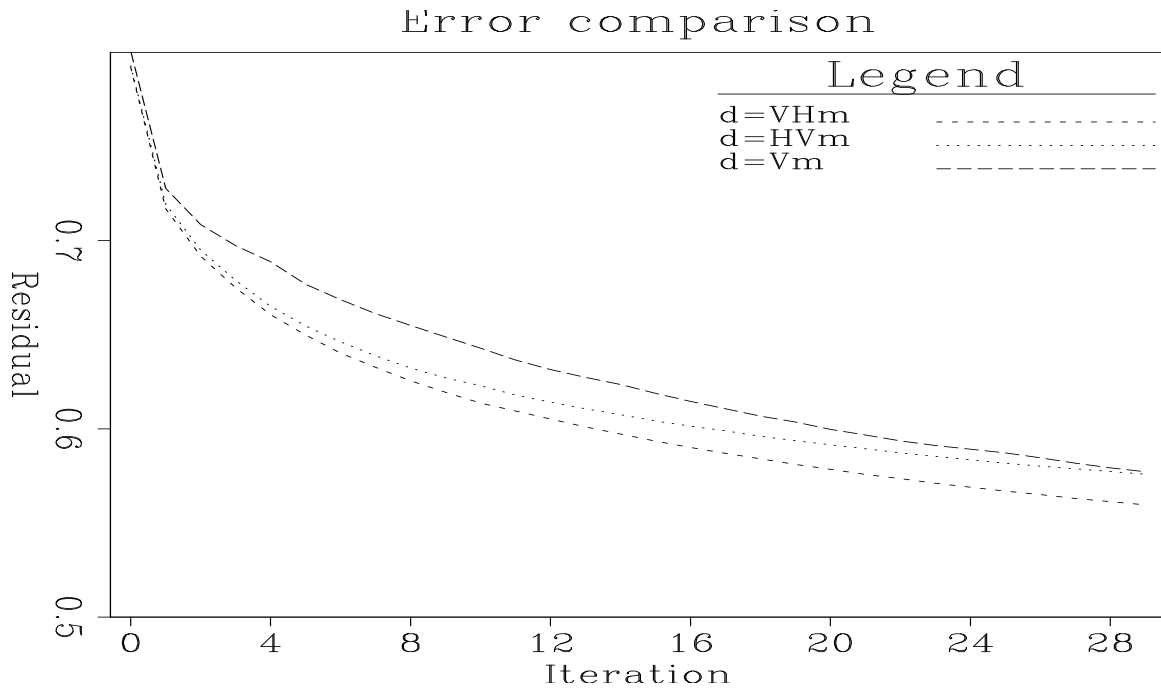


Figure 3: Comparison of rates of convergence for the synthetic data. While there is relatively little difference in the magnitudes of the final residuals, the two best rates are obtained with the half-derivative filter. `marie1-elf.residual-compare` [ER]

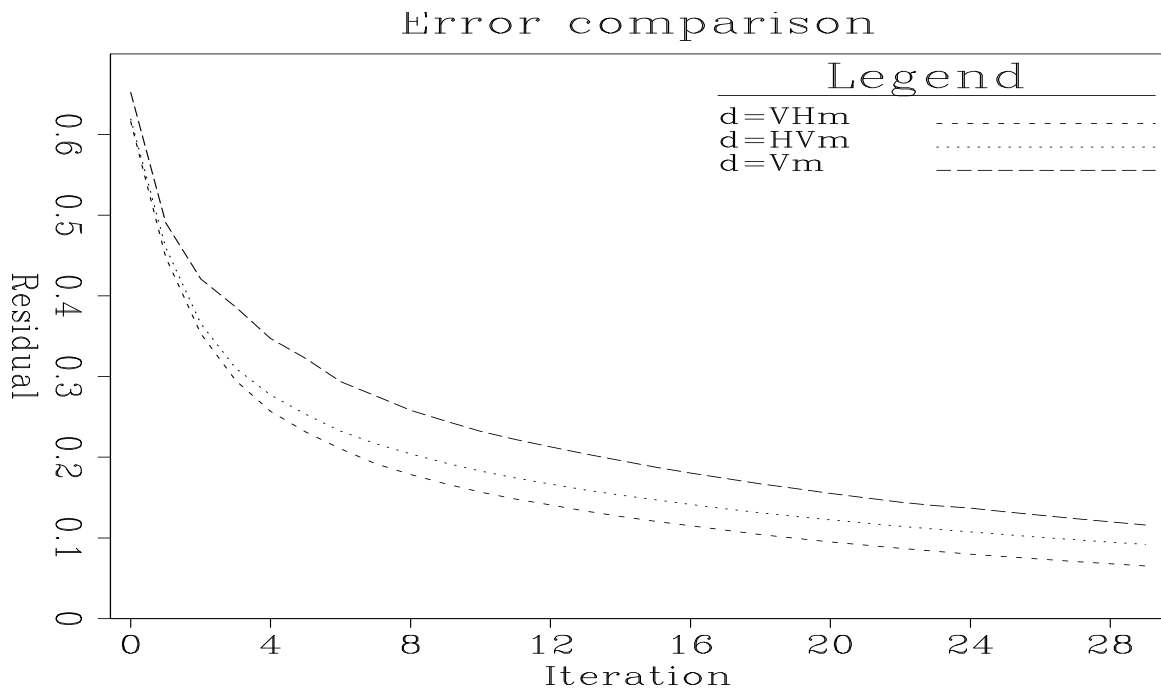


Figure 4: Comparison of rates of convergence for the real data. The best rate is obtained for the system $d = VHm$. `marie1-real.residual-compare` [ER]

should cause even more divergence than the rho filters he did use. While not yet confirmed, these results may have been due to the CG algorithm he used. Lumley used the CG method described by Hestenes and Steifel (1952) which can be unstable (Fomel, 1996). The results in this paper were obtained with the CG method described by Claerbout (1986).

CONCLUSION

I have shown that the half-derivative filter may be used effectively in CG velocity-transform inversion. The rate of convergence for the system $d = V H m$ was slightly faster than that for $d = H V m$ but both of these systems had better convergence rates than a system that did not use the half-derivative filter at all.

ACKNOWLEDGEMENTS

I would like to thank Sergey Fomel for getting me started on this project. It began as a class lab and ended up here through a long, strange journey.

REFERENCES

- Claerbout, J. F., 1986, Conjugate gradient tutorial: SEP-48, 351–358.
- Claerbout, J. F., 1993, Huygen's waveforms and half-order derivatives: SEP-77, 403–408.
- Claerbout, J. F., 1995, Basic Earth Imaging: Stanford Exploration Project.
- Fomel, S., 1996, Least-square inversion with inexact adjoints. Method of conjugate directions: A tutorial: SEP-92, 253–265.
- Hestenes, M. R., and Steifel, E., 1952, Methods of conjugate gradients for solving linear systems: J. Res. Nat. Bur. Stand., 49, 409–436.
- Lumley, D. E., 1994, Estimating a pseudounitary operator for velocity-stack inversion: SEP-82, 63–78.

Estimating rock porosity and fluid saturation using only seismic velocities

James G. Berryman,¹ Patricia A. Berge,² and Brian P. Bonner³

ABSTRACT

Evaluation of the fluid content in deep earth reservoirs or of fluid contaminants in shallow earth environments has required the use of geophysical imaging methods such as seismic reflection prospecting. The processing of these seismic data has involved meticulous care in determining the changes in reflected seismic amplitude as the point of observation for the received signals at the earth's surface is moved away from the seismic source (Ostrander, 1984). The now commonly used method called AVO (for Amplitude Versus Offset) is based on theories of fluid-saturated and partially saturated rocks that have been available since the 1950's. Here we present a new synthesis of the same physical concepts that uses some of the same data as AVO (compressional wave velocities) together with some different data (shear wave velocities) in a scheme that is much simpler to understand and apply, yet yields the desired information about porosity and fluid saturation. The method is designed especially for near surface applications and for use with crosswell and VSP data, but it can also be applied to reflection seismic data assuming that reliable interval velocities are available. Since the new method does not require hard-to-obtain wave amplitude information, it can be used for a wider range of seismic source-receiver configurations, including crosswell seismic transmission tomography (well-to-well), vertical seismic profiling (well-to-surface), as well as seismic reflection profiling (surface-to-surface), since reflection data can be used but are not a necessity.

INTRODUCTION

Resolution of various practical and scientific issues in the earth sciences depends on knowledge of fluid properties underground. In environmental cleanup applications, the contaminant to be removed from the earth is often a liquid such as gasoline or oil, or ground water contaminated with traces of harmful chemicals. In commercial oil and gas exploration, the fluids of interest are hydrocarbons in liquid or gaseous form. In analysis of the earth structure, partially melted rock is key to determining temperature and local changes of structure in the earth's

¹email: berryman@sep.stanford.edu

²Lawrence Livermore National Lab, P. O. Box 808, L-201, Livermore, CA 94550
email: berge1@llnl.gov

³Lawrence Livermore National Lab, P. O. Box 808, L-201, Livermore, CA 94550
email: bonner1@llnl.gov

mantle. In all cases the tool commonly used to analyze the fluid content is measurements of seismic (compressional and shear) wave velocities in the earth. Depending on the application, the sources of these waves may be naturally occurring such as earthquakes, or man-made such as reflection seismic surveys at the surface of the earth, vertical seismic profiling, or still more direct measurements using logging tools in either shallow or deep boreholes.

Underground fluids occupy voids between and among the solid earth grains. When liquid or gas completely fills interconnecting voids, a well-known result due to Gassmann (1951) predicts how the composite elastic constants that determine seismic velocities should depend on the fluid and drained rock or soil elastic constants and densities [also see tutorial by Berryman (1999)]. The formulas due to Gassmann are low frequency (seismic) results and both laboratory and well-log measurements of wave velocities have been observed to deviate markedly from Gassmann's predictions at higher (sonic and ultrasonic) frequencies. This is especially so for partial saturation conditions (*i.e.*, when the fluid in each pore is a mixture of gas and liquid). In some cases these deviations can be attributed (Berryman *et al.*, 1988; Endres and Knight, 1989; Mavko and Nolen-Hoeksema, 1994; Dvorkin and Nur, 1998) to "patchy saturation," meaning that some void regions are fully saturated with liquid and others are filled with gas. When the concept of patchy saturation is applicable, Gassmann's formulas apply locally (but not globally) and must be averaged over the volume to obtain the overall seismic velocity of the system. In other cases, neither Gassmann's formulas nor the "patchy saturation" model seem to apply to seismic data. In these cases a variety of possible reasons for the observed velocity discrepancies have been put forward, including viscoelastic effects (velocity decrement due to frequency-dependent attenuation), fluid-enhanced softening of intragranular cementing materials, chemical changes in wet clays that alter mechanical properties, etc.

The objective of the present study therefore has been to find a method of using seismic data to estimate porosity and saturation, regardless of whether the rock or soil fits the Gassmann, the patchy saturation, or some other model. Seismic data typically provide two measured parameters, v_p and v_s (compressional and shear wave velocities, respectively). Simple algebraic expressions relate v_p and v_s to the Lamé parameters λ and μ of elasticity theory, and the overall density ρ . These relationships are well-known (Ewing *et al.*, 1957; Aki and Richards, 1980), but the parameter λ is seldom used to analyze seismic data. Our first new way of displaying seismic data is to plot data points in the $(\rho/\mu, \lambda/\mu)$ -plane — instead of (for example) the (v_p, v_s) -plane. (Note that $\rho/\mu = 1/v_s^2$.) The advantage of this plot is that, when the liquid and gas are either mixed homogeneously throughout (Gassmann's assumption) or are fully segregated throughout (patchy saturation), most of the data will fall along one or the other of two straight lines. Significant deviations from these two expected behaviors then provide a clear indication that the data violate some of the assumptions in Gassmann's simple model, and furthermore provide clues to help determine which assumptions are being violated. Our second innovation in displaying seismic data is to plot the data points in the $(\rho/\lambda, \mu/\lambda)$ -plane. This second approach involves the use of an easily understood mathematical trick that leads naturally to universal and easily interpreted behavior; virtually all laboratory data on partial saturation for similar rocks that we have analyzed plot with minimal scatter along straight lines in this plane. The length and slope of these lines have quantitative predictive capabilities for measurements of both partial saturation and porosity. We have used sonic and ultrasonic

laboratory data in the present study, but the results provide very strong indications that equally useful relationships among seismic parameters, porosity, and saturation will be obtained from seismic data collected at lower frequencies in the field.

BASICS OF ELASTIC WAVE PROPAGATION

For isotropic elastic materials there are two bulk elastic wave speeds (Ewing *et al.*, 1957; Aki and Richards, 1980), compressional $v_p = \sqrt{(\lambda + 2\mu)/\rho}$ and shear $v_s = \sqrt{\mu/\rho}$. Here the Lamé parameters λ and μ are the constants that appear in Hooke's law relating stress to strain in an isotropic material. The constant μ gives the dependence of shear stress on shear strain in the same direction. The constant λ gives the dependence of compressional or tensional stress on extensional or dilatational strains in orthogonal directions. For a porous system with porosity ϕ (void volume fraction) in the range $0 < \phi < 1$, the overall density of the rock or sediment is just the volume weighted density given by $\rho = (1 - \phi)\rho_s + \phi[S\rho_l + (1 - S)\rho_g]$, where ρ_s , ρ_l , ρ_g are the densities of the constituent solid, liquid and gas, respectively, and S is the liquid saturation, *i.e.* the fraction of liquid-filled void space in the range $0 \leq S \leq 1$ (Domenico, 1974). When liquid and gas are distributed uniformly in all pores and cracks, Gassmann's equations say that, for quasistatic isotropic elasticity and low frequency wave propagation, the shear modulus μ will be mechanically independent of the properties of any fluids present in the pores, while the overall bulk modulus $K \equiv \lambda + \frac{2}{3}\mu$ of the rock or sediment including the fluid depends in a known way on porosity and elastic properties of the fluid and dry rock or sediment (Gassmann, 1951). Thus, in the Gassmann model, the Lamé parameter λ is elastically *dependent* on fluid properties, while μ is not. The density ρ also depends on saturation. At low liquid saturations, the fluid bulk modulus is dominated by the gas, and therefore the effect of the liquid on λ is negligible until full saturation is approached. This means that both seismic velocities v_p and v_s will decrease with increasing fluid saturation (Domenico, 1974; Wyllie *et al.*, 1956; Wyllie *et al.*, 1958) due to the "density effect," *i.e.*, the only quantity changing is the density which increases in the denominators of both v_p^2 and v_s^2 . As full saturation is approached, the shear velocity continues its downward trend, while the compressional velocity suddenly (over a very narrow range of change of saturation) shoots up to its full saturation value. An example (Murphy, 1982; 1984) of this behavior is shown in Figure 1a. This is the expected (ideal Gassmann) behavior of porous rocks at low frequencies (sonic and below).

PREDICTIONS OF THE THEORY

Gassmann's equation (Gassmann, 1951) for fluid substitution states that

$$K = K_{dr} + \frac{\alpha^2}{(\alpha - \phi)/K_m + \phi/K_f}, \quad (1)$$

where K_m is the bulk modulus of the solid mineral, K_{dr} is the bulk modulus of the drained porous frame, $\alpha = 1 - K_{dr}/K_m$ is the Biot-Willis (1957) parameter, ϕ is the porosity, and K

is the effective bulk modulus of the undrained fluid-mixture-saturated porous medium, where, for partial saturation conditions with homogeneous mixing of liquid and gas,

$$1/K_f = S_l/K_l + (1 - S_l)/K_g. \quad (2)$$

The saturation level of liquid is S_l , K_l is the bulk modulus of the liquid, and K_g is the bulk modulus of the gas. When S_l is small, (2) shows that $K_f \simeq K_g$, since $K_g \ll K_l$. As $S_l \rightarrow 1$, K_f remains close to K_g until S_l closely approaches unity. Then, K_f changes rapidly (over a small range of saturations) from K_g to K_l .

The bulk modulus K_f contains the only dependence on S_l in (1). Thus, for porous materials satisfying Gassmann's homogeneous fluid conditions and for low enough frequencies, the theory predicts that, if we use seismic velocity data in a two-dimensional plot with one axis being the saturation S_l and the other being the ratio $\lambda/\mu = (v_p/v_s)^2 - 2$, then the results will lie along a straight (horizontal) line until the saturation reaches $S_l \simeq 1$ (around 95% or higher), where the curve formed by the data will quickly rise to the value determined by the velocities at full liquid saturation.

On the other hand, if the porous medium contains gas and liquid mixed in a heterogeneous manner, so that patches of the medium hold only gas while other patches hold only liquid, then the theory predicts that, depending to some extent on the spatial distribution of the patches, the results will deviate from Gassmann's results. If we consider the most extreme cases of spatial distribution possible, which are laminated regions of alternating liquid saturation and gas saturation, then the effective bulk modulus at low frequencies will be determined by an average of the two extreme values of (1): $K(S_l = 0) = K_{dr}$ and $K(S_l = 1)$. Using saturation as the weighting factor, the harmonic mean and the mean are the well-known results for these two extremes of behavior. Of these two, the one that differs most from (1) is the mean. But, on our plot, the results for the mean will again lie along a straight line, So this time the line goes directly from the dry (or unsaturated $S_l = 0$) value to the fully saturated value ($S_l = 1$). The two straight lines described are rigorous results of the theory, and form two sides of a triangle that will contain all data for partially saturated systems, regardless of the type of saturation present.

FIRST NEW METHOD OF DATA DISPLAY

In order to separate effects of liquids on Lamé's parameter λ from well-understood effects of liquids on the density ρ , while taking full advantage of the fluid-effect independence of shear modulus μ , we will now combine the v_p and v_s data into a new type of plot. To take advantage of the predictions of the theory described above, we will plot seismic velocity data in a two-dimensional array with one axis being $\rho/\mu = 1/v_s^2$ and the other being the ratio $\lambda/\mu = (v_p/v_s)^2 - 2$. Now, the ratio $\rho/\mu = 1/v_s^2$ acts as a proxy for S which we do not know, but both S and ρ/μ are simply linear functions of S in the region of low frequencies being considered. For porous materials that satisfy Gassmann's homogeneous fluid condition the result should be a straight (horizontal) line until the saturation reaches $S \simeq 1$ (around 95% or higher), where the data should quickly rise to a value determined by the velocities

at full liquid saturation. This behavior is observed in Figure 1b. Note that, although this behavior is qualitatively similar to that of v_p in Figure 1a, we are now using only the seismic velocities themselves (no saturation data are required to generate this plot, although in this case saturation can be inferred at least qualitatively). The behavior we observe here is traditional Gassmann-Domenico predictions (Domenico, 1974) for partial saturation.

If all the other assumptions of the Gassmann model are satisfied, but the liquid and gas are not distributed uniformly (so that different pores have different saturation levels), then we have the circumstances that may better fit the “patchy saturation” model (Berryman *et al.*, 1988; Endres and Knight, 1989; Mavko and Nolen-Hoeksema, 1994; Dvorkin and Nur, 1998). In that case, for the plot of λ/μ vs. ρ/μ , instead of data following a horizontal line with a jump up at the high saturation end (*e.g.*, Figure 1b), the ideal patchy saturation model (for completely segregated liquid and gas pockets) would predict that the data should lie on another straight line connecting to the two end points (dry and saturated) on this plot. These straight lines have been superimposed on the plots [obtained using data from Murphy (1982; 1984) and from Knight and Nolen-Hoeksema (1990)] for Figures 1b, 1d, and 1f. The anticipated behavior has been observed in Figure 1b and in other data not shown here, but two distinctly different types of behavior are observed in Figures 1d and 1f.

Plots of velocity versus saturation and of λ/μ versus ρ/μ for two sandstones that apparently do not behave according to Gassmann’s model are shown in Figures 1c-1f. These apparent deviations from the range of expected behaviors (from purely homogeneous mixed fluids to purely segregated patchy saturation) are resolved by including another display for these three sandstones (Murphy, 1982; 1984; Knight and Nolen-Hoeksema, 1990) in Figures 2a,c,e and corresponding plots for three limestones (Cadoret, 1993; Cadoret *et al.*, 1995; Cadoret *et al.*, 1998) in Figures 2b,d,f. Now the ratio λ/μ is plotted versus *saturation* measured in the laboratory, and we observe in all these cases that the basic plot structures we had anticipated for Figures 1b, 1d, and 1f are in fact confirmed. What we learn from this observation is that the quantity ρ/μ , which we wanted to use as a proxy for the saturation S , is *not* always a good proxy at high frequencies. We can safely attribute the discrepancies in Figures 1d and 1f to effects of high frequency dispersion as predicted by Biot’s theory (Biot, 1956a; 1956b; 1962). Even the seemingly odd negative slope of the patchy saturation lines in Figure 1f can be understood as a predicted high frequency effect on the shear velocity (Berryman, 1981).

This first new plotting method is limited by the implicit assumptions that the shear modulus is independent of the presence of fluids and that frequency dispersion for shear velocity is negligible. The assumption that the materials’ shear properties are independent of the fluid is based on theoretical predictions about mechanical behavior only, and any chemical interactions between fluid and rock that might soften grain contacts could easily account for some of these discrepancies. Fluid-induced swelling of either interstitial or intergranular clays is another possible source of discrepancy as are fluid-induced pressure effects if the fluid is over-pressured and therefore tending to severely weaken the rock. All of the chemical effects mentioned should become active with even very small amounts of fluid present, but probably do not have very significant frequency dependence (at least within the seismic frequency band). On the other hand, we must also take into account Biot’s theory (Biot, 1956a; 1956b; 1962) of acoustics in porous media, which generalizes Gassmann’s theory to higher frequencies and has

been shown to be a very reliable predictor of behavior in simple porous systems (Berryman, 1995). There are frequency dependent (dispersion) effects predicted by Biot's theory that can lead to complications difficult to resolve with the severely frequency-band limited data that are normally available.

Fortunately, Cadoret and colleagues (Cadoret, 1993; Cadoret *et al.*, 1995; Cadoret *et al.*, 1998) have in recent years performed a very extensive series of tests on limestones, including both ultrasonic and sonic experiments and with different means of achieving various levels of partial saturation. Figure 3b shows results obtained for an Estailades limestone at 500 kHz. This material behaves very much like the sandstones we have already considered here, and appears to obey the Gassmann predictions very well all the way up to the ultrasonic frequency regime. There were several other limestones that were found to have similar if not quite such good behavior. On the other hand, there were two limestone samples (a granular Lavoux limestone and an Espeil limestone) that were found to have very strong dispersion in the ultrasonic frequency band. These materials do not behave as expected when the data are plotted as in either Figure 1 or Figure 2. However, since extensional wave and shear wave data (Cadoret, 1993; Cadoret *et al.*, 1995; Cadoret *et al.*, 1998) at 1 kHz were also collected for these same samples, we have computed the necessary quantities using standard formulas and plotted them for these two materials in Figures 2d and 2f. We see that even for these two badly behaved materials (in the ultrasonic band) the plots at lower frequency become easy to interpret again. These results provide a very strong indication that plots such as those in Figure 1 will be readily interpreted for all porous materials at seismic frequencies.

ANOTHER NEW METHOD OF DATA DISPLAY

By making two seemingly small changes in the method of display, we now arrive at one of the main points of this paper. Since the expected behavior for Gassmann materials as observed in Figure 1b is a horizontal straight line for most values of saturation (*i.e.*, λ/μ is expected to be almost constant until high saturation levels are reached), it is natural to consider dividing ρ/μ by λ/μ , and then plotting the points again in the $(\rho/\lambda, \mu/\lambda)$ -plane. In the straight-line portion of the curve from Figure 1b, the only effect will be a change of scale, but large changes will result in the points representing full saturation or nearly full saturation. The results of this new plotting method are displayed in Figure 3. We observe that in all cases the result is apparently a straight line. This linear behavior is expected for a Gassmann material, since λ is just a scaling factor, μ is unaffected by saturation, and ρ is linearly dependent on saturation. It would also be expected for a non-Gassmann material in which the effect of fluids on λ was negligible compared to the effect on μ . It may also be expected for the case of patchy saturation if chemical interactions cause μ to change with saturation, because then μ for the porous medium would be some weighted average of μ for the dry case and μ for the fully saturated, chemically altered portions of the rock.

Figure 3a shows the same sandstone data as Figure 1. Similar data for five limestone samples (Cadoret, 1993; Cadoret *et al.*, 1995; Cadoret *et al.*, 1998) are plotted in Figure 3b. The straight line correlation of the data in this display is clearly confirmed by the limestone data.

Numerous other examples of the correlation have been observed. No examples of appropriate data for partially saturated samples with major deviations from this behavior have been observed, although an extensive survey of available data sets has been performed for materials including limestones, sandstones, granites, unconsolidated sands, and some artificial materials such as ceramics and glass beads. This straight line correlation is a very robust feature of partial saturation data. The mathematical trick that brings about this behavior will be explained in simple terms below following a brief discussion of the usefulness of this display.

We now have two new methods of data display, both using the Lamé parameter λ in a critical role. We therefore call this pair of plotting methods the “ λ -diagrams.”

POROSITY CORRELATION

An additional feature of displays of the type presented in Figure 3 is that the slopes of the straight lines, at least for samples of similar material character, are inversely correlated with the porosity of the samples. This observation is highlighted in Figures 3c and 3d. Figure 3c shows results from a series of fused glass-bead samples (Berge *et al.*, 1995) of uniform composition that was fabricated, with lower porosities being achieved by varying temperatures and length of sintering times. The porosities are distributed almost perfectly in Figure 3c, with the lower porosity lines having higher slopes and higher porosity lines having lower slopes. The experimental error in the stated porosity measurements $\simeq \pm 0.6\%$, so that the main discrepancy observed here with misalignment between the samples at $\phi = 36.0\%$ and $\phi = 36.5\%$ suggests that this display may provide a more sensitive means of determining the porosity. Figure 3d shows similar behavior for very low porosity granite (Nur and Simmons, 1969), having $\phi \simeq 1\%$; as the pressure is increased, the porosity in the material is steadily decreased mostly due to crack closure.

WHY THE SECOND DISPLAY IS ALWAYS APPROXIMATELY LINEAR

We can understand both the linearity and the apparent dependence of the data correlation on porosity in the second plotting method shown in Figure 3 by understanding some simple facts about such displays. Consider a random variable X . If we display data on a plot of either X vs. X or $1/X$ vs. $1/X$, the result will always be a perfect straight line. In both cases the slope of the straight line is exactly unity and the intercept of the line is the origin of the plot $(0, 0)$. Now, if we have another variable Y and plot Y/X vs. $1/X$, then we need to consider two pertinent cases: (1) If $Y = \text{constant}$, then the plot of Y/X vs. X will again be a straight line and the intercept will again be the origin, but the slope will be Y , rather than unity. (2) If $Y \neq \text{constant}$ but is a variable with small overall variation (small dynamic range), then the plot of Y/X vs. $1/X$ will not generally be exactly a straight line. The slope will be given approximately by the average value of Y and the intercept will be near the origin, but its precise value will depend on the correlation (if any) of Y and X . In our second method of plotting, the variable λ/ρ plays the role of X and the variable $v_s^2 = \mu/\rho$ plays the role of Y . The plots are approximately linear because this method of display puts the most highly variable combination of constants λ/ρ in

the role of X , and the least variable combination of constants v_s^2 in the role of Y . Furthermore, the slope of the observed lines is therefore correlated inversely with the porosity ϕ because the slope is approximately the average value of v_s^2 which is well-known to decrease monotonically with increasing porosity.

ON UNIQUENESS OF λ -DIAGRAMS

Since the possible linear combinations of the elastic bulk and shear moduli (K and μ) is infinite, it is natural to ask why (or if) $\lambda = K - \frac{2}{3}\mu$ is special? Is there perhaps some other combination of these constants that works as well or even better than the choice made here? There are some rather esoteric reasons based on recent work (Berryman *et al.*, 1999) in the analysis of layered anisotropic elastic media that lead us to believe that the choice λ is indeed special, but we will not try to describe these reasons here. Instead we will point out some general features of the two types of plots that make it clear that this choice is generally good, even though others might be equally good or even better in special circumstances. First, in the diagram using the $(\rho/\mu, \lambda/\mu)$ -plane, it is easy to see that *any* plot of data using linear combinations of the form $(\rho/\mu, (\lambda + c\mu)/\mu)$, where c is any real constant, will have precisely the same information and the display will be identical except for a translation of the values along the ordinate by the constant value c . Thus, for example taking $c = \frac{2}{3}$, plots of $(\rho/\mu, K/\mu)$ will have exactly the same interpretational value as those presented here. But if we now reconsider the second type of plot for each of these choices, we need to analyze plots of the form $(\rho/(\lambda + c\mu), \mu/(\lambda + c\mu))$. Is there an optimum choice of the parameter c that makes the plots as straight as possible whenever the only variable is the fluid saturation? It is not hard to see that the class of best choices always lies in the middle of the range of values of λ/μ taken by the data. So setting $-c = \frac{1}{2}(\min(\lambda/\mu) + \max(\lambda/\mu))$ will always guarantee that there are very large positive and negative values of $\mu/(\lambda + c\mu)$, and therefore that these data fall reliably (if somewhat approximately) along a straight line. But the minimum value of λ/μ has an absolute minimum of $-\frac{2}{3}$, based on the physical requirement of positivity of K . So $c < \frac{2}{3}$ is a physical requirement, and since $\max \lambda/\mu \simeq +\frac{2}{3}$ is a fairly typical value for porous rocks, it is expected that an optimum value of $c \leq 0$ will generally be obtained using this criterion. Thus, plots based on bulk modulus K instead of λ will not be as effective in producing the quasi-orthogonality of porosity and saturation that we have obtained in the second style of plotting. We conclude that the choice λ is not unique (some other choices might be as good for special data sets) but it is nevertheless an especially simple choice and also expected to be quite good for most real data.

CONCLUSIONS

The new plotting strategies described in this paper provide promising new methods for estimating both porosity and saturation from seismic data as well as for distinguishing types of fluid saturation present in the earth. The methods will apply to low frequency (seismic) data whether or not they fit Gassmann's model (Gassmann, 1951) or a patchy saturation model (Berryman

et al., 1988; Endres and Knight, 1989; Mavko and Nolen-Hoeksema, 1994; Dvorkin and Nur, 1998). At these low frequencies, the type of saturation present (well-segregated liquids and gases, homogeneous fluid mixtures, or some patchy saturation state intermediate between these two extremes) determines the location of data points on the $(\rho/\mu, \lambda/\mu)$ -plane. High frequency (ultrasonic) data are more likely to contain wave attenuation and dispersion effects that complicate our analyses, but as shown here they nevertheless do not seriously affect our interpretations based on Lamé's elastic parameter λ as long as the data are taken in a range of frequencies that avoids the very largest dispersive effects. We find porosity is correlated inversely with the slopes of the data-distribution lines in the $(\rho/\lambda, \mu/\lambda)$ -plane (see Figure 3). This fact can be used to sort field data into subsets having similar material characteristics and porosities for display on the more sensitive $(\rho/\mu, \lambda/\mu)$ plots. The main conclusion associated with Figure 2 is that saturation is an approximately (within normal data scatter) monotonic function of λ/μ (as in Figure 1), and therefore also of μ/λ (as in Figure 3). So saturation can be estimated from knowledge of location along the lines of Figure 3 and relative changes of saturation can be determined with a high level of confidence. After sorting seismic data by material characteristics and porosity using the $(\rho/\lambda, \mu/\lambda)$ -diagram, the resulting data subsets can then be displayed in the $(\rho/\mu, \lambda/\mu)$ -plane and used to infer the local states of saturation.

ACKNOWLEDGMENTS

We thank Bill Murphy and Rosemarie Knight for providing access to their unpublished data files. We thank Norman H. Sleep for his insight clarifying the significance of our second method of plotting seismic data.

REFERENCES

- Aki, K., & Richards, P. G., 1980, *Quantitative Seismology: Theory and Methods*, Vols. I & II, W. H. Freeman and Company, New York.
- Berge, P. A., Bonner, B. P., & Berryman, J. G., 1995, Ultrasonic velocity-porosity relationships for sandstone analogs made from fused glass beads: *Geophysics* **60**, 108–119.
- Berryman, J. G., 1981, Elastic wave propagation in fluid-saturated porous media: *J. Acoust. Soc. Am.* **69**, 416–424.
- Berryman, J. G., 1995, Mixture theories for rock properties: *Rock Physics and Phase Relations: A Handbook of Physics Constants*, American Geophysical Union, Washington, D.C., pp. 205–228.
- Berryman, J. G., 1999, Origin of Gassmann's equations: *Geophysics* **64**, *in press*; **SEP-102**, October, 1999, pp. 133–137.
- Berryman, J. G., Grechka, V. Y. & Berge, P. A., 1999, Analysis of Thomsen parameters for finely layered VTI media: *Geophys. Prospect.* **47**, 959–978; **SEP-94**, pp. 247–261.

- Berryman, J. G., Thigpen, L., & Chin, R. C. Y., 1988, Bulk elastic wave propagation in partially saturated porous solids: *J. Acoust. Soc. Am.* **84**, 360–373.
- Biot, M. A., 1956a, Theory of propagation of elastic waves in a fluid-saturated porous solid. I. Low-frequency range: *J. Acoust. Soc. Am.* **28**, 168–178.
- Biot, M. A., 1956b, Theory of propagation of elastic waves in a fluid-saturated porous solid. II. Higher frequency range: *J. Acoust. Soc. Am.* **28**, 179–1791.
- Biot, M. A., 1962, Mechanics of deformation and acoustic propagation in porous media: *J. Appl. Phys.* **33**, 1482–1498.
- Biot, M. A., and D. G. Willis, 1957, The elastic coefficients of the theory of consolidation: *J. Appl. Mech.* **24**, 594–601.
- Cadoret, T., 1993, *Effet de la saturation eau/gaz sur les propriétés acoustiques des roches. Étude aux fréquences sonores et ultrasonores*. Ph.D. Dissertation, Université de Paris VII, Paris, France.
- Cadoret, T., Marion, D., & Zinszner, B., 1995, Influence of frequency and fluid distribution on elastic wave velocities in partially saturated limestones: *J. Geophys. Res.* **100**, 9789–9803.
- Cadoret, T., Mavko, G., & Zinszner, B., 1998, Fluid distribution effect on sonic attenuation in partially saturated limestones: *Geophysics* **63**, 154–160.
- Domenico, S. N., 1974, Effect of water saturation on seismic reflectivity of sand reservoirs encased in shale: *Geophysics* **39**, 759–769.
- Dvorkin, J. & Nur, A., 1998, Acoustic signatures of patchy saturation: *Int. J. Solids Struct.* **35**, 4803–4810.
- Endres, A. L., & Knight, R., 1989, The effect of microscopic fluid distribution on elastic wave velocities. *Log Anal.* **30**, 437–444.
- Ewing, W. M., Jardetsky, W. S., & Press, F., 1957, *Elastic Waves in Layered Media*, McGraw-Hill, New York.
- Gassmann, F., 1951, Über die elastizität poröser medien: *Vierteljahrsschrift der Naturforschenden Gesellschaft in Zürich*, **96**, 1–23.
- Knight, R., & Nolen-Hoeksema, R., 1990, A laboratory study of the dependence of elastic wave velocities on pore scale fluid distribution: *Geophys. Res. Lett.* **17**, 1529–1532.
- Mavko, G. & Nolen-Hoeksema, R., 1994, Estimating seismic velocities at ultrasonic frequencies in partially saturated rocks: *Geophysics* **59**, 252–258.
- Murphy, William F., III, 1982, *Effects of Microstructure and Pore Fluids on the Acoustic Properties of Granular Sedimentary Materials*, Ph.D. Dissertation, Stanford University.

- Murphy, William F., III, 1984, Acoustic measures of partial gas saturation in tight sandstones. *J. Geophys. Res.* **89**, 11549–11559.
- Nur, A., & Simmons, G., 1969, The effect of saturation on velocity in low porosity rocks. *Earth and Planet. Sci. Lett.* **7**, 183–193.
- Ostrander, W. J., 1984, Plane-wave reflection coefficients for gas sands at non-normal angles of incidence: *Geophysics* **49**, 1637–1648.
- Wyllie, M. R. J., Gregory, A. R., & Gardner, L. W., 1956, Elastic wave velocities in heterogeneous and porous media: *Geophysics*, **21**, 41–70.
- Wyllie, M. R. J., Gregory, A. R., & Gardner, G. H. F., 1958, An experimental investigation of factors affecting elastic wave velocities in porous media: *Geophysics* **23**, 459–493.

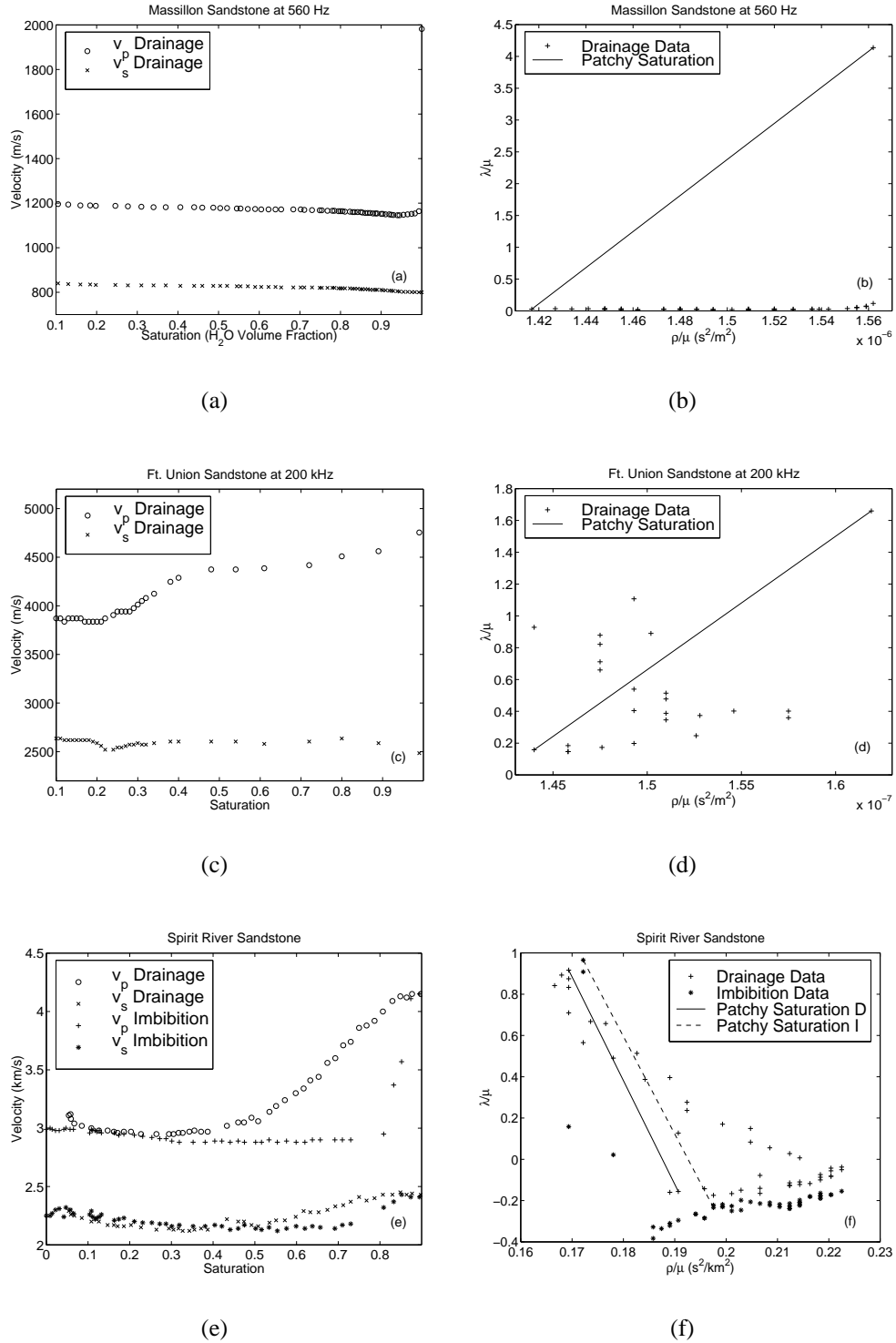


Figure 1: Compressional and shear velocities for Massillon and Ft. Union sandstone measured by Murphy (1982; 1984) and for Spirit River sandstone measured by Knight and Nolen-Hoeksema (1990).

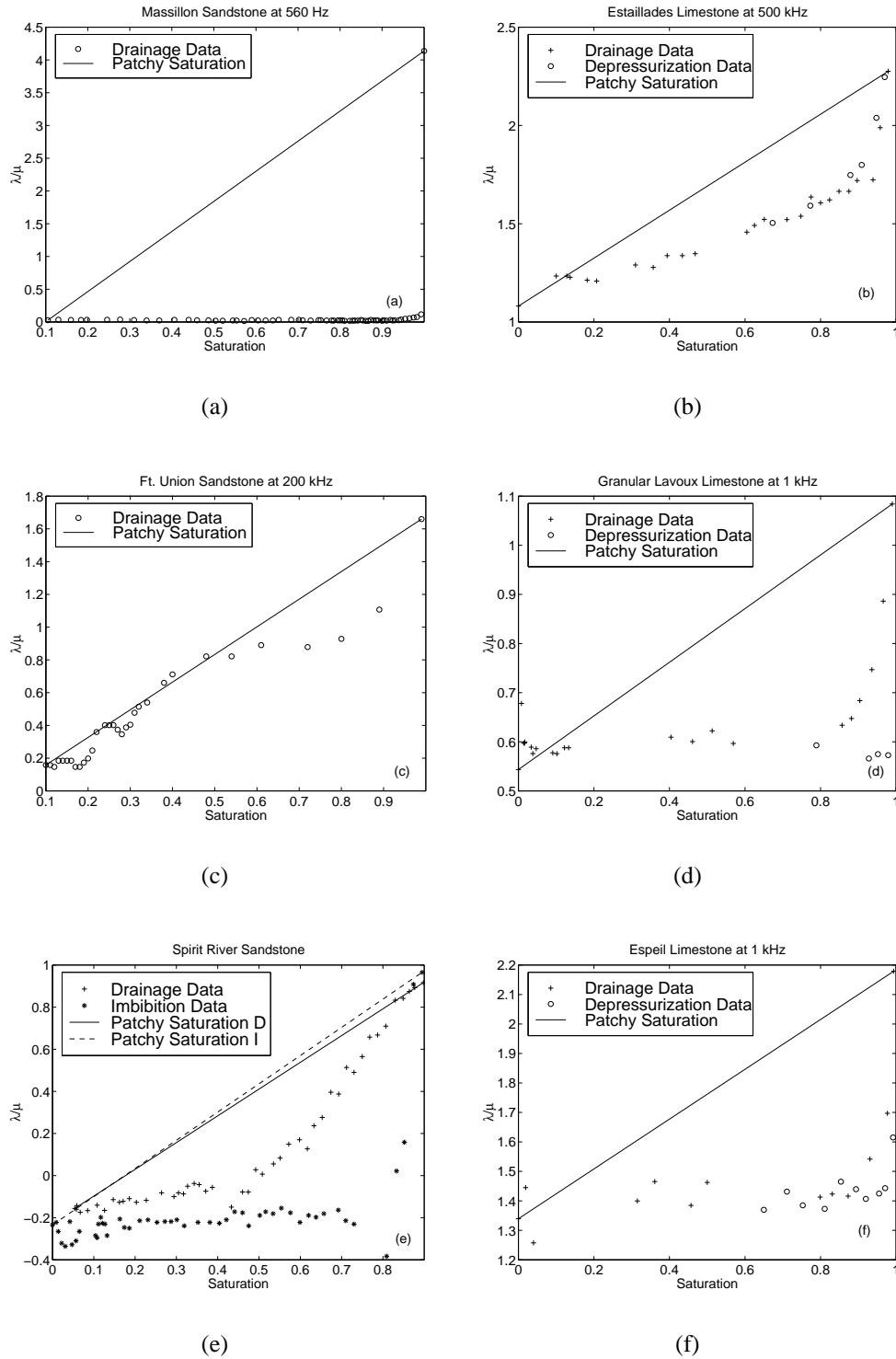


Figure 2: Ratio λ/μ versus saturation for the three sandstones (Murphy, 1982; 1984; Knight and Nolen-Hoeksema, 1990) of Figure 1 and for three limestones (Cadoret, 1993; Cadoret *et al.*, 1995; Cadoret *et al.*, 1998).

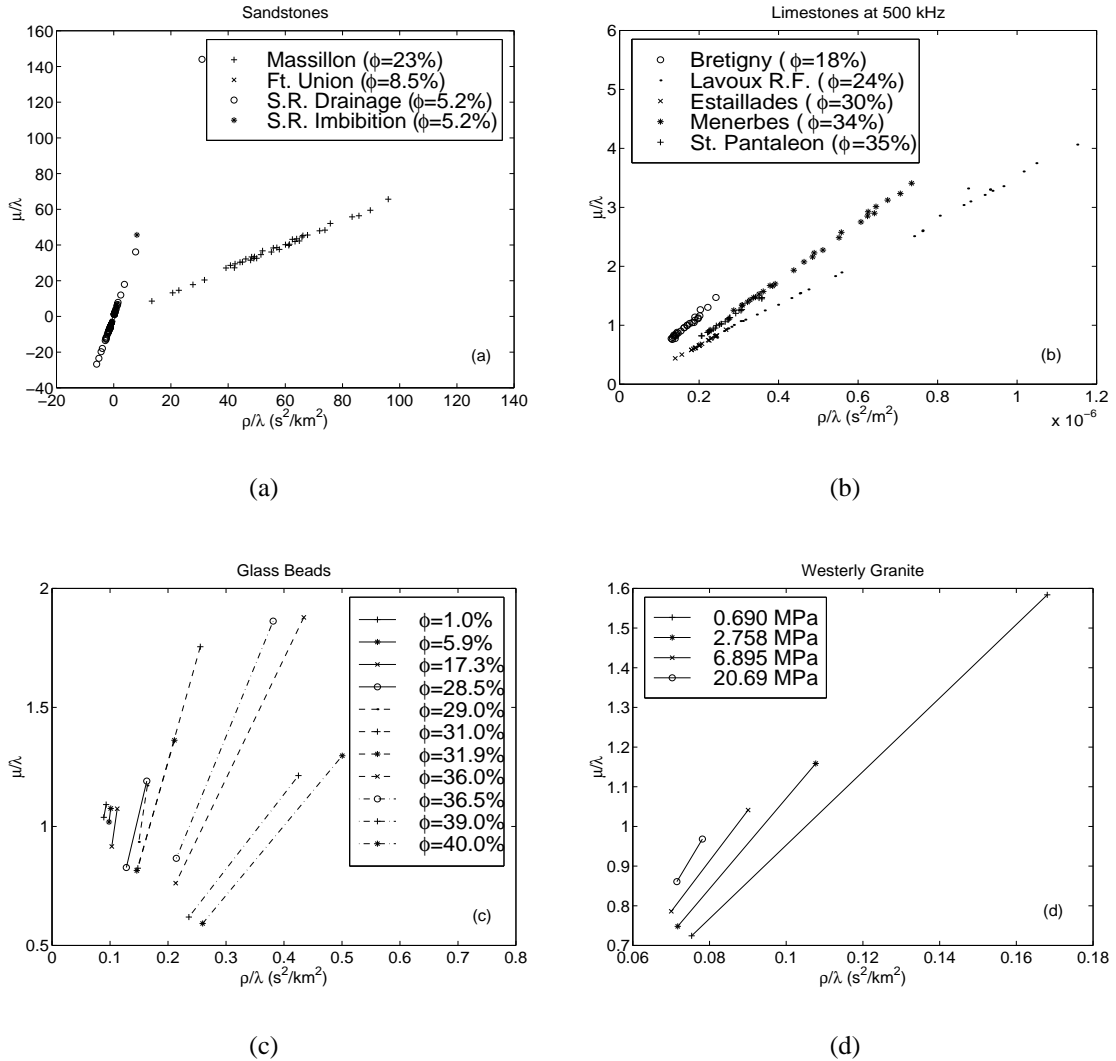


Figure 3: Examples of the correlation of slopes with porosity: (a) three sandstones (Murphy, 1982; 1984; Knight and Nolen-Hoeksema, 1990), (b) five limestones (Cadoret, 1993; Cadoret *et al.*, 1995; Cadoret *et al.*, 1998), (c) 11 fused glass-bead samples (Berge *et al.*, 1995), (d) Westerly granite (Nur and Simmons, 1969) at four pressures. The observed trend is that high porosity samples generally have lower slopes than lower porosities on these plots, although there are a few exceptions as discussed in the text. These trends are easily understood since the slopes are determined approximately by the average value of v_s^2 for each material, which is a decreasing function of porosity.

Seismic attribute sensitivity to velocity uncertainty

*Carmen Mora and Biondo Biondi*¹

ABSTRACT

This paper explores the relationship between velocity uncertainty and AVO-related seismic attributes in a dataset from the Blake Outer Ridge, offshore from Florida and Georgia. From an initial velocity model, several realizations were generated that are perturbations of the original velocity model. Prestack wave-equation migration was applied to the data for each velocity realization. In the migrated CMP gathers, velocity coherence was measured by applying semblance analysis. Also, several seismic attributes were calculated in the migrated CMP gathers, including AVO intercept, AVO gradient, and near - far offset stack. Preliminary results from attribute versus velocity coherence crossplots at the range of CMPs studied suggest that, for the case of maximum semblance coherence measurements, attribute values are more dispersed for lower coherence values and more localized for higher coherence values. These results are not definitive, and further work is needed to improve the velocity coherence measures.

INTRODUCTION

Velocity estimation is a very important and difficult step in the seismic imaging problem. Because of the non-uniqueness in the velocity estimation, understanding the relationship between velocity models and seismic attributes could contribute insight into the seismic imaging problem. Therefore, the objective of this study is to understand the sensitivity of seismic attribute response to velocity uncertainty.

In recent years, there has been an enthusiastic use of seismic attributes to predict reservoir properties. Many new attributes have been designed (Chen and Sidney, 1997) in the hope of finding any relationship between attributes and the reservoir properties that can be used in prediction. However, although the ability to generate numerous seismic attributes has improved, physical relationships between attributes and reservoir properties are not always well understood. In order to decide which attributes to use for this research, we have focused our attention on some "better understood" attributes, in other words, those that can be related to physical parameters, such as amplitude versus offset (AVO), reflectivity, acoustic impedance, compressional-wave velocity (V_p), and shear-wave velocity (V_s). For this particular study, we have chosen AVO-related attributes because of the physical relation between the variation of reflection/transmission coefficients and incident angle and elastic rock parameters like V_p , V_s , and density ρ (Castagna et al., 1993).

¹email: cmora@sep.stanford.edu, biondo@sep.stanford.edu

The problem of velocity estimation and its relationship with AVO

AVO analysis requires previous prestack migration of the data, and velocity estimation is a key factor for this imaging problem. Velocity estimation affects AVO response because it modifies the position of the events and the resulting amplitude values (Grubb and Tura, 1997). On the other hand, because of the difficulty of estimating velocity models in complex areas, it is important to understand the sensitivity of AVO attributes to variation in velocity models.

The aim of the work described in this report is to find any relation between AVO-related seismic attributes and velocity uncertainty that could be used to generate confidence measures for AVO inversion, and to support the imaging problem by discriminating between different velocity models from AVO-related attributes.

AVO theory

The variation of seismic reflection coefficients with offset can be used as a direct hydrocarbon indicator (Ostrander, 1984; Swan, 1993), which is supported in the AVO analysis theory. The physical relation between the variation of reflection/transmission coefficients with incident angle (and offset) and rock parameters has been widely investigated. This relation is established in the Zoeppritz equations, which relate reflection and transmission coefficients for plane waves and elastic properties of the medium. Because of the nonlinearity of the Zoeppritz equations, several approximations have been generated, such as those presented by Aki and Richards (1997) and Shuey (1985). Equation (1) presents Shuey's simplification, which comprises three terms characterizing the reflection coefficient, $R(\theta)$, at normal incidence, at intermediated angles, and at the approach to the critical angle:

$$R(\theta) = R_0 + \left[A_0 R_0 + \frac{\Delta\sigma}{(1-\sigma)^2} \right] \sin^2\theta + \frac{1}{2} \frac{\Delta V_p}{V_p} (\tan^2\theta - \sin^2\theta) \quad (1)$$

The simplified versions of the Zoeppritz equations allow the computation of AVO inversion to estimate elastic parameters from the observed variation of reflection amplitude with angle.

From AVO analysis, several attributes can be generated, such as AVO intercept, which is referred to the normal incidence reflection coefficient, and AVO gradient, which is the coefficient of $\sin^2\theta$ in the second term of equation (1). In the case of the attributes we use in this work, we call them AVO-related attributes because these attributes are not calculated from CMP gathers in the offset domain but rather from CMP gathers in the offset ray parameter domain. In this domain, the offset ray parameter is related to the aperture angle instead of the incident angle (Prucha et al., 1999).

SEISMIC DATA

The seismic data used for this study come from a marine dataset recorded at the Blake Outer Ridge, offshore from Florida and Georgia. This dataset consists of 1024 CMP gathers with

a spacing, after interpolation, of 25 m. Figure 1 is a stack section of the data after migration, which shows two interesting reflectors of opposite polarity: a bottom simulating reflector (BSR) and a flat reflector. The BSR is a characteristic seismic horizon associated with the base of a methane-hydrate stability zone. Ecker (1998) has shown that this reflector marks the transition from hydrated to gas-saturated sediments. Her analysis also suggests that the flat reflector beneath the BSR marks the transition from gas-saturated to brine-saturated sediments.

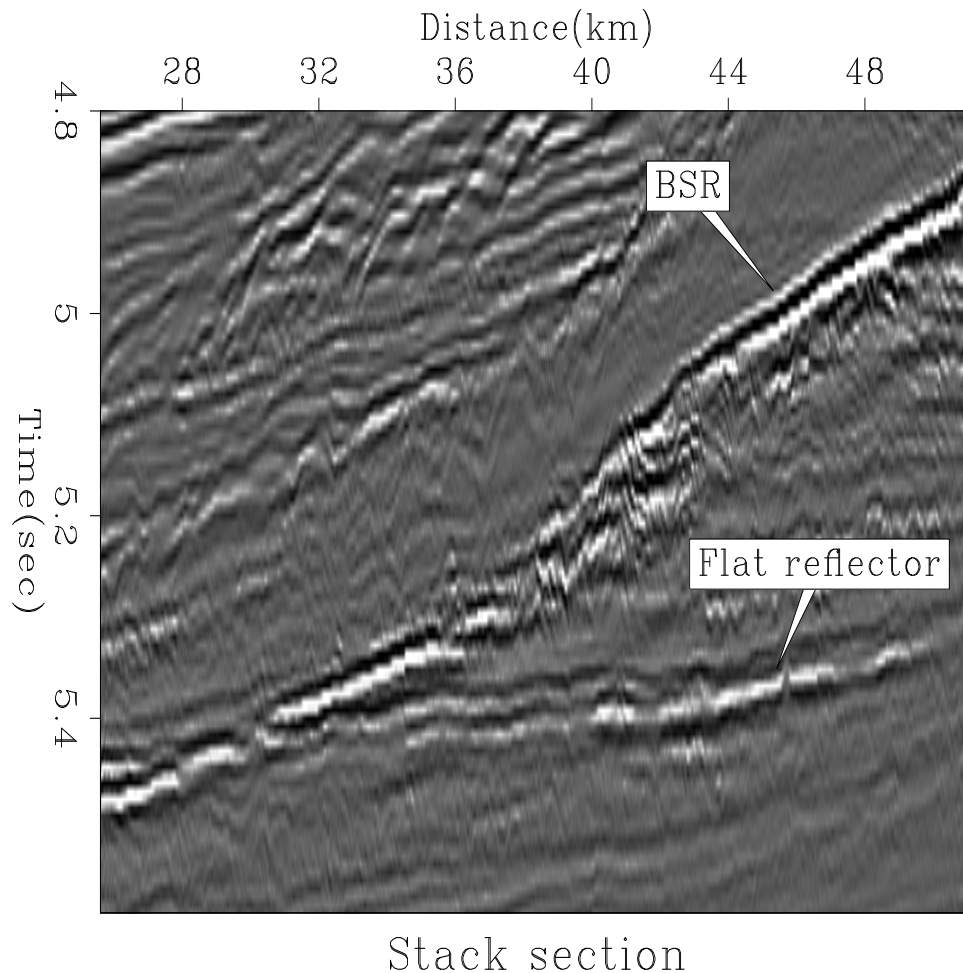


Figure 1: Stack section of the data after migration `cmora1-Stack-gas-ann` [CR]

PROCEDURAL STEPS

To identify any relation between AVO-related seismic attributes and velocity uncertainty, we generated several crossplots of attribute versus velocity coherence measures. The procedure for generating the final data to be plotted is illustrated in Figure 2. From an initial velocity model, we generated several realizations that are perturbations of the original velocity model.

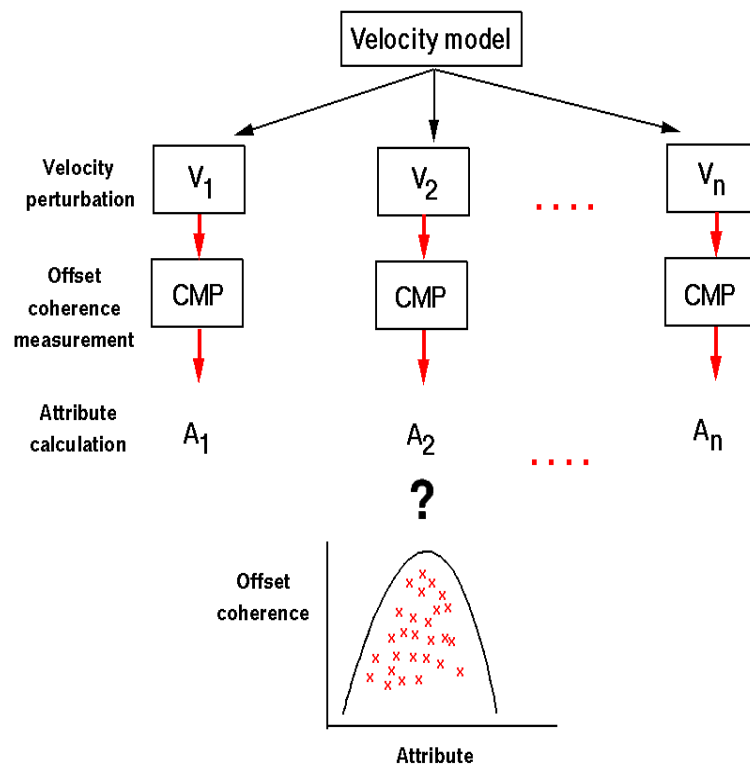


Figure 2: A procedural scheme for generating the crossplots of attribute versus velocity coherence [cmora1-esq] [NR]

The original model used for this work is shown in Figure 3. There is a low velocity zone beneath the BSR associated with the zone of gas-saturated sediments. Because of the complexity of this zone, the velocity estimation is difficult and migration velocity may contain errors. We assume these errors are zero-mean random variations, therefore, we introduce this kind of perturbation into the original velocity model to generate each realization. Figure 4 shows an

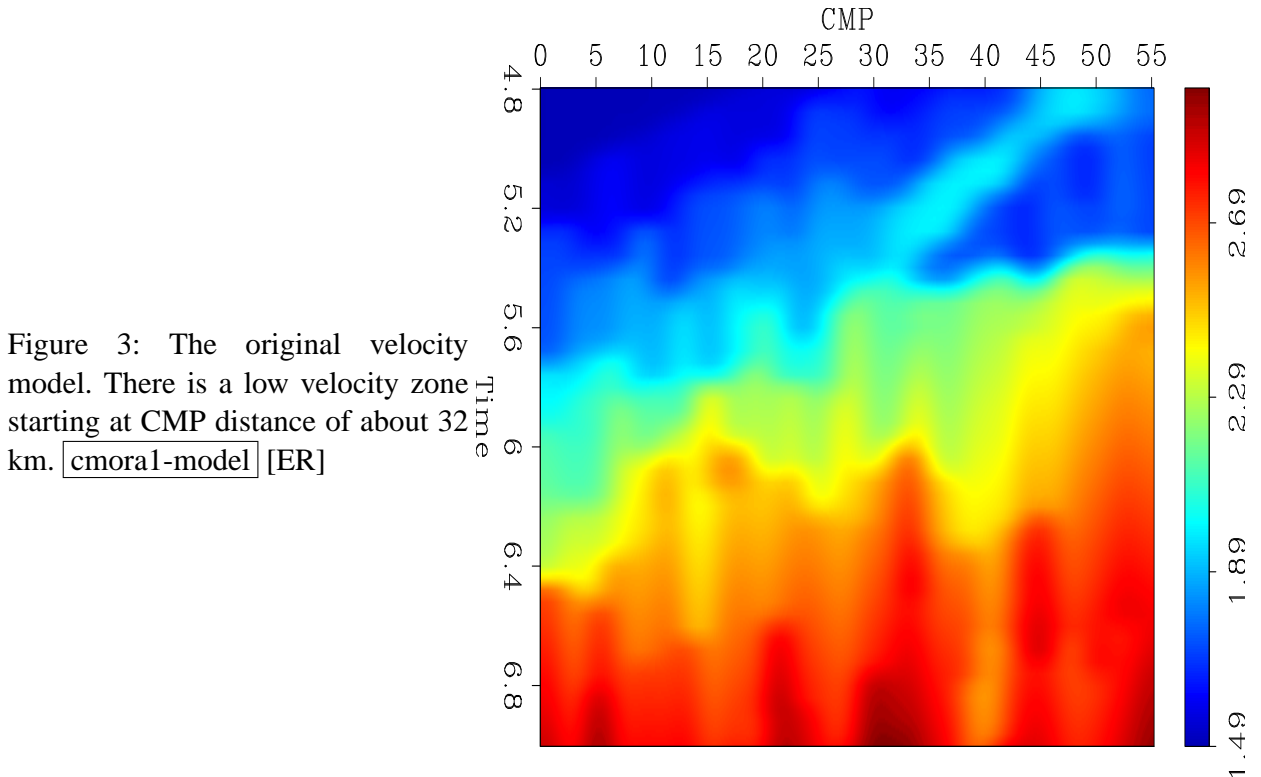


Figure 3: The original velocity model. There is a low velocity zone starting at CMP distance of about 32 km. `cmora1-model` [ER]

example of the velocity perturbation associated with realization number 50, and the resulting velocity model.

Using each modified velocity model, prestack wave-equation migration (Prucha et al., 1999) was applied to the data. The resulting image is a function of the offset ray parameter p_{hx} , which is related to the aperture angle θ , the dip ϕ along the in-line direction, and the velocity function $V(z, m)$, as follows:

$$p_{hx} = \frac{2 \sin \theta \cos \phi}{V(z, m)} \quad (2)$$

Figure 5 shows the result of applying the prestack wave-equation migration to the seismic data, using velocity realization number 50.

In the migrated CMP gather, offset coherence and AVO attributes were calculated. The coherence measures allow us to discriminate good and bad velocity models: the higher the coherence measure, the better the velocity model.

To measure the coherence associated with each velocity model, semblance analysis was applied to the resulting migrated CMPs. Figure 6 shows the semblance panel for realization

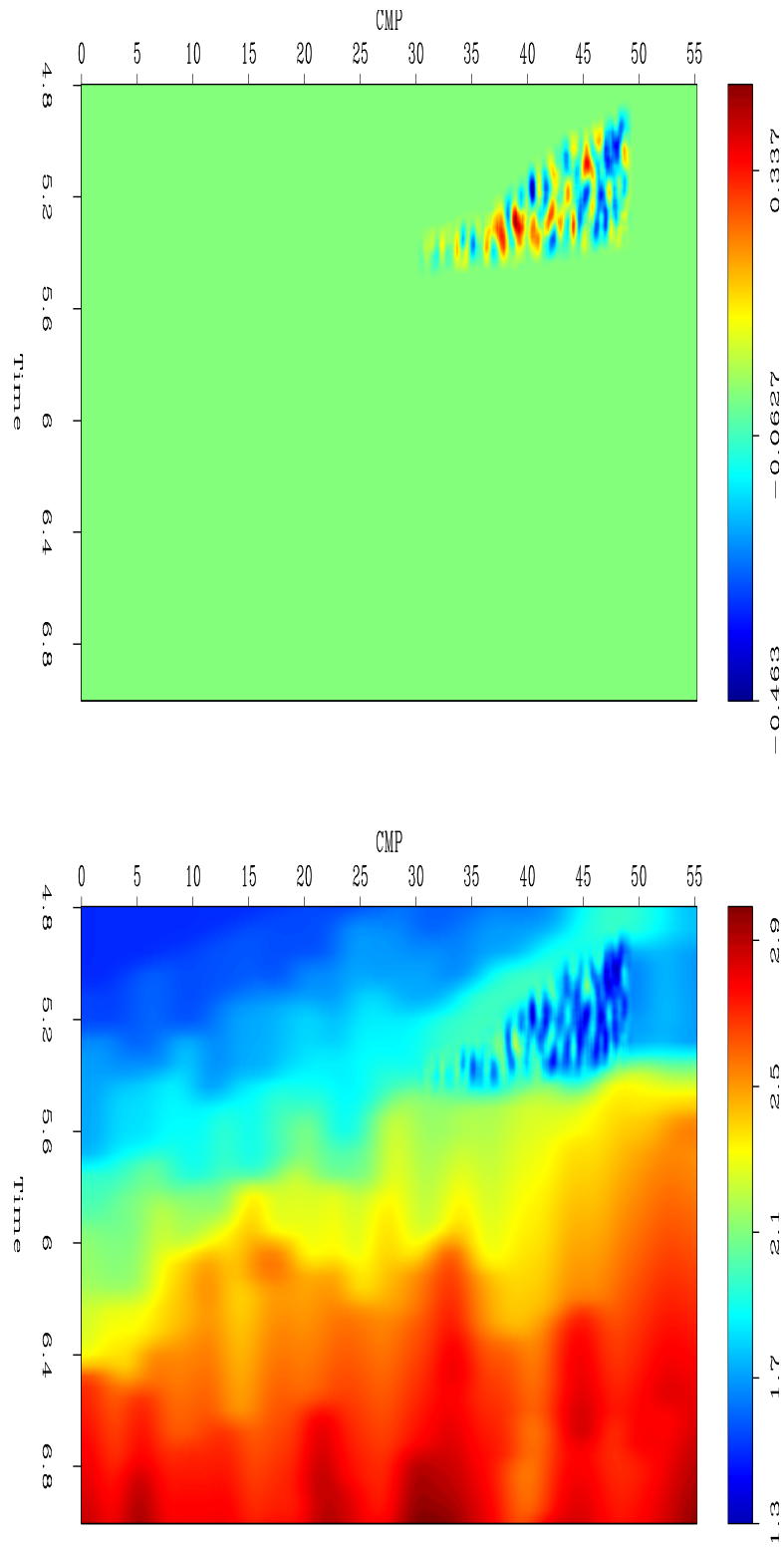


Figure 4: A velocity perturbation (top) and the resulting velocity model (bottom) for realization number 50 `cmora1-pert-velmod-50` [ER]

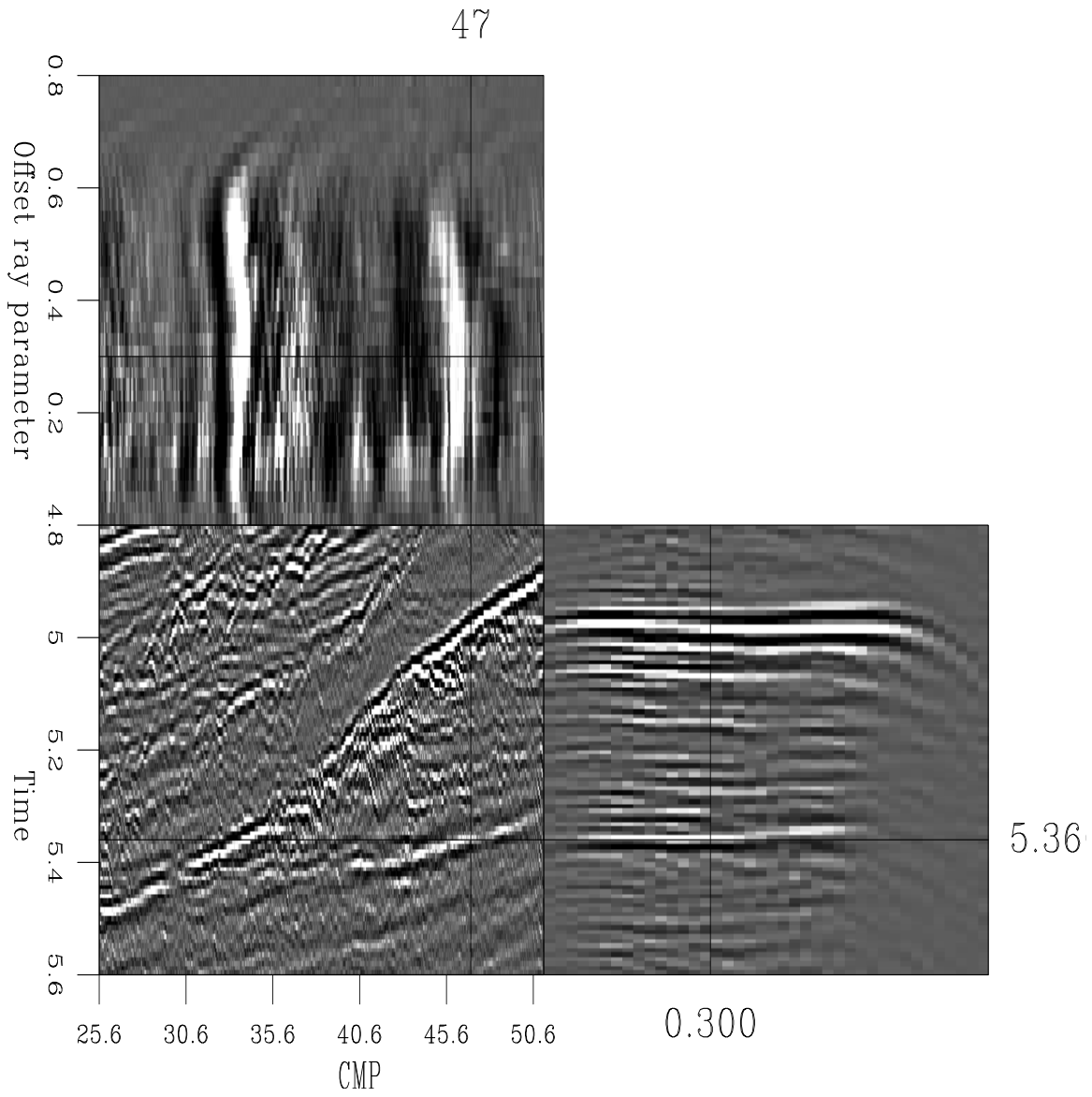


Figure 5: Time, CMP, and offset ray parameter slices of the migration result for velocity realization number 50 `cmora1-migration` [CR]

number 50. Two coherence measures were generated for each CMP, maximum semblance and delta velocity. Maximum semblance is calculated by picking the maximum semblance value in the semblance panel associated with each realization. Delta velocity is calculated as the difference between the velocity associated with the maximum semblance and the stacking velocity used for inverse normal moveout (NMO), as shown in Figure 7.

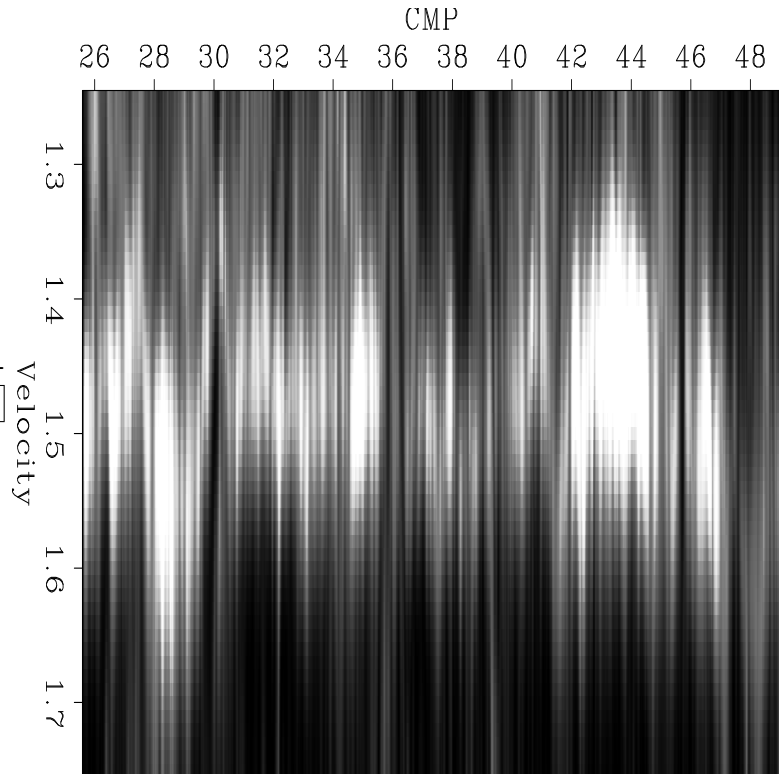


Figure 6: The semblance panel for realization number 50 [cmora1-sem.50] [CR]

To analyze the reflectivity as a function of reflection angle (AVO analysis), we examined the CMP gathers in the offset ray parameter domain. As Figure 8 shows, in this domain the event of interest is not completely flat; there is some residual moveout in the event that affects the amplitude picking at the far offset. To correct for this problem, we applied a residual moveout correction, mute some traces at the near and far offsets, and picked the maximum amplitude value at the flat reflector considering a time window instead of the exact time of the reflector. Figure 9 shows the amplitude versus offset ray parameter curves for the 50 realizations on CMP at a distance of 47 km.

With these picked amplitudes, we calculated the attributes: intercept, gradient, and near-far offset stack. The intercept and gradient attributes are the zero crossing and slope of the best straight-line approximation (least-squares curve fitting) for the amplitude values. The near-far offset attribute is the difference between the stacking amplitudes at the near and far offset.

Because of the discontinuities along the flat reflector (see Figure 5) and to avoid tuning effects caused by the BSR reflector, we examined the results in some stronger parts of the reflector. We chose some CMPs around distance 47 km for the attribute versus coherence plots. The next section presents the resulting plots.

Figure 7: The semblance plot for CMPs at 46.9 to 47.1 km. For each curve, the maximum semblance measurement is the maximum value, and the delta velocity measurement is the difference between the velocity corresponding to the maximum semblance and the stacking velocity used for inverse NMO (1.5 km/s).
cmora1-sem-graph.50 [CR]

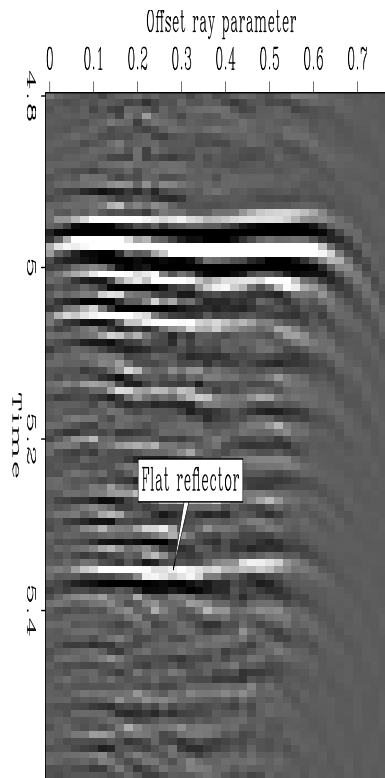
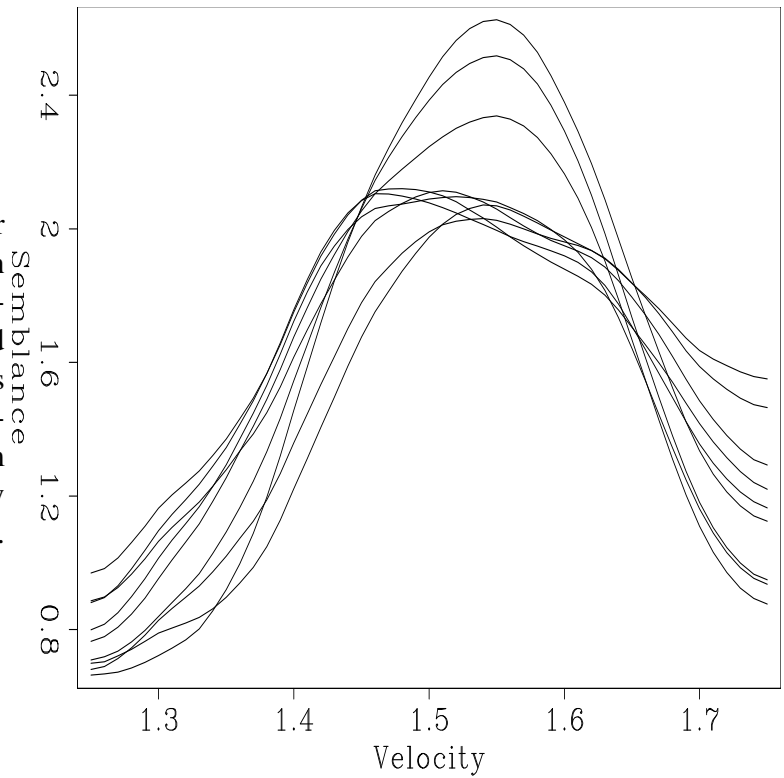
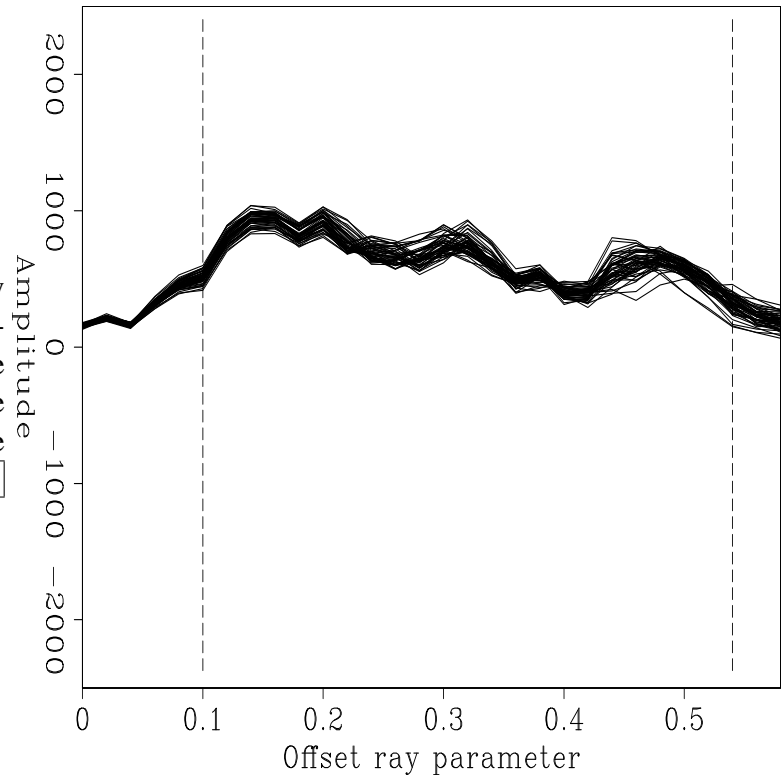


Figure 8: The CMP gather at a distance of 47 km cmora1-cmp-ann [CR]

Figure 9: Amplitude versus offset ray parameter curves for the 50 realizations at a CMP gather at a distance of 47 km. The dashed lines show the range of offsets considered for the AVO analysis. `cmora1-avo-47-r1-50` [CR]



RESULTS

According to Koefoed's conclusion mentioned by Shuey (1985), when the underlying medium has a greater longitudinal velocity and a greater Poisson's ratio, the reflection coefficient tends to increase with increasing angles of incidence. We could expect this AVO behavior at the flat reflector, assuming the hypothesis (Ecker, 1998) that this reflector marks the transition from gas-saturated to brine-saturated sediments, and because gas-saturated sediments exhibit abnormally low Poisson ratios (Ostrander, 1984).

However, in Figure 9 we can see that the general tendency has the opposite behavior—decreasing amplitude values with increasing offset ray parameter—even though in the near offset the reflection coefficient tends to increase with increasing offset ray parameter, as expected. There are several possible explanations for this discrepancy. Perhaps the original hypothesis—that the flat reflector marks the transition from gas-saturated to brine-saturated sediments—doesn't hold. On the other hand, the discrepancy may be the result of procedural problems associated, for example, with the fact that the attributes we considered are not strictly AVO attributes.

From the calculated coherence measures and attribute values at some CMPs around distance 47 km, we generated the crossplot of attribute versus coherence shown in Figures 10 through 15. In general, it is difficult to establish definitive tendencies of attributes and velocity coherence. However, for the case of maximum semblance coherence measures, as is shown in Figures 10, 11, and 12, attribute values are more dispersed for lower coherence values, and

more localized for higher coherence values. We sorted the coherence values and generated five groups of data samples, then calculated the variance and standard deviation for each group. For the case of the maximum semblance, the results suggest that attribute values tend to have higher variance and higher standard deviation as coherence values decrease. Figures 16, 17, and 18 show the standard deviation results corresponding to the maximum semblance plots in Figures 10, 11, and 12.

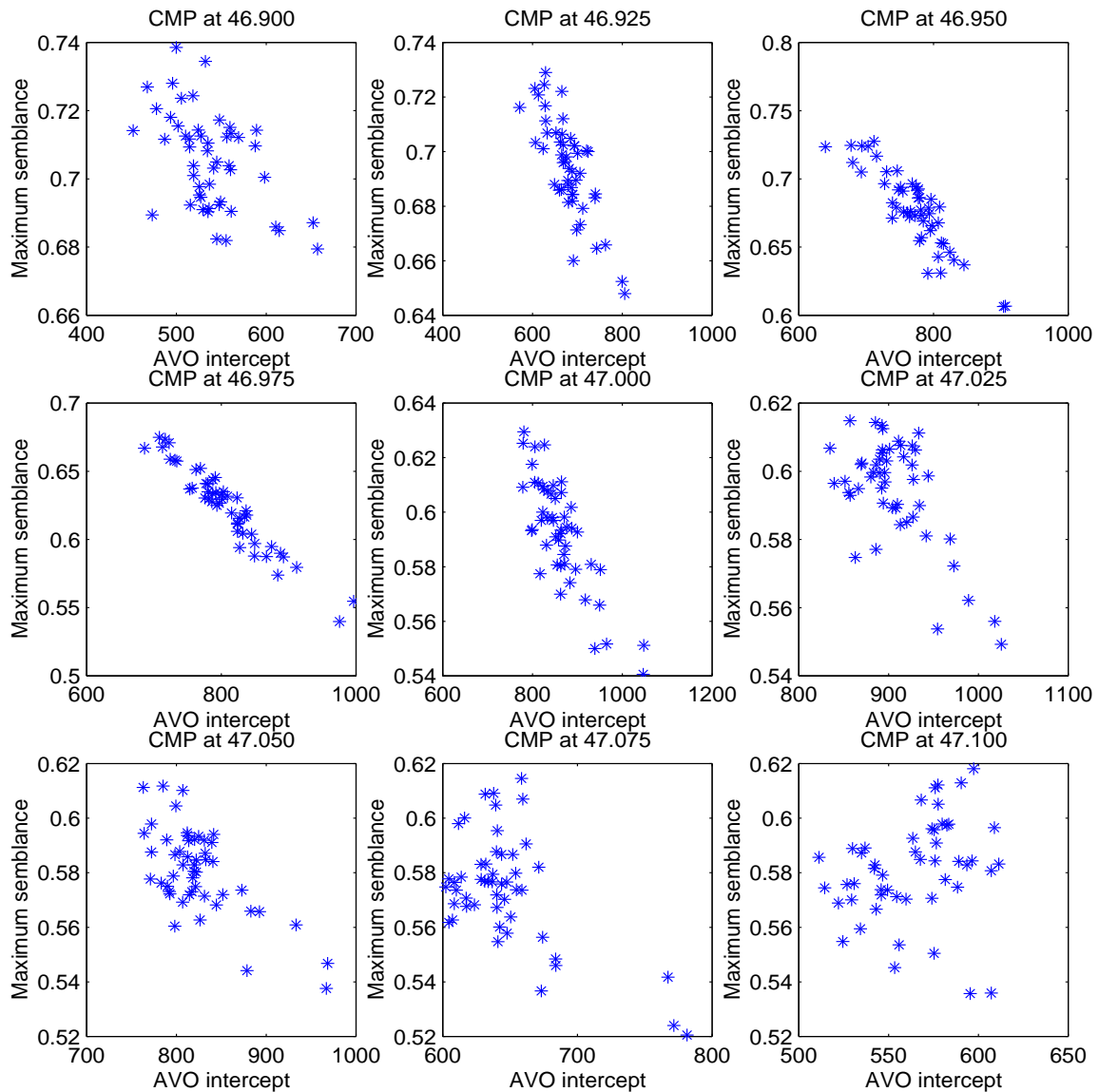


Figure 10: Intercept versus maximum semblance for CMPs from 46.9 to 47.1 km
cmora1-int-max [CR]

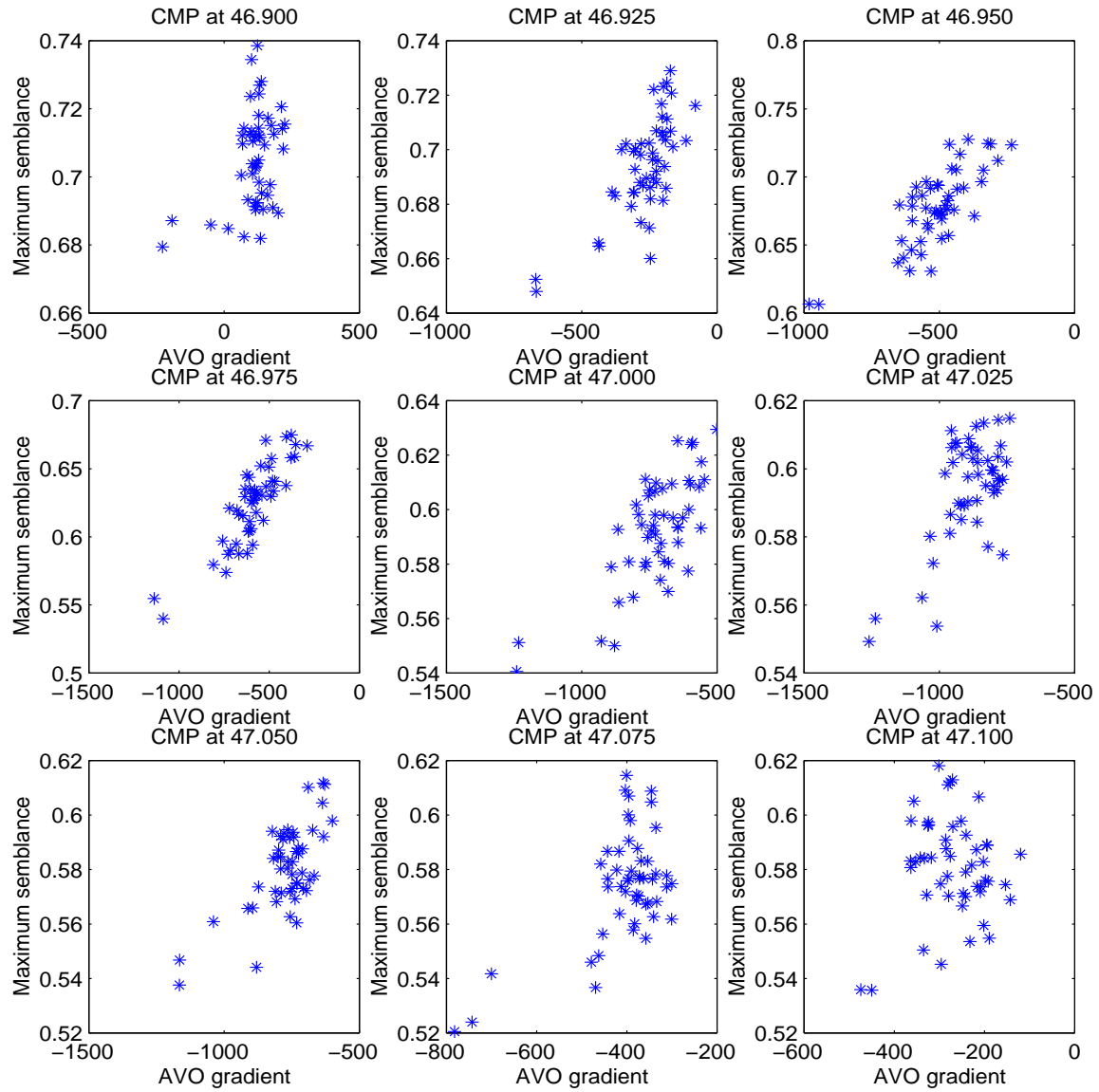


Figure 11: Gradient versus maximum semblance for CMPs from 46.9 to 47.1 km
cmora1-grad-max [CR]

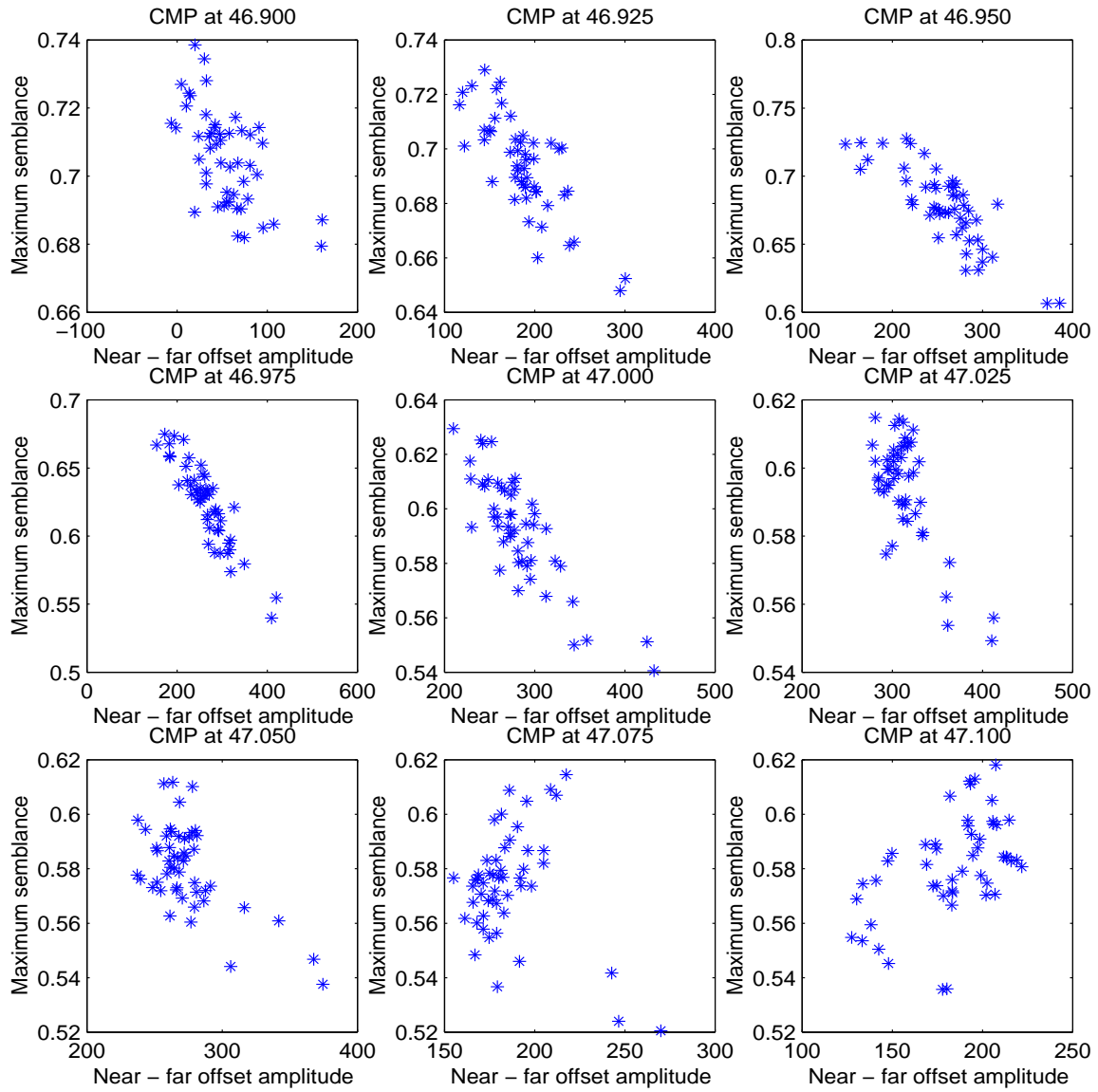


Figure 12: Near - far offset amplitude versus maximum semblance for CMPs from 46.9 to 47.1 km `cmora1-stack-max` [CR]

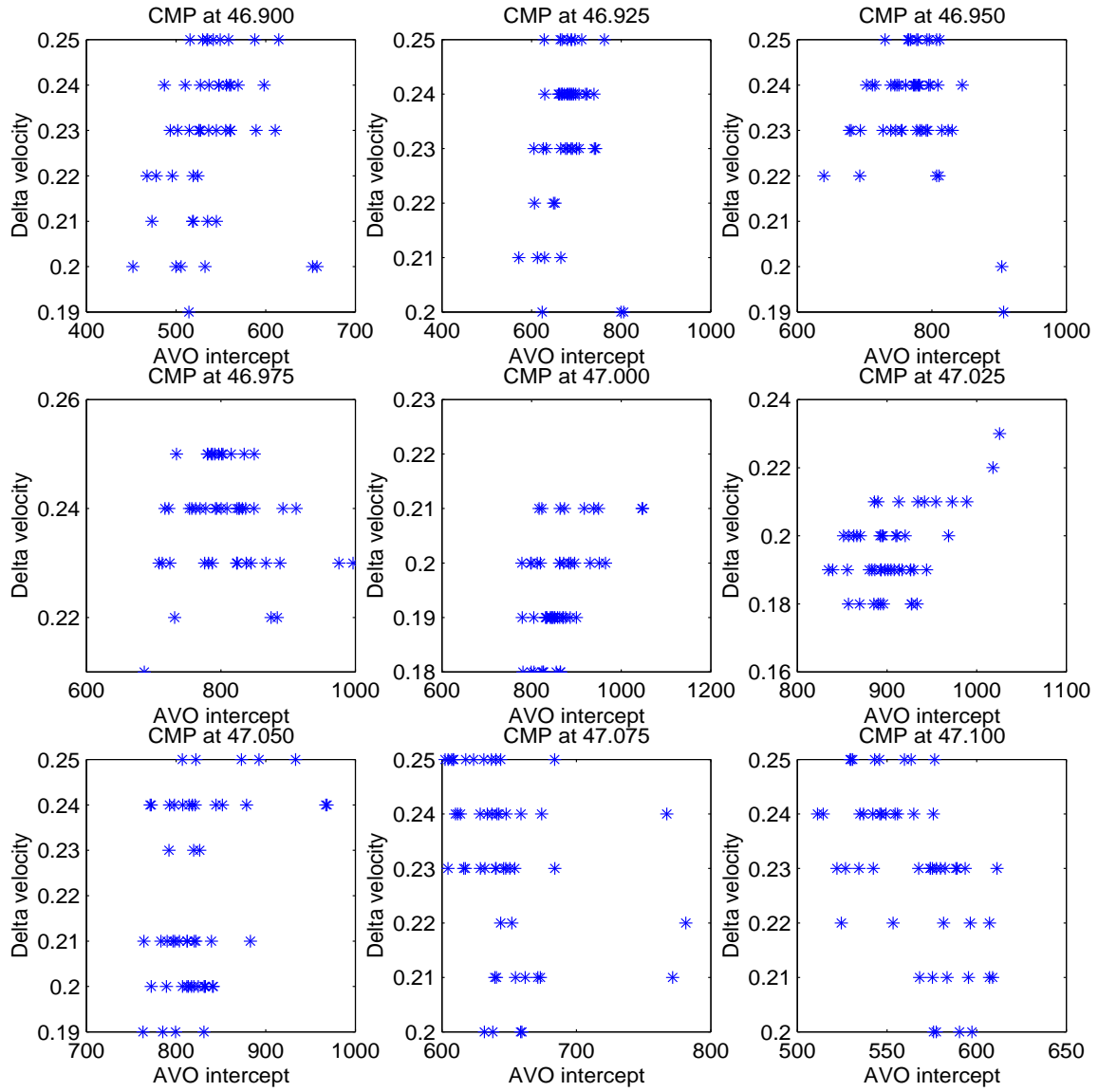


Figure 13: Intercept versus delta velocity for CMPs from 46.9 to 47.1 km `cmora1-int-delta` [CR]

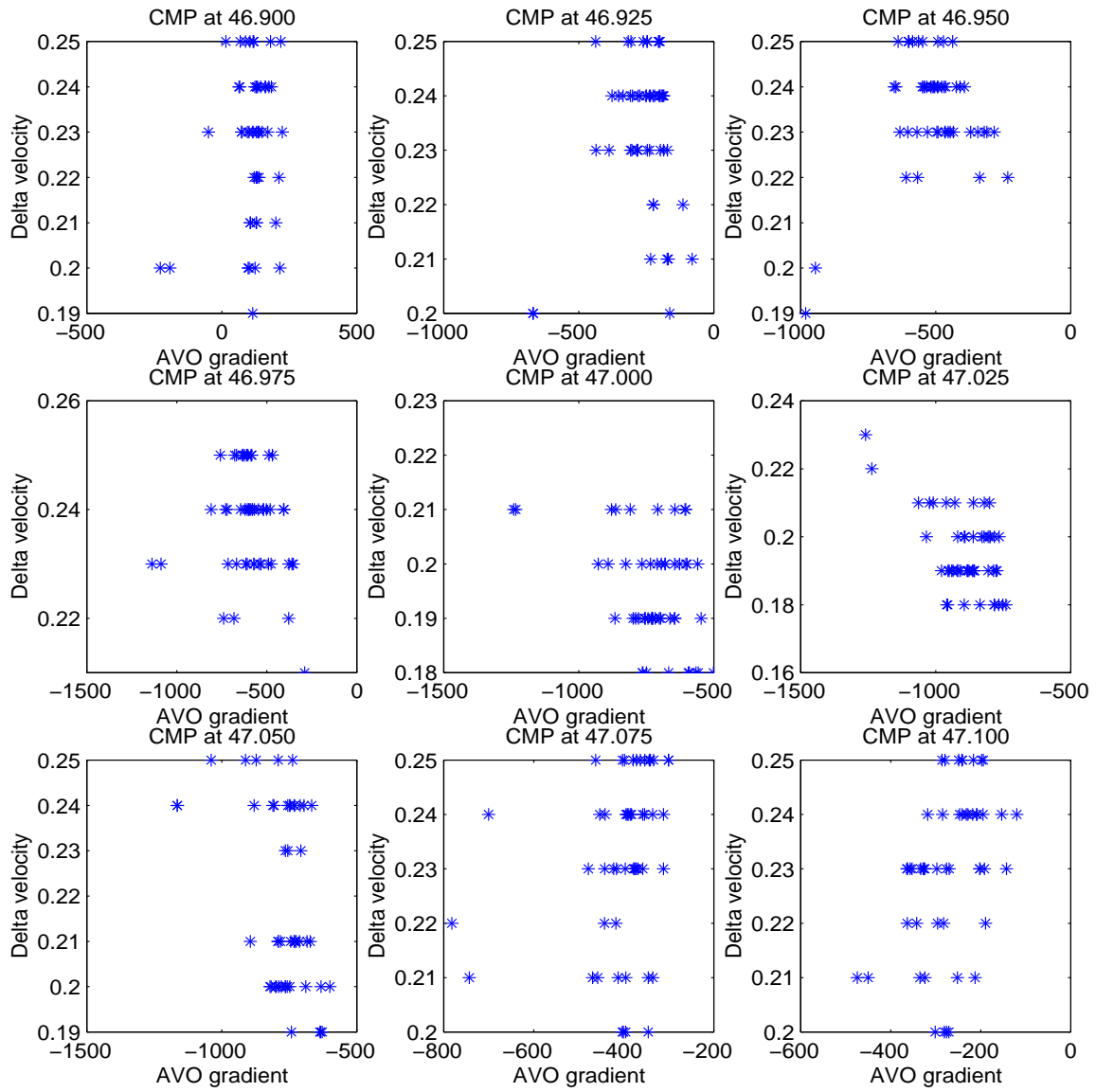


Figure 14: Gradient versus delta velocity for CMPs from 46.9 to 47.1 km cmora1-grad-delta
[CR]

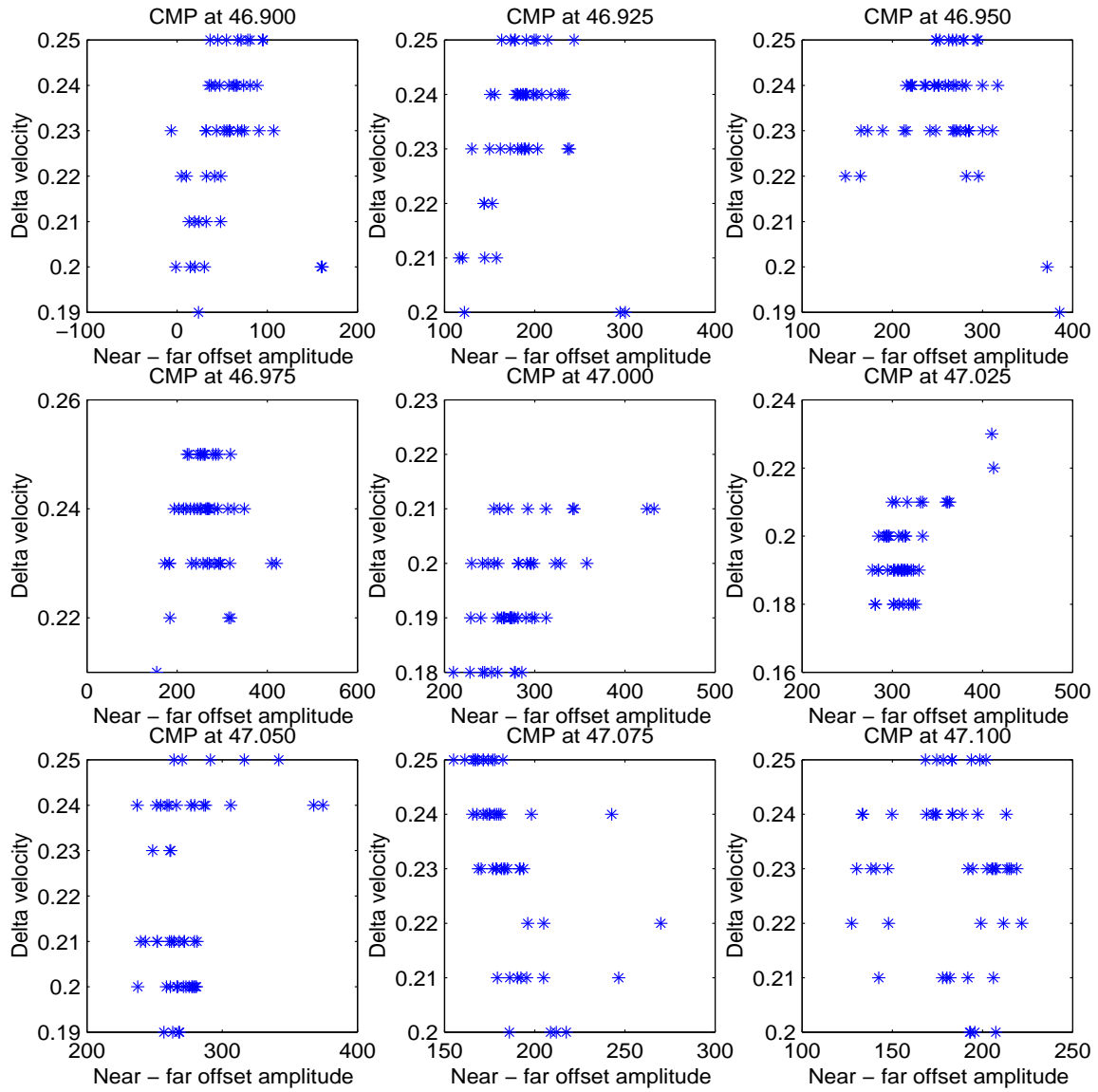


Figure 15: Near - far offset amplitude versus delta velocity for CMPs from 46.9 to 47.1 km
cmora1-stack-delta [CR]

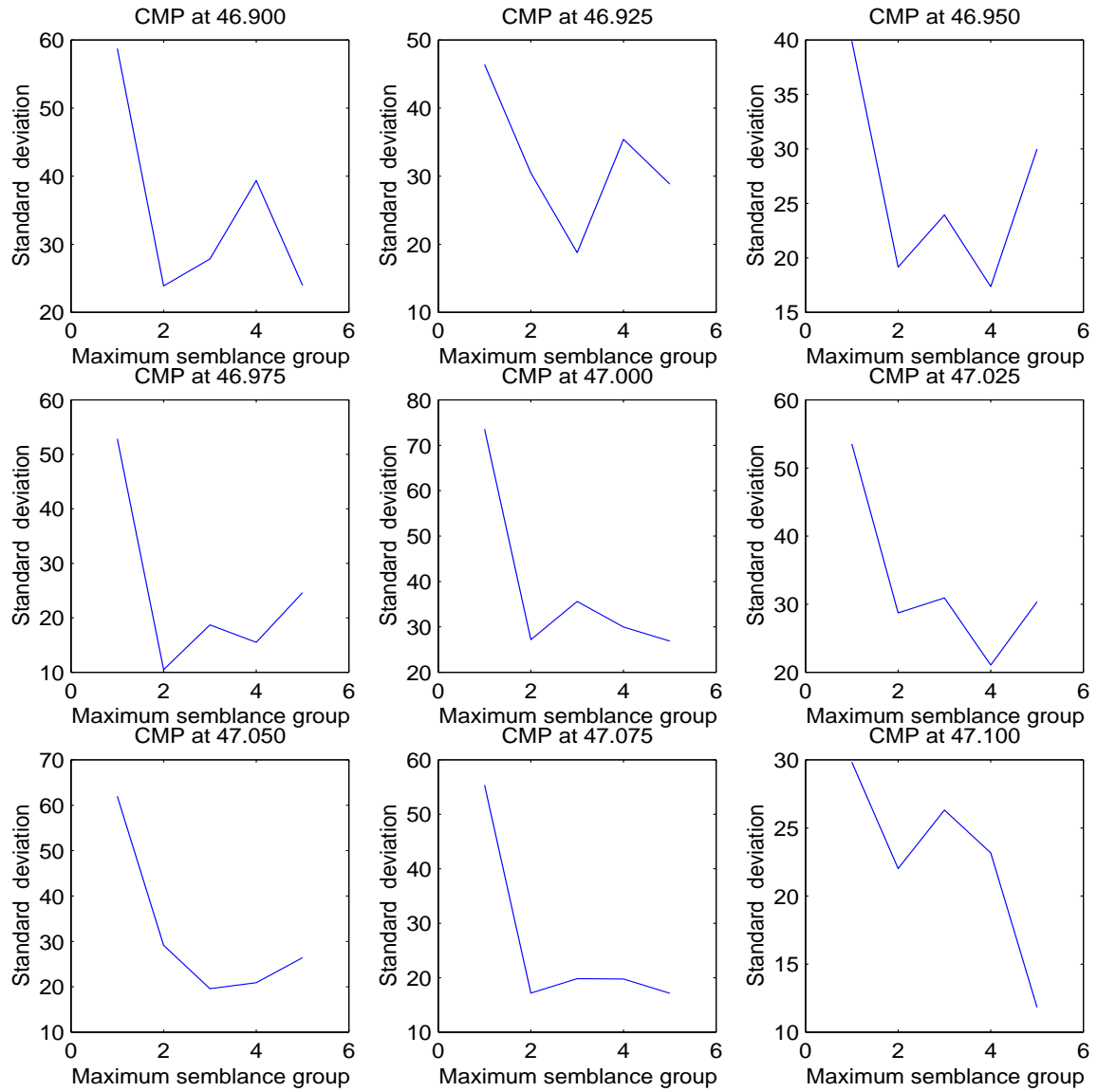


Figure 16: Maximum semblance group versus standard deviation corresponding to plots in Figure 10 `cmora1-std` [CR]

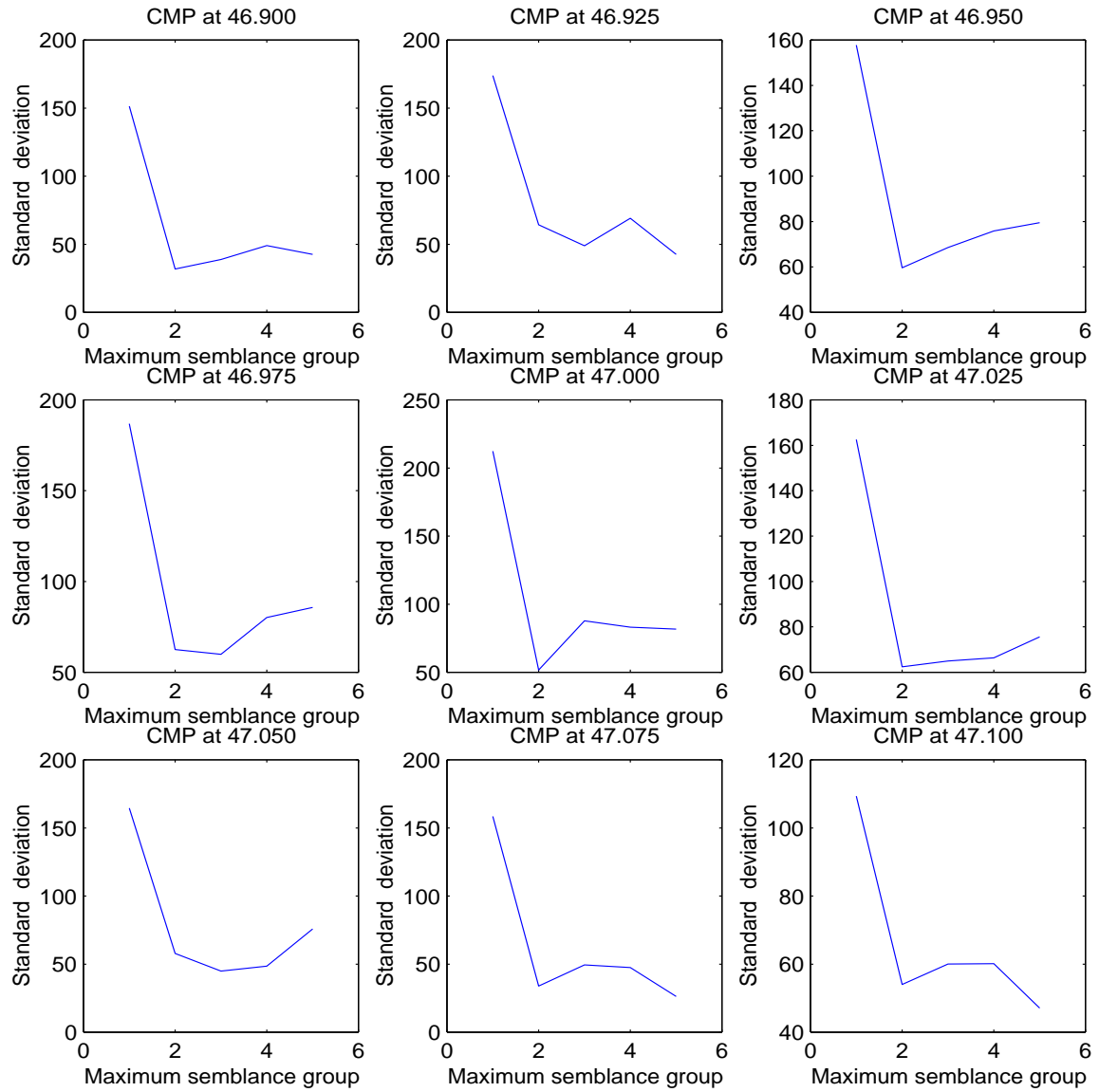


Figure 17: Maximum semblance group versus standard deviation corresponding to plots in Figure 11 `cmora1-std2` [CR]

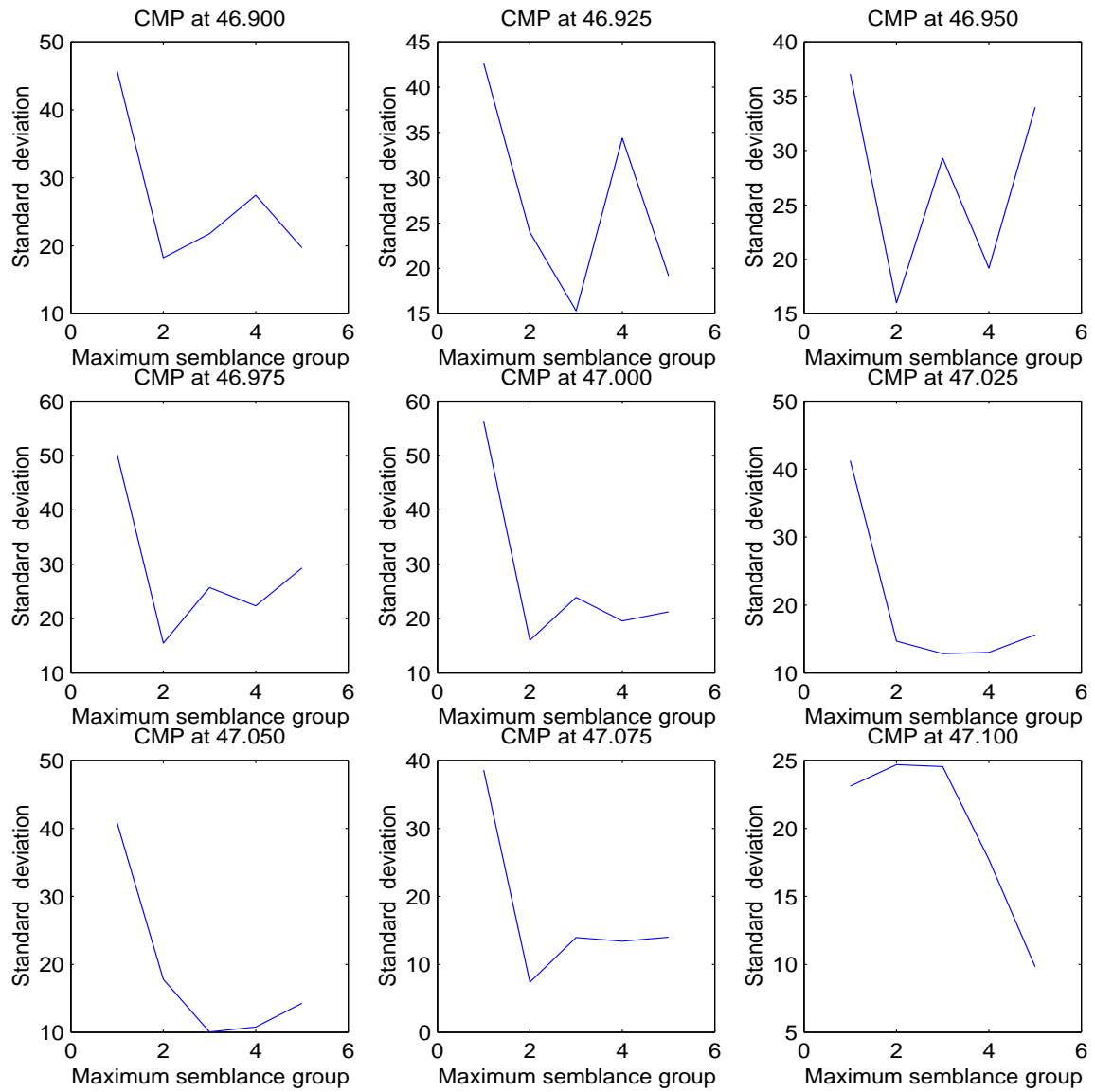


Figure 18: Maximum semblance group versus standard deviation corresponding to plots in Figure 12 `cmora1-std3` [CR]

CONCLUSION

Preliminary results from attribute versus coherence crossplots at the range of CMPs studied suggest that, for the case of maximum semblance coherence measurements, attribute values are more dispersed for lower coherence values and more localized for higher coherence values. For more definitive results, we need to do further work to improve the velocity coherence measures.

The next steps should comprise analysis of other regions of the flat reflector, use of additional coherence measurements (like the amount of residual moveout correction), and testing with a simpler data set. We also think it is important to investigate this problem using a synthetic model that allows more control over the data.

ACKNOWLEDGMENTS

We would like to thank Robert Clapp for the permission to use his semblance analysis code and for his support during the development of this work.

REFERENCES

- Aki, K. I., and Richards, P. G., 1997, *Quantitative seismology: Theory and methods*: W. H. Freeman and Company, New York.
- Castagna, J. P., Batzle, M. L., and Kan, T. K., 1993, Rock physics—the link between rock properties and avo response *in* Castagna, J. P., and Backus, M. M., Eds., *Offset dependent reflectivity—Theory and practice of AVO analysis*:: Society of Exploration Geophysics, 135–171.
- Chen, Q., and Sidney, S., 1997, Seismic attribute technology for reservoir forecasting and monitoring: *The Leading Edge*, **16**, no. 5, 445–456.
- Ecker, C., 1998, *Seismic characterization of methane hydrate structures*: Ph.D. thesis, Stanford University.
- Grubb, H., and Tura, A., 1997, Interpreting uncertainty measures for AVO migration/inversion: 67th Annual Internat. Mtg., Soc. Expl. Geophys., Expanded Abstracts, 210–213.
- Ostrander, W. J., 1984, Plane-wave reflection coefficients for gas sands at nonnormal angles of incidence: *Geophysics*, **49**, no. 10, 1637–1648.
- Prucha, M. L., Biondi, B. L., and Symes, W. W., 1999, Angle-domain common image gathers by wave-equation migration: *SEP-100*, 101–112.
- Shuey, R. T., 1985, A simplification of the Zoeppritz equations: *Geophysics*, **50**, no. 4, 607–614.

Swan, H. W., 1993, Properties of direct AVO hydrocarbon indicators *in* Castagna, J. P., and Backus, M. M., Eds., Offset dependent reflectivity—Theory and practice of AVO analysis:: Society of Exploration Geophysics, 78–92.

Seismic pattern recognition via predictive signal/noise separation

Morgan Brown and Robert G. Clapp¹

ABSTRACT

Manual stratigraphic interpretation of modern 3-D seismic images is a tedious and time-consuming process. We present a method based on nonstationary predictive signal/noise separation for automatically recognizing the occurrence of an arbitrary, predefined pattern, or *facies template*, in seismic images. Similarity of local data windows to the facies template is measured by an attribute which has an easily interpretable physical meaning. The method is tested on 2-D synthetic and real seismic images, and is shown to reliably detect the presence of unconformities in both. An extension of the method to 3-D should be quite straightforward, and early performance assessments hint that the extension will not be hindered severely by computational issues.

INTRODUCTION

Loosely defined, the process of stratigraphic interpretation is the analysis of the dip distribution (or *dip spectrum*) of a seismic image in small neighborhoods and the corresponding association of local geology with a given stratigraphic sequence. The interpreter's job, illustrated in Figure 1, is both tedious and time-consuming if performed manually, considering the large size of modern 3-D surveys. For instance, if a given sedimentary unit is best defined by its relative distance from a pervasive geologic unconformity, the interpreter must first identify the location of the unconformity over the entire seismic volume.

To make the stratigraphic interpretation of large 3-D image volumes feasible, an automatic approach is required to search an image locally for the likely presence of a predefined ordered pattern, or *facies template*. Randen et al. (1998) presented an automated scheme which analyzes local dip spectra to detect reflector terminations in seismic images, and hint that such an approach could be used to detect unconformities and recognize facies patterns. Neural networks have been applied to this end, but the results are often non-intuitive.

We present a scheme which automatically searches a seismic image for an arbitrary facies template, and then outputs a *similarity attribute* which expresses the data's relative local resemblance to the template. To compute the similarity attribute, we recast this problem of pattern recognition to one of signal/noise separation, i.e., treating the facies template as the "noise model", we seek to remove an optimal amount of it from small data windows, then define the attribute as the local noise-to-signal ratio. It follows that the similarity attribute is

¹email: morgan@sep.stanford.edu, bob@sep.stanford.edu

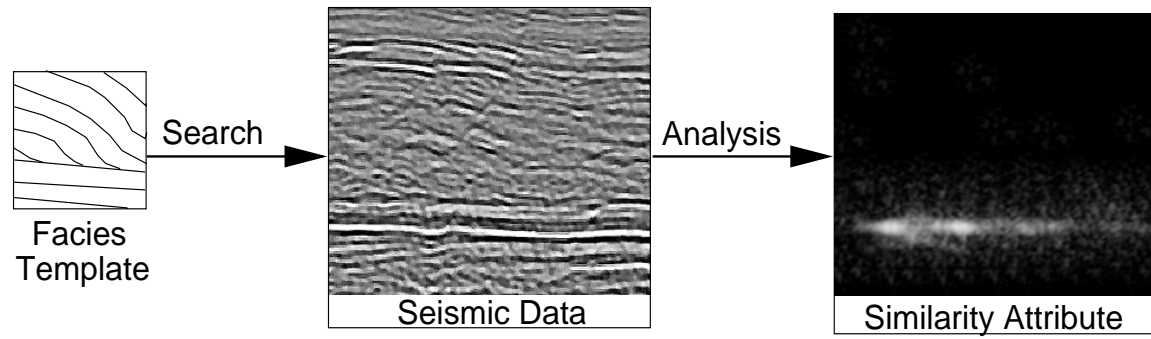


Figure 1: Stratigraphic interpretation: Given a facies template (left), search a seismic image locally (center) for likely matches to the template, then output (right) an attribute which illustrates some measure of local similarity between the template and the seismic image.

`morgan2-algorithm` [NR]

both physically meaningful and optimal in one (least squares) sense.

We first test the scheme on a 2-D synthetic seismic image with two unconformities, and find that both are detected reliably. We then perform the same test on a 2-D real seismic image, and successfully detect an unconformity. The performance of the scheme is encouraging, and there is considerable room for optimization.

METHODOLOGY

Consider local windows of the seismic image to be the simple superposition of signal and noise:

$$\mathbf{d} = \mathbf{s} + \mathbf{n}. \quad (1)$$

The frequency domain representation of the Wiener optimal reconstruction filter for uncorrelated signal and noise is (Castleman, 1996; Leon-Garcia, 1994):

$$\mathbf{H} = \frac{\mathbf{P}_s}{\mathbf{P}_s + \mathbf{P}_n} \quad (2)$$

where \mathbf{P}_s and \mathbf{P}_n are the power spectra of the unknown signal and noise, respectively. Multiplication of \mathbf{H} with the data spectrum gives an optimal (in the least squares sense) estimate of the spectrum of the unknown signal.

Abma (1995) and Claerbout (1999) solved a constrained least squares problem to separate signal from spatially uncorrelated noise:

$$\begin{aligned} \mathbf{Nn} &\approx 0 \\ \epsilon \mathbf{Ss} &\approx 0 \end{aligned} \quad (3)$$

subject to $\leftrightarrow \mathbf{d} = \mathbf{s} + \mathbf{n}$

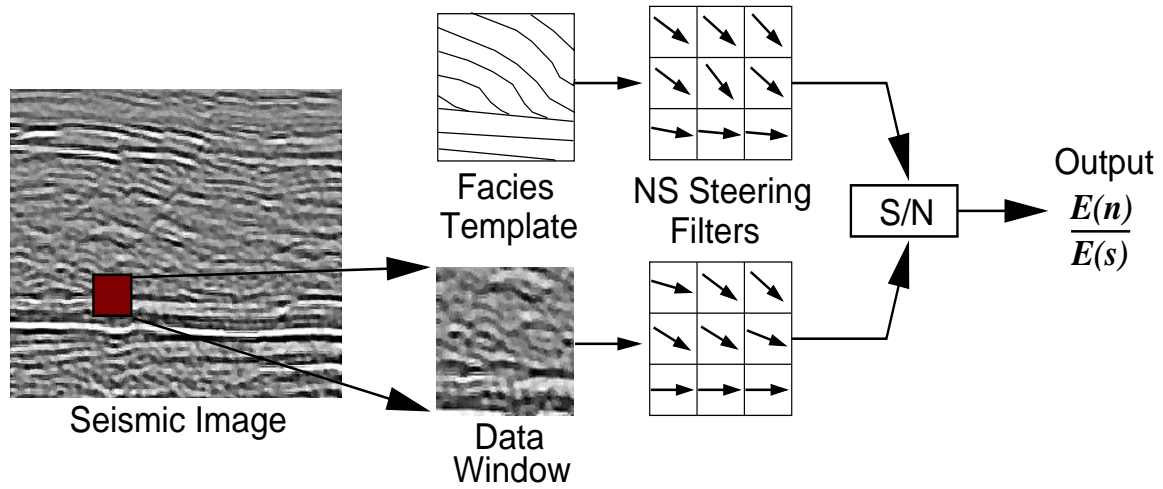


Figure 2: For each output point, extract a neighboring window of data the same size as the facies template. Capture the local dip spectra of the facies template and data window with simple nonstationary “steering filters”. Treating the facies template as the “noise” model, apply a predictive signal/noise separation technique to extract energy from the data window where the local dip coincides with that of the template. The output, simply the noise-to-signal ratio, is then a valid measure of local similarity. morgan2-algorithm2 [NR]

where the operators \mathbf{N} and \mathbf{S} represent $t - x$ domain convolution with prediction-error filters (PEF’s) which decorrelate the unknown noise \mathbf{n} and signal \mathbf{s} , respectively, and the factor ϵ balances the energies of the residuals. Explicitly minimizing the quadratic objective function suggested by equation (3) leads to the following expression for the predicted signal:

$$\mathbf{s} = \mathbf{N}^T \mathbf{N} (\mathbf{N}^T \mathbf{N} + \epsilon^2 \mathbf{S}^T \mathbf{S})^{-1} \mathbf{d} \quad (4)$$

Since the frequency response of the PEF approximates the inverse spectrum of the data used to estimate it, we see that Abma’s approach is similar to Wiener reconstruction.

If the noise is assumed a priori to be spatially uncorrelated, as in Abma (1995), the noise decorrelator \mathbf{N} is simply the identity. Gaussian noise is in the nullspace of the PEF estimation, so the signal decorrelator \mathbf{S} can be estimated reliably from the *data*, i.e., $\mathbf{S} = \mathbf{D}$, where \mathbf{D} is a data decorrelating filter. Otherwise, if the noise is correlated spatially, an explicit noise model is required to estimate \mathbf{N} , and an approach like the one used by Spitz (1999) to estimate \mathbf{S} . Modifying equation (3) to reflect Spitz’s choice of $\mathbf{S} = \mathbf{D}\mathbf{N}^{-1}$ and applying the constraint $\mathbf{n} = \mathbf{d} - \mathbf{s}$ gives

$$\begin{aligned} \mathbf{N}\mathbf{s} &\approx \mathbf{N}\mathbf{d} \\ \epsilon\mathbf{D}\mathbf{N}^{-1}\mathbf{s} &\approx \mathbf{0}. \end{aligned} \quad (5)$$

When solved iteratively, the problem can be preconditioned to improve convergence. Following Fomel et al. (1997), we can make the change of variables

$$\mathbf{s} = (\mathbf{D}\mathbf{N}^{-1})^{-1}\mathbf{p} = \mathbf{N}\mathbf{D}^{-1}\mathbf{p} \quad (6)$$

and rewrite equation (5):

$$\begin{aligned} \mathbf{NND}^{-1}\mathbf{p} &\approx \mathbf{Nd} \\ \epsilon\mathbf{p} &\approx 0. \end{aligned} \quad (7)$$

Brown et al. (1999) solved equation (7) iteratively to suppress ground roll with complicated moveout patterns, where \mathbf{S} and \mathbf{N} are nonstationary $t - x$ -domain PEF's. Clapp and Brown (1999) did the same for multiple reflections.

Unfortunately, the estimation of nonstationary PEF's is computationally costly, and it is often difficult to ensure that the filters are minimum-phase, a necessary requirement for stable deconvolution, as in equation (7). For the application at hand, the final result is not the estimated signal and noise, but simply the noise-to-signal ratio. It follows that the separation need not be perfect - just good enough to distinguish between regions of the data with gross similarity to the facies template from the rest of the data. A properly stacked or migrated seismic image should have no "crossing dips," and so can be conceptualized as a single-valued spatial function of local dip angle. Not surprisingly, we have found that simple three-point "steering filters" (Clapp et al., 1997), work well for the noise and data decorrelating filters, \mathbf{N} and \mathbf{D} , required to solve equation (7). The only thing needed to set up the steering filters is an estimate of the local dip field of the data and facies template, for which the automatic dip scanning technique of Claerbout (1992) produces satisfactory results.

Assuming that a given 2-D wavefield $u(t, x)$ is planar with unknown local dip p , the operator

$$\frac{\partial}{\partial x} + p \frac{\partial}{\partial t} \quad (8)$$

will extinguish it. If δ_x and δ_t are finite difference stencils for the continuous partial derivatives above, then equation (8) can be rewritten as a convolution, and hence cast as a univariate optimization for p :

$$r = (\delta_x + p\delta_t) * u(t, x) \approx 0. \quad (9)$$

Differentiating the quadratic functional $r^T r$ with respect to p gives an optimal estimate of the local dip:

$$p = -\frac{\delta_x u \cdot \delta_t u}{\delta_t u \cdot \delta_t u} \quad (10)$$

RESULTS

Synthetic Data Test

Figure 3 shows the synthetic seismic dataset and associated local dip estimate. Figure 4 shows the facies templates used to test the algorithm and their corresponding local dip estimates. The seismic data is a 200x100 2-D slice of the "quarter dome" 3-D model used to test seismic coherency algorithms (Claerbout, 1999; Schwab, 1998), and is characterized by two unconformities. The facies templates, 30x30 points each, are designed to resemble the upper and

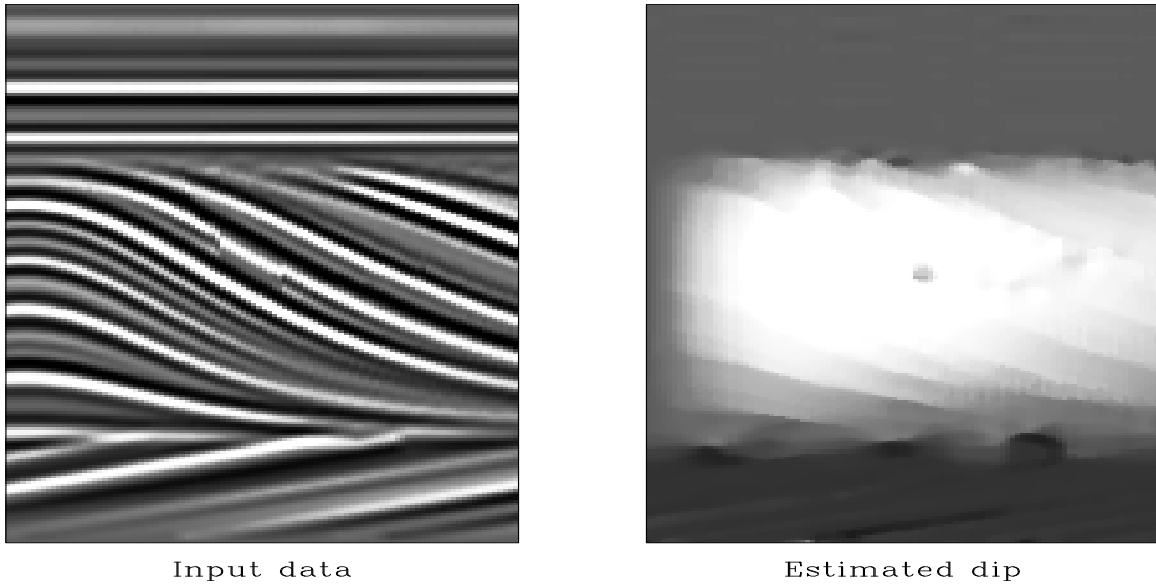
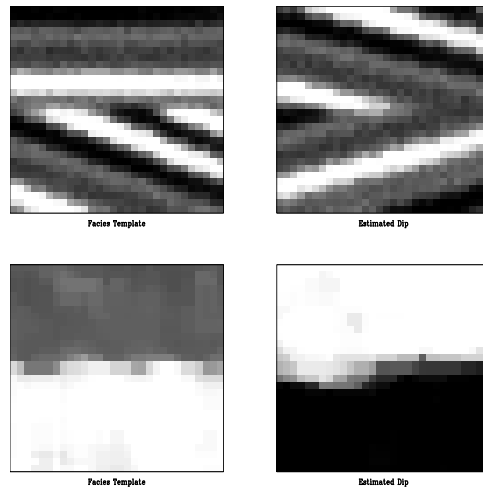


Figure 3: Left: Synthetic data, a modification of the “quarter-dome” model. Right: Estimated local dip. `morgan2-syn-datshow` [ER]

Figure 4: Top: Facies templates, corresponding to the upper and lower unconformities in the data (Figure ??), respectively. Bottom: Estimated local dip of facies templates shown above. `morgan2-syn-trnshow` [ER]



lower unconformities, respectively, but are not windowed directly from the data itself. Notice that the dip changes continuously across the faces of the unconformities.

Figures 5 and 6 show the output of the pattern recognition program, where the experiments were designed to detect the upper and lower unconformities, respectively. The results are good, but expected, given the high quality of the estimated dip, and provide adequate proof of concept.

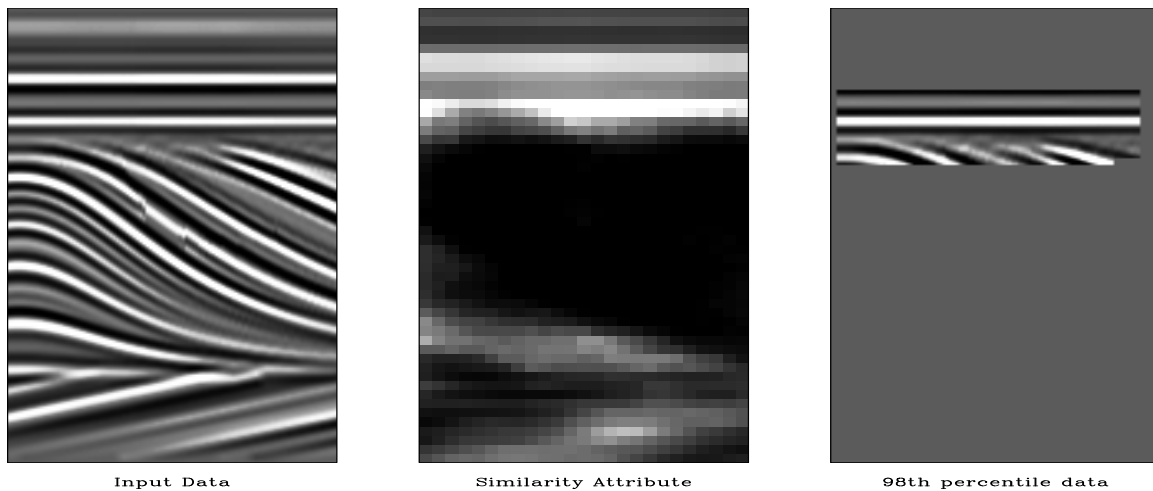


Figure 5: Left: Synthetic data. Center: Output similarity attribute, relative to upper unconformity. Right: Local data windows corresponding to the 98th percentile and higher values in the similarity attribute. `morgan2-syn-pmatch2` [ER]

Real Data Test

Figure 7 shows the real 2-D seismic image and its associated local dip estimate. The image processed here is a 200x200 subwindow from a migrated 2-D section originally acquired by Mobil over a Gulf of Mexico prospect. The upper portion of the windowed data is characterized by an unconformity. Figure 8 shows the facies template used to test the algorithm and the corresponding local dip estimate. The 50x50 template was created artificially and is designed to resemble the unconformity in the data.

The quality of the dip estimates is critical to the success of the algorithm, but unfortunately these estimates are more prone to error with real data than they are for synthetic data (Compare Figures 3 and 7). In order to maximize the spatial coherency of the input data, and hence the robustness of the dip estimate, some smoothing of the data may be required prior to processing. In this case, the estimated dip field was smoothed using a local weighted mean filter, where the weights are the so-called “normalized correlation” measure of Claerbout (1992) - roughly speaking, a measure of the data’s local “plane-waveness”. Figure 9 shows the output of the pattern recognition program. The results are good, having effectively done the same job as a human interpreter, even with a less-than-perfect dip estimate (Figure 8).

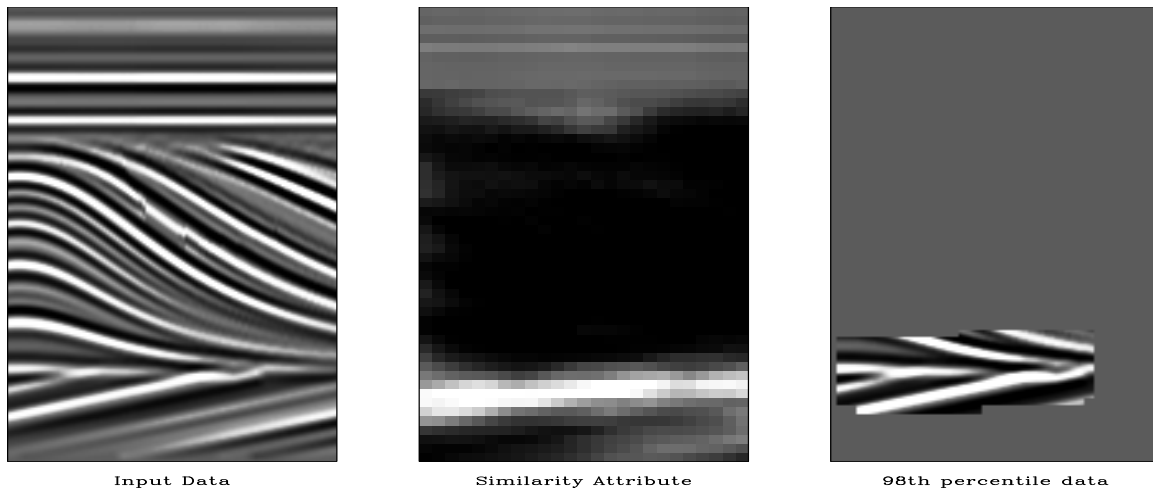


Figure 6: Left: Synthetic data. Center: Output similarity attribute, relative to lower unconformity. Right: Local data windows corresponding to the 98th percentile and higher values in the similarity attribute. `morgan2-syn2-pmatch2` [ER]

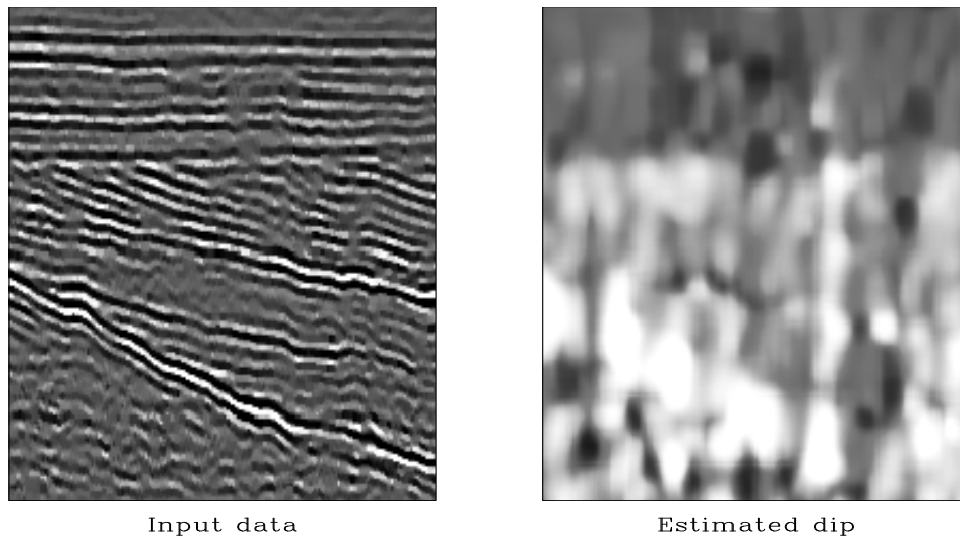
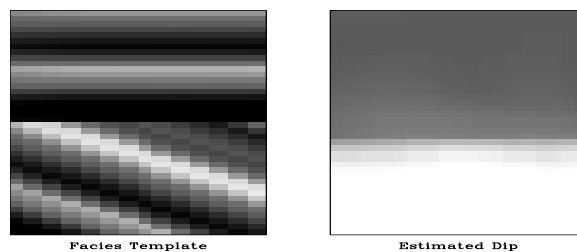


Figure 7: Left: Sub-window from real 2-D seismic image. Right: Estimated local dip. `morgan2-seis-datshow` [ER]

Figure 8: Left: Facies templates, corresponding to the unconformities in the upper part of the data (Figure 7). Right: Estimated local dip. `morgan2-seis-trnshow` [ER]



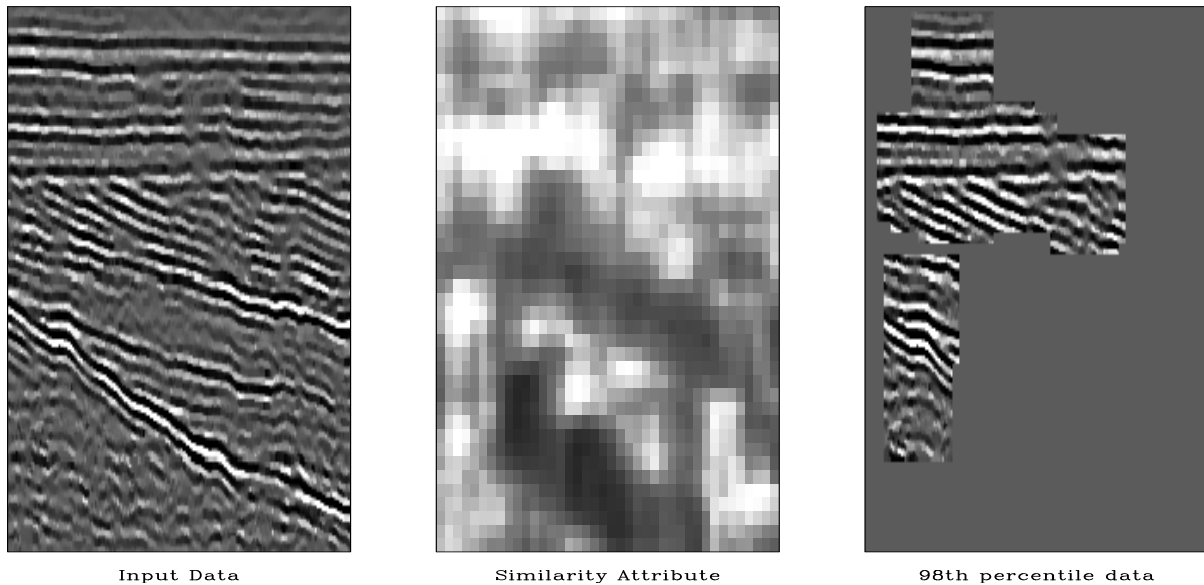


Figure 9: Left: Window from real 2-D seismic image. Center: Output similarity attribute, relative to lower unconformity. Right: Local data windows corresponding to the 98th percentile and higher values in the similarity attribute. `morgan2-seis-pmatch2` [ER]

DISCUSSION

Given quality local dip estimates of the facies template and seismic image, our approach may seem like overkill. The simplest alternative would be a direct subtraction approach, i.e., extract small windows the same size as the facies template from the seismic image's dip estimate, then take the RMS difference of it and the facies template's dip estimate and sum to get the attribute value. Such an approach would surely suffer from the extreme sensitivity of Claerbout's (1992) dip estimation technique to discontinuities in the data. The estimated local dip is anomalously high at discontinuities, and would thus skew a sum of squared differences. Bednar (1997) defined the dip estimate as a coherency attribute based on this property.

A second alternative method might use the fact that any decorrelating filter whitens the spectrum of the data. If a decorrelating filter is obtained for the facies template, then convolved with the seismic image, the local spectrum of the output should be whitest where the image most resembles the facies template. Unfortunately, this would require some measure of whiteness, i.e., how closely does the local autocorrelation of the residual resemble a spike, so in some sense we'd be back to square one. In any case, the authors have found through experience that direct interpretation of the residual to this end is often nonintuitive.

In practice, the method will interpret some regions which are obviously *not* the same geologic feature as the facies template as such. This brings up an important caveat: the program interprets data in terms of local dip spectrum only; *not* contextually. Such contextual interpretation is best done by a human, and certainly this will remain true for some time. Our method simply makes human interpretation of 3-D images *feasible* by directing the interpreter to the

regions of the data which have a local dip spectrum which *might* match the facies template. Look for regions in Figure 9 which have a similar dip spectrum as the template of Figure 8 – you should be able to find many.

The algorithm we presented is still in prototype stage, but nonetheless, we are encouraged by the performance characteristics. The algorithm required approximately five minutes on a single processor of our SGI Origin 200 to compute the real data example (Figure 9), including the dip estimation. We subsampled the 200x100-point output space by a factor of five, both spatially and temporally, for a total of 1600. These figures are not stunningly good, considering that the number of output points in many 3-D seismic images may number a million or more, but two facts leave room for improvement. First, since the output depends only on the input, the algorithm is highly parallelizable. Second, since the actual signal/noise separation panels are not output, we have found that the number of iterations per output point may be cut radically, say to five or less.

Our approach may also be useful in AVO analysis. AVO anomalies are relatively easy to spot, meaning a simple facies template, but the sheer volume of the data makes hand interpretation tedious.

Currently our approach operates on 2-D data only, and we believe that the extension to 3-D is possible, but there are theoretical issues to take stock of. Fomel (1999) discusses these issues in detail; I paraphrase his work here. In 2-D, the dip p is a scalar value; in 3-D it is a vector: $\mathbf{p} = [p_x \ p_y]^T$. Plane waves in 3-D can be extinguished (Schwab, 1998) by a cascade of convolutional operators similar to the operator of equation (8). The matrix equivalent of such an operator is nonsquare and thus noninvertible. Unfortunately, for this application, we require the inverse, i.e., equation (7). Dubbing this composite operator \mathbf{A} , Fomel forms $\mathbf{A}^T \mathbf{A}$ and performs spectral factorization to produce a single minimum phase operator.

REFERENCES

- Abma, R., 1995, Least-squares separation of signal and noise with multidimensional filters: Ph.D. thesis, Stanford University.
- Bednar, J. B., 1997, Least squares dip and coherency attributes: SEP-95, 219–225.
- Brown, M., Clapp, R. G., and Marfurt, K., 1999, Predictive signal/noise separation of groundroll-contaminated data: SEP-102, 111–128.
- Castleman, K. R., 1996, Digital image processing: Prentice-Hall.
- Claerbout, J. F., 1992, Earth Soundings Analysis: Processing versus Inversion: Blackwell.
- Claerbout, J., 1999, Geophysical estimation by example: Environmental soundings image enhancement: Stanford Exploration Project, <http://sepwww.stanford.edu/sep/prof/>.
- Clapp, R. G., and Brown, M., 1999, Applying sep's latest tricks to the multiple suppression problem: SEP-102, 91–100.

- Clapp, R. G., Fomel, S., and Claerbout, J., 1997, Solution steering with space-variant filters: SEP-95, 27-42.
- Fomel, S., Clapp, R., and Claerbout, J., 1997, Missing data interpolation by recursive filter preconditioning: SEP-95, 15-25.
- Fomel, S., 1999, Plane wave prediction in 3-D: SEP-102, 101-110.
- Leon-Garcia, A., 1994, Probability and random processes for electrical engineering: Addison-Wesley.
- Randen, T., Reymond, B., Sjulstad, H. I., and Soenneland, L., 1998, New seismic attributes for automated stratigraphic facies boundary detection: New seismic attributes for automated stratigraphic facies boundary detection:, 68th Annual Internat. Mtg., Soc. Expl. Geophys., Expanded Abstracts, 628-631.
- Schwab, M., 1998, Enhancement of discontinuities in seismic 3-D images using a Java estimation library: Ph.D. thesis, Stanford University.
- Spitz, S., 1999, Pattern recognition, spatial predictability, and subtraction of multiple events: The Leading Edge, 18, no. 1, 55-58.

Origin of Gassmann's equations

James G. Berryman¹

ABSTRACT

A short tutorial on the derivation of Gassmann's equations is provided.

INTRODUCTION

Gassmann's relations are receiving more attention as seismic data are increasingly used for reservoir monitoring. Correct interpretation of underground fluid migration from seismic data requires a quantitative understanding of the relationships among the velocity data and fluid properties in the form of fluid substitution formulas, and these formulas are very commonly based on Gassmann's equations. Nevertheless, confusion persists about the basic assumptions and the derivation of Gassmann's (1951) well-known equation in poroelasticity relating dry or drained bulk elastic constants to those for fluid saturated and undrained conditions. It is frequently stated, for example, but quite incorrect to say that Gassmann *assumes* the shear modulus is constant, *i.e.*, mechanically independent of the presence of the saturating fluid. This note clarifies the situation by presenting an unusually brief derivation of Gassmann's relations that emphasizes the true origin of the constant shear modulus *result*, while also clarifying the role played by the shear modulus in the derivation of the better understood result for the bulk modulus.

DERIVATION FOR ISOTROPIC POROUS MEDIA

I now present a very concise, but nevertheless complete, derivation of Gassmann's famous results. For the sake of simplicity, the analysis that follows is limited to isotropic systems, but it can be generalized with little difficulty to anisotropic systems (Gassmann, 1951; Brown and Korringa, 1975; Berryman, 1998). Gassmann's (1951) equations relate the bulk and shear moduli of a saturated isotropic porous, monomineralic medium to the bulk and shear moduli of the same medium in the drained case and shows furthermore that the shear modulus *must be* mechanically independent of the presence of the fluid. An important implicit assumption is that there is no chemical interaction between porous rock and fluid that affects the moduli; if such effects are present, we assume the medium is drained (rather than dry) but otherwise neglect chemical effects for this argument. Gassmann's paper is concerned with the quasistatic

¹email: berryman@sep.stanford.edu

(low frequency) analysis of the elastic moduli and that is what we emphasize here also. Generalization to higher frequency effects and complications arising in wave propagation due to frequency dispersion are well beyond the scope of what we present.

In contrast to simple elasticity with stress tensor σ_{ij} and strain tensor e_{ij} , the presence of a saturating pore fluid in porous media introduces the possibility of an additional control field and an additional type of strain variable. The pressure p_f in the fluid is the new field parameter that can be controlled. Allowing sufficient time (equivalent to a low frequency assumption) for global pressure equilibration will permit us to consider p_f to be a constant throughout the percolating (connected) pore fluid, while restricting the analysis to quasistatic processes. The change ζ in the amount of fluid mass contained in the pores is the new type of strain variable, measuring how much of the original fluid in the pores is squeezed out during the compression of the pore volume while including the effects of compression or expansion of the pore fluid itself due to changes in p_f . It is most convenient to write the resulting equations in terms of compliances s_{ij} rather than stiffnesses c_{ij} , so for an isotropic porous medium (chosen only for the sake of its simplicity) the basic equation to be considered takes the form:

$$\begin{pmatrix} e_{11} \\ e_{22} \\ e_{33} \\ -\zeta \end{pmatrix} = \begin{pmatrix} s_{11} & s_{12} & s_{12} & -\beta \\ s_{12} & s_{11} & s_{12} & -\beta \\ s_{12} & s_{12} & s_{11} & -\beta \\ -\beta & -\beta & -\beta & \gamma \end{pmatrix} \begin{pmatrix} \sigma_{11} \\ \sigma_{22} \\ \sigma_{33} \\ -p_f \end{pmatrix}. \quad (1)$$

The constants β and γ appearing in the matrix on the right hand side will be defined later. It is important to write the equations this way rather than using the inverse relation in terms of the stiffnesses, because the compliances s_{ij} appearing in (1) are simply and directly related to the drained constants λ_{dr} and μ_{dr} (the Lamé parameters for the isotropic porous medium in the drained case) in the same way they are related in normal elasticity (the matrix s_{ij} is just the inverse of the matrix c_{ij}), whereas the individual stiffnesses c_{ij}^* (the * superscript indicates the constants for the saturated case) obtained by inverting the equation in (1) must contain coupling terms through the parameters β and γ that depend on the porous medium and fluid compliances. Using the standard relations for the isotropic moduli, I find that

$$s_{11} = \frac{1}{E_{dr}} = \frac{\lambda_{dr} + \mu_{dr}}{\mu_{dr}(3\lambda_{dr} + 2\mu_{dr})} = \frac{1}{9K_{dr}} + \frac{1}{3\mu_{dr}} \quad (2)$$

and

$$s_{12} = -\frac{\nu_{dr}}{E_{dr}} = \frac{1}{9K_{dr}} - \frac{1}{6\mu_{dr}}, \quad (3)$$

where the drained Young's modulus E_{dr} is defined in terms of the drained bulk modulus K_{dr} and shear modulus μ_{dr} by the second equality of (2) and the drained Poisson's ratio is determined by

$$\nu_{dr} = \frac{\lambda_{dr}}{2(\lambda_{dr} + \mu_{dr})}. \quad (4)$$

The fundamental results of interest (Gassmann's equations) are found by considering the saturated (and undrained) case such that

$$\zeta \equiv 0, \quad (5)$$

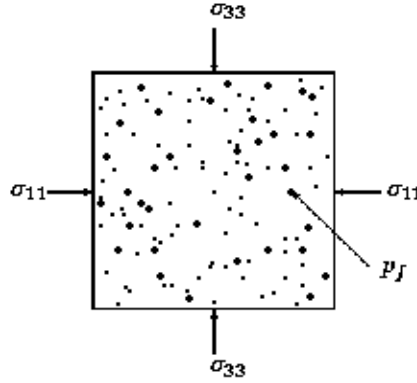


Figure 1: Vertical and horizontal applied stresses are given by σ_{33} and σ_{11} , respectively. The pore pressure is p_f . [jim2-poroelast3] [NR]

which — by making use of (1) — implies that the pore pressure must respond to external applied stresses according to

$$p_f = -\frac{\beta}{\gamma}(\sigma_{11} + \sigma_{22} + \sigma_{33}). \quad (6)$$

Equation (6) is often called the “pore-pressure buildup” equation (Skempton, 1954). Then, using this result to eliminate both ζ and p_f from (1), I obtain

$$\begin{pmatrix} e_{11} \\ e_{22} \\ e_{33} \end{pmatrix} = \begin{pmatrix} s_{11}^* & s_{12}^* & s_{12}^* \\ s_{12}^* & s_{11}^* & s_{12}^* \\ s_{12}^* & s_{12}^* & s_{11}^* \end{pmatrix} \begin{pmatrix} \sigma_{11} \\ \sigma_{22} \\ \sigma_{33} \end{pmatrix} = \left[\begin{pmatrix} s_{11} & s_{12} & s_{12} \\ s_{12} & s_{11} & s_{12} \\ s_{12} & s_{12} & s_{11} \end{pmatrix} - \frac{\beta^2}{\gamma} \begin{pmatrix} 1 & 1 & 1 \\ 1 & 1 & 1 \\ 1 & 1 & 1 \end{pmatrix} \right] \begin{pmatrix} \sigma_{11} \\ \sigma_{22} \\ \sigma_{33} \end{pmatrix} \quad (7)$$

where s_{ij}^* is the desired compliance including the effects of the trapped fluid, while s_{ij} is the compliance in the absence of the fluid. Since for elastic isotropy there are only two independent coefficients (s_{11} and s_{12}), I find that (7) reduces to one expression for the diagonal compliance

$$s_{11}^* = s_{11} - \frac{\beta^2}{\gamma}, \quad (8)$$

and another for the off-diagonal compliance

$$s_{12}^* = s_{12} - \frac{\beta^2}{\gamma}. \quad (9)$$

If K^* and μ^* are respectively the undrained bulk and shear moduli, then (2) and (3) together with (8) and (9) imply that

$$\frac{1}{9K^*} + \frac{1}{3\mu^*} = \frac{1}{9K_{dr}} + \frac{1}{3\mu_{dr}} - \frac{\beta^2}{\gamma}, \quad (10)$$

and

$$\frac{1}{9K^*} - \frac{1}{6\mu^*} = \frac{1}{9K_{dr}} - \frac{1}{6\mu_{dr}} - \frac{\beta^2}{\gamma}. \quad (11)$$

Subtracting (11) from (10) shows immediately that $1/2\mu^* = 1/2\mu_{dr}$ or equivalently that

$$\mu^* = \mu_{dr}. \quad (12)$$

Thus, the first *result* of Gassmann is that, for purely mechanical effects, the shear modulus for the case with trapped fluid (undrained) is the same as that for the case with no fluid (drained). Then, substituting (12) back into either (10) or (11) gives one form of the result commonly known as Gassmann's equation for the bulk modulus:

$$\frac{1}{K^*} = \frac{1}{K_{dr}} - \frac{9\beta^2}{\gamma}. \quad (13)$$

I want to emphasize that the analysis presented shows clearly that (12) is a definite *result* of this analysis, *not an assumption*. In fact, we must have (12) in order for (13) to hold, and furthermore, if (13) holds, then so must (12). Thus, monitoring any changes in shear modulus with changes of fluid content (say through shear velocity measurements) provides a test of both Gassmann's assumptions (homogeneous frame, no chemical effects, & low frequencies) and results.

To obtain one of the more common forms of Gassmann's result for the bulk modulus, first note that

$$3\beta = \frac{1}{K_{dr}} - \frac{1}{K_g} \equiv \frac{\alpha}{K_{dr}}, \quad (14)$$

where K_g is the grain modulus of the solid constituent present and α is the Biot-Willis parameter (Biot and Willis, 1957). Furthermore, the parameter γ is related through (6) to Skempton's pore-pressure buildup coefficient B , so that

$$\frac{3\beta}{\gamma} = B. \quad (15)$$

Substituting these results into (13) gives

$$K^* = \frac{K_{dr}}{1 - \alpha B}, \quad (16)$$

which is another form (Carroll, 1980) of Gassmann's standard result for the bulk modulus.

ACKNOWLEDGMENTS

I thank Michael L. Batzle and Patricia A. Berge for helpful comments on the manuscript.

REFERENCES

Berryman, J. G., 1998, Transversely isotropic poroelasticity arising from thin isotropic layers: in *Mathematics of Multiscale Materials*, K. M. Golden, G. R. Grimmett, R. D. James, G. W. Milton, and P. N. Sen (eds.), Springer, New York, pp. 37–50.

Biot, M. A., and D. G. Willis, 1957, The elastic coefficients of the theory of consolidation: *J. App. Mech.* **24**, 594–601.

Brown, R. J. S., and J. Korringa, 1975, On the dependence of the elastic properties of a porous rock on the compressibility of the pore fluid: *Geophysics* **40**, 608–616.

Carroll, M. M., 1980, Mechanical response of fluid-saturated porous materials: in *Theoretical and Applied Mechanics*, F. P. J. Rimrott and B. Tabarrok (eds.), Proceedings of the 15th International Congress of Theoretical and Applied Mechanics, Toronto, August 17–23, 1980, North-Holland, Amsterdam, 1980, pp. 251–262.

Gassmann, F., 1951, Über die Elastizität poroser Medien: *Veierteljahrsschrift der Naturforschenden Gesellschaft in Zürich* **96**, 1–23.

Skempton, A. W., 1954, The pore-pressure coefficients *A* and *B*: *Geotechnique* **4**, 143–147.

Seismic velocity decrement ratios for regions of partial melt near the core-mantle boundary

James G. Berryman¹

ABSTRACT

For regions of partial melt in the lower mantle, both compressional and shear wave velocities decrease monotonically with increasing melt volume fraction. It has been observed that regions close to the core-mantle boundary thought to contain partial melt have a velocity decrement ratio (relative change in shear velocity over relative change of compressional velocity) of about 3. This is certainly a high value for this ratio and arguments based on effective medium theories have been given to show that such values are predicted for partial melt systems. The present work confirms the value of 3 near the core-mantle boundary. It is shown, furthermore, that the velocity decrement ratio can be estimated without detailed knowledge of, or assumptions about, the microstructure of the partial melt system by using Gassmann's equation of poroelasticity together with some reasonable assumptions about the change (or lack of change) of the density and bulk modulus for lower mantle pressure and temperature conditions.

INTRODUCTION

A number of recent papers (*Williams and Garnero, 1996; Revenaugh and Meyer, 1997; Wen and Helmberger, 1998a; 1998b*) have shown that the ratio of seismic velocity decrements $d \ln v_s / d \ln v_p$ (where v_s is the shear velocity, v_p is the compressional velocity) is approximately equal to 3 in ultralow velocity zones near the the core-mantle boundary (see *Young and Lay (1987)* for a review of CMB issues). Changes in both numerator and denominator are negative but the ratio has been found to be on the order of 3, and because this value is so high it is generally argued that these results provide evidence of partial melt in these regions. The rock physics analyses used in these papers are generally based on classical effective medium theories such as those reviewed by *Watt et al. (1976)*. The main problem with such analyses is that the results tend to be quite sensitive to the assumed microstructure of the partial melt system [see *Williams and Garnero (1996)*] and therefore may not be truly representative of the system being studied. I will give a different derivation here of the velocity decrement ratio that highlights the key assumptions that must be made to arrive at this ratio. This approach shows how general and insensitive to microstructure the *ratio* really is for partial melt systems, and shows furthermore how to analyze deviations from the assumptions made. The methods presented may also be extended to permit estimates of changes not only of the ratio but also of

¹email: berryman@sep.stanford.edu

the two seismic velocities themselves. A procedure for doing so is outlined at the end of the paper.

SEISMIC VELOCITIES FOR PARTIAL MELT SYSTEMS

The velocities, v_p and v_s , are related to the bulk (K) and shear (μ) moduli and the density (ρ) of the system by the well-known relations:

$$v_p = \sqrt{\left(K + \frac{4}{3}\mu\right) / \rho}, \quad (1)$$

and

$$v_s = \sqrt{\mu / \rho}. \quad (2)$$

These results are usually derived for elastic systems, but are also valid for poroelastic systems when the frequencies are small enough, and seismic frequencies are virtually always small enough.

Velocity analysis

It is not hard to show that the bulk and shear moduli can both be assumed to be decreasing functions of the volume fraction of partial melt. When there is no melt, the solid material constants are K_g for the purely solid (or grain) bulk modulus and μ_g for the purely solid shear modulus. As solid transforms into melt, the melt volume fraction is ϕ and the remaining solid volume fraction is $1 - \phi$. General relations for the changing elastic constants for small to modest values of ϕ are

$$K_{sat} = K_g(1 - c_1\phi), \quad (3)$$

and

$$\mu_{sat} = \mu_g(1 - c_2\phi). \quad (4)$$

The new symbols used here are K_{sat} for bulk modulus of solid containing pores saturated with melt, μ_{sat} for shear modulus of solid containing pores saturated with melt, and c_1 and c_2 are nonnegative, dimensionless parameters. (If we were to do perturbation theory for small ϕ around the solid limit, then these parameters would be constant, independent of ϕ . But, we will instead use a more rigorous approach based on Gassmann's equation (Gassmann, 1951) and arrive at exact results for c_1 that incorporate ϕ dependence and are therefore valid for a much wider range of values than would be possible using perturbation theory.) If in addition we make the assumption which is commonly made about these systems [see Williams and Garnero (1996)] that the melt density is approximately the same as that of the solid material, then we have the additional formula for changes in density

$$d\rho \simeq 0. \quad (5)$$

$$d \ln v_p = \frac{1}{2} d \ln \left(K_{sat} + \frac{4}{3} \mu_{sat} \right) \simeq -\frac{1}{2} \frac{c_1 K_g + c_2 \frac{4}{3} \mu_g}{K_g + \frac{4}{3} \mu_g} \phi, \quad (6)$$

and

$$d \ln v_s = \frac{1}{2} d \ln \mu_{sat} \simeq -\frac{1}{2} c_2 \phi. \quad (7)$$

To simplify the expression in (6) further, we can make use of the well-known approximation that

$$\frac{v_p}{v_s} \simeq 2. \quad (8)$$

(We relax this strong assumption later in the paper.) Substituting (1) and (2) into (8) shows that

$$K_g \simeq \frac{8}{3} \mu_g, \quad (9)$$

which when substituted into (6) shows that

$$d \ln v_p \simeq -\frac{1}{6} (2c_1 + c_2) \phi. \quad (10)$$

Gassmann's equation

How does the constant c_1 depend on the fluid bulk modulus in a region of partial melt? The analysis usually quoted for addressing this problem in regions of partial melt have normally used some type of classical effective medium theory, which is most appropriately used for systems in which the inclusions are both disconnected and of small volume fraction ϕ . However, partial melt systems in the upper mantle are generally believed to be dominated by connected tubes of melt lying along grain edges (*Waff and Bulau, 1979; Mavko, 1980; Toramaru and Fujii, 1986*). When the fluid is in pressure-temperature equilibrium with its surroundings, it therefore makes sense to consider Gassmann's equations (*Gassmann, 1951; Berryman, 1995*) from the theory of poroelasticity for the system. This approach is particularly appealing for this problem because, except for an assumption of fluid connectedness, Gassmann's equations do not depend explicitly on the microgeometry, and this simplification should permit universal behavior to be predicted by the resulting theory.

Gassmann's equation for fluid substitution is often written to emphasize the change in saturated bulk modulus K_{sat} from that of the drained bulk modulus K_{dr} . The well-known result is

$$K_{sat} = K_{dr} + \frac{\alpha^2}{(\alpha - \phi)/K_g + \phi/K_f}, \quad (11)$$

where ϕ is the fluid-saturated porosity, K_g is the solid or grain material bulk modulus, K_f is the bulk modulus of the saturating fluid (the melt for this application), and

$$\alpha = 1 - \frac{K_{dr}}{K_g} \quad (12)$$

is the Biot-Willis (or effective stress) parameter. Formula (11) can be rearranged to emphasize how the saturated bulk modulus changes as the value of K_f deviates from the value of the solid bulk modulus K_g . The result is

$$K_{sat} = K_g(1 - c_1\phi), \quad (13)$$

where

$$c_1 = \frac{K_g/K_f - 1}{1 + (\phi/\alpha)(K_g/K_f - 1)}. \quad (14)$$

An important observation follows easily from (14). If the fluid bulk modulus satisfies $K_f \equiv K_g$, then $c_1 \equiv 0$ and the saturated bulk modulus is the same as that of the solid material. This is a definite prediction of Gassmann's formula. This is *not* a surprising result however, because it is also a quite general prediction of homogenization theory (for example, the well-known Hashin-Shtrikman bounds (Hashin and Shtrikman, 1963) also degenerate to a constant value when the constituents have the same moduli). If $K_f = K_g$ then the bulk modulus is actually uniform throughout the medium. The point of (14) is that it shows in addition how to compute deviations from this case when $K_f \neq K_g$ but $K_f \simeq K_g$. The result is independent of the details of the geometry of the melt system as long as the melt is connected (percolating) throughout the volume.

Predicted decrement ratio

To complete the analysis we need one more fact or approximation. We have assumed that the density of the melt differs little from that of the solid. The Birch-Murnaghan equations (Birch, 1938; 1952; Anderson, 1989) show that the bulk moduli of solid systems change in a predictable way as a function of the changing density. A similar result for simple liquids known as Rao's rule (Rao, 1941) also shows that the bulk modulus of many pure (*i.e.*, single constituent) liquids is also a simple function of the density. Based on these results, if the density of the melt is the same as that of the surrounding solid, then we expect the bulk modulus of the melt to differ very little (on the order of a few per cent) even though the shear modulus has dropped from a finite value to zero. We have shown in the preceding paragraph that, if the fluid inclusions have the same bulk modulus as the solid, then $K_{sat} = K_g$ and $c_1 = 0$. We expect this approximation to have the same level of validity as the approximation that the density is constant (which is to say that we think of it as a reasonable first approximation). With this approximation substituted into (10), we find that

$$\frac{d \ln v_s}{d \ln v_p} \simeq 3. \quad (15)$$

This is correct as long as $c_2 \neq 0$. But the shear modulus will necessarily decrease as the melt fraction increases, since, for fixed overall shear distortion, less shear energy can be stored in the system, and this implies that $c_2 > 0$. Computing the actual value of c_2 requires a model of the microstructure, but the result (15) shows that the precise value c_2 is not required to obtain the desired result in (15), since it cancels out of the final formula.

EXTENSION, EXAMPLES, AND EXPERIMENT

If the actual ratio v_p/v_s differs significantly from (8), then we can repeat the calculation using the parametrization

$$\frac{v_p}{v_s} = 2\sqrt{1 - \delta}, \quad (16)$$

where δ is a small number on the order of $\delta \simeq 0.5$ or less. The general result then becomes

$$\frac{d \ln v_s}{d \ln v_p} \simeq \frac{3v_p^2}{4v_s^2} = 3(1 - \delta), \quad (17)$$

showing, for example, that solid material $v_p/v_s \simeq 1.4$ or 1.7 implies a decrement ratio $\simeq 1.5$ or 2.2 , respectively. A plot of these results is shown in Figure 1, where various models (*Doornbos and Mondt, 1979; Dziewonski and Anderson, 1981; Kennett and Engdahl, 1991*) of the velocities at the core-mantle boundary are used to provide specific examples of the predictions obtained using this approach. For comparison, the value anticipated for olivine at 2 GPa in the upper mantle is also plotted to show that the results obtained are very close to those of *Mavko (1980)*, who used much more detailed model calculations to arrive at the result. (*Mavko (1980)* found, using various assumed microstructures and a self-consistent effective medium approach, that the expected change was about 10% in shear velocity and about 5% in compressional velocity, giving a decrement ratio of about 2 – which compares favorably with the result 2.2 obtained here for olivine.) Table 1 lists the special values used for the plot.

To see how these results compare with the observations, consider the plots of *Revenaugh and Meyer (1997)* showing that, for the most credible models of lower mantle deviations from IASP91, the seismic velocity decrement can lie in the range from 2 to 5, with the most likely value being approximately equal to 3.

TABLE 1. Seismic v_p/v_s ratios and predicted velocity decrement ratios at the core-mantle boundary for some standard earth models, and olivine at 2 GPa.

Earth Model	v_p/v_s	$d \ln v_s/d \ln v_p$
PEMC-L01	1.9105	2.738
PREM	1.8866	2.669
IASP91	1.8751	2.637
Material		
Olivine	1.72	2.219

CONCLUSIONS

This analysis has shown that a seismic velocity decrement ratio of about 3 is expected in partial melt systems at the core mantle boundary based on an elementary use of Gassmann's equations (Gassmann, 1951) and some simple assumptions about small changes in density and bulk modulus near the CMB.

Corrections to these results can also be computed using the formulas presented. If the density changes significantly, then (6) and (7) must be modified using (1) and (2). Rao's rule (Rao, 1941) can then be used to obtain estimates of K_f , and these results substituted into (14). Effective medium theory (Watt *et al.*, 1976; Berryman, 1995) is required in these more precise calculations to determine K_{dr} for use in (12) and again in (14), and similarly to determine c_2 for the shear modulus.

ACKNOWLEDGMENTS

I thank Pat Berge for suggesting this problem and Jeff Roberts for numerous helpful discussions about partial melt systems.

REFERENCES

- Anderson, D. L., 1989, *Theory of the Earth*, Blackwell, Boston, pp. 90–91.
- Berryman, J. G., 1995, Mixture theories for rock properties: in *Rock Physics and Phase Relations: American Geophysical Union Handbook of Physical Constants*, T. J. Ahrens (ed.), AGU, New York, pp. 205–228.
- Biot, M. A., and D. G. Willis, 1957, The elastic coefficients of the theory of consolidation: *J. App. Mech.* **24**, 594–601.

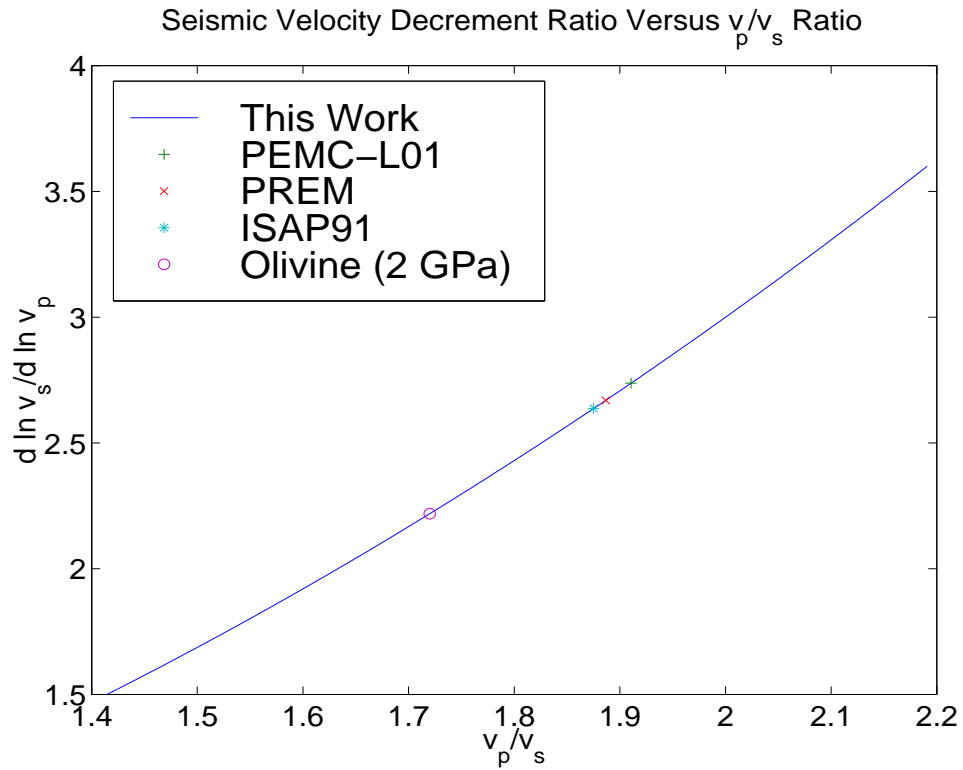


Figure 1: Plot of the dependence of the theoretically predicted seismic velocity decrement ratio on the v_p/v_s ratio. Specific points shown correspond to values of v_p/v_s for the lower mantle just above the core-mantle boundary for various models: PEMC-L01 (*Doornbos and Mondt, 1979*), PREM (*Dziewonski and Anderson, 1981*) and IASP91 (*Kennett and Engdahl, 1991*). For comparison, the result for olivine at 2 GPa with $v_p/v_s \simeq 1.72$, which would be typical of upper mantle conditions, is also shown. jim3-various [NR]

- Birch, F., 1938, The effect of pressure upon the elastic parameters of isotropic solids, according to Murnaghan's theory of finite strain: *J. Appl. Phys.* **9**, 279–288.
- Birch, F., 1952, Elasticity and constitution of the Earth's interior: *J. Geophys. Res.* **57**, 227–286, 1952.
- Doornbos, D. J., and J. C. Mondt, 1979, *P* and *S* waves diffracted around the core and the velocity structure at the base of the mantle: *Geophys. J. R. Astron. Soc.* **57**, 381–395.
- Dziewonski, A. M., and D. L. Anderson, 1981, Preliminary Reference Earth Model: *Phys. Earth Planet. Inter.* **25**, 297–356.
- Gassmann, F., 1951, Über die Elastizität poröser Medien: *Veierteljahrsschrift der Naturforschenden Gesellschaft in Zürich* **96**, 1–23.
- Hashin, Z., and S. Shtrikman, 1963, A variational approach to the elastic behavior of multiphase materials: *J. Mech. Phys. Solids* **11**, 127–140.
- Kennett, B. L. N., and E. R. Engdahl, 1991, Traveltimes for global earthquake location and phase identification: *Geophys. J. Int.* **105**, 429–465.
- Mavko, G. M., 1980, Velocity and attenuation in partially molten rocks: *J. Geophys. Res.* **85**, 5173–5189.
- Rao, M. R., 1941, Velocity of sound in liquids and chemical constitution: *J. Chem. Phys.* **9**, 682–686.
- Revenaugh, J., and R. Meyer, 1997, Seismic evidence of partial melt within a possibly ubiquitous low-velocity layer at the base of the mantle: *Science* **277**, 670–673.
- Toramaru, A., and N. Fujii, 1986, Connectivity of melt phase in a partially molten peridotite: *J. Geophys. Res.* **91**, 9239–9252.
- Waff, H. S., and J. R. Bulau, 1979, Equilibrium fluid distribution in an ultramafic partial melt under hydrostatic stress conditions: *J. Geophys. Res.* **84**, 6109–6114.
- Watt, J. P., G. F. Davies, and R. J. O'Connell, 1976, Elastic properties of composite materials: *Rev. Geophys. Space Phys.* **14**, 541–563.
- Wen, L. and D. V. Helmberger, 1998a, Ultra-low velocity zones near the core-mantle boundary from broadband PKP precursors: *Science* **279**, 1701–1703.
- Wen, L. and D. V. Helmberger, 1998b, A two-dimensional P-SV hybrid method and its application to modeling localized structures near the core-mantle boundary: *J. Geophys. Res.* **103**, 17901–17918.
- Williams, Q., and E. J. Garnero, 1996, Seismic evidence for partial melt at the base of Earth's mantle: *Science* **273**, 1528–1530.
- Young, C. J., and T. Lay, 1987, The core-mantle boundary: *Annual Rev. Earth Planet. Sci.* **15**, 25–46.

Additions to SEPlib

*Robert G. Clapp*¹

ABSTRACT

The release of this report coincides with the release of new version of the SEP software "SEPlib". The new version of SEPlib contains a significant number of new features that allows better handling of 3-D data. The release also includes support for running Seismic Unix (SU) programs with SEP data, a new installation mechanism, and machine independent makefile rules that should allow easy building of SEP reports.

INTRODUCTION

SEPlib in its current form began in the early 1990s as a collection of utility and graphic programs (Claerbout, 1991; Dellinger and Tálás, 1992). In 1994 Nichols et al. (1994) introduced a new I/O interface that made working with files, pipes, and sockets a much simpler matter. In 1995 SEP began adding the ability to work with 3-D and irregular data, creating SEP3D (Biondi et al., 1996). These changes allowed SEP students to begin working with 3-D data, but it was notoriously difficult. The initial software was buggy (especially when dealing with large files), the process to read the data could be convoluted, and there was a lack of utility programs that could deal with 3-D data. In the process of adding the ability to deal with 3-D datasets and new platforms, the amount of time spent on general code maintenance decreased. As a result SEPlib became difficult to install and difficult to use.

The new version of SEPlib fixes many of the problems seen in earlier versions. A number of new functions and programs have been added to deal with irregular data and large data sizes. In addition two new libraries have been added. The first simplifies the accessing of data, and the second, complimentary, library allows SU programs to be used with SEPlib datasets. To make it easier to use SEPlib a new installation mechanism has been added. The new install mechanism not only makes it easier to install SEPlib, but also to use the software written for this and other SEP reports.

3-D SUPPORT

The design of SEPlib3D seemed ideal for 3-D data. Unfortunately, as is often the case, the path from design to implementation was littered with seen and unforeseen hurdles. At this time we

¹email: bob@sep.stanford.edu

have overcome many of these stumbling blocks.

Large files

One problem when handling 3-D data is their large size. Much of SEPlib used an `int` to specify the location within a file. Unfortunately, the dynamic range of an `int` is limited to 2GB. As a result, many of the SEPlib library had to be rewritten to handle the additional file size in a rather opaque manner² that could still efficiently access files. In addition to dealing with the 2GB limit in our own software, we had to overcome problems with Unix systems and standards that did not account for more than 2GB file sizes. For example, only recently has Linux begun to support file sizes over 2GB and portable `tar`'s are limited to 2GB files. To get around these limitations Dave Nichols wrote some preliminary support for multiple-file datasets. This support has been expanded upon to allow the user to create a dataset composed of multiple files, each not exceeding a user provided file size in Megabytes `filesize`.

The support for multiple file dataset provided two other benefits. First, the dreaded `File system full` error is avoided. By specifying multiple directories for the datapath `datapath=/scrka1/bob/;/scrka2/bob/` SEPlib will switch the directory it's writing its binary data to when the file system is full or when a user-specified size limit (`dirsize`) is reached. Second, `Cat3d` can create a virtual SEPlib dataset by concatenating and updating grid and header pointers, but leaving the large binary data files untouched.

The initial implementation of SEPlib3D did not allow piping between programs. As a result, many large, intermediate results were required. The new version of SEPlib allows piping by opening up additional sockets for the header and the grid. However piping is only allowed between SEPlib3D programs when certain conditions are met:

- `init_3d()` is called at the beginning of the program
- `sep_3d_close()` is called before the first writing of data
- no parameters (such as the number of traces) are changed after `sep_3d_close`
- data is written sequentially by the first program and read sequentially by the second
- the first and second programs read and write the same type of information (data, header, and/or grid)

Superset

SEP3D is good at dealing with 3-D data, but requires a significant coding overhead. As a result Clapp and Crawley (1996) wrote SEPF90, a Fortran90 library that simplified dealing with 3-D data. Unfortunately the design, like all early prototypes, had serious limitations. Among them,

²There is no machine independent way to specify an integer with more dynamic range.

- it forced referencing through a structure to access the data (something that was incredibly slow with early Fortran90 versions)
- it required programs to be written in Fortran90 (even though many programs are more suited for C)
- it did not easily allow for headers and data to be read separately (a very powerful option in SEP3D)

The new version of SEPlib comes with a replacement for SEPF90, *superset*. The purpose of *superset* is the same, but the implementation is significantly different. The basic idea of *superset* is to maintain an invisible *sep3d* structure copy of each SEPlib3D dataset. The structure contains

- the type of data (float, complex, byte, integer)
- the type of SEPlib file (regular, header, grid)
- the axes of the data (*n, o, d, label, unit*)
- the header keys associated with the data (key name, key type, key format)
- current section of the grid being processed
- current section of the headers being processed
- mapping from the headers to the traces

This internal structure can be initialized through a SEPlib tag, from another structure, or created manually by the programmer. Information is passed to and from the structure through a *sep3dtag*.

Reading of any SEPlib data then can be done in two simple steps: First the programmer makes a call to read in the headers (either all or a portion) and is returned the number of headers read. The library will automatically read in the grid, find the valid headers, check for a *data_record_number* and create a list of pointers to the traces. Once the headers have been read the user can ask for all of the data associated with the header block to read in, or read in sections of the data.

Writing is also simple. The programmer first initializes the output format files. He then makes a call(s) to write data (data, headers, and/or grid), and finally asks for the number of traces in the dataset to be updated in the format files if it wasn't known until the end of the program. The library does all the work figuring out what files to write, what trace number it is currently writing out, etc.

For added convenience I also wrote a F90 module which provides wrappers around the C function calls. The module allows the programmer to access a Fortran90 type which contains all properties of the dataset (except the header and grid values). The programmer than can then access and modify these values. When done they can synchronize the C and Fortran90 version. This added flexibility further simplifies dealing with SEPlib3D data.

SU SUPPORT

The creation of the `superset` library made possible another new element included in this release of SEPlib: the ability to use SU programs with SEPlib data. A SEPlib3D dataset with a header is similar but more free form than the SU format. SEPlib3D allows the user to have any number of keys in any order, named arbitrary, and doesn't require them to be in the same order as the data. SU data is a single file containing a series of traces. Each trace is made up to 82 keys and data. Access is done almost exclusively sequentially, through the `puttr` and `gettr` routines. The routines `gettr` and `puttr` are in turn aliased to `fgettr` and `fputtr`, where the `f` refers to a file. The library `sepsu` contains two new routines: `tgettr` and `tputtr`, which instead use the `sep3dtag` to access the data. These two routines are calls to the `superset` library read and write routines with a conversion to and from the SU `segy` structure. To add a little more flexibility the library provides some additional command line arguments:

nmem the library buffers it reads and writes. **nmem** is the number of traces that buffers.

sukey=sepkey tells the library that **sepkey** should be treated as this **sukey**

sukey.fract=val tells the library to scale the key value it reads by **val** and writes by **1./val**

suinput tells the program that the input file is in SU format

suoutput tells the program that the output file should be in SU format

The following program converts from SEPlib3D to SU, and shows just how easy it is to write code that can take advantages of both software packages.

Example

```
segy tr;
int main(int argc, char **argv)
{
    int i;
    int verb;
    /* hook up getpar */
    initpar(argc,argv);  getch_add_string("suoutput=1");
    initargs(argc, argv);
    verb=1000000;
    getch("verb", "d", &verb);
    requestdoc(1);  i=0;
    if (!gettr(&tr)) err("can't get first trace");
    do {  i++;
        fputtr(stdout, (&tr));
        if(i%verb==1) fprintf(stderr, "converted %d  traces \n", i);
    } while (gettr(&tr));
}
```

```
    } while (gettr(&tr));  
    return EXIT_SUCCESS;  
}
```

In the above, the `gettr` reads SEPlib3D and the `fputtr` writes out SU data. One thing to note is the `EXIT_SUCCESS`. In order to make SEPlib3D data work the total number of traces must be known. The `EXIT_SUCCESS` call is aliased to a call to `finish_susep` which updates the number of traces if it has changed within the program. To compile and run SU programs you need to:

- have the SEPlib include directory specified before the SU include directory
- link with `libsepsu.a` and `libsuperset.a` before linking with any of the SU libraries

INSTALLATION

For the last few years SEP has required anyone who wanted to install SEPlib to wade through and edit a series of complicated configuration Makefiles. This system was convenient for us, but difficult to near impossible for anyone outside SEP. Part of the difficulty was that SEPlib relied heavily on machine dependent `ifdefs` for:

- compiler options
- locations of programs and libraries
- different locations of functionality of the basic C libraries

With each new version of an operating system we were left with the choice of creating more `ifdef's` or not completely supporting the old OS. Looking at past experience I was left with three choices: continue the `ifdef` cycle, simplify SEPlib so it wasn't reliant on so many non-standard operations (required less `ifdef`), or find a different way to do the installation. I chose to follow the third option, and found some tools that were well suited for the purpose.

Automake, Autoconf, Libtool

Gnu's Not Unix (GNU) provides a series of utilities that install easily and run successfully on an amazing number of platforms. Their installation mechanism involves running a shell script `configure` that examines features of an operating system and then creates machine dependent makerules, header files, and code. From the distributor point of view this involves learning to integrate two programs, `Autoconf` and `Automake` into your software.

Autoconf Creates a configuration script that determines machine dependent features

For the distributor `Autoconf` can remove the need for almost all machine dependent `ifdef`'s in your code. Unfortunately, the removal of these `ifdef`'s does not come without a cost. Generally machine dependent `ifdef`'s are replaced with feature dependent `ifdef`'s, and a resulting test is written to determine whether the installing machine has the feature. For example replacing a machine dependent `ifdef` which was dependent on whether numbers represent in big or little Endian fashion with corresponding `ifdef` and test.

Automake Creates makefile rules for creating libraries and binaries from a list of source files and required linked libraries

Generally `Automake` replaced all of SEP's makerules by replacing our standard shorthand conventions with a more generic shorthand convention. The advantage of the `Automake` philosophy is it is faster, provides automatic distribution, install, and clean mechanisms that are not too easy to implement.

Both programs do an excellent job in supporting variations in C compilers but are significantly lacking in their Fortran support. As a result the writing of many Fortran tests and the changing of the `Automake` source code were necessary. For instructions on how to install SEPlib see the attached Appendix.

REPRODUCIBLE RESEARCH

The idea that research is reproducible is one of the basic tenets of good research. SEP has a long history in attempting to define and produce reproducible research. Unfortunately what we have discovered is that our definition of "reproducible" has always been very subjective, and on the most part limited to reproducible at SEP.

SEP's began its quest for reproducibility with the introduction of interactive documents (Claerbout, 1990). We then started producing SEP reports on CDROM and adopting the GNU, makefile system as our framework for reproducibility (Schwab et al., 1996). This method effectively created a snapshot of the current SEP environment and guaranteed that if you had a certain type of a computer, a certain OS, and the CDROM you could reproduce SEP research. Unfortunately, OS's change quickly and CDROMS aren't an ideal distribution mechanism. Recently we have abandoned CDROMs and instead use a web based method to distribute our research, but we still make an attempt to test every report for reproducibility (Prucha, 1999). The web based solution is a better distribution method but requires you to have

- the author's source code
- the version of SEPlib they used to produce the results
- the a version of the SEP makefile rules that they used to produce the results

Overall, a system that requires even more work than the CDROM solution.

This version of SEPlib attempts to correct some of these issues. The SEPlib configure script will produce a set of SEPlib makerules that are tuned to the platform where it is run, but should compile all of the SEPlib codes. This system allows SEP research to reproduce on any platform where the configure script can be successfully run.

ACKNOWLEDGMENTS

I would like to thank Matt Schwab who pointed a number of years ago that GNU configure was the way to go.

REFERENCES

Biondi, B., Clapp, R., and Crawley, S., 1996, Seplib90: Seplib for 3-D prestack data: SEP-92, 343-364.

Claerbout, J. F., 1990, Active documents and reproducible results: SEP-67, 139-144.

Claerbout, J. F., 1991, Introduction to Seplib and SEP utility software: SEP-70, 413-436.

Clapp, R. G., and Crawley, S., 1996, SEPF90: SEP-93, 293-304.

Dellinger, J., and Tálas, S., 1992, A tour of SEPlib for new users: SEP-73, 461-502.

Nichols, D., Karrenbach, M., and Urdaneta, H., 1994, What's new in SEPLIB?: SEP-82, 257-264.

Prucha, M., 1999, Revisiting the half-derivative filter: SEP-102, 137-142.

Schwab, M., Karrenbach, M., and Claerbout, J., 1996, Making scientific computations reproducible: SEP-92, 327-342.

APPENDIX A

Programs in **bold** are new to SEPlib, programs in *italics* have been significantly modified (often converted from Fortran 77 to C or Fortran 90).

UTILITIES

Programs that perform utility (non-seismic) functions.

Unix

This group of programs perform functions similar to their corresponding UNIX commands, but on SEPlib datasets.

Program	
<i>Cp3d</i>	Copy a history and binary file
Ls	List all SEPlib history and associated binary files
<i>Mv3d</i>	Move a SEP77 history and binary file
<i>Rm3d</i>	Remove a history and binary file
Zero	Create a null SEPlib file

Vector

Programs that perform vector operations, where the vector is defined as an SEP dataset.

Program	Purpose
Add	Add two SEPlib real datasets
<i>Cabs</i>	Take the Complex absolute value of a complex dataset
<i>Cabs2</i>	Take the Complex absolute values squared of a complex dataset
Cadd	Add two complex datasets
<i>Conj</i>	Take the conjugate of a complex dataset
Math	Generic routine to do vector operations on files
Log	Take the log of a file
Scale	Scale a dataset
<i>Cmult</i>	Perform complex multiplication of two datasets
arithpar	Perform mathematical operations on SEPlib history file parameters
<i>Cmplx</i>	Create a complex dataset from two real datasets
<i>Rtoc</i>	Convert a real dataset to complex by setting the imaginary part to 0
<i>Imag</i>	Take the imaginary part of a complex dataset
atoF	convert typed numbers to a SEPlib dataset
<i>Real</i>	Take the real part of a complex dataset
<i>Pow</i>	Raise a SEPlib dataset to a power

Cube

Do operations that rely on the SEPlib hypercube format.

Program	Purpose
Cat	concatenate SEPlib-2D datasets
Merge	Merge SEPlib-2D datasets
Pad	Pad with zeros a SEPlib Dataset
<i>Window3d</i>	Window a SEPlib dataset
Reverse	Reverse an axis of a 2-D dataset
Transp	Transpose an axis of a 2-D dataset
Interleave	Interleave the traces of two 2-D datasets
Window	Window a 2-D dataset
Cat3d	Concatenate SEPlib-3D datasets
Fold3d	Calculate the fold of a SEPlib dataset
<i>Grid_fold</i>	Calculate the fold of a given set of gridding parameters
Sort3d	Sort and grid a SEPlib-3D dataset
Stack3d	Stack a SEPlib-3D dataset
Stack	Stack a SEPlib-2d dataset

Headers

Programs that operate on header values.

Program	Purpose
<i>Headermath</i>	Perform mathematical operation on header keys
<i>Create3d</i>	Create a SEPlib-3D dataset from SEPlib-2D dataset(s)
<i>Synch3d</i>	Synch the headers and data of a SEPlib-3D dataset
<i>Window_key</i>	Window a SEPlib dataset according to a key

Info

Programs that give information about SEPlib datasets.

Program	Purpose
Attr	Calculate the attributes of a SEPlib data file
Dd	Convert back and forth from an ascii-binary file
Disfil	Display the values of a SEPlib data set
Get	Get values from a SEPlib history file
<i>In3d</i>	Print a description of a SEPlib dataset
<i>Dis3dhead</i>	Display header keys
<i>Attr3dhead</i>	Display the attributes (min,max,etc) of header keys

SEISMIC

Programs that do seismic operations.

Filter

Programs that do some type of filtering.

Program	Purpose
Again	Arctangent gain
Agc	Automatic gain control
Balance	Trace balancing
Gpow	Apply a gainpow to a dataset
Lpfilt	Low-pass (Butterworth) filtering
Clip	Clip a dataset
<i>Interp</i>	Interpolate a SEPlib dataset
<i>Trcamp</i>	Calculate total amp/energy
<i>Ft3d</i>	Fourier transform a complex dataset
Energy	Calculate energy in a running window
Edit	Patching driver
Fx2d	2-D FX decon
Txdec	2-D TX decon
<i>Spectra</i>	Obtain averaged amplitude spectra
Bandpass	Bandpass a dataset
Envelope	Analytic signal amplitude
Halfint	Take a half-derivative of a dataset
<i>Smooth</i>	Smooth a dataset with triangular filters
Filter	Filter a dataset
Mute	Mute a SEPlib-2D dataset
Noise	Add noise or create noise
Median	Median filter a dataset
Tpow	Raise a dataset by a power of the time axis

Model

Programs that do modeling.

Program	Purpose
Aniso2d	Anisotropic heterogeneous elastic modeling
Iso2d	Isotropic heterogeneous elastic model
Gauss	Create a model with Gaussian blobs
<i>Spike</i>	Create a model with spikes
<i>Kirmod3d</i>	Perform $v(z)$ Kirchoff modeling
Vel	Create a velocity model
Marine_geom3d	Create a typical marine geometry
Gfgradz	Create $v(z)$ traveltimes and amplitudes
Scat3d	Create scatterers (for input to Kirmod3d)

Velocity

Programs that work with velocity.

Program	Purpose
Unmo	Inverse nmo
Vconvert	Convert velocity (z-t) (interval-depth)
Velan	Perform 2-D velocity analysis
Velan3d	Perform 3-D velocity analysis
Hypint	Velocity space transform (integration)
Hypmovie	Velocity space transform movie
Hypsum	Velocity space transform
MCvfit	Monte Carlo automatic velocity picks
Stretch	Generic stretching routine
NMO	Perform NMO on SEPlib-2D dataset
Nmo3d	Perform NMO on a SEPlib-3D dataset
Radial	Transform a 2-D dataset to radial trace domain
Radnmo	Do radial NMO

Travel times

Routines that calculate travel times.

Program	Purpose
FMEikonal	Calculate travel times using fast marching eikonal
MTTmaps	Band limited maximum energy Green's function maps
Hwt3d	Rays or travel times using Huygens wavefront tracing

Imaging

Programs that to do imaging.

Program	Purpose
Phase	Do phase shift migration
Stolt	Do stolt migration

Anisotropy

Software dealing with anisotropic data.

Program	Purpose
Combine/combine	Combine two sets of elastic layer coefficients
Uncombine/uncombine	Subtract layer coefficients
Uncrack/uncrack	Compare fractured and unfractured rock sample
Crack/crack	Crack a set of elastic layer coefficients
Create/create	Create a stiffness tensor
Laymod/laymod	Create a layered of model
Laymod21/laymod21	Create a layered model with all 21 coefs.
Laymodthin/laymodthin	Create elastic parameter model with thin interbedding
Laythin1d/laythin1d	Create elastic parameters with two inter-bedded substances
Display/display	Display the parameters of a anisotropic dataset
Rotate/rotate	Rotate the coordinate frame

GRAPHICS

Programs that display graphics.

SEP VPLOT INTERFACE

SEP programs that interface with vplot to display functions.

Program	Purpose
Box	Draw a vplot balloon
Dots	Create a dot plot
Graph	Graph a function
Grey	Display a 2-D plane variable density plane
Histogram	Create a histogram
Operplot	Shaded box plot
Thplot	Hidden line plotting program
Ftplot	Plot Fourier amplitude or phase spectrum
Wiggle	Create a wiggle plot
Contour	Contour a dataset
Cubeplot	Create a cubeplot of a 3-D dataset

VPLOT

Vplot shell programs and pens for different devices.

Program	Purpose
Vppen/vppen	Generic vplot plotting routine
Xtpen/xtpen	XT vplot pen
vp_Movie	Combine vplot frames into a movie
vp_OverUnderAniso	Plot vplot frames vertically
vp_OverUnderIso	Plot vplot frames vertically, preserve ratio
vp_Overlay	Overlay vplot frames
vp_SideBySideAniso	Plot vplot frames horizontally
vp_SideBySideIso	Plot vplot frames horizontally, preserve ratio
vp_Unrotate	Unrotate vplot frames
vp_annotate	Annotate a vplot frame
plas	Convert vplot file to ascii
pldb	Convert vplot file to binary
Raspen/raspen	Create raster files
Pspen/pspen	Create postscript files
Tube/tube	Display a vplot file
pstexpen	Convert a vplot file to postscript

Movie

Programs that display 3-D volumes.

Program	Purpose
Rickmovie	A great movie program

TOOLS

Program	Purpose
sat	Handle f77 dynamic and temporary allocation, SEPlib shorthand
saw	Handle f77 memory, SEPlib shorthand
sawf90	Handle SEPlib shorthand in fortran90
cmsawf	Handle SEPlib shorthand for the CM5
ExtractPOD	Extract Pod documentation from f90 source code
Makedepend	Create f90 dependencies according module usage
key-word	Search directories for keywords
shortfort	Fold f77 lines
spp	Generic pre-processor
lop2f90	Convert linear-operator shorthand to ratfor
ratfor77	Convert from ratfor to fortran77
<i>ratfor90</i>	Convert from ratfor90 to fortran90
Snoop	Search directories for keywords

CONVERTERS

Programs that convert from or to SEP internal formats.

Program	Purpose
<i>Segy2sep</i>	Convert from SEG-Y to SEPlib
<i>Sep2su</i>	Convert from SEPlib to SU
<i>Su2sep</i>	Convert from SU to SEPlib
Byte2mpeg	Convert a SEPlib byte file to mpeg format
pstogif	Convert a postscript to gif
vplot2gif	Convert a vplot file to gif
vplot2mpeg	Convert a vplot file to mpeg
vplot2ras	Convert a vplot file to a raster plot

APPENDIX B

INSTALLING SEPLIB

SEPLib now uses a GNU-style configure mechanism for installation. So far this installation mechanism has been tested on:

- Linux (Redhat 5.0,5.2,6.0)
- IRIX6.5
- DecAlpha
- HPUX (10.1)
- Solaris (2.6)

It is the first release with this new installation mechanism so please report bugs to bob@sep.stanford.edu. Follow the following steps to install SEPLib

- Download the software, <ftp://sepftp.stanford.edu/pub/sep-distr/seplib-5.0.tar.gz>
- `gunzip seplib-5.0 -c |tar xf -`
- `cd seplib-5.0`
- Make sure `lex` or `flex` is in your path
- `./configure`
- `gmake install`

Following the above procedure should install the core seplib libraries and programs into the directory `/usr/local/SEP`.

`-prefix=/other/directory` specify another directory to install SEPLib in

`-with-local` install the less tested, newer portions of SEPLib

`-with-su=/su/directory` Compile SU support

`-with-motif=/motif/directory` Specify motif directory or `-without-motif` the absence of motif

`-with-ppm=/my/pbmplus/dir/` The directory containing the pbmplus package.

If you run into problems (for example you need to add an additional library path when compiling programs) you can often solve your problem by setting environmental variables that the configure script will then use. For example:

F90 The F90 compiler

F77 The F77 compiler

CFLAGS F90 compiler flags

F77FLAGS F77 compiler flags

F90FLAGS F90 compiler flags

LDFLAGS Directories and libraries to link when compiling C programs

F77LDFLAGS Directories and libraries to link when compiling F77 programs

F90LDFLAGS Directories and libraries to link when compiling F90 programs

CPFLAGS C Processor flags

etc Look `configure.in` in the main directory to find other variables that can be set in the environment

APPENDIX C

SETTING UP THE SEP ENVIRONMENT

Before running SEPlib do the following:

create **/.datapath** SEPlib files are composed of ascii/binary pairs. The ascii portion describes the data (the size, the type, and the location of the binary). The binary portion is the actual data. The two are separated to allow processing to be done in a centralized location (a home directory for example) while the data is written where ever there is space. The datapath file tells SEPlib where to put binary data and should look something like this:

```
datapath=/scrka3/bob/ ; /scrka2/bob/
spur      datapath=/scrka2/bob/
oas       datapath=/scrsa1/bob/
vesuvio   datapath=/SDA/bob/
santorin  datapath=/scrsa4/bob/
```

By default SEPlib first checks the command line for `datapath=`, then the directory where the program is run for a `.datapath` file, and finally the home directory. The above `.datapath` files tells SEPlib to put binary data by default in `/scrka3/bob` and if it runs out of space in `/scrka2/bob`, but when on the computer "santorin" to put the data in `/scrsa4/bob`.

setenv VPLOTSPOOLDIR `/tmp/` The next step is to tell SEPlib where to put temporary vplot files. It is best to put these in a location such as `/tmp` which is periodically cleaned.

setenv VPLOTFONTDIR `SEPINC``DIR`

This tells vplot where to find fonts.

setenv SEPINC `SEPINC``DIR`

The final step is only necessary if you want to compile and run programs from SEP reports, theses, or books. This environmental variable is needed by our `Makefile`'s to find out its compile and install rules.

Short Note

SEP's data library

Robert G. Clapp, Morgan Brown, Louis Vaillant, Carmen Mora, Marie Prucha, and Yi Zhao¹

INTRODUCTION

One of the requirements for graduation at SEP is to prove that a student's ideas will work on real seismic data. SEP sponsors have been very generous over the years in providing SEP with real seismic datasets. In the past we have kept these datasets on a variety of different tape formats and with decidedly mixed levels of documentation. This summer SEP organized a mini-seminar in an attempt to organize these datasets. This paper, and the accompanying web page ², provides a summary of the data library project, and provides examples of some of the datasets SEP researchers have available to test their ideas on.

GOAL

In the past 25 years SEP sponsors have provided SEP with numerous datasets. Early datasets were a few cmps or shot gathers. Over time SEP has added large 2-D surveys, multi-component dataset, 3-D prestack and post-stack, and even 4-D time lapse datasets. Unfortunately these datasets were not carefully cataloged and or generally left in easily accessible state. As a result, finding a dataset to apply a particular technique to could be an arduous task. The goal of the *SEP datalib Mini-Seminar* was to make finding and using SEP's datasets easier. Each dataset was researched and processed so the following form could be filled out:

- Location of raw data
- Location of velocity model
- Stack of data
- Zero offset Migration
- Past usage of data

¹**email:** bob@sep.stanford.edu, morgan@sep.stanford.EDU,
cmora@sep.stanford.EDU, marie@sep.stanford.edu, yi@sep.stanford.EDU

louis@sep.stanford.EDU,

²http://sepwww.stanford.edu/pub/docs/sepdatalib/toc_html

- Geometry of data
- Characteristics with data
- History of data (when acquired and by whom)
- Preprocessing on data
- Proprietary considerations

The inexpensive cost of large disks made it possible to put a large portion of the data online. All 2-D datasets and portions of every 3-D dataset are now stored online. The maturity of SEP3d (Biondi *et al.*, 1996; Clapp, 1999) allowed us to maintain a full description of each dataset while allowing the dataset to be sliced and diced.

EXAMPLE

Based on the items listed above, the following information was compiled for the Elf L7D dataset. Figures 1-5 were created for visualizing the data.

L7D DATA FILES

Raw Data The full dataset is as big as 45Gb, available on DLT tapes.

Common-azimuth Data To be done.

Velocity Model Located at /data_3d/elf_north_sea/L7d-vel.H

Velocity model created by Elf & IFP³ (Project “Helios”) using the so-called “SMART” method (Sequential Migration Aided Reflection Tomography). The structure of the salt dome is highly 3-D, with serious illumination problems under its edges (Figure 1).

Stack Located at /data_3d/elf_north_sea/L7d-near-nmo-stack-fine.H

Near-offset (0-1000m) NMO-stack

Zero-offset Migration Located at /data_3d/elf_north_sea/comaz_zo_salt_fine.h

Prestack 2-D line

Usage none (yet).

Geometry Acquisition: 2 sources, *x* streamers (most likely 3).

In3d:

```
-----
***** L7d_all.H *****
4 -esize Synched data_format-xdr_float
-----
n1=1500 o1=0.000000 d1=0.004000 label1=time
n2=7411523 o2=1.000000 d2=1.000000 label2=trace number
Data: in=/scrsa3/louis/Elf/Data/L7d_all.H@
```

³Institut Francais du Pétrole

7411523 elements, 44469138000 bytes in data file

Attr3dhead:

key	min	max	mean	nzero	rms	norm
cdp	2900.0000	3900.0000	3389.9319	7411523	3400.5400	9257668.44
offset	186.0000	3571.0000	1764.1710	7411523	1989.4291	5416044.20
ncdp_s	2773.4941	3926.8994	3438.5354	7411523	3449.2773	9390351.31
nligne_s	1346.6554	1520.4437	1428.9248	7411523	1429.5942	3891943.38
ncdp_g	2772.9077	4026.9609	3341.0813	7411523	3352.4868	9126847.67
nligne_g	1347.1848	1528.9202	1429.6726	7411523	1430.3911	3894112.88
s_x	-1686.7405	13691.9580	7180.4541	7411523	8044.3945	21900150.11
s_y	1416.3849	5761.0933	3473.1201	7411523	3641.2247	9912910.97
g_x	-1694.5596	15026.1074	5881.0698	7411522	6939.6676	18892629.00
g_y	1429.6204	5973.0039	3491.8162	7411523	3671.1157	9994286.74
nline	1354.4266	1515.5315	1429.2987	7411523	1429.9876	3893014.44
aoffset	185.6369	3571.9861	1764.5095	7411523	1989.8103	5417081.89
azimuth	-1.2745	1.5323	-0.0261	7411431	0.1345	366.08
cmp_x	-8.3235	13338.0527	6530.7617	7411522	7446.8040	20273262.93
cmp_y	1610.6659	5638.2871	3482.4683	7411523	3654.9572	9950296.70
offset_x	-3463.4939	3383.3154	-1299.3843	7411523	1980.6512	5392147.21
offset_y	-990.2041	786.0776	18.6959	7411431	190.6978	519157.71

Problem Multipathing - Illumination problems / Shadow zones - Common-angle gathers

History of Data Dataset given to SEP in 1998, originally for testing AMO and common-azimuth migration. The contact at Elf Exploration Production is Henri Calandra⁴.

Preprocessing A correction of amplitude has been applied: geometrical spreading

$$A(t) = \left(\frac{t}{250} \right)^{+1.8}$$

Also, the multiples due to sea bottom have already been removed.

Proprietary Considerations The L7d data are free to be used by SEP only, including publications in articles or SEP reports with the usual acknowledgements to Elf Aquitaine.

FIGURES

Some other dataset placed in the data library include Figures6-17.

ACKNOWLEDGMENTS

We would like to thank all the sponsors for their contributions for data over the last 25 years.

⁴email: henri.calandra@elf-p.fr

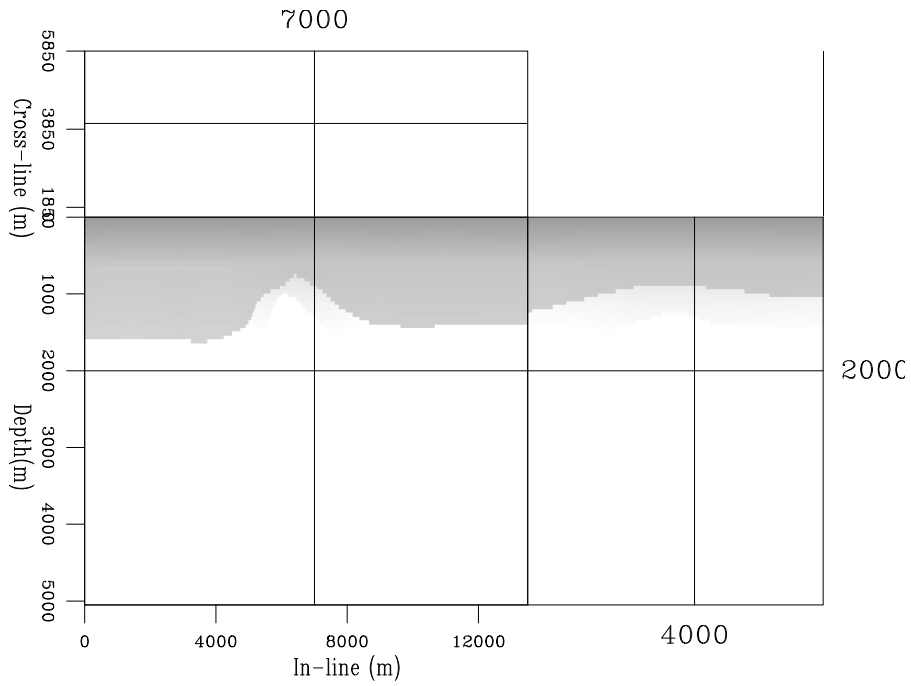


Figure 1: Elf "SMART" velocity model `bob3-vel-model` [NR]

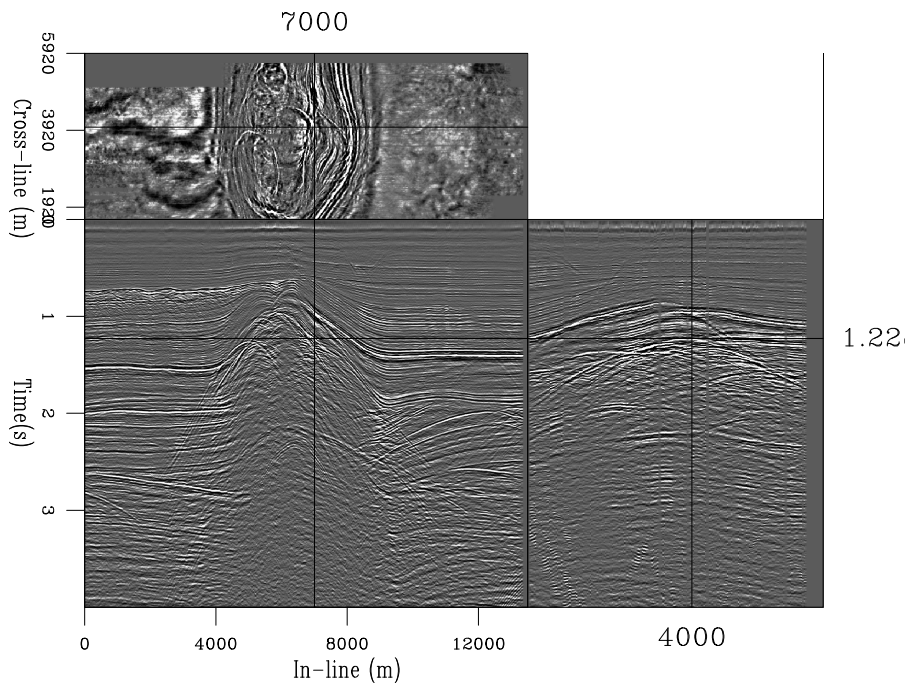


Figure 2: NMO-stack of the near offsets (0-1000m) `bob3-nmo-stack` [NR]

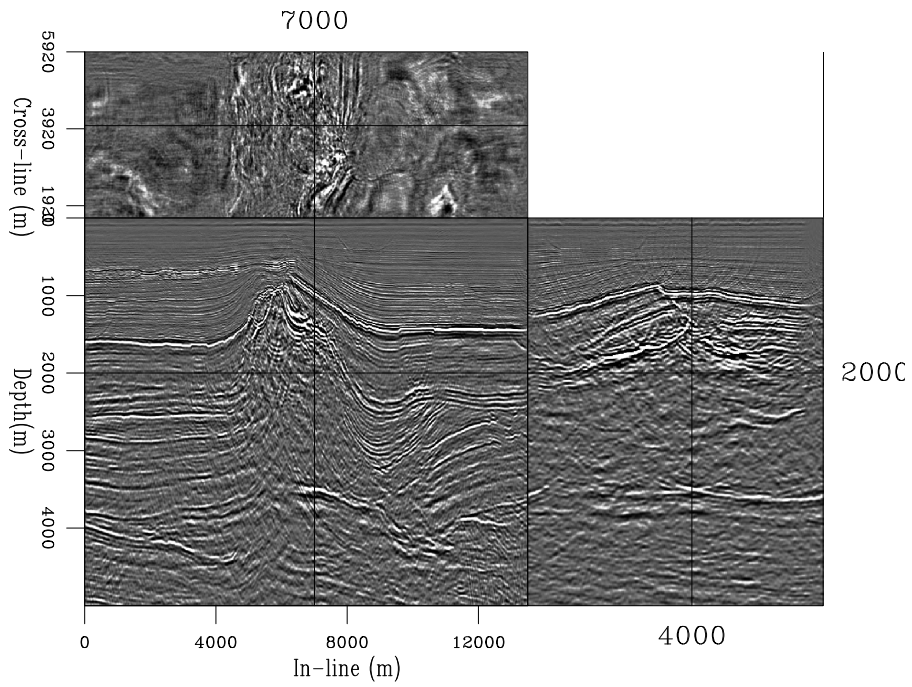


Figure 3: Zero-offset migration of the near offsets (0-1000m) `bob3-zo-mig` [NR]

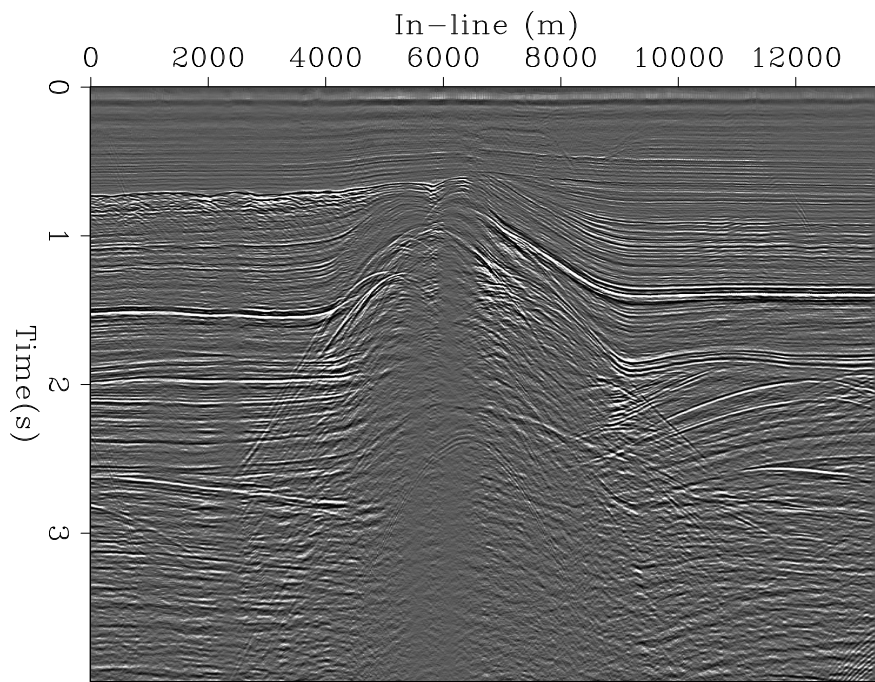


Figure 4: NMO-stack of the near offsets (0-1000m), section corresponding to the 2-D synthetic data `bob3-2D-line-nmo-stack` [NR]

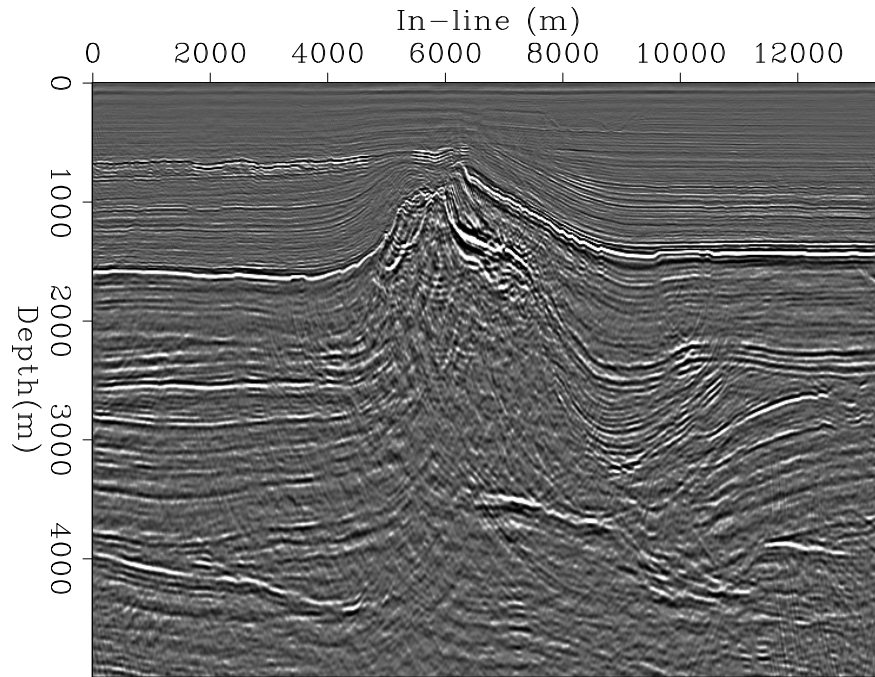


Figure 5: Zero-offset migration of the near offsets (0-1000m), section corresponding to the 2-D synthetic data `bob3-2D-line-zo-mig` [NR]

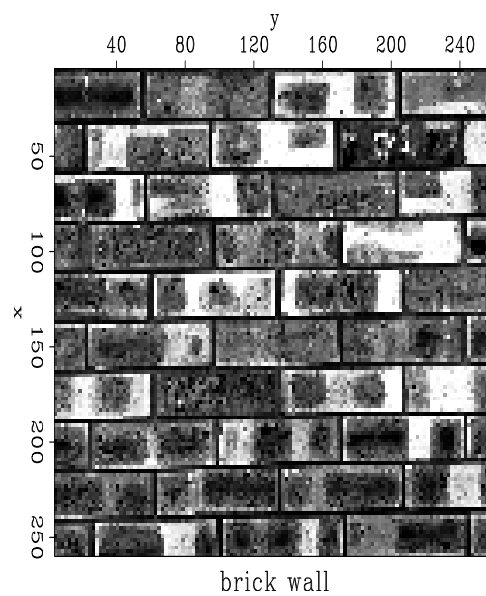
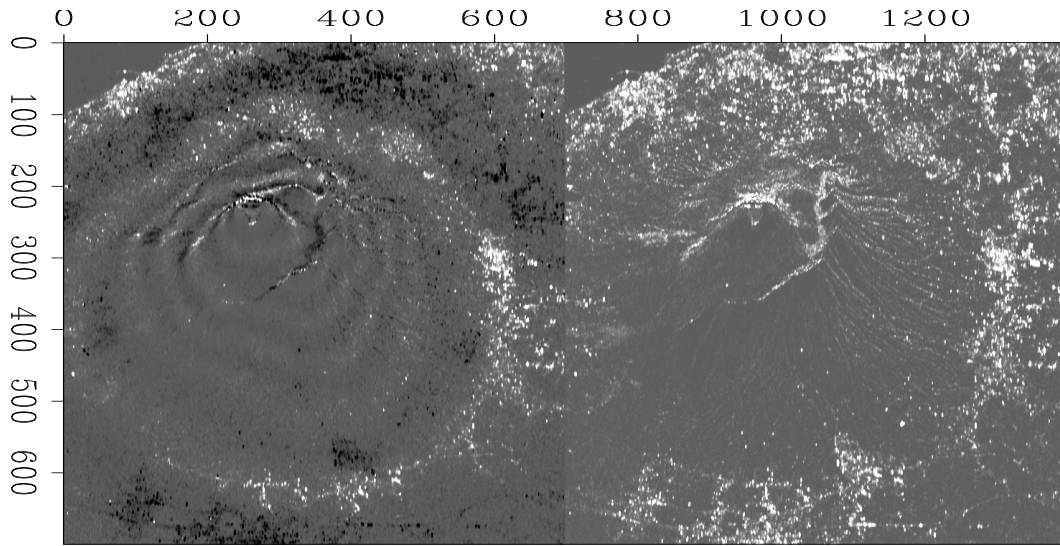


Figure 6: A brick wall texture. `bob3-brick` [NR]



Vesuvius: phase/magnitude

Figure 7: Mount Vesuvius SAR data. `bob3-vesuvius` [NR]

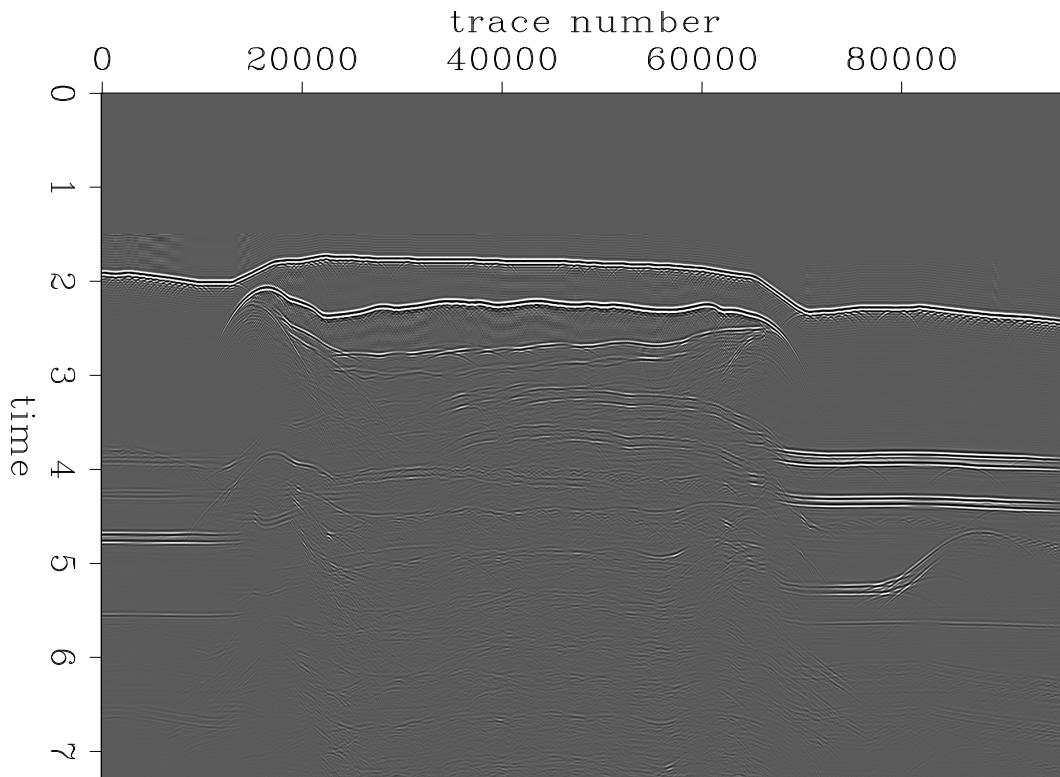
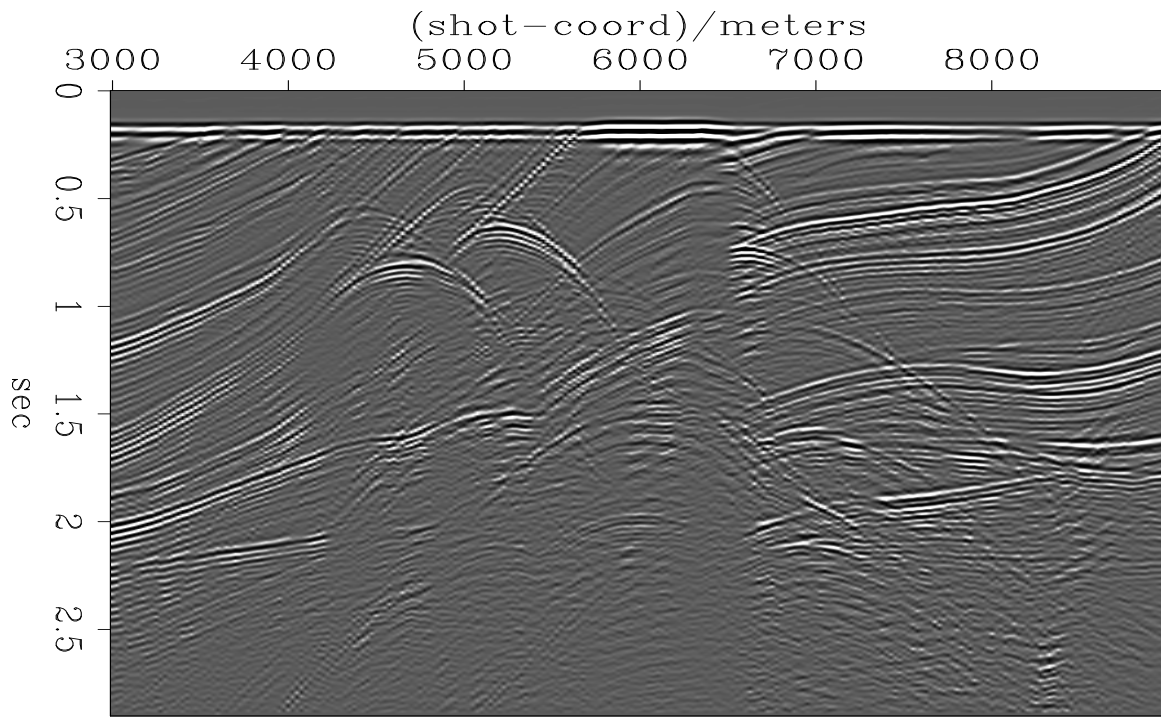
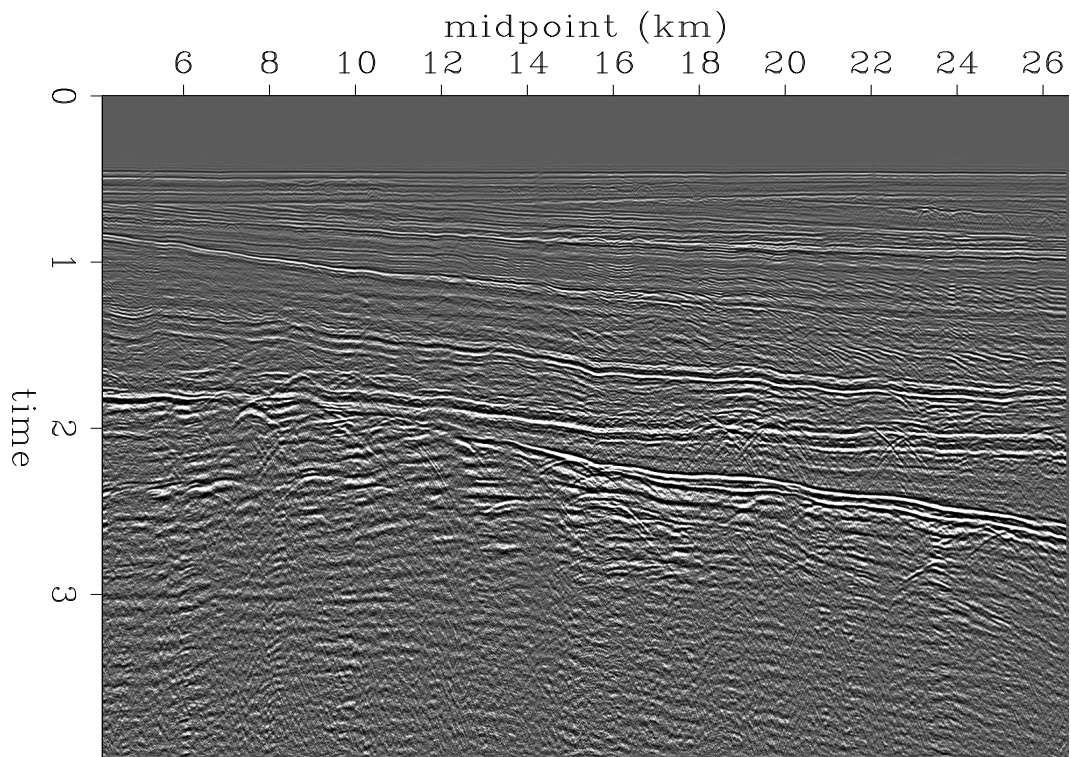


Figure 8: Stack of BP multiple synthetic. `bob3-bp-stack` [NR]



Near offset section

Figure 9: Near offset section of Marmousi dataset. `bob3-marmnear` [NR]Figure 10: Stack of Mobil-AVO dataset. `bob3-mobil-stack` [NR]

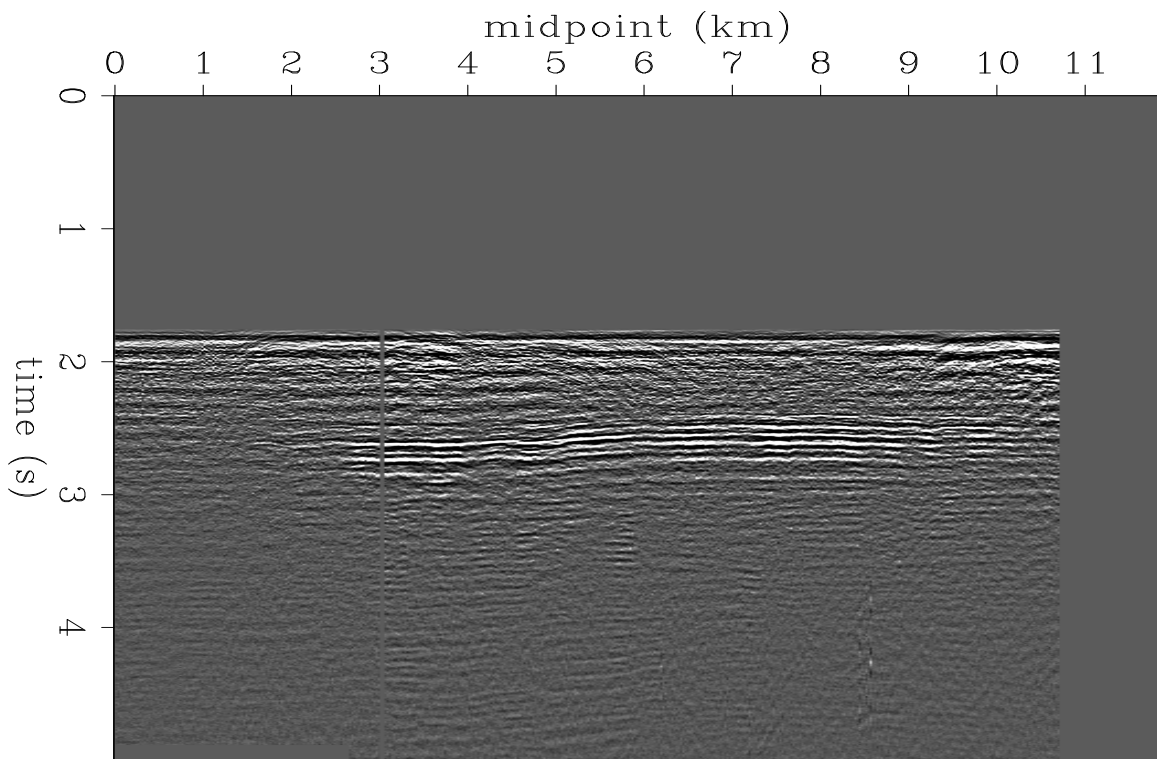


Figure 11: Near offset section of Kjartansson thesis data. `bob3-kjar-near` [NR]

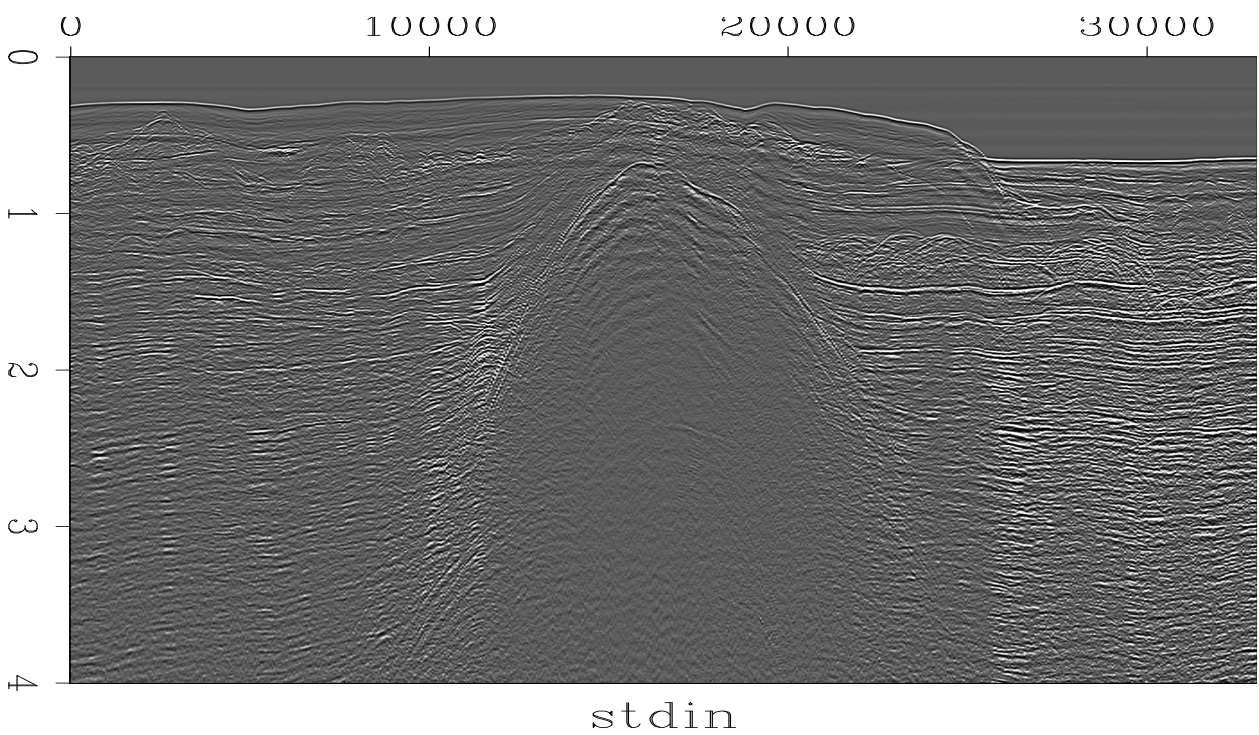


Figure 12: Near offset section of line 1 of Amoco data over a Gulf salt body. `bob3-amoco-salt-near1` [NR]

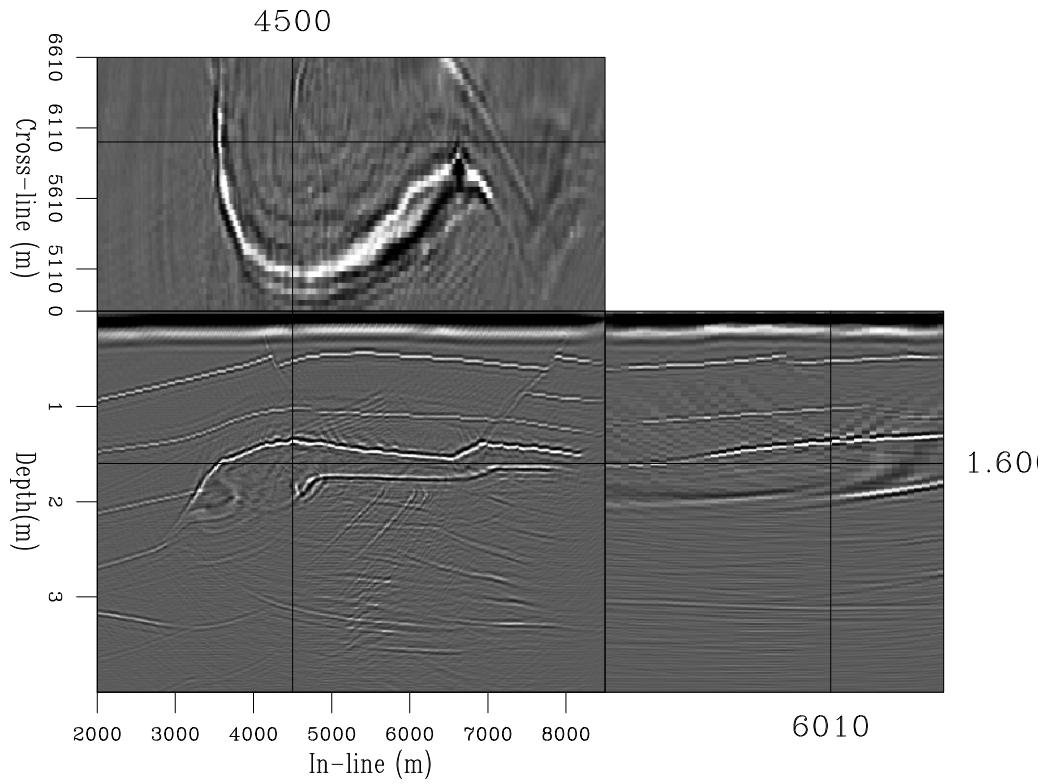


Figure 13: Two-pass migration of SEG Salt synthetic `bob3-seg-salt-twopass` [NR]

REFERENCES

- Biondi, B., Clapp, R., and Crawley, S., 1996, Seplib90: Seplib for 3-D prestack data: SEP-92, 343-364.
- Clapp, R. G., 1999, Additions to seplib: SEP-102, 201-218.

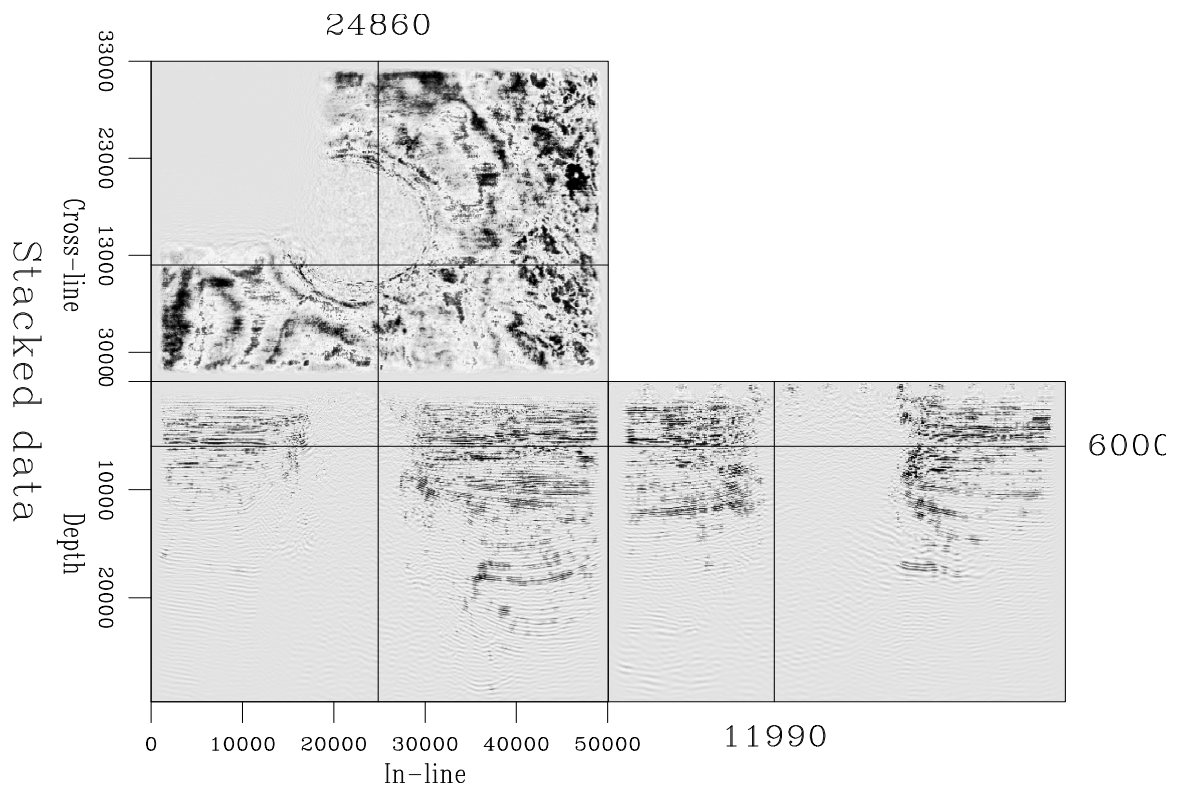


Figure 14: Depth, In-line and cross-line slices from 3-D Stack data bob3-unocal-salt-stack
 [NR]

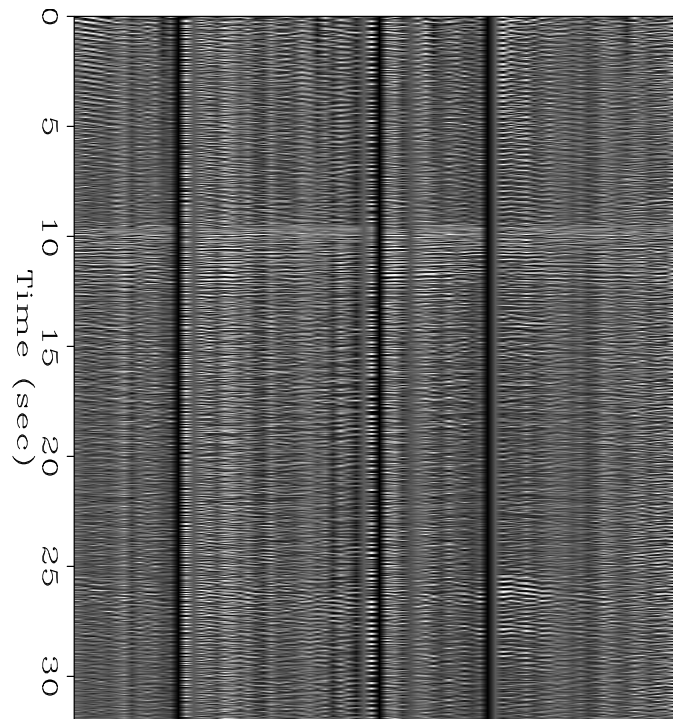


Figure 15: SEP passive dataset. Partial stack data corresponding to record number 46. Note the blast arrival around 9.7 seconds. `bob3-pstack46` [NR]

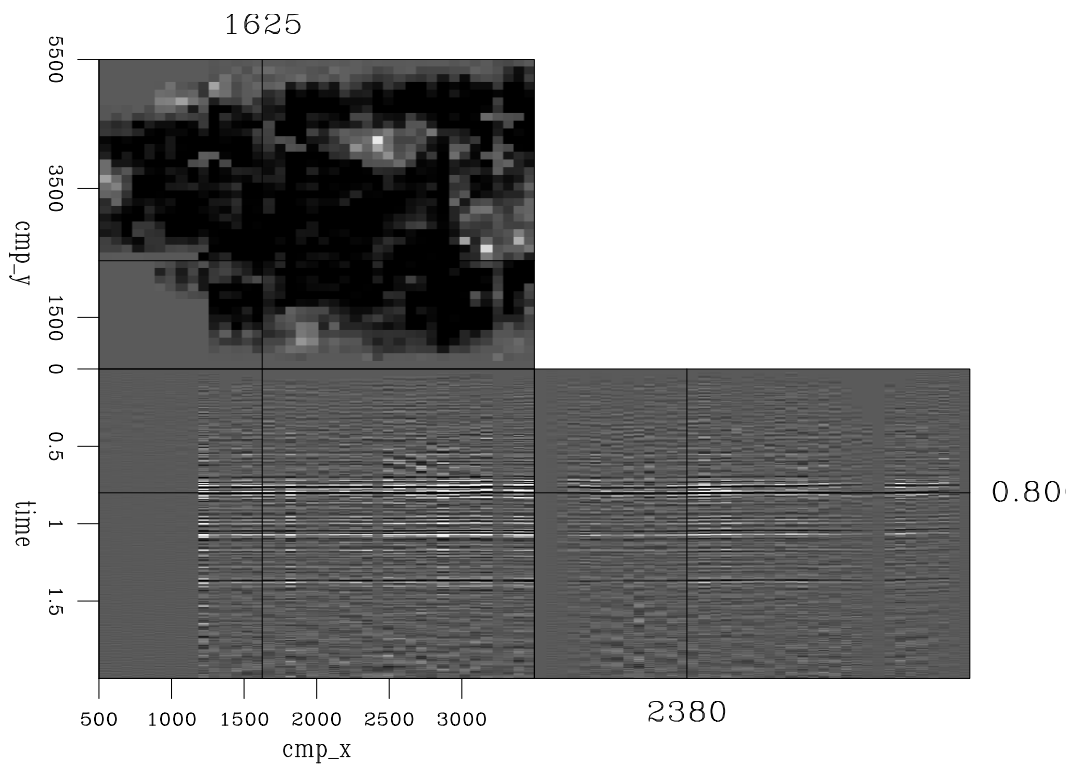
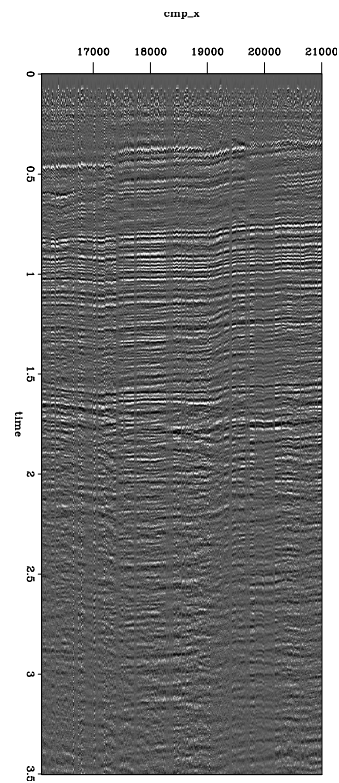


Figure 16: Stacked data of a land acquisition dataset acquired by Pan-Canadian. `bob3-shorn-stack` [ER]

Figure 17: Near offset stacked data of Jupiter North-Sea dataset.
`bob3-jupiter-stack` [ER]



Testing Linux multiprocessors for seismic imaging

Biondo Biondi, Robert G. Clapp, and James Rickett¹

ABSTRACT

Benchmarks of our “production” codes show that Pentium-based multi-processors computers running the Linux operating system are attractive options for SEP’s next computational server(s). A four-processor SGI 1400 L (500 Mhz Pentium III Xeon) has consistently performed as well as, or better than, our SGI Origin 200 (180 Mhz R10000). We used the Portland Group’s `pgf90` compiler to compile our benchmarking codes, that are parallelized with OpenMP directives. This compiler has proven to generate efficient code, though the support of some F90 and OpenMP features is still immature.

INTRODUCTION

SEP’s present computer servers (18-processor Power Challenge and 4-processor Origin 200) fall short from delivering the computer power needed to perform research in advanced algorithms for 3-D wave-equation migration, 3-D velocity estimation, and 3-D wavefield interpolation. We are therefore evaluating the choices for our next computer server (or servers). Computers based on commodity processors (Intel) have attractive prices, and seem to have finally caught up in floating-point performances with computers based on processors specialized for floating-point computations (SGI-MIPS, SUN-Ultra, etc). Further, memory and disk-storage are much better priced for Intel-based computers than for any other. We are thus evaluating Intel-based Linux multi-processors systems. At the moment the choice is between systems based on dual-processor Pentium III and systems based on four-processor Pentium III Xeon. In the near future (end of 1999?), it should be also possible to purchase eight-processor Pentium III Xeon system. We evaluated a dual-processor Pentium III marketed by VA Linux Systems (StartX MP Workstation) and a four-processor Pentium III Xeon kindly loaned to us for evaluation by SGI (SGI 1400L).

The main goal for the tests that we report here is to determine whether we can run efficiently our “production” codes on multi-processors Linux systems. For several years now SEP has operated Linux computers as desktops. We are satisfied by the experience, to the point that all our desktops are Intel PC’s running Linux. However, we perform the heavy-duty parallel computations on our SGIs. One of the authors (JR) performed some tests running parallel programs across our network of Linux desktop PC’s using PVM message passing as

¹email: biondo@sep.stanford.edu

a parallel-programming tool. However, no parallel “production” codes runs across the Linux network. Our question has a software component as well as a hardware component. First, Linux kernels before 2.2 had notoriously poor performance when running multi-threaded applications, and even for 2.2 the overhead of starting new threads is higher than on Irix (Bee Bednar, private communication). Second, the most of our production codes are parallelized with a shared-memory model, and the parallelism is achieved using SGI or OpenMP compiler directives. The F77/F90 compiler that we presently use on Linux (from NAGWare) does not support these parallel-programming style. Therefore, we need to look at alternative compilers; we evaluated the Portland Group F90 compiler.

We run our benchmarks on four computers:

- 1) 18-CPU - SGI Power Challenge
 - CPU: 75 Mhz - MIPS R8000
 - L2-Cache: 75 Mhz - 4MB
 - Memory: 2 GB
 - Operating System: Irix 6.5
 - Compiler: MIPSpro f90 version 7.2.1
- 2) 4-CPU - SGI Origin 200
 - CPU: 180 Mhz - MIPS R10000
 - L2-Cache: 120 Mhz - 1MB
 - Memory: 512 MB
 - Operating System: Irix 6.5
 - Compiler: MIPSpro f90 version 7.2.1
- 3) 4-CPU - SGI 1400L
 - CPU: 500 Mhz - Intel Pentium III Xeon
 - L2-Cache: 500 Mhz - 2MB
 - Memory: 1 GB
 - Operating System: Linux 2.2.5 (Red Hat 6.0)
 - Compiler: PGI pgf90 version 3.1-1
- 4) 2-CPU - VA Linux StartX MP Workstation
 - CPU: 500 Mhz - Intel Pentium III
 - L2-Cache: 250 Mhz - 512KB
 - Memory: 256 MB
 - Operating System: Linux 2.2.7 (Red Hat 6.0)

- Compiler: PGI pgf90 version 3.1-1

Hardware-wise we were interested both in the relative performance of Intel-based computers compared with MIPS-based computers, as well as the absolute parallel efficiency of Intel-based computers when running multi-threaded applications. In particular, we tried to analyze the following issues regarding Intel-based multiprocessor performances:

- Floating-point performance.
- Effects of different secondary cache sizes (2MB and 512KB) and speeds (255 Mhz and 500 Mhz) on performance of production runs.
- Problems caused by memory-access conflicts when running multi-threaded applications.

To answer these questions in a context as much relevant as possible with our environment, we run three different programs that cover the most of the types of computations that we routinely perform: a FFT-intensive split-step migration, a Kirchhoff migration, and an implicit finite-difference migration.

SPLIT-STEP MIGRATION

This test was performed using the Gendown3D package that has been used to perform common-azimuth migration (Biondi, 1999) and wave-equation migration velocity analysis (Biondi and Sava, 1999). The package has been developed to facilitate the implementation of a wide range of frequency-domain depth-continuation operators, their adjoint operators, and their related scattering operators (Biondi and Sava, 1999). It is targeted to coarse-grain shared-memory multi-processors architectures, like our Power Challenge, and achieves good parallel performances. However, flexibility of the package and simplicity of the module implementing the individual operators had higher priority than efficiency. No attempt at all was made to optimize the single-processor performance for cache-based systems.

The package is multi-threaded across frequencies for each depth-continuation step. Each thread performs computations independently on a different slice of the data, including the FFTs and the application of the phase-shift operator. The summation over frequency is performed serially, as well as the I/O for both the data and the velocity function. The velocity function is shared (not replicated) between threads.

A few changes needed to be done to the code to make it run correctly on the PGI compiler. The most significant, and annoying of them, was related to F90 allocatable arrays. The PGI compiler requires the program to allocate these arrays when passed as arguments to lower level subroutines, even when they are never used in the computations. A simple work-around, to avoid allocating more memory than necessary, is to allocate these arrays with the axes length of one when they are not used.

To analyze the effects of out-of-cache computations, we run the benchmarks on two different sized problems. A “small problem”, for which two frequency slices (one for the input and one for the output) fitted into the L2-caches of all computers tested, and a “large problem” for which two frequency slices did not fit into the L2-caches of any of the computers tested.

On the SGI platforms, the package usually uses the FFTs provided by SGI mathematical libraries. Obviously, these libraries are not available (yet?) on Linux platforms. Therefore, we downloaded a public domain FFT library called FFTW (Frigo and Johnson, 1999). This library achieves good performances, and is quite flexible. It supports multi-dimensional FFTs with arbitrary lengths of the axes, and a flag (`FFTW_THREADSafe`) can be set during initialization to make safe sharing some pre-computed data (e.g., table of twiddle factors) between threads. We run the benchmarks with both the SGI native FFTs and the FFTW library and show the results for both cases. It turns out that the FFTW library is somewhat slower than the native SGI library, but it achieves respectable performances, on the Power Challenge. On the Origin 200 it is considerable slower than the native library even on a single processor. This slow down is more pronounced for out-of-cache problems than for in-cache ones.

To average-out abnormal temporary system behavior, the tests were run on many depth steps for a total computation time of at least five minutes even for the small problem running on several CPUs.

Small problem results

First, we analyze the results for the small problem. We display the results as relative speeds normalized by the speed achieved on one CPU of the Power Challenge by the program using the public domain FFT library; that is, the slowest possible run. The relative speeds are computed from elapsed time measured on systems as empty as possible.

Figure 1 shows these relative speeds for all the computations performed to solve the small problem, excluded one-time initializations. The measured speed are plotted with solid lines, while the dashed lines correspond to the ideal parallel speed up for each program. As expected, the slowest runs were on the Power Challenge (lines labeled 1 and 2), that is also the oldest among the computers we tested.

The four-processor Xeon (line 6) is the fastest of all computers, running even faster than the O200 with native FFTs (line 4). The dual-processor Pentium III (line 5) runs slightly slower than the Xeon, likely because of the slower I/O. The parallel speed-up for all cases is reasonable, though for such small problem the serial I/Os handicap the parallel runs.

Figure 2 shows the relative speeds for the whole parallel portion of the code. A good parallel speed-up is achieved in all cases, indicating that when the problem fits in cache there is no degradation of performances caused by contentions between threads in accessing memory. The dual-processor Pentium III runs about 10% slower than the Xeon, and shows slightly worse parallel speed-up. Since the CPU run at the same speed, this difference can be attributed to the smaller and slower secondary cache.

Figure 3 shows the relative speeds for the FFTs, and has a similar interpretation as Figure 2.

Notice, that this is the case for which the Xeon out-performs the Power Challenge the most, with the four processors running about fourteen times faster than one R8000. The Origin 200 and the dual-processor Pentium III scale the worse for the FFTs, probably because of slower caches.

Large problem results

Next, we analyze the results for the large problem. Figure 4 shows the relative speeds for all the computations performed to solve the large problem, excluded one-time initializations. In relative terms, the SGIs performs better than Intel-based computers for this large problems, both as single-CPU speed and as parallel speed up. The MIPS-processors' performances are less affected by out-of-cache computations than the Pentium III's because the memory bandwidth of the SGI systems is better balanced with the CPU speed. Actually, for the large problem, the parallel speed-up improves on the SGIs because the large problem is more computationally intensive than the small one, and thus the serial I/O are less of an handicap. On the contrary, the parallel speed-up of the Pentiums is little worse than for the small problems. This is a possible indication of memory contentions between threads in accessing memory.

Figure 5 shows the relative speeds for all the computations performed in parallel. The SGIs show almost perfect parallel speed-up, indicating no contentions in accessing memory. On the contrary, the parallel speed-up on the Xeon is similar to the one shown in Figure 4, indicating that the loss in parallel efficiency is likely caused by memory contentions, and not by the serial I/Os. Somewhat surprisingly, the FFTs seem to run in parallel without loss of performances on all machines (Figure 6), with the exception of the dual-processor Pentium. It is possible that the memory access pattern of FFTs benefits from the larger and faster caches more than the rest of the computations.

KIRCHHOFF MIGRATION

Ideally, Kirchoff offset migration can be written to be almost perfectly parallel. Each node can be given a region of image space and the data within a given aperture of the imaging volume. Each node then independently read in the portion of the traveltimes table it needs, and sum the corresponding input data to form the output model. No communication between nodes is needed until all threads have finished their given imaging volumes.

Such an implementation was not possible for this test. In order to implement the parallel scheme above, each processor must be able to seek and read the traveltimes table while no other thread is operating on the file. OpenMP, accounts for such difficulty with the `CRITICAL` construct. Unfortunately, the `CRITICAL` construct is not handled correctly by the Portland Group's `pgf90` compiler. To overcome this limitation a section of the traveltimes were read in and then the output CMP's within this region were parallelized over.

For each of the four computers, we tested the speed both within the parallel region (Figure 7), and of the entire program (Figure 8). Within the parallel region all four machines

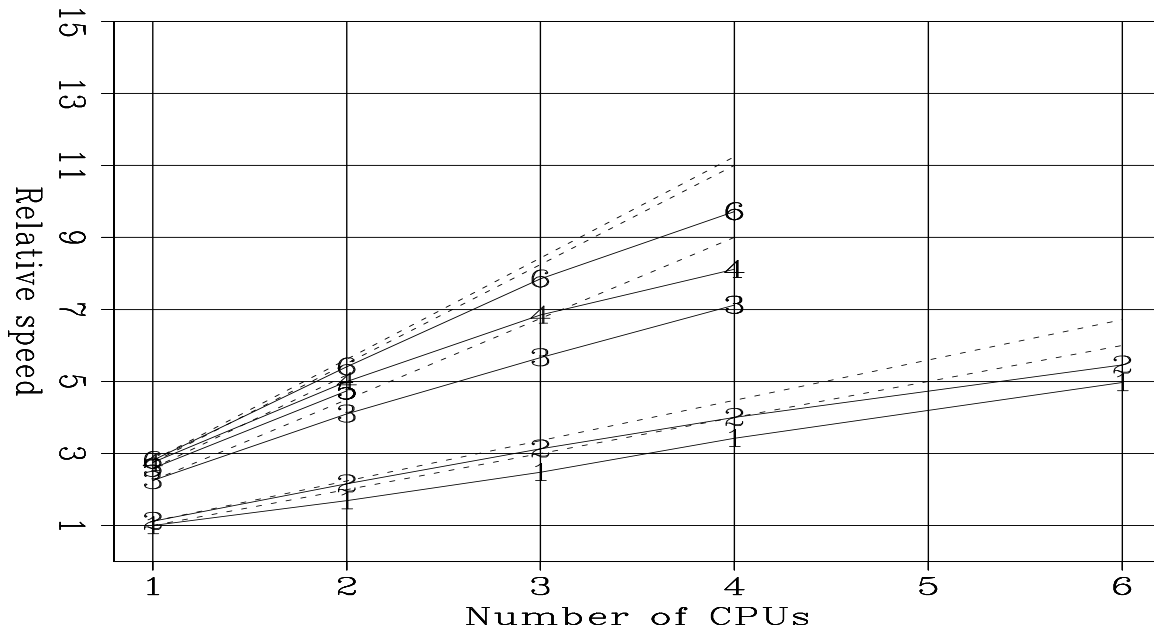


Figure 1: Relative speeds as a function of number of CPU for all the computations in the small problem: 1) Power Challenge (FFTW), 2) Power Challenge (SGILIB), 3) O200 (FFTW), 4) O200 (SGILIB), 5) Dual-processor Pentium III (FFTW), 6) Four-processor Xeon (FFTW). One processor Power Challenge has a speed of 1. The dashed lines correspond to the ideal parallel speed up. `biondo2-Small-All` [NR]

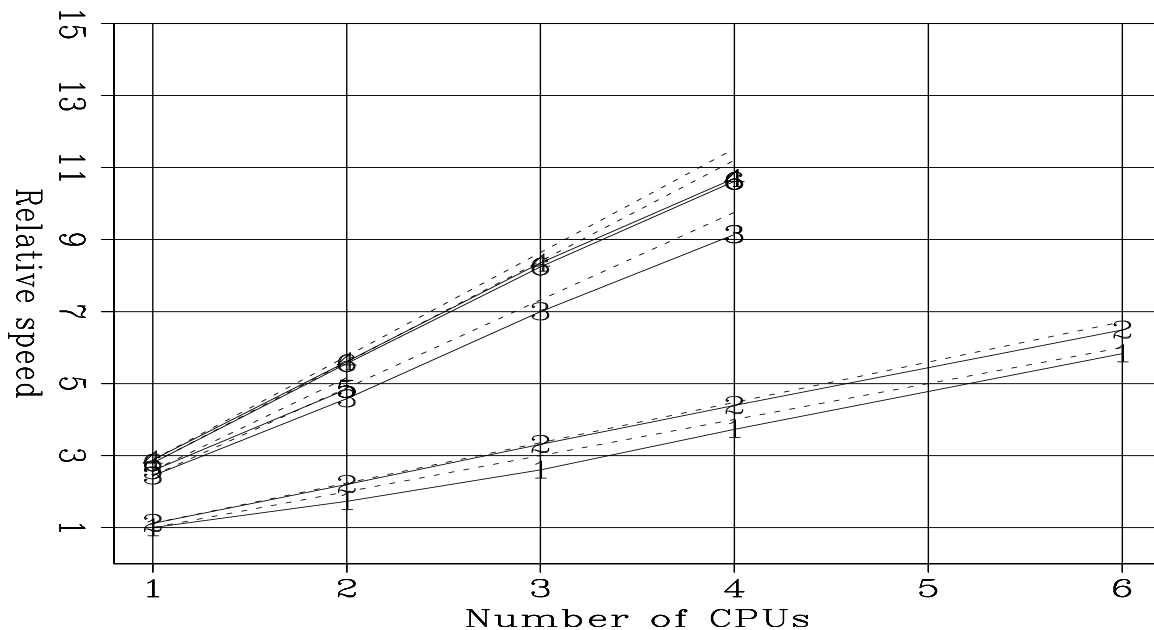


Figure 2: Relative speeds as a function of number of CPU for all the parallel computations in the small problem: 1) Power Challenge (FFTW), 2) Power Challenge (SGILIB), 3) O200 (FFTW), 4) O200 (SGILIB), 5) Dual-processor Pentium III (FFTW), 6) Four-processor Xeon (FFTW). One processor Power Challenge has a speed of 1. The dashed lines correspond to the ideal parallel speed up. `biondo2-Small-par-All` [NR]

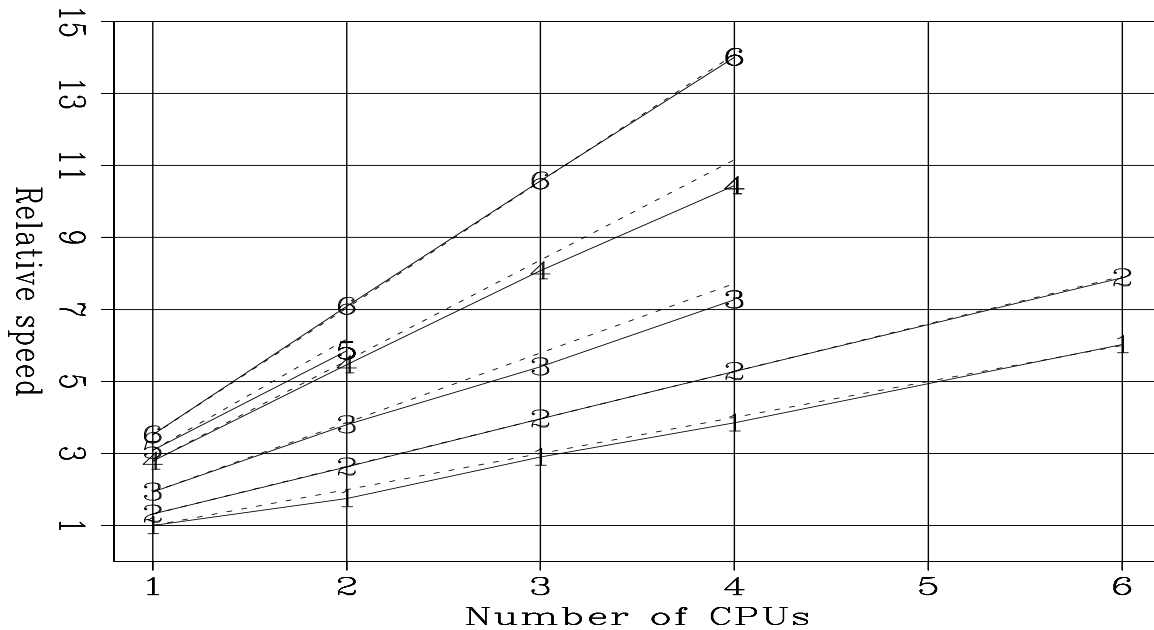


Figure 3: Relative speeds as a function of number of CPU for the computations of the FFTs in the small problem: 1) Power Challenge (FFTW), 2) Power Challenge (SGILIB), 3) O200 (FFTW), 4) O200 (SGILIB), 5) Dual-processor Pentium III (FFTW), 6) Four-processor Xeon (FFTW). One processor Power Challenge has a speed of 1. The dashed lines correspond to the ideal parallel speed up. `biondo2-Small-fft-All` [NR]

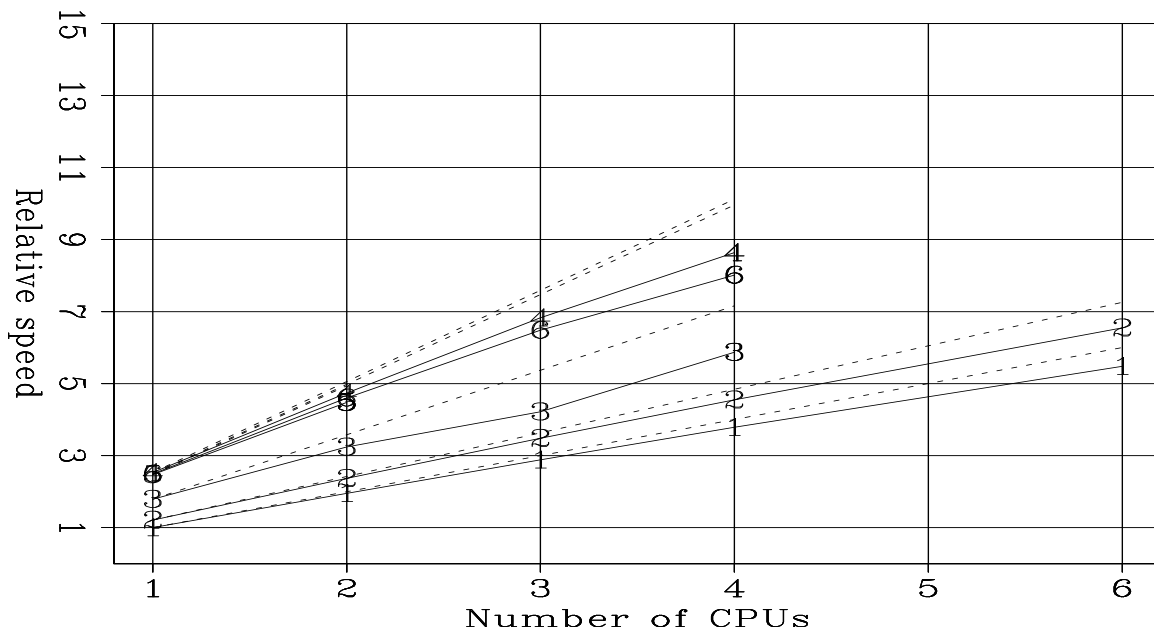


Figure 4: Relative speeds as a function of number of CPU for all the computations in the large problem: 1) Power Challenge (FFTW), 2) Power Challenge (SGILIB), 3) O200 (FFTW), 4) O200 (SGILIB), 5) Dual-processor Pentium III (FFTW), 6) Four-processor Xeon (FFTW). One processor Power Challenge has a speed of 1. The dashed lines correspond to the ideal parallel speed up. `biondo2-Large-All` [NR]

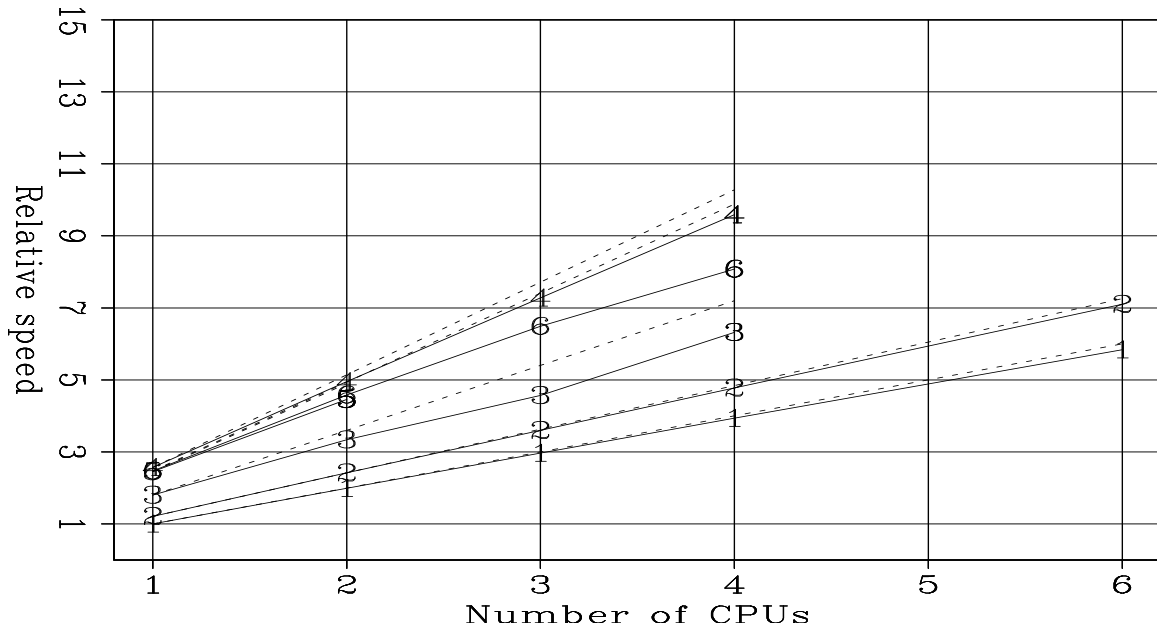


Figure 5: Relative speeds as a function of number of CPU for all the parallel computations in the large problem: 1) Power Challenge (FFTW), 2) Power Challenge (SGILIB), 3) O200 (FFTW), 4) O200 (SGILIB), 5) Dual-processor Pentium III (FFTW), 6) Four-processor Xeon (FFTW). One processor Power Challenge has a speed of 1. The dashed lines correspond to the ideal parallel speed up. `biondo2-Large-par-All` [NR]

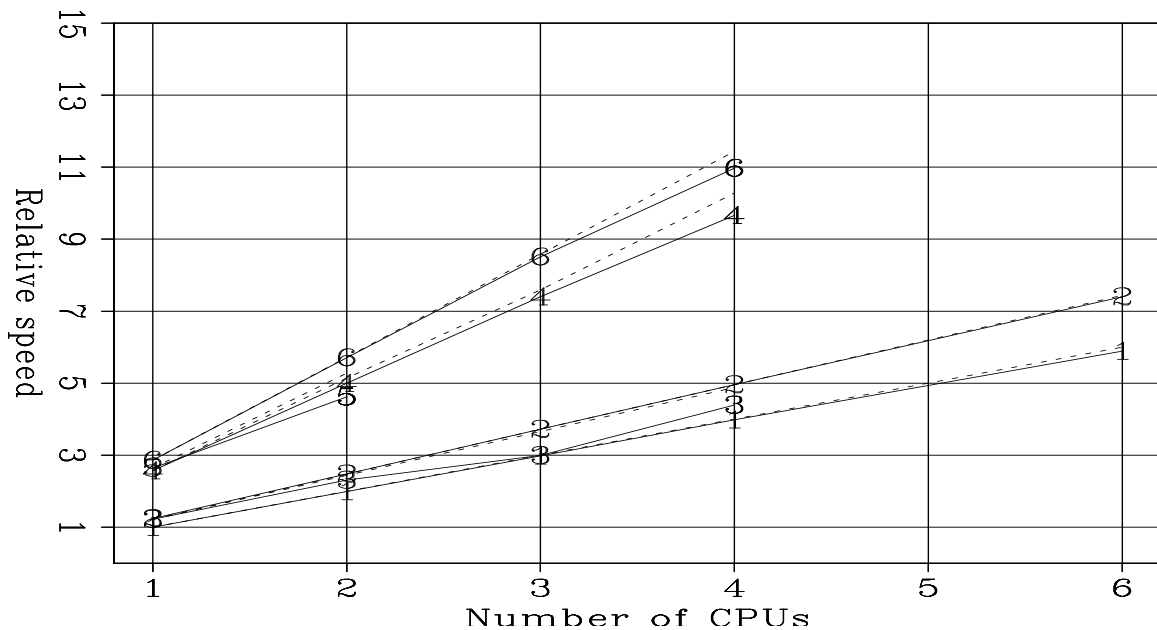


Figure 6: Relative speeds as a function of number of CPU for the computations of the FFTs in the large problem: 1) Power Challenge (FFTW), 2) Power Challenge (SGILIB), 3) O200 (FFTW), 4) O200 (SGILIB), 5) Dual-processor Pentium III (FFTW), 6) Four-processor Xeon (FFTW). One processor Power Challenge has a speed of 1. The dashed lines correspond to the ideal parallel speed up. `biondo2-Large-fft-All` [NR]

scaled fairly well. The notable exception being the Origin 200 when going across the Cray Link cable (from two to three processors). For overall speed within the parallel region the Xeon four-processor machine performed the best.

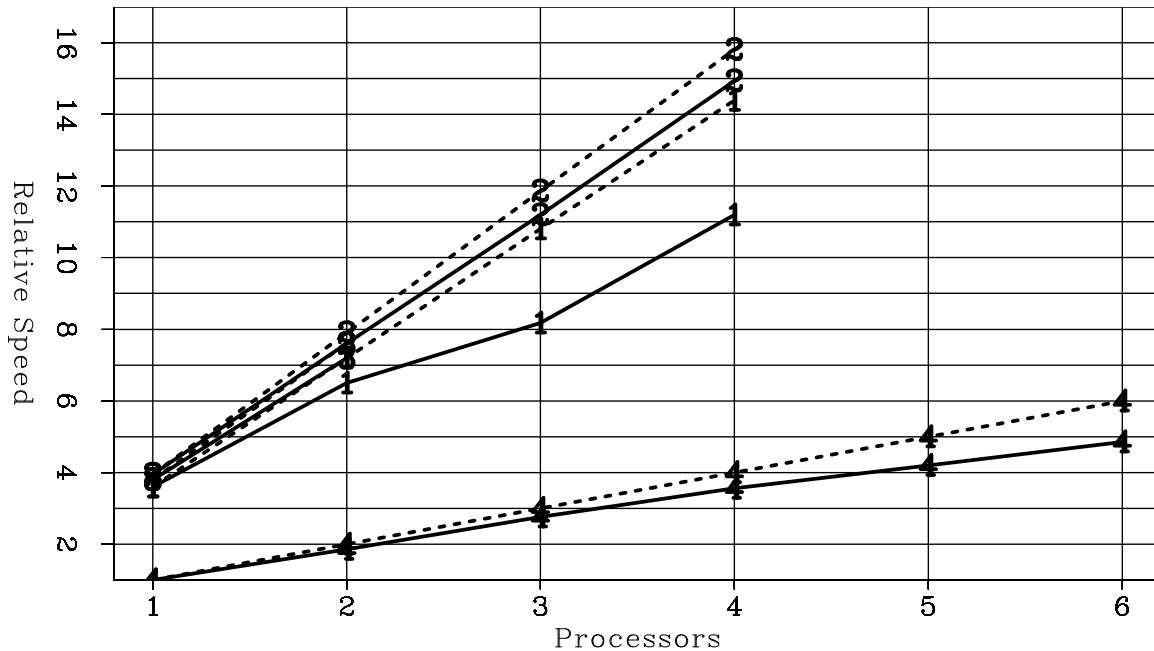


Figure 7: Relative speed of the parallel portion of the Kirchoff migration on the various testing platforms. **1** represents the SGI, Origin 200; **2** is the SGI 1400L ; **3** is the VA Start X MP; and **4** is the SGI Power Challenge. In each case the solid line represent actual performance, the dashed lines ideal performance. `biondo2-kirch.par` [NR]

For the entire code the results were more interesting. Because Kirchoff migration is so I/O intensive, the performances of the machine's I/O became important. Where the advantage of the Xeon versus the Power Challenge was nearly 4:1 on four processors within the parallel region it was only 2.5:1 when I/O was taken into account. The VA Start X performed particularly poorly when accounting for I/O. Its speed advantage compared to the Power Challenge dropped from 3.9 to 2.1 when accounting for I/O. The VA's I/O problem seems to be more hardware rather than OS related. The Xeon was running the same OS, and saw its speed advantage drop only from 4.1 to 2.7.

PGF90 compiler issues

To make the performance testing as equivalent as possible it was necessary to write a code that worked on the subset of OpenMP features supported by the SGI and Portland Group compilers. For these tests the limiting factor was definitely the Portland Group's F90 compiler. In the process, we encountered a number of bugs/features with the Portland Group's compiler:

CRITICAL: The critical region statement did not function properly.

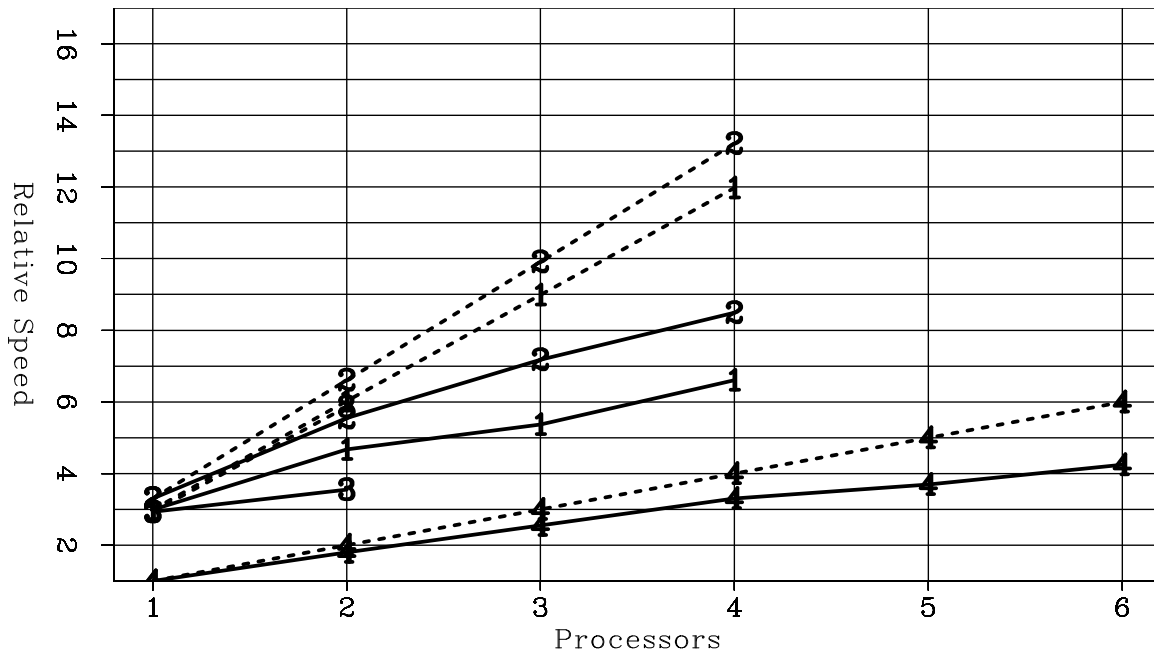


Figure 8: Relative speed of the total execution time of the Kirchoff migration on the various testing platforms. **1** represents the SGI, Origin 200; **2** is the SGI 1400L ; **3** is the VA Start X MP; and **4** is the SGI Power Challenge. In each case the solid line represent actual performance, the dashed lines ideal performance. `biondo2-kirch.tot` [NR]

array sections: Passing array sections through to subroutine was prone to produce incorrect results.

pointer arrays and C: The compiler sometimes had trouble communicating with gcc when passing F90 pointer arrays. This is not really a bug because according to F90 specifications the memory layout of pointer arrays is not defined. However, all other F90 compilers we used so far interface with gcc without problems.

IMPLICIT FINITE-DIFFERENCE MIGRATION

The third and final test benchmarking test was the migration of 2-D prestack and 3-D post-stack datasets with implicit finite-differences. The code used for these tests was developed to implement a range of wavefield extrapolation operators, including implicit finite-difference migration in the helical coordinate system (Rickett et al., 1998). For these benchmarking test cases, we used the 65° operator described by Lee and Suh (1985), and for the 3-D test, rather than inverting the full extrapolation matrix, we made the splitting approximation. We used the LAPACK (Anderson et al., 1995) subroutine `cgtsv` to solve the resulting tridiagonal systems.

Compiler notes

The code was written in vanilla Fortran90 with OpenMP compiler directives, to ensure a level of portability. Initial development was done simultaneously on the SGI platform, and a Linux workstation with the NAGware F90 compiler, again for reasons of portability. Unfortunately, when recompiling the code on with the Portland Group F90 compiler, we ran into the compiler bugs described above that necessitated rewriting of large portions of the code.

Results

Figures 9 and 10 show the finite-difference benchmark results for the four platforms. As in the previous tests there was little separating the MIPS-based quad processor SGI with the Intel Xeon-based quad processor Linux. The results appear to be similar to the larger split-step migration benchmark.

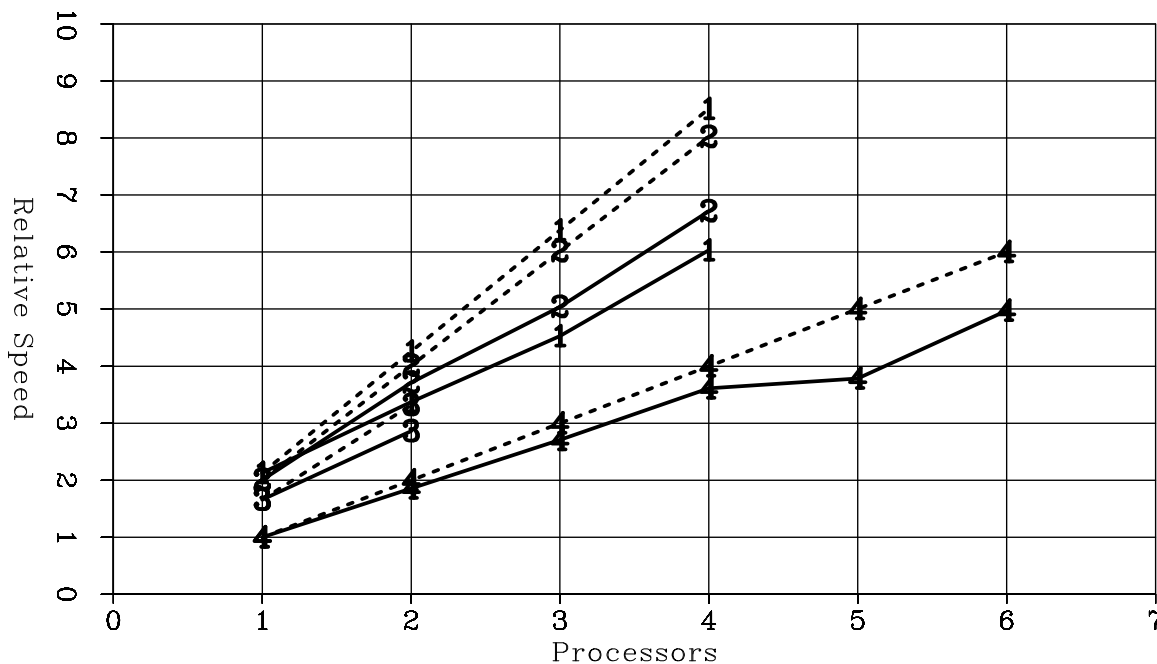


Figure 9: Relative speed of the parallel portion of the finite-difference migration on the various testing platforms. **1** represents the SGI, Origin 200; **2** is the SGI 1400L ; **3** is the VA Start X MP; and **4** is the SGI Power Challenge. In each case the solid line represent actual performance, the dashed lines ideal performance. `biondo2-fdmig.par` [NR]

CONCLUSIONS

The computational speed and the I/O speed achieved by the Linux server (SGI 1400L) when running our benchmarks give us confidence that we can run efficiently “production” codes

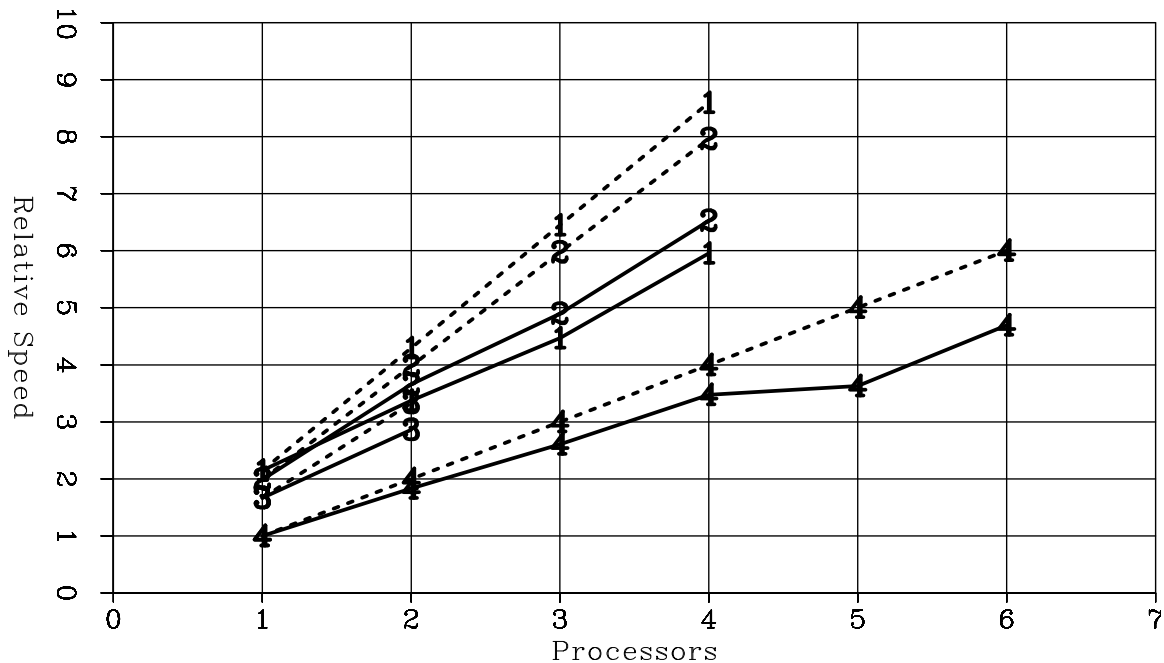


Figure 10: Relative speed of the total execution time of the finite-difference migration on the various testing platforms. **1** represents the SGI, Origin 200; **2** is the SGI 1400L ; **3** is the VA Start X MP; and **4** is the SGI Power Challenge. In each case the solid line represent actual performance, the dashed lines ideal performance. `biondo2-fdmig.tot` [NR]

on Intel-based multi-processors running Linux as OS. The price-performances of these systems are very attractive compared with the MIPS-based SGI systems. One drawback of the Linux-Intel solution is that only four-processor systems are available at the moment, and eight-processor systems in the near future. SGI's Origin 2000 can scale up to 128 processors. However, the price-performances of the Origin 2000 is not attractive when compared with clustering several Intel based multi-processors.

We measured a slight difference in computational performances between the dual-processor Pentium and the four-processor Xeon; but probably these differences are not enough to justify the large cost differential between Pentium III processors with small caches (512 KB) and large caches (2MB). The substantial difference in I/O performance between the two systems is safely attributable to the fact that the dual-processor system was packaged as a workstation instead of as a server.

The Portland Group's F90 compiler proved to be a workable solution to compile our F90 codes. It generates efficient code, though it does not support all F90 and OpenMP features as robustly as we wished. Being a relatively new product, we are confident that the problems we observed will rapidly disappear as new versions are released.

ACKNOWLEDGMENTS

We are grateful to SGI for loaning SEP the 1400L system that we used for our tests. We are also grateful to PGI for granting us several extensions to our evaluation licenses for the `pgf90` compiler, and for giving us access to a pre-release version of their 3.3-1 release.

REFERENCES

- Anderson, E., Bai, Z., Bischof, C., Demmel, J., and Dongarra, J., 1995, *Lapack users' guide: Release 2.0*: Society for Industrial and Applied Mathematics, 2nd edition.
- Biondi, B., and Sava, P., 1999, Wave-equation migration velocity analysis: *SEP-100*, 11–34.
- Biondi, B., 1999, Subsalt imaging by common-azimuth migration: *SEP-100*, 113–124.
- Frigo, M., and Johnson, S. G., 1999, FFTW: <http://www.fftw.org/>.
- Lee, M. W., and Suh, S. Y., 1985, Optimization of one-way wave-equations (short note): *Geophysics*, **50**, no. 10, 1634–1637.
- Rickett, J., Claerbout, J., and Fomel, S., 1998, Implicit 3-D depth migration by wavefield extrapolation with helical boundary conditions: *SEP-97*, 1–12.

Short Note

Reproducible research - results from SEP-100

Marie L. Prucha, Robert G. Clapp, Sergey Fomel, Jon Claerbout, and Biondo Biondi¹

INTRODUCTION

SEP has been striving to create reproducible research for many years. Our first attempts at reproducible documents began with the introduction of interactive documents (Claerbout, 1990). We then moved on to putting SEP reports on CDROMs and using “cake” (Nichols and Cole, 1989) so that the results could be recreated using the author’s own processing flow. Later we updated to the GNU make system (Schwab and Schroeder, 1995). Now SEP reports are available online and can be downloaded. Sponsors can see exactly how most of the figures in each paper are created, and those with the type of environment we have at SEP can recreate most of the figures themselves. This paper will explain what we consider reproducible research to be, why we go through the effort of making our research reproducible, how we test reproducibility, and the results of the testing on our last report, SEP-100.

REPRODUCIBLE RESEARCH

Reproducible research can be easily recreated by people other than the author. Whenever possible, the authors of SEP papers make their figures either easily reproducible (ER) or conditionally reproducible (CR). An easily reproducible figure can be deleted and quickly rebuilt by anyone interested in the result. To recreate the figure, the author provides the necessary input data, makerules, parameter files, and source code. A conditionally reproducible figure can be reproduced, but it may require input data that is not provided because of size or proprietary issues, special system requirements such as parallel processing or special software, or it may take more than 20 minutes to rebuild. Both ER and CR figures assume that the environment they are being recreated in has X-windows, SEPlib, SEP makerules, and Fortran77, Fortran90 and C compilers. If a figure can’t be reproduced, such as a hand-drawn picture, it is marked NR for non-reproducible.

¹email: marie@sep.Stanford.EDU, bob@sep.Stanford.EDU, sergey@sep.Stanford.EDU,
jon@sep.Stanford.EDU, biondo@sep.Stanford.EDU

IMPORTANCE OF REPRODUCIBILITY

We feel that reproducibility is important for helping other researchers understand and build from our research. Any other researcher can see exactly how each reproducible figure is created. Reproducibility also allows the author to go back to old work and try new ideas. Many SEP students rely heavily on the reproducibility of their old reports when thesis-writing time arrives.

TESTING REPRODUCIBILITY

Each SEP report is tested for reproducibility. Each paper is tested in four categories: ER reproducibility, CR reproducibility, clean rules, and independence. ER figure reproducibility is tested by deleting all ER figures and attempting to rebuild them using the author's makerules. All CR figures are checked to make certain that they do have accurate makerules. The clean rule check means that no files except the ER figures should be created in the build process, no files other than the results exist in the results directory, and no object or binary files exist after the clean rules are run. Finally, no makerules may attempt to access binaries outside of the paper directory. These requirements are considerably stricter than they have been in past years.

RESULTS FROM THE LAST REPORT

The testing of SEP-100 was completed before it was made available as an electronic document last spring. All testing was carried out on an IRIX 6.5 operating system. The ER testing was done first. The results are shown in the following table.

Testing Round	No. of ER figs	No. that failed	% that passed
1	95	7	92.6%
2	93	2	97.8%
3	93	0	100.0%

The CR testing was carried out on a paper-by-paper basis. If one CR figure failed, the paper failed. The results are in the following table.

Testing Round	No. of CR figs	No. of papers	No. that failed	% that passed
1	105	22	10	54.5%
2	105	22	2	90.9%
3	105	22	0	100.0%

The NR figures were examined by the editors of each paper to determine if the figure should be considered non-reproducible or if the author needed to try to make it reproducible. There were 48 NR figures before the reproducibility testing for the ER and CR figures began and 50 NR figures after the testing was complete.

CONCLUSIONS

Overall, the reproducibility of SEP-100 was good, even before the testing. Testing on this report (SEP-102) is in progress.

REFERENCES

- Claerbout, J. F., 1990, Active documents and reproducible results: SEP-**67**, 139–144.
- Nichols, D., and Cole, S., 1989, Device independent software installation with CAKE: SEP-**61**, 341–344.
- Schwab, M., and Schroeder, J., 1995, Reproducible research documents using GNUmake: SEP-**89**, 217–226.

SEP ARTICLES PUBLISHED OR IN PRESS

- Alkhalifah, T., Biondi, B., and Fomel, S., 1998, Time-domain processing in arbitrarily inhomogeneous media: 68th Ann. Internat. Meeting, Soc. Expl. Geophys., Expanded Abstracts, 1756–1759.
- Alkhalifah, T., 1998, An acoustic wave equation for anisotropic media: 68th Ann. Internat. Meeting, Soc. Expl. Geophys., Expanded Abstracts, 1913–1916.
- Bachrach, R., and Rickett, J., 1999, Ultra shallow seismic reflection in depth: examples from 3D ultra shallow survey with application to joint seismic and GPR imaging: 69th Ann. Internat. Meeting, Soc. Expl. Geophys., Expanded Abstracts, 488–491.
- Biondi, B., and Sava, P., 1999, Wave-equation migration velocity analysis: 69th Ann. Internat. Meeting, Soc. Expl. Geophys., Expanded Abstracts, 1723–1726.
- Biondi, B., Fomel, S., and Chemingui, N., 1998, Azimuth moveout for 3-D prestack imaging: *Geophysics*, **63**, no. 2, 574–588.
- Biondi, B., 1998a, Azimuth moveout vs. dip moveout in inhomogeneous media: 68th Ann. Internat. Meeting, Soc. Expl. Geophys., Expanded Abstracts, 1740–1743.
- Biondi, B., 1998b, Cost-effective prestack depth imaging of marine data: Ann. Internat. Meeting, Offshore Technology Conference.
- Biondi, B., 1998c, Robust reflection tomography in the time domain: 68th Ann. Internat. Meeting, Soc. Expl. Geophys., Expanded Abstracts, 1847–1850.
- Chemingui, N., and Biondi, B., 1999, Data regularization by inversion to common offset (ICO): 69th Ann. Internat. Meeting, Soc. Expl. Geophys., Expanded Abstracts, 1398–1401.
- Claerbout, J., 1998a, Multidimensional recursive filters via a helix: *Geophysics*, **63**, 1532–1541.
- Claerbout, J., 1998b, Multidimensional recursive filters via a helix with application to velocity estimation and 3-D migration: 68th Ann. Internat. Meeting, Soc. Expl. Geophys., Expanded Abstracts, 1995–1998.
- Clapp, R., Biondi, B., Fomel, S., and Claerbout, J., 1998, Regularizing velocity estimation using geologic dip information: 68th Ann. Internat. Meeting, Soc. Expl. Geophys., Expanded Abstracts, 1851–1854.
- Crawley, S., Clapp, R., and Claerbout, J., 1999, Interpolation with smoothly nonstationary prediction-error filters: 69th Ann. Internat. Meeting, Soc. Expl. Geophys., Expanded Abstracts, 1154–1157.
- Crawley, S., 1998, Shot interpolation for Radon multiple suppression: 68th Ann. Internat. Meeting, Soc. Expl. Geophys., Expanded Abstracts, 1238–1241.

- Guitton, A., and Symes, W. W., 1999, Robust and stable velocity analysis using the Huber function: 69th Ann. Internat. Meeting, Soc. Expl. Geophys., Expanded Abstracts, 1166–1169.
- Prucha, M., Biondi, B., and Symes, W., 1999, Angle-domain common-image gathers by wave-equation migration: 69th Ann. Internat. Meeting, Soc. Expl. Geophys., Expanded Abstracts, 824–827.
- Rickett, J., and Claerbout, J., 1999a, Acoustic daylight imaging via spectral factorization: Helioseismology and reservoir monitoring: 69th Ann. Internat. Meeting, Soc. Expl. Geophys., Expanded Abstracts, 1675–1678.
- Rickett, J., and Claerbout, J., 1999b, Acoustic daylight imaging via spectral factorization: Helioseismology and reservoir monitoring: *The Leading Edge*, **18**, 957–960.
- Rickett, J., and Claerbout, J., 1999c, Time-distance helioseismology, spectral factorization and hydrocarbon reservoir monitoring: Time-distance helioseismology, spectral factorization and hydrocarbon reservoir monitoring:, The 9th SOHO Workshop, “Helioseismic Diagnostics of Solar Convection and Activity”.
- Sava, P., and Fomel, S., 1998, Huygens wavefront tracing: A robust alternative to ray tracing: 68th Ann. Internat. Meeting, Soc. Expl. Geophys., Expanded Abstracts, 1961–1964.
- Sava, P., and Fomel, S., 2001, 3-D travelttime computation by Huygens wavefront tracing: *Geophysics*, **66**, no. 3, in press.

SEP PHONE DIRECTORY

Name	Phone	Login Name
Berryman, James	723-1250	berryman
Biondi, Biondo	723-1319	biondo
Brown, Morgan	723-6006	morgan
Claerbout, Jon	723-3717	jon
Clapp, Robert	723-0253	bob
Crawley, Sean	723-0253	sean
Fomel, Sergey	725-1334	sergey
Gratwick, Douglas	723-5647	doug
Guitton, Antoine	723-6007	antoine
Lau, Diane	723-1703	diane
Mora, Carmen	723-5911	cmora
Prucha, Marie	723-0253	marie
Rickett, James	723-6007	james
Rosales, Daniel	723-5647	daniel
Sava, Paul	723-0463	paul
Vaillant, Louis	723-0463	louis

SEP fax number: (650) 723-0683

E-MAIL

Our Internet address is “sep.stanford.edu”; i.e., send Jon electronic mail with the address “jon@sep.stanford.edu”.

WORLD-WIDE WEB SERVER INFORMATION

The current login name for the sponsors' area on our world-wide web server (<http://sepwww.stanford.edu>) is “sepsponsor2”. The current password is: ss2&sep2

Research Personnel

James G. Berryman received a B.S. degree in physics from Kansas University (Lawrence) in 1969 and a Ph.D. degree in physics from the University of Wisconsin (Madison) in 1975. He subsequently worked on seismic prospecting at Conoco. His later research concentrated on sound waves in rocks – at AT&T Bell Laboratories (1978-81) and in Earth Sciences at Lawrence Livermore National Laboratory (1981-). He is currently a physicist in the Earth and Environmental Sciences Directorate at LLNL. Continuing research interests include seismic and electrical methods of geophysical imaging and waves in porous media containing fluids. He is a member of APS, AGU, SEG, and EEGS.



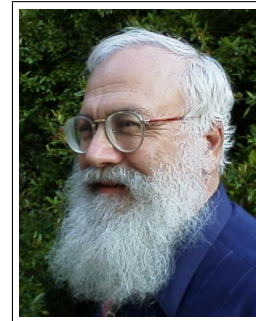
Biondo L. Biondi graduated from Politecnico di Milano in 1984 and received an M.S. (1988) and a Ph.D. (1990) in geophysics from Stanford. SEG Outstanding Paper award 1994. During 1987 he worked as a Research Geophysicist for TOTAL, Compagnie Francaise des Petroles in Paris. After his Ph.D. at Stanford Biondo worked for three years with Thinking Machines Co. on the applications of massively parallel computers to seismic processing. After leaving Thinking Machines Biondo started 3DGeo Development, a software and service company devoted to high-end seismic imaging. Biondo is now Associate Professor (Research) of Geophysics and leads SEP efforts in 3-D imaging. He is a member of SEG and EAGE.



Morgan Brown received a B.A. in Computational and Applied Mathematics from Rice University in 1997 and is currently completing a Ph.D. at SEP. Morgan worked as a research intern with Western Geophysical in 1997 and with Landmark Graphics in 2000. He is a member of SEG.



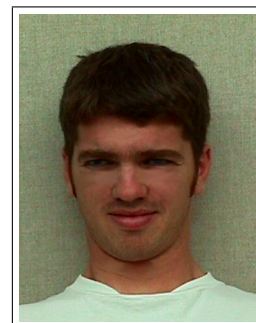
Jon F. Claerbout (M.I.T., B.S. physics, 1960; M.S. 1963; Ph.D. geophysics, 1967), professor at Stanford University, 1967. Best Presentation Award from the Society of Exploration Geophysicists (SEG) for his paper, *Extrapolation of Wave Fields*. Honorary member and SEG Fessenden Award “in recognition of his outstanding and original pioneering work in seismic wave analysis.” Founded the Stanford Exploration Project (SEP) in 1973. Elected Fellow of the American Geophysical Union. Authored three published books and five internet books. Elected to the National Academy of Engineering. Maurice Ewing Medal, SEG’s highest award. Honorary Member of the European Assn. of Geoscientists & Engineers (EAGE). EAGE’s highest recognition, the Erasmus Award.



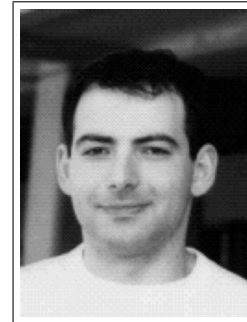
Robert Clapp received his B.Sc.(Hons.) in Geophysical Engineering from Colorado School of Mines in May 1993. He joined SEP in September 1993, received his Masters in June 1995, and his Ph.D. in December 2000. He is a member of the SEG and AGU.



Sean Crawley Graduated from Arizona, joined SEP, and best of all got married in 1994. He received his Masters in 1996. His current research interests are interpolation and multiple suppression.



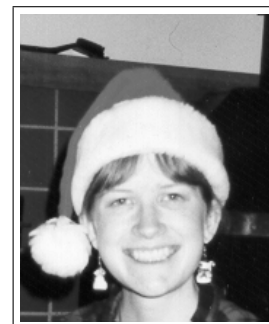
Sergey Fomel received his Diploma in Geophysics from Novosibirsk University in 1990. From 1990 to 1994 he worked at the Institute of Geophysics (Siberian Branch of the Russian Academy of Sciences) in Novosibirsk. He joined the Stanford Exploration Project in 1994 and received a Ph.D. in Geophysics in 2001. During six months of 1998 Sergey worked at Schlumberger/Geco-Prakla in England. He is a member of SEG, AGU, and SIAM.



Carmen Mora received her B.S. in Computer Engineering (1986) and her M.S. in Computer Science (1992) from Universidad Simon Bolivar, Venezuela. From 1986 to 1994 she worked as a system developer and system administrator in UNIX platforms. She has been employed by PDVSA INTEVEP S.A. since 1993, working mainly in the development of scientific visualization tools for seismic data. In January 1999, she joined SEP and she received her M.S. degree in Geophysics in December 2000. She is currently working at PDVSA INTEVEP S.A.



Marie Prucha received her B.Sc.(Hons.) in Geophysical Engineering from Colorado School of Mines in May 1997. She joined SEP in September 1997 and received her MS in June 1999. She is currently working towards a Ph.D. in geophysics. She is a member of SEG.



James Rickett graduated with a B.A. in Natural Science from Cambridge University in 1994, and obtained an M.Sc. in Exploration Geophysics from Leeds University in 1995. He is currently working towards a Ph.D. in geophysics at Stanford, and is a member of the SEG and the EAGE.



Paul Sava graduated in June 1995 from the University of Bucharest, with an Engineering Degree in Geophysics. Between 1995 and 1997 he was employed by Schlumberger GeoQuest. He joined SEP in 1997, received his M.Sc. in 1998, and continues his work toward a Ph.D. in Geophysics. His main research interest is in seismic imaging using wave-equation techniques. He is a member of SEG, EAGE and the Romanian Society of Geophysics.



Louis Vaillant graduated from the Ecole des Mines de Paris (M.S.) and joined SEP in December 1998 for his military obligation, supported by Elf Exploration Production. He spent one summer with Elf UK at the Geoscience Research Centre in London (1997), and worked on earthquake rupture processes at the Ecole Normale Supérieure de Paris (1998). Louis' current research is on wave-equation migration. He is a member of SEG.



Yi Zhao received his B.S. degree in 1995 and M.S. degree in 1998 in Geophysics from University of Science and Technology of China (Hefei, China).



Sponsors of the Stanford Exploration Project, 1998-99